STUDIES IN LIQUID AND ION CHROMATOGRAPHY

By

AKINDE FLORENCE KADJO

DISSERTATION

Submitted in partial fulfillment of the requirements

for the degree of Doctor of Philosophy at

The University of Texas at Arlington

December, 2017

Arlington, Texas

Supervising Committee:

Purnendu K. Dasgupta, Supervising Professor

Kevin Schug

Krishnan Rajeshwar

Jongyun Heo

ACKNOWLEDGEMENTS

I am infinitely grateful to my research advisor Dr Dasgupta; I most likely wouldn't be an analytical chemist today without the valuable impact he had on me as a teacher when I was a student in his undergraduate quantitative Chemistry course. Thank you for believing in me more than I do myself. I can't find enough words to express how grateful I am, thank you for your patience, your support, your guidance and your teachings. I am blessed to be your student.

Thanks to my Committee members Kevin Schug, Krishnan Rajeshwar, and Jongyun Heo for your support and valuable input during my time at UTA.

Thank you to all of my coworkers and people that helped me during my time as a graduate student. I have learned greatly from each one of you and we have spent memorable moments together. Thank you Philip, Hongzhu, Brian, Dr Huang, Min, Chuchu, Fereshteh, Stephanie, Mai, Sajad, Younes, Bikash, Noohn, and Catrina.

I would also like to acknowledge Kannan Srinivasan, Daniel W. Armstrong and Farooq Wahab.

DEDICATION

To my parents Bosson and Akissi, thank you for being such wonderful parents, thank you for the sacrifices you made for my siblings and I, thank you for ingraining in us the love of sciences.

To my Aunt Magni, thank you for being there for my siblings and us, thank you for your support and your love. You are my role model.

To my uncle Hilaire and his wife Ginger, words cannot express how grateful I am to the both of you, I wouldn't be here getting a PhD without your support. Thank you for guiding us, for setting an example and for being our second parents here.

To my brothers and sisters David, Emma, Theo, Elodie and Danielle, thank you so much for your support, guidance, love and for being part of my life.

To my Aunt Marthe and Uncle Jacque, thank you for your support and love.

To my cousins Lydie and Sonia, thank you so much for your support and love.

So many people have influenced my life in so many ways; I would like to thank all of them even though I have not named them.

LIST OF FIGURES (or Illustrations)

LIST OF TABLES

ABSTRACT

STUDIES IN LIQUID AND ION CHROMATOGRAPHY

Akinde Florence Kadjo, Ph.D.

The University of Texas at Arlington, 2017

Supervising Professor: Purnendu K. Dasgupta

Height- and area-based quantitation approaches reduce two-dimensional data to a single value. For a calibration set, there is a single height- or area-based quantitation equation. We introduce a new quantitation method; a Width based method that consists of using the width of a peak ($\boldsymbol{W_h}$), at any height $\boldsymbol{h}$, (a fixed height, not a fixed fraction of the peak maximum), leading to any number of calibration curves. This particularity of width-based quantitation (WBQ) allows the quantitation of peaks over very large scales, making the quantitation of truncated peaks possible. We showed that WBQ can offer superior overall performance (lower root mean square relative error over the entire range) compared to area- or height-based linear regression methods, rivaling weighted linear regression, provided that response is uniform near the height used for width measurement. WBQ forces one to not ignore the 2-dimensionality of a peak and all of the information from the peak one can obtain; which allows the detection and quantitation of impurity down to 1% of impurity.

TABLE OF CONTENTS

CHAPTER ONE: Introduction

1.1 Introduction to the dissertation

My research throughout my graduate studies has been multifaceted, as encouraged by my advisor and immensely appreciated by me. In this dissertation, I have chosen to focus on the Width based characterization of chromatographic peaks. It is based on the following two papers: Analytical Chemistry, 2017, 89, 3884–3892[1] and Analytical Chemistry, 2017, 89, 3893–3900[2]. To better fit the dissertation format, they have been broken down into multiple chapters and reorganized to include the supporting information that were also part of the original paper. This work, that constitutes the main body of the dissertation, is introduced in section 1.2.

The other projects in which have participated in a major fashion are included in the appendices (A to C). Their relegation to the appendices is not suggestive of their importance or significance. However, unlike chapters 2-12, these are reproduced essentially as they were published. My minor but not insignificant contributions to other projects have also been listed in the appendixes (D to G). One of the thing that I have learned as a graduate student is that not all of the projects get to successful completion, so I have also listed and very briefly discussed projects that were left unfinished in appendix H. The projects that are currently ongoing and will hopefully get completed by the end of this term are listed in appendix I.

Appendix A is about a new way of quantitating the amount of blood in dry blood spots using Ring disk electrode conductometry[3]. Dry Blood Spots (DBS) analysis is widely used for screening neonatal metabolic disorders in most developed countries and for the detection of HIV/AIDS in third world countries. It consists of collecting blood samples directly from the punctured wound to a filter paper. The exact amount of blood in terms of volume, spotted of the paper, is unknown. Quantitative analysis requires the exact volume of blood in the punch. Current approaches to quantitate the blood volume are carried out using the spot area or better by sodium analysis, typically by flame photometry. The former

has a high error percentage due to the fact that the amount of blood per unit area actually depends on a number of factors, while the latter is a destructive technique that wastes almost half of the blood spot extract. We have shown electrical conductivity of the extract to be a reliable and nondestructive measure of quantifying blood volume in DBS, as blood electrolyte levels are relatively constant. This is also a rare example where a Ring Disk Electrode is used as a conductivity probe; the theoretical approaches to using one in a finite volume is outlined. I was the first author of the paper; it appeared in *Analytical Chemistry*.

Appendix B discusses the temporal change of ion composition in an area of unconventional oil and gas drilling. There is increasing concern about Produced water (from unconventional oil and gas drilling) contamination of groundwater in rural areas where private wells are the primary source of water for human consumption. The *temporal ion analysis of shallow groundwater in an area of unconventional oil and gas drilling* project is a part of a much bigger project involving the Dasgupta and the Schug lab for the comprehensive ground water analysis in the areas mentioned above that resulted in several papers.[4,5,6] My responsibility during the collaborative project was to perform Anions analysis through Ion Chromatography of the ground water samples. Rather than reproducing these papers in the appendix, I have chosen to summarize the particular aspect that emphasizes these data in this appendix. Therefore, I will focus on the change of major anions composition in the ground water wells over a 13 month period divided in 4 phases. All of the ion chromatographic data in these papers was generated by me.

Appendix C is a comment on a published article that purports to solve an important problem. The method, reported by a well-known Laboratory at the University of Zurich reported the rapid (under 1 min) measurement of blood cyanide.[7] In a 2012 article in the Royal Society of Chemistry Journal *Analytical Methods*, Männel Croisé and Zelder (Prof. Zelder is currently the head of the Graduate School in Chemical and Molecular Sciences at the University of Zurich) reported a method takes advantage of the binding of cyanocobinamide $CN(H_2O)Cbi^+$ and cyanide to form the complex dicyanocobinamide $(CN)_2Cbi$ which is spectrally distinct from the former. However the chemistry seemed to violate reported thermodynamic and kinetic data. We showed through experimentation using spiked bovine and porcine blood that the method really measures only free cyanide,

the amount that has already bound to heme is not measured. The detected amount of cyanide was dependent on its incubation time in blood. In a real case of cyanide poisoning, a significant amount of cyanide will be bound to methemoglobin, and the amount of total cyanide and hence the necessary amount of an antidote, will be underestimated. I was the first author of the paper; it appeared in *Analytical Methods*.

Appendix D reports on the enigmatic ion exchange behavior of Myo-Inositol Phosphates.[8] Myo-inositol mono-, di-, tri-, tetra-, pentakis-, and hexakisphosphate (InsP1, InsP2, InsP3, InsP4, InsP5, InsP6) were separated using hydroxide eluent. Their retention order on an anion exchanger is unusual - it is not monotonically related with the charge on the ion and at the same hydroxide eluent concentration, retention is greatly dependent on the eluent metal cation. The paper unravels why this is so. A number of separations were reported because of the very large number of isomers, separation was often incomplete. I developed mathematical deconvolution methods, implemented in Microsoft Excel™, to decipher the peaks. I was the third author in a four-author manuscript in *Analytical Chemistry*.

In appendix E, Conductometric Detection of Volatile Weak Acids in a Suppressed Anion Chromatography System is made possible with High Sensitivity.[9] Specifically, in suppressed hydroxide eluent ion chromatography, anions are converted to the corresponding acids (while the eluent is converted to water) by an ion exchange device termed a suppressor. While strong acids are then sensitively detected conductometrically, weak acids are not - some are so poorly ionized that they are not detected at all. Volatile acids like H_2S and HCN in the suppressor effluent, however, can be transferred across to a gas-permeable membrane, through which a very dilute base solution is flowing. The conductivity of this effluent base solution is monitored, negative peaks result from its neutralization by the acid. Several aspects of the system are not immediately intuitive to operate optimally. In a coaxial analyte transfer system the flows are best operated co-current rather than countercurrent. A low ratio of the receptor/donor flow rates improves sensitivity but deteriorates resolution. I carried out extensive simulations towards this optimization, this appaered both in the main paper and more extensively in the supporting information. The technique can in principle be used in many other systems involving

membrane transfer. I was second author in a three-author publication in *Analytical Chemistry*.

Appendix F investigates the impact of sampling frequency, response times and embedded signal filtration in fast, high efficiency liquid chromatography.[10] The responses produced by different present generation instruments were evaluated and a square-wave driven light emitting diode source was used to reveal the nature of the embedded filter. The simplest traditional filter used in analytical instrumentation is the RC filter where the output signal is connected to ground via a serial combination resistor (R) and followed by a capacitor (C). The output signal is collected from the junction of the R and C elements. The product of R and C is typically called the time constant (τ). For a Gaussian peak, it is possible to predict how the half width ($W_{0.5}$) will change as a function of $\tau/W_{0.5}$. I created a table that listed the increase in $W_{0.5}$ and the peak asymmetry at 5% and 10% of peak height after processing through an RC filter as a function of $\tau/W_{0.5}$. With the use of the dimensionless parameter $\tau/W_{0.5}$, rather than the absolute value of τ, the effects on an initially ideal Gaussian peak becomes independent of the $W_{0.5}$. Alternative to using or interpolating values in this table, I also provided an Excel workbook containing appropriate macros in the Supplementary information that accepts $W_{0.5}$ for the raw peak (assumed to be Gaussian) as the input and provides the output for any time constant chosen, automatically generating all the peak parameters of interest that were listed in the Table. Another similar program, provided in the supplementary information allowed inputting the actual x-y data array for a peak, which may not be Gaussian and observing the filter effects. I was the third author in a four-author "Tutorial" paper in *Analytica Chimica Acta.*

Appendix G explores a novel ion-pair chromatography (IPC) approach for liquid chromatography electrospray ionization mass spectrometry (LC-ESI-MS) where the eluent does not contain any ion-pairing reagent (IPR).[11] The ion-paring reagent normally causes major problems in ESI-MS. In this Transient Ion-Pairing Separation (TIPS) approach reported for the first time in this paper published in *Analytical Chemistry*, the IPR is injected like the sample, just ahead of the sample. Conditions are adjusted such that the IPR elutes before or after the separated sample constituents during which time flow is directed

away from the mass spectrometer. This prevents both ion suppression and ion source contamination. I carried out extensive simulations that demonstrates the basic separation process in TIPS. An IPR is injected and moves along according to its own chromatographic characteristics (retention factor). A pair (or more) of analytes is then injected and moves along rapidly without separation until it comes in contact with the IPR zone where their retention factor increases and is a function of the local IPR concentration and is different for the different analytes, resulting in the separation of the analytes as they move down the IPR zone. An illustrative video was generated by simulation, where the various retention factors can be input by the user and the progress of the different components down the column can be represented in a 4-bit color code, were given as a supplementary file and more details given in the Supporting Information. I was the fourth author in a five-author paper.

1.2 Introduction to Width Based Characterization

Since the inception of quantitative chromatography, the height and/or area of a peak have been used for quantitation. Area is a true representation of the solute quantity while the peak height is an oft-used substitute.[12] Chromatograms were once recorded manually; analog chart recording appeared in early 60's.[13] Area measurements were made with a *planimeter*, or approximated by triangulation, or paper cut-outs of peaks weighed.[14] The first digital integrators appeared in the mid-70's.[15,16] Today one or more high performance liquid chromatography (HPLC) manufacturers allow data collection at 200 Hz.[17] High speed data acquisition is vital to preserve the fidelity of resolution in fast HPLC.[10] Data rates up to 500 Hz are used in commercial gas chromatography (GC) systems;[18] and up to 20 kHz in research GC-GC systems.[19] Available software generates area- or height-based calibration plots and quantitates chromatographic peaks with little or no user input.

Height is better than area especially if peaks are poorly resolved;[12,20] it is less affected by asymmetry and overlap (high asymmetry increases overlap probability).[21,22] Over a large concentration span, area linearity is better and area is preferred for better

accuracy and precision.[12,23] Noise filtration may affect peak heights but not area.[24] But both are affected by detector non-linearity. In the case of detector saturation, changing parameters e.g., a different wavelength[25] or isotopologue[26] is advised.

Typical practice of area- and height-based quantitation involve a single standard linear regression equation for quantitation. Standard linear regression minimizes absolute errors; the relative error (RE), often more important, may become large at low concentrations. Herein we describe the principles of width-based quantitation (WBQ). We show that WBQ often provides less overall RE where the height or area data does not quite fit a linear relationship, especially due to divergence from linearity at higher concentrations, whether because of detector characteristics or chromatographic conditions. WBQ has previously been used in Flow-Injection Analysis (FIA), pioneered by Ramsing et al.[27] , Stewart;[28] and Dasgupta.[29,30] However, these experiments have generally used an exponential dilution chamber or other dispersing elements to create conditions in which at least one side of the peak has an exponential profile so a (pseudo)-linear relationship can be established between the peak width $\boldsymbol{W_h}$ at some fixed height $\boldsymbol{h}$ and the logarithm of the concentration (ln $\boldsymbol{C}$). Such deliberate dispersion would be an anathema to chromatographers. Also, except when an exponential dilutor is used, the calibration equations have no fundamental mathematical basis.

Applying WBQ to chromatography also requires a mathematical basis of relating width to concentration. It is an adage that chromatographic peaks cannot be described by a single mathematical model,[12] but efforts to do so through various modified Gaussian models (see [31] and citations therein) have long abounded. However, an explicit expression of width at any height from such models is not straightforward. We propose a general model that provides good fits to both Gaussian and non-Gaussian peaks and allows explicit expression of the width at any height, thus providing a sound basis for WBQ. We examine here the advantages/disadvantages of WBQ. Note that $\boldsymbol{W_h}$ refers to measurements at some fixed height $\boldsymbol{h}$ and not at some fixed fraction of the peak maximum ($\boldsymbol{h_{max}}$), e.g., when asymmetry is measured at 5% or 10% of $\boldsymbol{h_{max}}$.

At high concentrations, the signal may enter a nonlinear response region or even be truncated from detector/data system limitations, causing area- and especially height-based quantitation to fail. However, if measured at signal levels before the onset of nonlinearity/saturation, the width may still be unaffected. A related situation arises in detection after post-column reagent (PCR) addition. Often the PCR itself exhibits a finite detector response, contributing to the background and noise.[32,33] One would like to limit the amount of the added reagent. But this restricts the upper limit of measurement: Insufficient PCR would truncate the analyte peak. WBQ is also applicable in this case. Even a combination of such situations that produce unusual (**W**- or **M**-shaped) peak responses can be successfully quantitated.

Width can obviously be measured at many heights. Width data at multiple heights can be exploited in many ways: First, peak asymmetry is often specified as an index of non-ideality. The simplest expression is b/a where a and b are respectively the leading and trailing half-widths of the peak at some specific values of the relative height, typically 0.05 or 0.10. The U. S. Pharmacopeia defines *symmetry factor* or *tailing factor* as $(\boldsymbol{a} + \boldsymbol{b})/2\boldsymbol{a}$ at 0.05 of the peak height.[34] The skewness from the third central moment is another asymmetry index. But no single numeric index can adequately describe peak symmetry. Pápai and Pap[35] discussed many alternatives and suggested a complex five-step method to assess peak symmetry. We propose a scalable (concentration-independent) depiction of peak variance as a function of the relative height to provide a holistic picture of peak asymmetry.

Second, describing a chromatographic peak goes beyond symmetry. A more complete and numerically tractable description of *shape* is needed. It is recognized that the *shape* is generally analyte concentration independent: without column overloading, a well-behaved analyte peak is scalable. Impurity perception is based on shape change, but quantitative diagnostic criteria are elusive. A numerical description of peak shape allows any departure from the pure analyte benchmark to be statistically identified, without requiring the analyte and impurity to behave differently in some multidimensional detection scheme (e.g. differences in optical absorption spectrum, etc.).

CHAPTER TWO: Principles of Width-Based Quantitation

2.1 Gaussian Peaks

Chromatographic peaks are ideally Gaussian, the expected norm for a partition process. Many real peaks are highly symmetric, but rarely truly Gaussian. Still this is an appropriate beginning point. We assume for simplicity that our Gaussian peak is centered at zero time ($\boldsymbol{t} = 0$); thence:

$$\boldsymbol{h = h_{max} * e^{-\frac{t^2}{2*s^2}}} \quad ...(1)$$

where $\boldsymbol{s}$ is the standard deviation of the Gaussian peak.

In order to calculate the width $\boldsymbol{W_h}$ at any particular height $\boldsymbol{h}$, the corresponding $\boldsymbol{t}$ values on the ascending and descending sides of the peak ($\boldsymbol{t_{h,a}}$, and $\boldsymbol{t_{h,d}}$, respectively) are first needed. These are:

$$\begin{cases} \boldsymbol{t_{h,a} = -s\sqrt{2 \ln \bar{h}}} \\ \boldsymbol{t_{h,d} = s\sqrt{2 \ln \bar{h}}} \end{cases} \quad ...(2)$$

where $\boldsymbol{\bar{h} = h_{max}/h}$.

The width is then the difference between these two *t* values:

$$\boldsymbol{W_h = t_{h,d} - t_{h,a} = 2s\sqrt{2 \ln \bar{h}}} \quad ...(3)$$

Hence,

$$\boldsymbol{\ln h_{max} = \left(\frac{1}{8s^2}\right) * W_h^{\,2} + \ln h} \quad ...(4)$$

If $\boldsymbol{h}$ is small enough to be in the linear response domain of the detector/analyte/column system, the ascending peak at $\boldsymbol{h}$ has no foreknowledge of whether the peak maximum will remain within the linear response domain, or in the extreme case, become completely clipped. Similarly, when descending through $\boldsymbol{h}$ on the

trailing edge, it has no memory of the actual maximum value registered. Consequently $\boldsymbol{h_{max}}$ computed from eq 4 is the height *that would have been registered if the analyte peak remained within the linear domain* regardless of whether it was actually so. Therefore, $\boldsymbol{h_{max}}$ computed from eq 4 is linearly related to the concentration $\boldsymbol{C}$, giving more general forms of eq 4:

$$\ln \boldsymbol{C} = \boldsymbol{a}\boldsymbol{W_h}^{\boldsymbol{2}} + \boldsymbol{b} \quad ...(5)$$

where $\boldsymbol{a}$ and $\boldsymbol{b}$ are constants.

2.2 Non-Gaussian Peaks

Non-Gaussian peaks (tailing, fronting, or both) have been modeled as exponential or polynomial modified Gaussian peaks.[36-39] The width at a fixed height for a specific function is easily numerically computed; obtaining generally applicable analytical expressions is another matter. For most non-Gaussian peaks, the peak is also asymmetric: the trailing edge of the peak is not a mirror image of the leading edge. Thus far peak modeling has focused on using a single function. We propose here to model the peak as two separate generalized Gaussian distribution (GGD) functions. The most general situation is where the two GGD functions may not share a common apex or have the same amplitude, as illustrated in Figure 2.1:

$$\boldsymbol{h} = \begin{cases} \boldsymbol{h_{max1}} * \boldsymbol{e}^{-\frac{|t-\epsilon|^{\nu}}{\alpha}}, & \boldsymbol{t < q} \\ \boldsymbol{h_{max2}} * \boldsymbol{e}^{-\frac{|t-\varepsilon|^{u}}{\beta}}, & \boldsymbol{t \geq q} \end{cases} \quad ...(6)$$

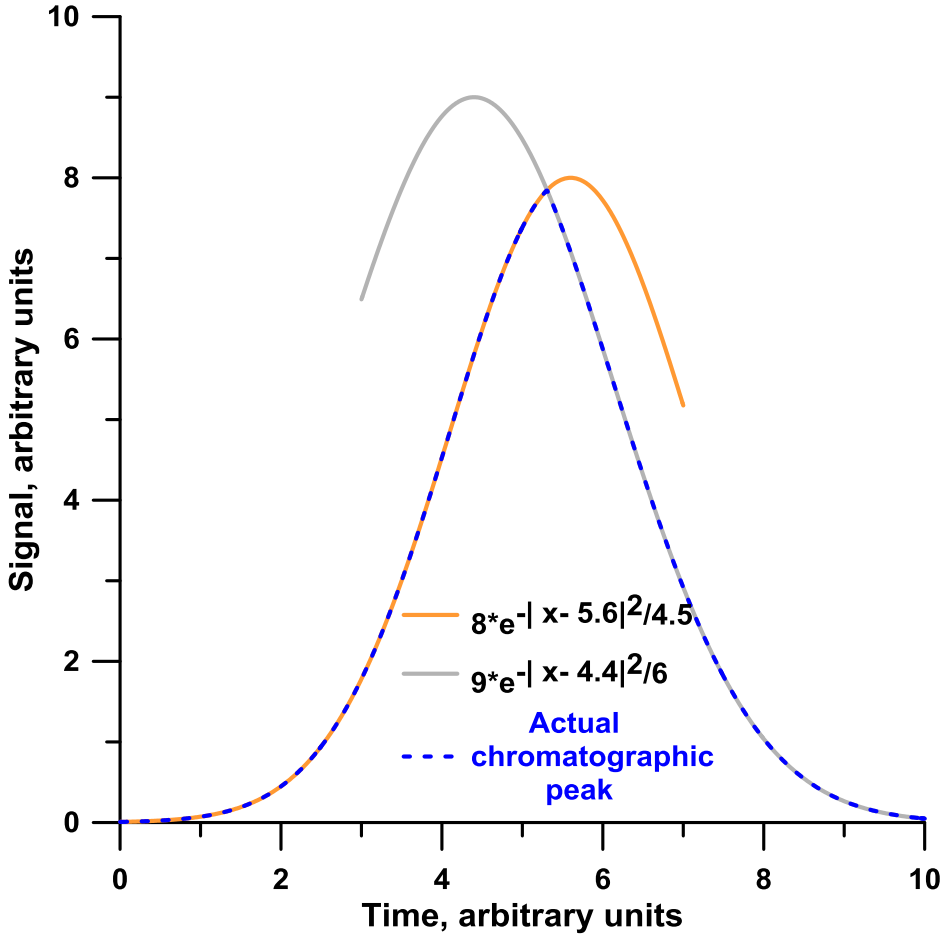

Figure 2.1. An illustrative example of a chromatogram modeled by two independent GGD functions. In this most general case, the two neither have the same amplitude, nor share a common apex. The actual chromatographic peak respectively follows the peak with the earlier and latter apices at t>5.3 and t<5.3, respectively, that time point acting as the limiter for the applicable GGD function.

However, essentially all real peaks we have looked at fit very well with a shared apex with the two GGD functions thus having the same amplitude. Any departure observed occurs very close to the peak apex or the base, neither extreme being of great value to WBQ. Again, assuming peak apex location at $\boldsymbol{t} = 0$:

$$\boldsymbol{h} = \begin{cases} \boldsymbol{h_{max}} * \boldsymbol{e}^{-\frac{|t|^{m}}{a}}, & \boldsymbol{t < 0} \\ \boldsymbol{h_{max}} * \boldsymbol{e}^{-\frac{t^{n}}{b}}, & \boldsymbol{t \geq 0} \end{cases} \quad ...(7)$$

where the top/bottom equations pertain respectively to leading/trailing halves of the peak. In proceeding similar to that for eq 3,

$$W_h = (a \ln \bar{h})^{1/m} + (b \ln \bar{h})^{1/n} \quad ...(8)$$

where the first and second term on the right pertain to the leading and trailing halves, respectively and may be independently pursued for shape considerations,[40] and also possibly for quantitation. Parameter limitations in eqs 6-8 are easily imposed. Peak shape considerations (Figures 2.2 and 2.3) will indicate that for real chromatographic peaks the values of m and n in eq 8 will generally lie between 1 and 2, $1/m$ and $1/n$ (eq 8) therefore falling between 1 and 0.5).

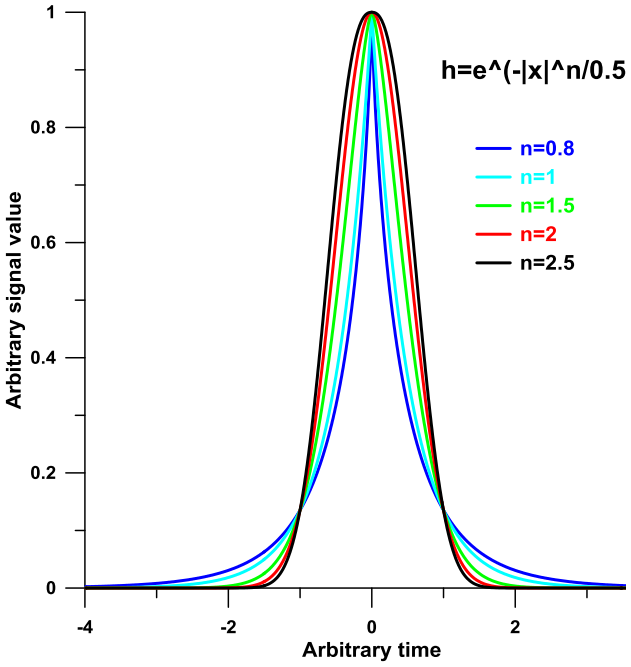

Figure 2.2. Generalized Gaussian functions with different exponent values ranging from 0.8 to 1.5. The Gaussian band has n = 2. Note at low exponent values close to 1 the shape is more like that of a Laplace distribution or Lorentzian function, not common in chromatographic bands.

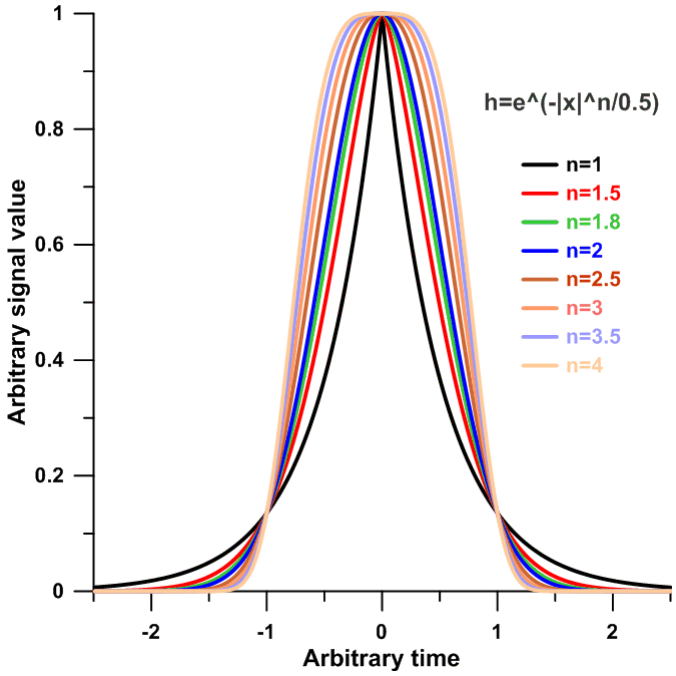

Figure 2.3. Generalized Gaussian functions with different exponent values ranging from 1 to 4. The Gaussian band has n = 2. Note at high exponent values >2 the peak top becomes increasingly flat, not observed in chromatographic bands in the absence of peak overlap.

If W_h is measured between 5-95% of h_{max} ($1/\bar{h}$ = 0.05-0.95, $\bar{h}$ = 1.05-20). Within these constraints, it is readily shown that W_h can be expressed by a single term with ≤1% Root Mean Square (RMS) error (see supporting information of ref 1):

$$W_h = (p(ln\bar{h}))^q \quad ...(9)$$

As an illustration, we chose some simple random values for the variables in eq. 7, that also results in a far from Gaussian peak:

$$h = \begin{cases} h_{max} * e^{-\frac{(-t)^2}{0.5}}, & t < 0 \\ h_{max} * e^{-\frac{t}{0.33}}, & t \geq 0 \end{cases} \quad ...(10)$$

The peak resulting from these two functions is illustrated in Figure 2.4**.**

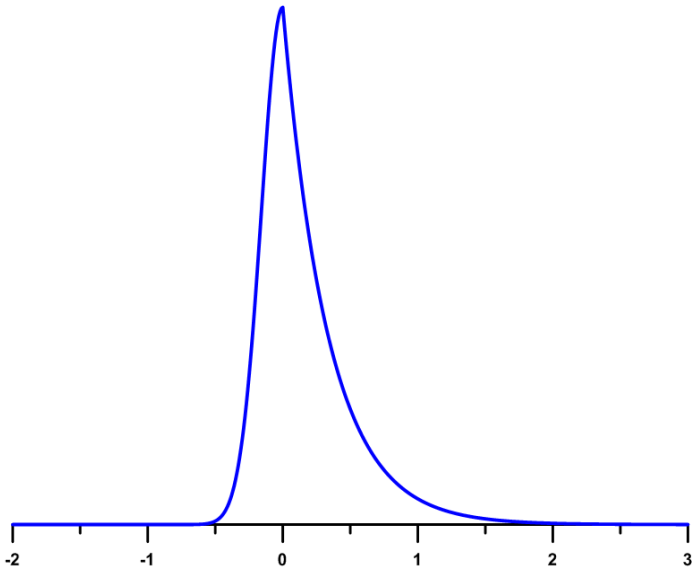

Figure 2.4. Plot of equation 10 (illustrative NonGaussian peak generated by two different functions).

Following eq 8, W_h for this peak can be explicitly given as:

$$W_h = 0.33 * ln\,\bar{h} + 0.5 * \sqrt{ln\,\bar{h}} \quad ...(11)$$

This is approximated with high accuracy following eq 9 to:

$$W_h \approx 0.8329 * \left[ln\, \bar{h}\right]^{0.7234} \quad ...(12)$$

ln h_{max} can in this case be then expressed as:

$$\ln h_{max} = 1.29 * W_h{}^{1.38} + \ln h \quad ...(13)$$

Fits to similar equations for a number of illustrative real peaks are shown in Figures 2.5 and 2.6.

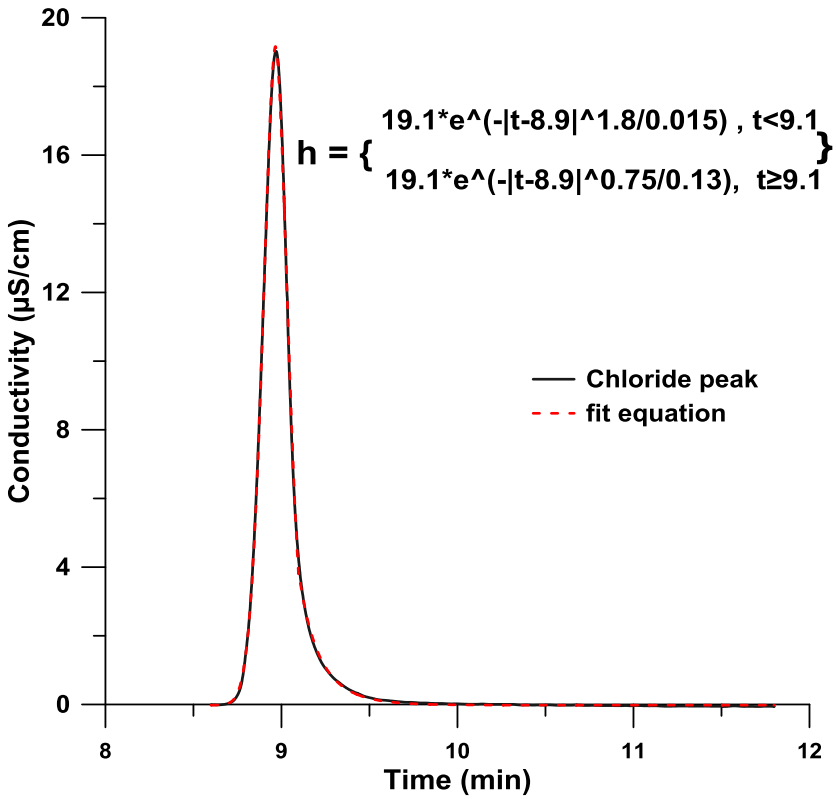

Figure 2.5. We use ion chromatographic data in this figure. Illustrative Fits of chloride (2 nmol injected) to eq 6. From 1%-99% of peak height, RMS error as % of h_{max}: 0.66% (r^2 = 0.9996).

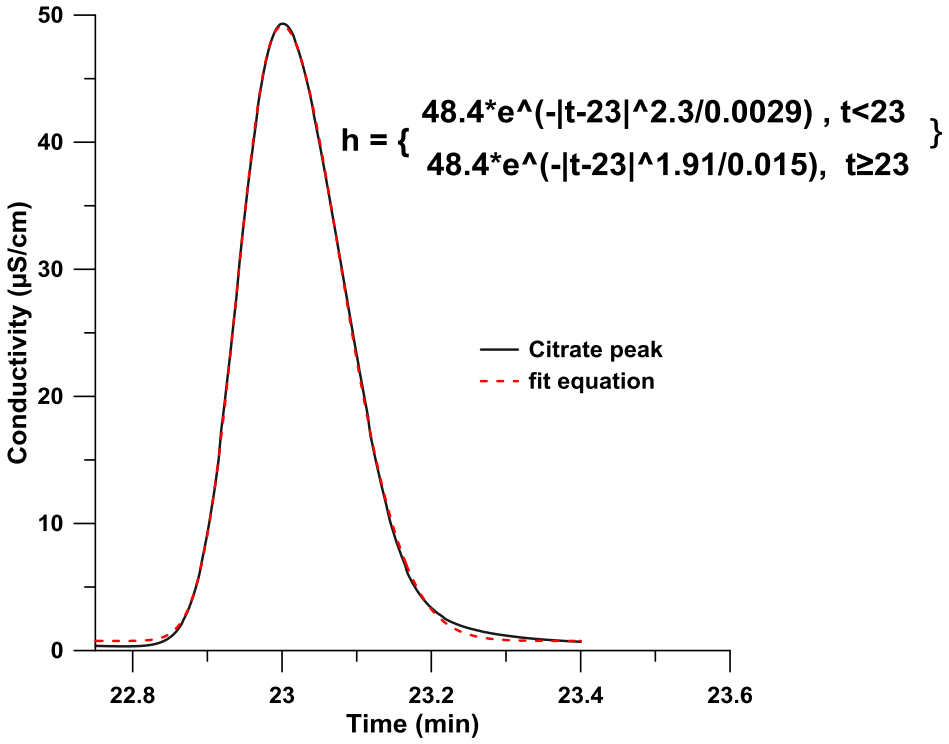

Figure 2.6. Fit of experimental citrate peak (10 nmol injected) to eq 6. RMS error as % of h_{max}: 0.55% (r2 0.9998)

WBQ is fundamentally based on h_{max} being linearly related to C. For quantitation, the general relation of C as a function of W_h (and *vice-versa*) are best expressed by:

$$\ln C = aW_h^{\,n} + b \quad ...(14)$$

Eq 5, representing a purely Gaussian peak, is simply a special case of eq 14 with n=2. It is worthwhile noting that values of n >2 produces a flat-top (increasingly with increasing n, see Figure 2.3), not common in chromatographic peaks.

CHAPTER THREE: Experimental Section

Ion chromatography (IC) data were generated with a ThermoFisher/Dionex IC-25 system with an isocratic pump or a ICS-5000 system with a gradient pump. Other components included G40 electrodialytic KOH eluent generator, injection volume of 10 µL (unless otherwise stated), 2 mm bore AG20/AS20 guard and separation column, LC30 temperature controlled oven (30 °C), ASRS-Ultra II anion suppressor in external water mode, and a conductivity detector intgrated in the system. For all real chromatograms, the data array picked for height/area measurement contained at least 5 sampled points on each side of the putative peak and a best fit baseline was drawn through the extreme 5 points on each side. The sum of all the ordinate values in the baseline-corrected data array was taken as the area and the maximum ordinate value as the height.

Caffeine chromatographic data were generated in using a 1290 HPLC system on an Eclipse XDB-C18 column (4.6 x 150 mm, dp =5 µm), using an isocratic 85:15 water:acetonitrile eluent at 1 mL/min. The diode array detector response time and slit width was set at 0.5 s and 4 nm, respectively. The absorbance measured at 272 nm averaged over 4 nm was referenced against measurements at 380 nm, averaged over 40 nm; all equipment were from Agilent.

An AD20 absorbance detector was used for absorbance measurement. All components were from www.thermofisher.com. For IC determination of formate and silicate, a permeative amine introduction system (PAID) which introduces diethylamine to detect acids, even very weak acids, was used prior to conductivity detection.

Simulations. For all simulations (all peaks Gaussian, standard deviation σ), the baseline was set at zero and the peak apex assigned a location of $\boldsymbol{t} = 0$. The area was calculated from -5 to +5 σ. The height was then taken as the value of the highest datum in that domain.

CHAPTER FOUR: WBQ with Illustrative Ion Chromatographic Data

An ion chromatographic data for Chloride over a 100-fold concentration range is quantitated. As none of the peaks are really Gaussian eq 14 rather than eq 5 was used throughout. Width was measured at 0.3, 0.4, and 0.5 µS/cm substantially above the baseline noise levels but still below the height of the lowest concentration peak. The best fit parameters were obtained using a nonlinear least squares sum minimization routine (Microsoft Excel SolverTM).

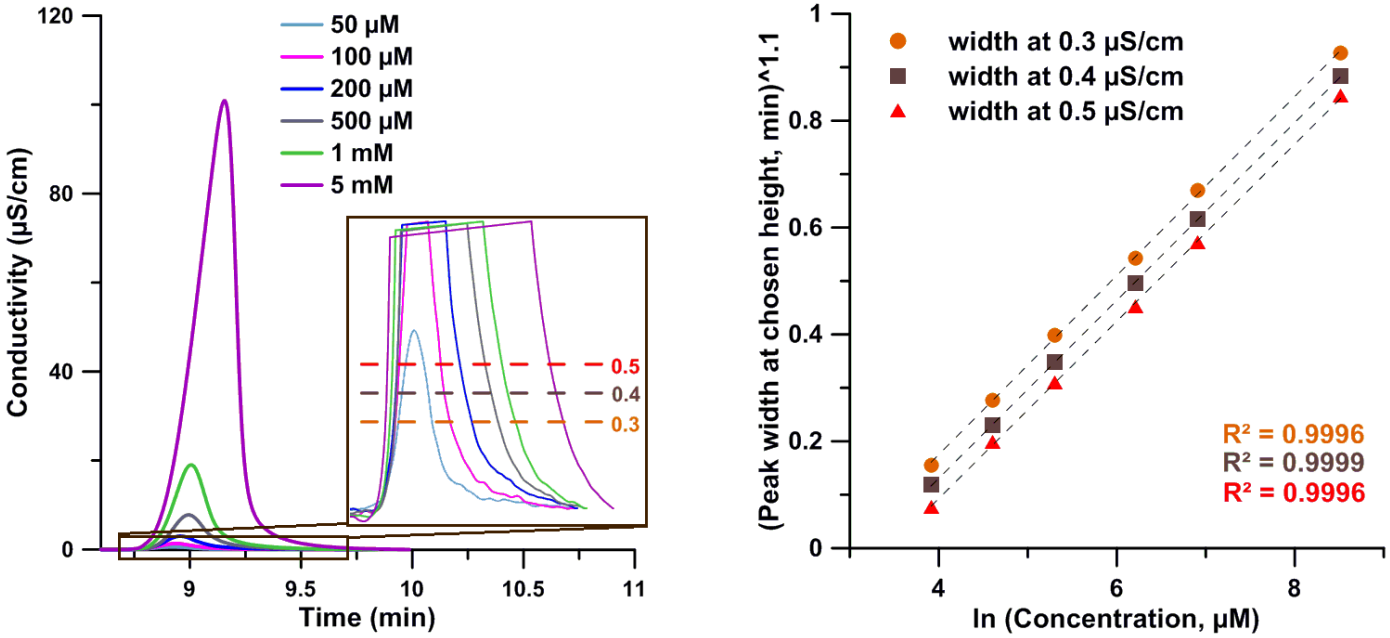

Figure 4.1. Responses of chloride eluted under gradient conditions. The peaks are not Gaussian but are without major fronting/tailing .Electrogenerated KOH gradient at 0.25 mL/min was used as follows: Time, min (Concentration, mM): 0(4), 3(4), 15(10), 19(40), 27(40), 27.5(4), 30(4). Injection volume 2 µL. Width-based calibration is on the right.

CHAPTER FIVE: Theoretical Limits of Uncertainty and Accuracy

In a typical quantitation situation, we refer to a plot of the measurand (height or area) against standard concentrations (the independent variable) as the calibration curve. For an unknown sample, the concentration is then interpreted from an appropriate equation that best fits the curve. In many practical situations, the major contributor to the errors and uncertainties in the ascertained concentrations is the imperfect fit of the calibration equation to the data. In a perfect world, an UV absorbance based quantitation system detection system should never, for example, have a finite intercept in a height- or area-based linear relationship with concentration. However, even in this ideal world, there are finite limits to the attainable accuracy and precision for the measurands. We first explore these limits below.

UV absorbance-based quantitation, arguably the most common practice in HPLC, is assumed. With an ideal zero intercept linear calibration equation, uncertainties in height/area are proportionately translated into quantitation uncertainty. We assume a perfectly Gaussian band with $\sigma = 1$ s under both no noise condition and a realistic amount of noise and stray light (0.05%). The base case has a *true* peak amplitude of 1 mAU. Because of stray light there will be a minute (-0.05%) error in the measured absorbance. The peak to peak baseline noise is assumed to be 20 μAU at a sampling frequency of 10 Hz (this is the best case for a present-day diode array detector, isocratic conditions, no refractive index-related noise). The true absorbance amplitude is not observed until the sampling frequency (f) is sufficiently high; however, the computed area is not affected.[10]

5.1 Height Measurement

Quantitation begins with ascertaining the beginning and the end of a peak, generally through a threshold slope or a minimum area specification. Within the domain of the peak so-defined, finding the height maximum is thereafter straightforward. The associated inaccuracy and uncertainty, are however, affected by noise. To simulate random noise, the results below represent 10,000 computational trials. Taking 1 mAU as the true value, the error in the average height ranges from -1.7% at 10 Hz to +1.6% at 50 Hz, a combined result of inadequate f (dominant factor at low f), noise, and stray light; the relative standard deviation of this perceived height (the uncertainty) is in the 0.3-0.4% range from 10-50 Hz (Figure 5.1). As will be seen below, precision improves as absorbance increases; accuracy behaves similarly until stray light induced error become dominant.

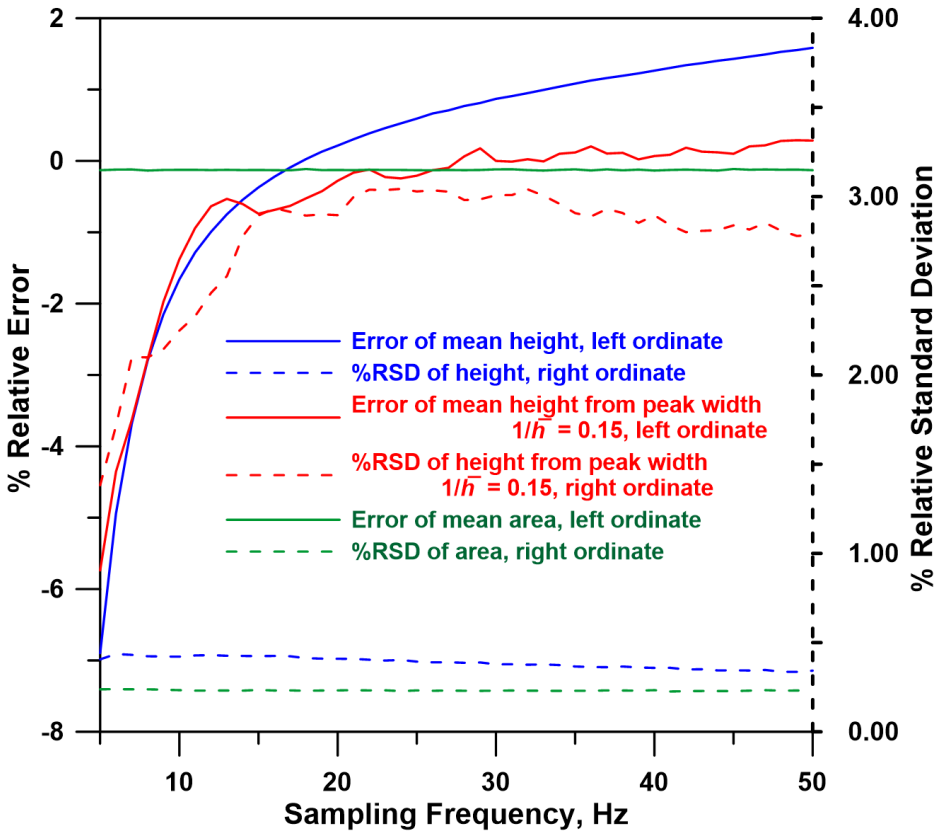

Figure 5.1. Relative bias (solid lines, left ordinate) and relative precision (dashed lines right ordinate) computed for a case of absorbance detection. The situation assumes a Gaussian analyte peak with a true absorbance amplitude of 1 mAU, a standard deviation of 1 s, 20 μAU of peak to peak random noise at 10 Hz and 0.05% stray light. The results shown

depict averages and standard deviations of 10,000 computational trials. Blue, red and green traces resectively depict height, width, and area-based quantitation. Width measured at a fixed height of 150 μAU.

5.2 Area Measurement

Here errors/uncertainties stem from locating the beginning and the end of the peak in a noisy baseline. The success of different algorithms used in commercial software differs; a comparison is beyond the scope of this paper. The accuracy is unaffected to within 0.01% with a detection span $\geq \pm 5\sigma$. A lower span does not capture all of the area, resulting in a negative error; a larger span only increases noise-induced uncertainty. With an integration span of $\pm 5\sigma$, the error is ~0.05%, arising primarily from stray light, while the uncertainty is ~0.2%. (Figure 5.1).

5.3 Width Measurement

To determine W_h, one must first find the temporal locations of the specified h on the ascending/descending edges (hereinafter designated $t_{h,a}$ and $t_{h,d}$, respectively) and thence determine W_h as $t_{h,d} - t_{h,a}$. No digitized ordinate value may precisely equal h, however if one takes the nearest point, its distance from the true location of h and the associated error will decrease with increasing sampling frequency (f) due to increased data density. Rather than the nearest point, t_h may be interpolated from discrete values h-h' and h+h'' corresponding respectively to the locations t' and t'' (adjacent, $f = 1/|(t'-t'')|$) whose corresponding ordinates bracket h. Predictably, any type of interpolation gives better results than the nearest point approach. We used the simplest, a linear interpolation method. If f is sufficiently high, more sophisticated interpolation methods (e.g., a cubic spline fit) do not further reduce error, see Table 5.1 for illustrative error magnitudes obtained using nearest datum and interpolations by linear, and 4-point spline methods.

Percent RMSRE, Chloride			
Height, µS/cm	**Nearest point**	**Linear interpolation**	**4-points spline fit**
0.1	9.34	2.55	2.55
0.2	4.84	3.38	3.38
0.3	3.41	2.20	2.20
0.4	2.23	0.92	0.92

Table 5.1. Illustrative relative errors for different methods for locating $t_{h,}$ the temporal (abscissa) location corresponding to the chosen height $\boldsymbol{h}$ in column 1. The chloride data are the same as those in Figure 4.1, data was collected at 10 Hz.

The interpolation error will decrease with increasing $\boldsymbol{f}$. The RMS error as a function of $\boldsymbol{f}$ across a span of $\boldsymbol{1/\overline{h}}$ = 0.05-0.95 is shown in Figure 5.2. At a given $\boldsymbol{f}$, the error will depend on the specific value of $\boldsymbol{h}$ where the width is measured, as well as how the sampled points line up relative to the peak position. The error is maximum when $\boldsymbol{h'}$ and $\boldsymbol{h''}$ are both significant ($\boldsymbol{h'\approx h''\neq 0}$) and a minimum when the sampled datum precisely falls on $\boldsymbol{h}$ ($\boldsymbol{h'}$ or $\boldsymbol{h''}$ = 0; if $\boldsymbol{h'}$=$\boldsymbol{h''}$=0, the error is zero). The error oscillation frequency increases and the amplitude decreases with increasing $\boldsymbol{f}$ (Figure 5.3). But regardless of $\boldsymbol{f}$, as a function of $\boldsymbol{h}$ the error decreases with decreasing sensitivity of $\boldsymbol{W_h}$ to changes in $\boldsymbol{h}$, a minimum is reached at $\boldsymbol{1/\overline{h}}$ of ~ 0.6 (see following section on optimum height); the error sign changes thereafter. Although in Figure 5.3 the minimum errors seem to reach zero in each oscillation cycle, a magnified view (Figure 5.4) will indicate that is not actually the case. Also, the absolute error magnitudes are acutely dependent on the relative alignment of the sampled data and the peak. For the error to be exactly zero, not only must one sampled point fall exactly on $\boldsymbol{t_{h,a}}$, $\boldsymbol{W_h}$ must be an exact multiple of $1/\boldsymbol{f}$ so that $\boldsymbol{t_{h,d}}$ coincides with another sampled point. In any case, these ideal no-noise case error magnitudes are overall too small to be of concern.

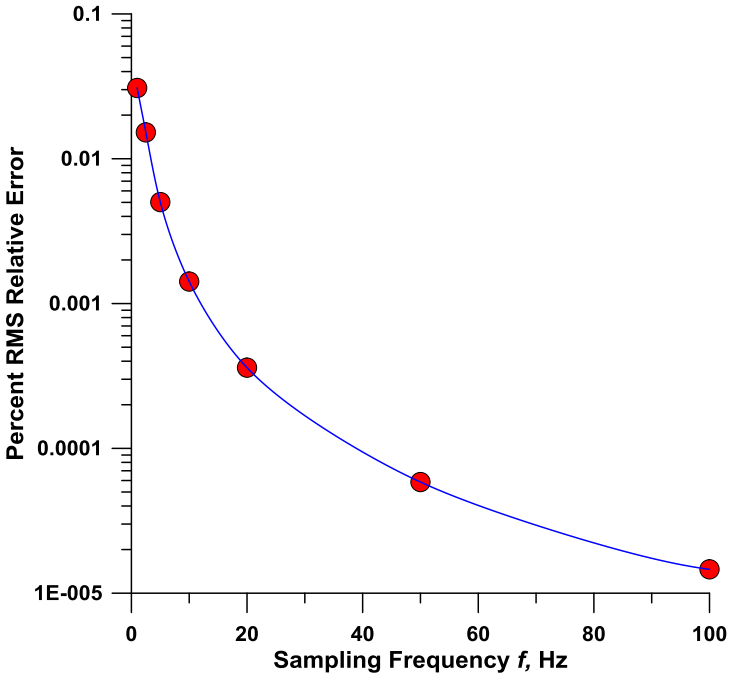

Figure5.2. RMS percent relative error across $\boldsymbol{1/\bar{h}}$ = 0.05-0.95 as a function of sampling frequency.

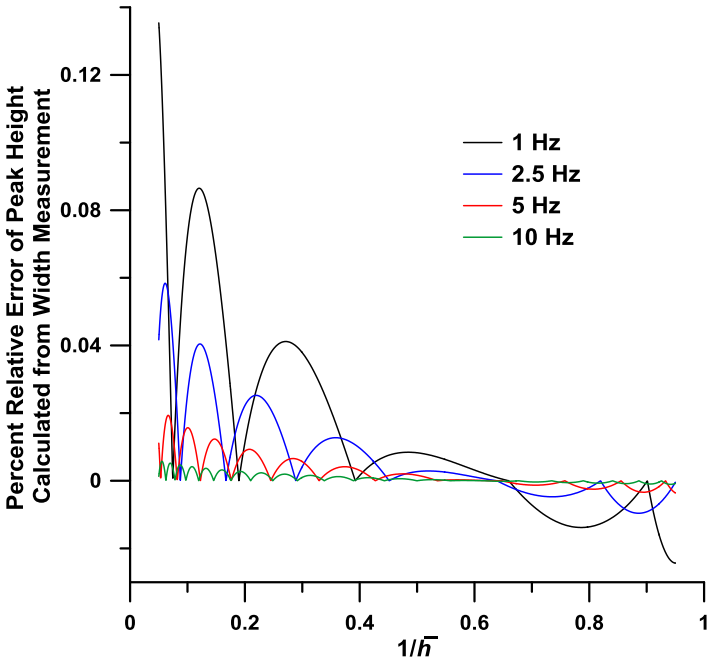

Figure 5.3. Relative error from linear interpolation as a function of sampling frequency at different $\mathbf{1/\bar{h}}$ values from 0.05 to 0.95 in steps of 0.005. These simulations assume no noise. Standard deviation of Gaussian peak is 1 s. Relative error is positive below the inflection point and negative above. Theoretically zero error should occur precisely at $\frac{\mathbf{1}}{\bar{\boldsymbol{h}}} = \frac{1}{\sqrt{e}}$ = 0.607.

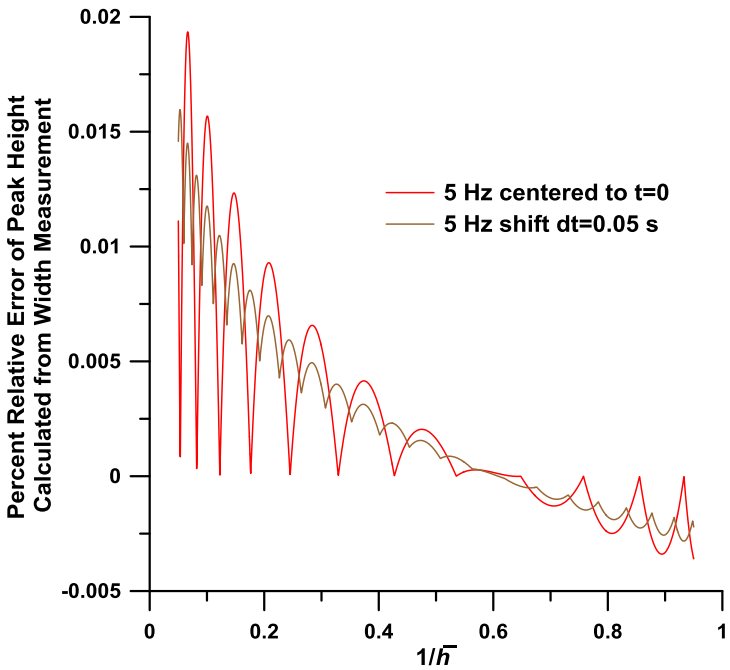

Figure 5.4. The red trace is the same as the red trace in Figure 5.3. The brown trace represents a slight shift in the alignment of the sampled data with the peak position but this results in a dramatic reduction of the amplitude of the error oscillations due to linear interpolation. However, the pattern does not change qualitatively.

5.3.1 Width Measurement in the Presence of Noise

Additional errors arise in locating t_h in the presence of noise. If t_h is sought ascending from the baseline, it is likely to be prematurely located because of noise, resulting in a W_h greater than the true value and thus a positive error in concentration. Conversely, if t_h is sought descending from the peak, premature identification will result in a negative error in concentration (see Figures 5.5 a,b).

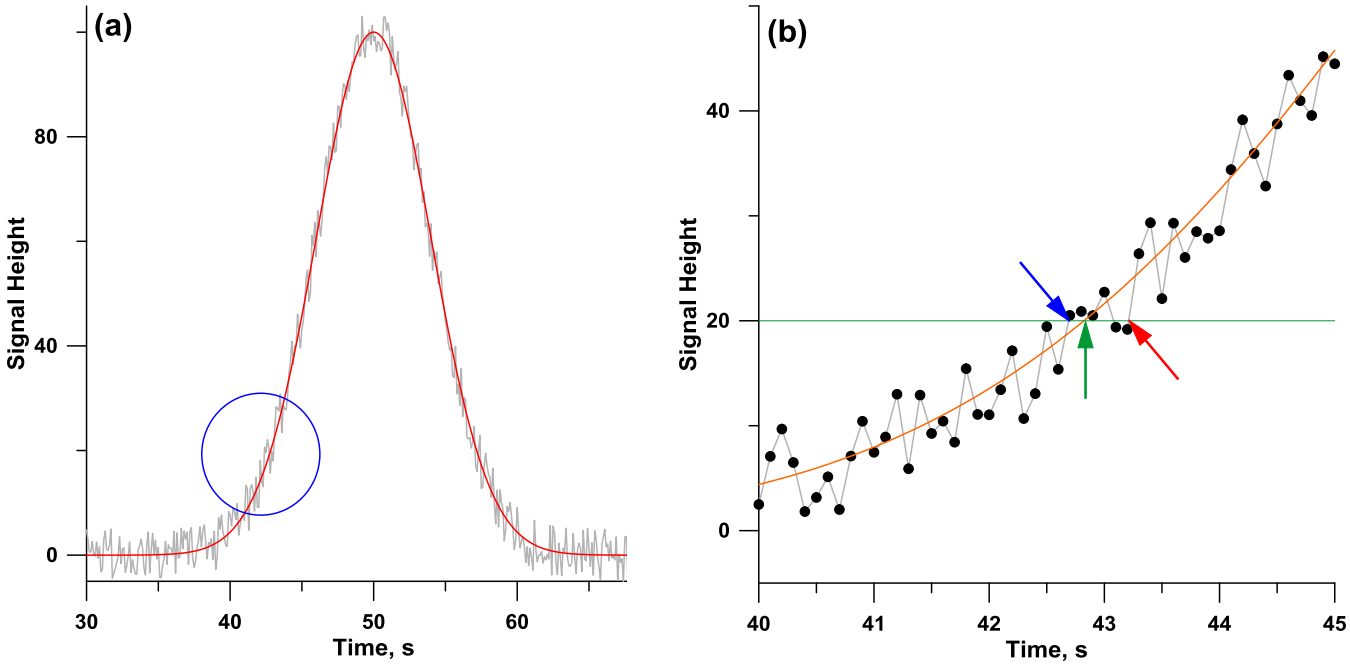

Figure 5.5. (a) The red line depicts a Gaussian peak without any noise and the same peak is shown with an arbitrary amount of random noise in the gray trace. The encircled area is shown magnified in panel **b. (b)** Encircled area in Panel **b** is shown magnified to depict the process how $t_{h,a}$ is determined at h=20. The true x-location corresponds to the tip of the green arrow where the green horizontal line (h = 20) intersects the red line. The discrete data was collected at 10 Hz. When finding $t_{h,a}$ descending from the top, the gray line between connecting successive points first intersects the green line at the tip of the red arrow (this will lead to a width smaller than the true width). Similarly when ascending from the bottom the $t_{h,a}$ is reached at a x-location corresponding to the tip of the blue arrow, which will lead eventually to a overestimation of the true width

Averaging the locations suggested from bottom-up and top-down searches will minimize the error, but not eliminate it. Note that if noise is truly random, each time an illustrative peak with noise is generated, the exact error will change. For this reason, we average the results of 10,000 computational trials in the presented data, as in Figure 5.1, which shows the relative error in concentration (assumed to be the same as the relative error in h_{max}), as predicted by WBQ using eq 5, plotted as a function of f. The error ranges from -1.4% at 10 Hz to <0.3% at 50 Hz, better than height quantitation (Figure 5.1). But the uncertainty (2-3% RSD) is significantly higher than either height or area based quantitation. However, given that WBQ is being performed here at a height actually below

the limit of quantitation (LOQ, defined as 10x noise level, equals 200 μAU), this uncertainty is hardly unacceptable. For a 10 mAU amplitude peak with width measurement at 1.5 mAU for example, the bias and precision improve significantly, e.g., to -0.5 % and 0.7%, respectively, at 20 Hz (Figure 5.6).

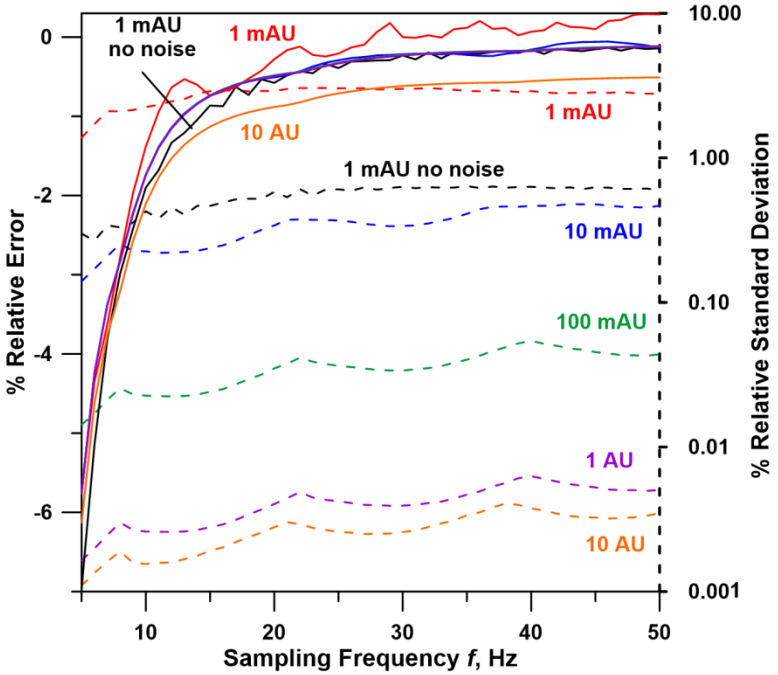

Figure 5.6. Relative error in determining the height (concentration) (solid lines, left ordinate) and relative standard deviation (dashed lines right ordinate, note logarithmic scaling) computed for a case of absorbance detection and width-based quantitation. The situation assumes a Gaussian analyte peak with a true absorbance amplitude of 1, 10, 100, 1000, and 10,000 mAU (red, blue, green, purple, and orange traces respectively), all measured at $\boldsymbol{1/\bar{h}}$ of 0.15, a standard deviation of 1 s. The peak to peak random noise is 20 μAU at 10 Hz. The relative stray light is assumed to be 0.05%. The results shown depict averages and standard deviations of 10,000 computational trials. The black trace indicates the 1 mAU case without any noise; it has an RSD higher than all the other higher absorbance traces with noise because the interpolation errors are still present and are relatively much greater at lower absorbance.

5.3.2 Optimum Height for Width Measurement

The precision can be improved by choosing a measurement height >150 μAU, even for the 1 mAU peak. We can deduce the optimum $1/\overline{\boldsymbol{h}}$ for measuring the width of a Gaussian peak. First principle considerations suggests that the minimum sensitivity of $\boldsymbol{W_h}$ to $\boldsymbol{h}$ occurs at $\frac{\boldsymbol{h_{max}}}{\sqrt{\boldsymbol{e}}}$, i.e., at ~60% of the peak maximum (Figure 5.7). However, the sensitivity remains relatively low and flat over a large span of $1/\overline{\boldsymbol{h}}$ from ~0.3 to 0.9, (and virtually constant between 0.4 and 0.8, Figure 5.7a). When constructing a width-based calibration curve, one is obligated to choose a height that accommodates the lowest concentration calibrant. However, advances in memory storage and computing speed makes it practical to store not just width-based calibration curves at several heights, but the entire profiles of the calibrant peaks. For an unknown, it is thus possible not only to refer to a stored width-based calibration at a height nearest to the ~60% of the unknown peak height, and to generate a calibration equation for this optimum height ($\boldsymbol{1/\overline{h}} \approx 0.6$) of the peak to be quantitated from the stored data on the fly. If calibration concentrations are not close enough to permit choosing $\boldsymbol{1/\overline{h}} \approx 0.6$ to accommodate concentrations below that of the unknown, an appropriate $\boldsymbol{h}$ is 90% of the $\boldsymbol{h_{max}}$ of the lowest concentration standard to be included in the calibration. Confining the calibration to the most relevant region improves accuracy.[41]

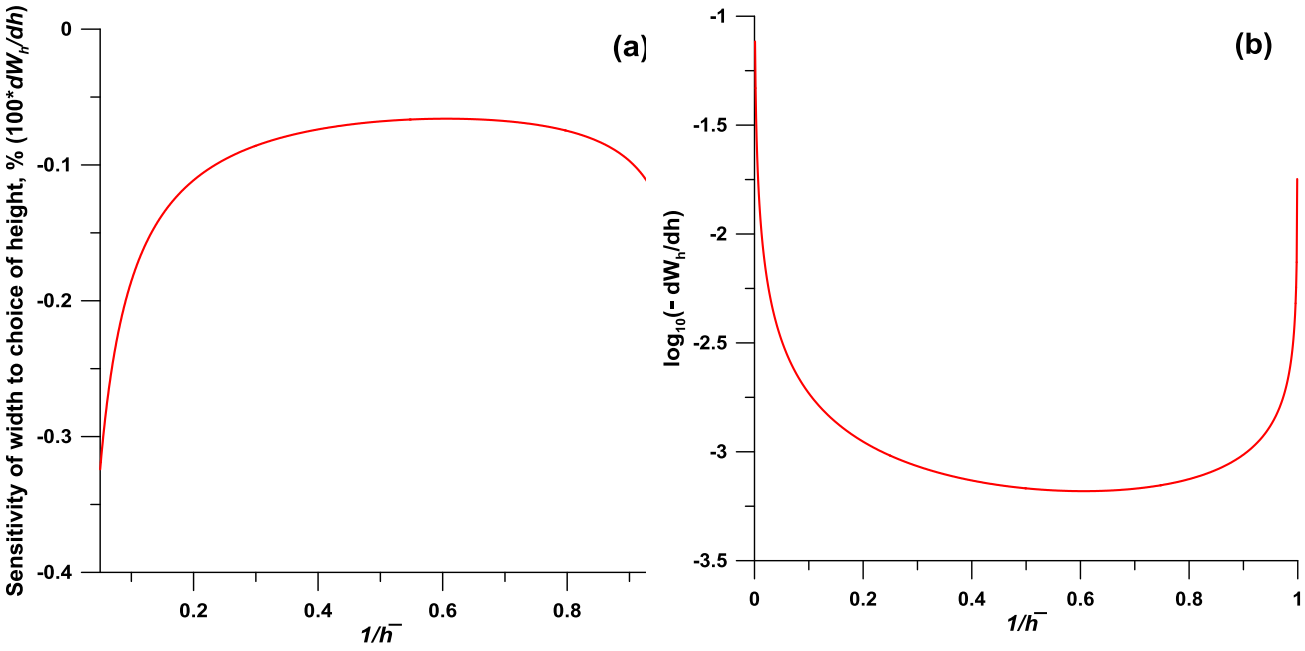

Figure 5.7. The sensitivity of the width measurement due to uncertainty in height is shown two different ways. Panel (a) covers the primary range of interest, 5% to 95% of peak height; the negative sign of the ordinate values results from the fact that width always decreases with increasing height, the absolute values have been multiplied by 100 to indicate percentage dependence. The magnitude of this sensitivity increases steeply at either end. To see the terminal ends, for an abscissa span of 0.1-99.9% of the peak height, we plot in panel (b) the log of $\boldsymbol{dW_h/dh}$, after changing its sign (to permit logarithmic depiction) vs. $\boldsymbol{1/\bar{h}}$

5.3.3 Sampling Frequency and Peak Amplitude

Figure 5.5 b makes it obvious that increased data density (increasing $\boldsymbol{f}$) will reduce the interpolation error as the error in locating $\boldsymbol{h}$ decreases. Accordingly, regardless of the precise height at which width is measured, the error steeply increases as $\boldsymbol{f}$ is lowered below 10 Hz (Figure 5.8). The curves for $\boldsymbol{h}$ = 150 μAU are less monotonic than those at 600 or 850 μAU because of the greater effect of noise. Otherwise, for all three values of $\boldsymbol{h}$, at $\boldsymbol{f} \geq$20Hz, the errors are all below 0.6%; the curves for $\boldsymbol{h}$ = 600 and 850 μAU can barely be distinguished; the relative errors are ~0.1% for both at 50 Hz. The major difference between measurement at $\boldsymbol{h}$ = 150 vs. 600 or 850 μAU is in the relative precision. Whereas in the entire $\boldsymbol{f}$ = 10-50 Hz span, the uncertainty for the $\boldsymbol{h}$ = 150 μAU measurement is always

above 2% (frequently near 3%), those for 850 and 600 μAU do not exceed ~0.6 and 1%, respectively. Similarly, at a fixed value for $\mathbf{1}/\bar{\boldsymbol{h}}$ =0.15 for width measurement, as the peak amplitude is increased in steps from 1 to 10,000 mAU, the value of $\boldsymbol{h}$ proportionally increases, accordingly reducing the relative noise and thus the relative uncertainty (Figure 5.6). In contrast, there is hardly any change in the accuracy with increasing peak absorbance until at very high absorbance when stray light-induced error becomes significant (the latter can obviously be avoided by measuring width at a lower height), the accuracy for 10-1000 mAU are all generally better than 0.5% at $\boldsymbol{f}$≥30Hz) and are all superior to that at 1 mAU. Measurement at 1.5 AU for a peak with 10 AU amplitude deteriorates the accuracy to ~1% but this is still far superior to what will be possible with height or area based quantitation at such an absorbance.

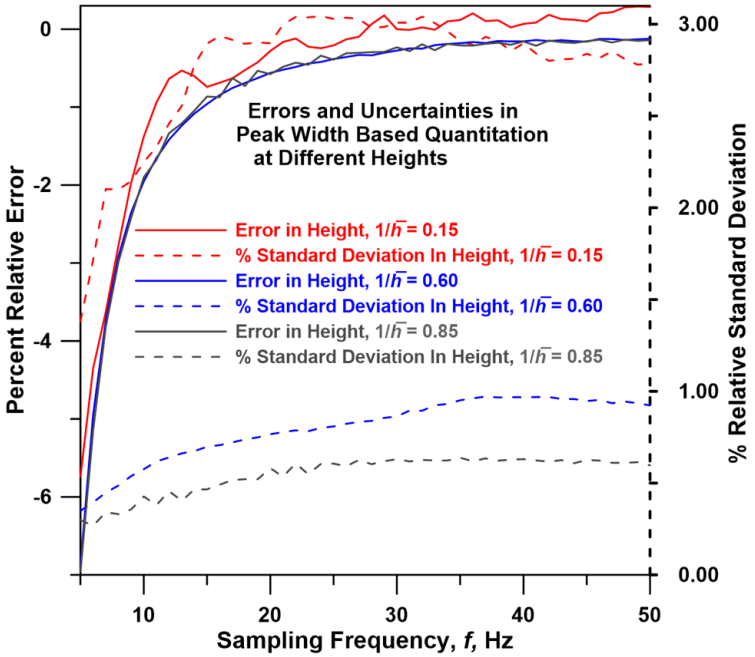

Figure 5.8. Relative error (or relative bias, solid lines, left ordinate) and relative standard deviation (or relative precision, dashed lines right ordinate) computed for a case of absorbance detection and width-based quantitation. The situation assumes a Gaussian analyte peak with a true absorbance amplitude of 1 mAU, a standard deviation of 1 s, 20 μAU of peak to peak random noise at 10 Hz and 0.05% stray light. The results shown depict averages and standard deviations of 10,000 computational trials. Red, purple and brown traces respectively measured at $\boldsymbol{1}/\bar{\boldsymbol{h}}$ of 0.15, 0.60 and 0.85.

CHAPTER SIX: Quantitation Performances of Width- Height- and Area-based Calibration Curves

Capillary scale IC data for isocratic separation of 7 anions over a 1000-fold concentration range was supplied by the manufacturer (Figure 6.1).

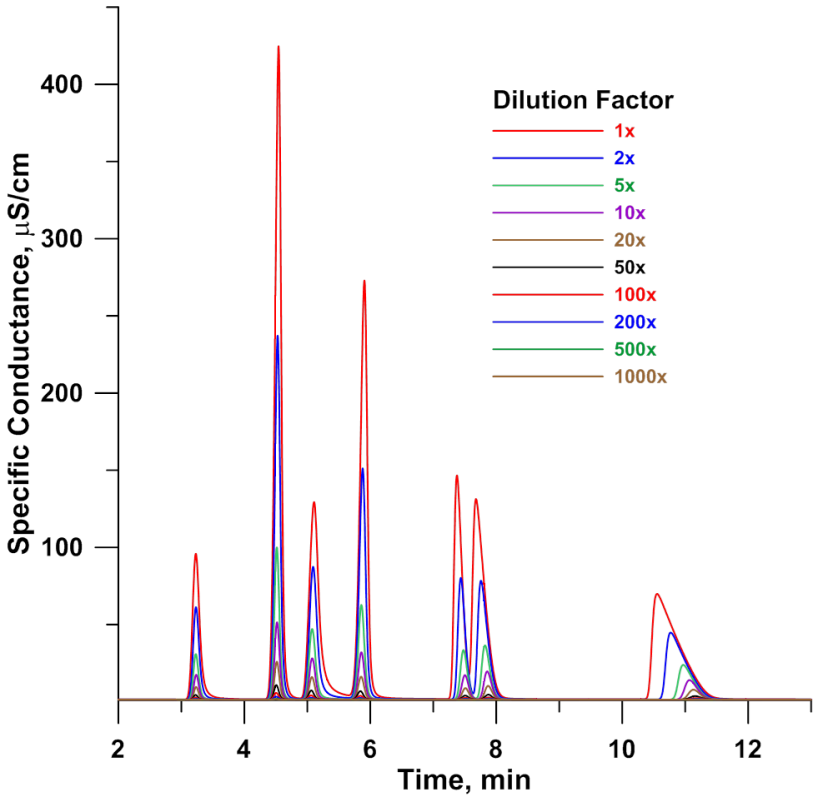

Figure 6.1. A 7-anion separation of standard mixtures over a 1000-fold concentration range. Dionex IonPac AS11-HC, 0.4 x 250 mm, Eluent: 30 mM KOH, isocratic, Dionex EGC-KOH (Capillary), Flow Rate: 10 µL/min, Inj. Volume: 400 nL, Temperature: 30 ˚C, Dionex ACES 300, AutoSuppression , recycle mode. Peak identities from left to right: Fluoride, Chloride, Nitrite, Sulfate, Bromide, Nitrate, Phosphate. Undiluted sample (indicated as 1x) contains in mg/L(mM): 20(1.05), 100(2.82), 100(2.17), 100(1.04).100(1.25), 100(1.61), 200(2.10) of respective anions. Dilution factors for more diluted samples indicated on Figure.

At the highest concentrations, every peak overlaps some with an adjacent one but with appropriate choices of the studied range and $\boldsymbol{h}$, overlap effects can be avoided. We quantitated fluoride, chloride and phosphate, as these are least affected by overlap. Area was measured by the "vertical cut from the valley" method that is least affected by overlap. As none of the peaks are really Gaussian eq 14 rather than eq 5 was used throughout. The best fit parameters to were obtained using a nonlinear least squares sum minimization routine (Microsoft Excel Solver™). The performance metrics appear in Table 6.1 and a sensitivity plot[42] is in Figure 6.2. The latter clearly indicates that overall response is not linear. WBQ is self-constrained to a height <~90% of $\boldsymbol{h_{max}}$ of the minimum concentration in the range ($\boldsymbol{C_{min}}$). As WBQ is ultimately dependent on the projected apex height, it performs best at an $\boldsymbol{h}$ near where the height-sensitivity to concentration is uniform. In contrast, the accuracy of area- or height-based quantitation suffers when the response across the range is non-uniform. WBQ outperforms the other approaches only when both criteria are met. In IC, detector response becomes increasingly non-uniform at higher concentrations. Figures 6.3 and 6.4 shows gradient chromatograms of three strong acid anions at concentrations up to 5 mM and three anions differing in pK_a at concentrations up to 10 mM, each over a hundred-fold span. Because of variable dissociation of weak acid analytes and the interplay of both electrostatic and hydrophobic retention mechanisms where gradient elution largely alters only the electrostatic push, fronting/tailing peaks are seen (Figure 6.4). In both cases WBQ outperforms area- or height-based quantitation, in both unweighted and weighted regression (Table 6.1), the reason seen in the sensitivity plots (Figure 6.5, 6.6). One concludes that (1) WBQ RMSRE is unaffected by weighting; the built-in logarithmic transformation of the concentration values is akin to $1/x^2$-weighting; (2) WBQ outperforms other quantitation methods if the response across the measurement span is not uniform but height-response is uniform where the WBQ height lies, and (3) there is no significant benefit to applying $1/x^2$-weighting to WBQ.

Analyte	Injected Concentration Range, mM (*n*)	Unweighted, % RMSRE (r^2)			$1/x^2$-weighted, % RMSRE (r^2)			Width Measurement Height (fraction of H_{max} of C_{min})
		Area	Height	Width Eq 14	Area	Height	Width Eq 14	
A. Peaks Without major Fronting/Tailing								
Chloride Figure 6.1	**5.6E-3 - 2.8 (9)**	**11** (1.0000)	192.4 (0.9968)	26.7 (0.9838)	**4.8** (0.9980)	5 (0.9834)	24.8 (0.9819)	0.66 (0.90)
	2.8E-2 - 2.8 (7)	**1.8** (1.0000)	61.4 (0.9967)	9.0 (0.9966)	**1.0** (1.0000)	5.3 (0.9798)	9 (0.9965)	2 (0.45)
	2.8e-3 - 0.28 (7)	34.6 (0.9996)	21.8 (0.9999)	**5.9** (0.9985)	6.8 (0.9888)	**5.5** (0.9950)	5.9 (0.9985)	0.1 (0.29)
Phosphate Figure 6.1	**4.2E-3 - 2.1 (9)**	57.1 (1.0000)	749.4 (0.9741)	**31.2** (0.9782)	**8.7** (0.9891)	17.2 (0.6395)	28 (0.9761)	0.1 (0.63)
	2.1E-2 - 2.1 (7)	**9.6** (1.0000)	232.9 (0.9751)	11.1 (0.9951)	**2.7** (0.9990)	19.4 (0.6507)	11.1 (0.9952)	0.5 (0.48)
	2.1E-3 - 0.21 (7)	56.2 (0.9988)	24.1 (0.9996)	**9.8** (0.9960)	9.7 (0.9740	**8.0** (0.9911)	9.8 (0.9944)	0.02 (0.29)
Fluoride Figure 6.1	**2.1E-3 - 1.05 (9)**	163.4 (0.9980)	650.3 (0.9781)	**26.2** (0.9836)	**5.6** (0.9921)	15.1 (0.7360)	22.4 (0.9824)	0.14 (0.56)
	1.05E-2 - 1.05 (7)	54.3 (0.9980)	201.1 (0.9786)	**16.6** (0.9891)	**5.2** (0.9837)	16.7 (0.7492)	16.6 (0.9883)	0.9 (0.63)
	1.05E-3 - 0.105 (7)	33.2 (0.9997)	15.6 (0.997)	**9.0** (0.9967)	6.5 (0.9875)	**6.2** (0.9953)	9 (0.9948)	0.04 (0.33)
Chloride Figure 6.3	**0.05-5.0 (6)**	53.5 (0.9990)	31.3 (0.9997)	**0.9** (1.0000)	9.5 (0.9697)	8.1 (0.9857)	**0.9** (1.0000)	0.40(0.65)
Bromide Figure 6.3	**0.05-5.0 (6)**	61.2 (0.9986)	80.4 (0.9977)	**5.4** (0.9988)	10.8 (0.9623)	15.6 (0.9315)	**5.3** (0.9990)	0.17 (0.76)
Nitrate Figure 6.3	**0.05-5.0 (6)**	67.1 (0.9985)	67.4 (0.9985)	**5.9** (0.9985)	13.2 (0.9497)	13.4 (0.9492)	**5.9** (0.9986)	0.17 (0.65)
B. Fronting/Tailing Peaks								
Formate Figure 6.4	**0.1-10.0 (8)**	110 (0.9939)	390 (0.9000)	**3.1** (0.9996)	13.7 (0.9159)	36.5 (-0.8452)	**3.1** (0.9996)	3.0 (0.51)
Nitrate Figure 6.4	**0.1-10.0 (8)**	7.2 (1.0000)	190 (0.9783)	**5.4** (0.9983)	3.7 (0.9993)	18.9 (0.7448)	**5.4** (0.9983)	2.0 (0.51)
Trifluoro acetate Figure 6.4	**0.1-10.0 (8)**	11.4 (0.9999)	54.5 (0.9985)	**3.3** (0.9996)	3.1 (0.9990)	6.4 (0.9830)	**3.3** (0.9996)	1.5 (0.37)

Table 6.1. Weighted and Unweighted %RMS Errors for. Area, Height, Width based Quantitation.

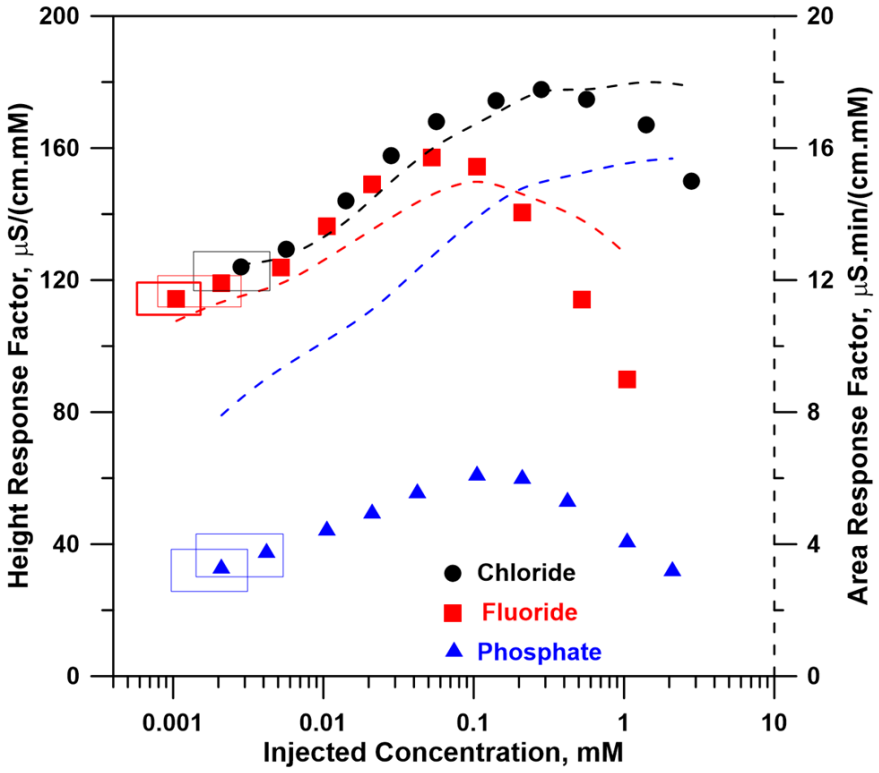

Figure 6.2. Sensitivity plots for area and height for fluoride, chloride and phosphate In Figures 6.1. Sensitivity is defined as the area or height signal divided by the injected concentration. None of the analytes has a uniform response across the span which will suggest strict linearity, fluoride having the worst linearity. The rectangular boxes indicate the height domain where width was measured - these are shown *only* for those situations where WBQ showed a lower RMSRE than either height and area in unweighted regression. The bold red box indicates that for two ranges of fluoride quantitation, both beginning with the lowest concentration, WBQ provided the lowest RMSRE. Note that near these height domains, response was more uniform than across the entire range.

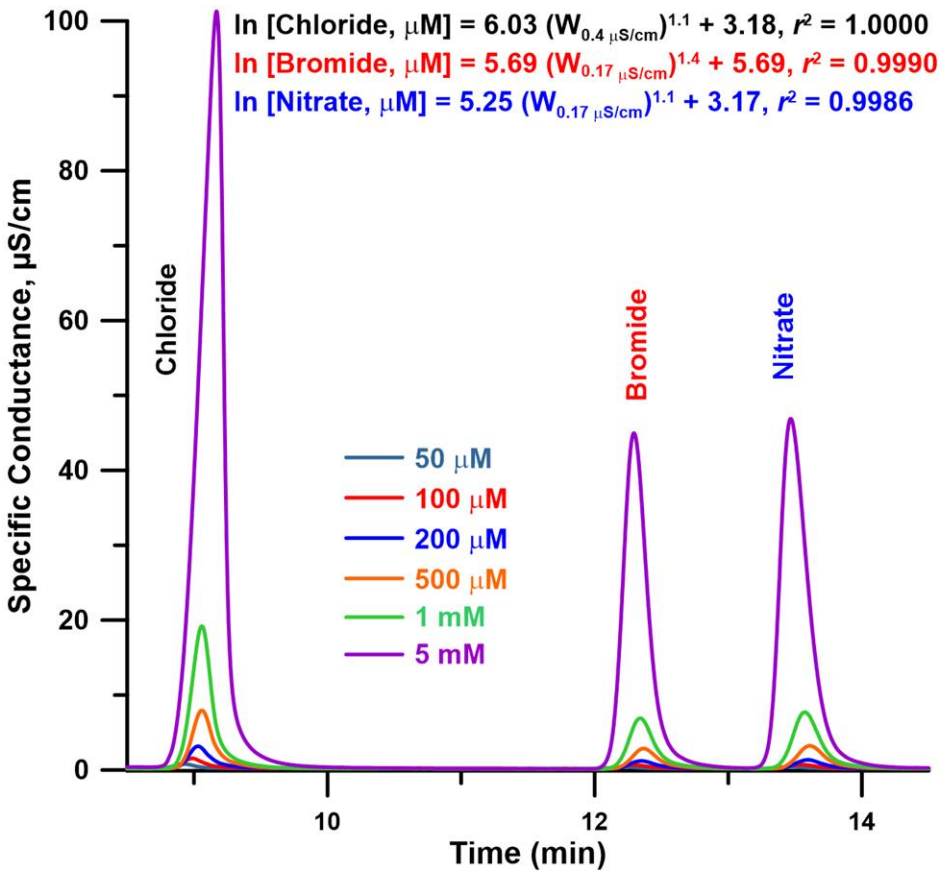

Figure 6.3. Responses of chloride, bromide and nitrate eluted under gradient conditions. The peaks are not Gaussian but are without major fronting/tailing. The standard deviation of the peaks for the best Gaussian fits from (left to right), are, respectively, 4.65, 5.78, and 6.01 s.Electrogenerated KOH gradient at 0.25 mL/min was used as follows: Time, min (Concentration, mM): 0(4), 3(4), 15(10), 19(40), 27(40), 27.5(4), 30(4). Injection volume 2 μL. Width was measured at 0.4, 0.17, and 0.17 μS/cm for chloride, bromide and nitrate, respectively, substantially above the baseline noise levels but still below the height of the lowest concentration peak in each case. Width-based calibration equations appear atop.

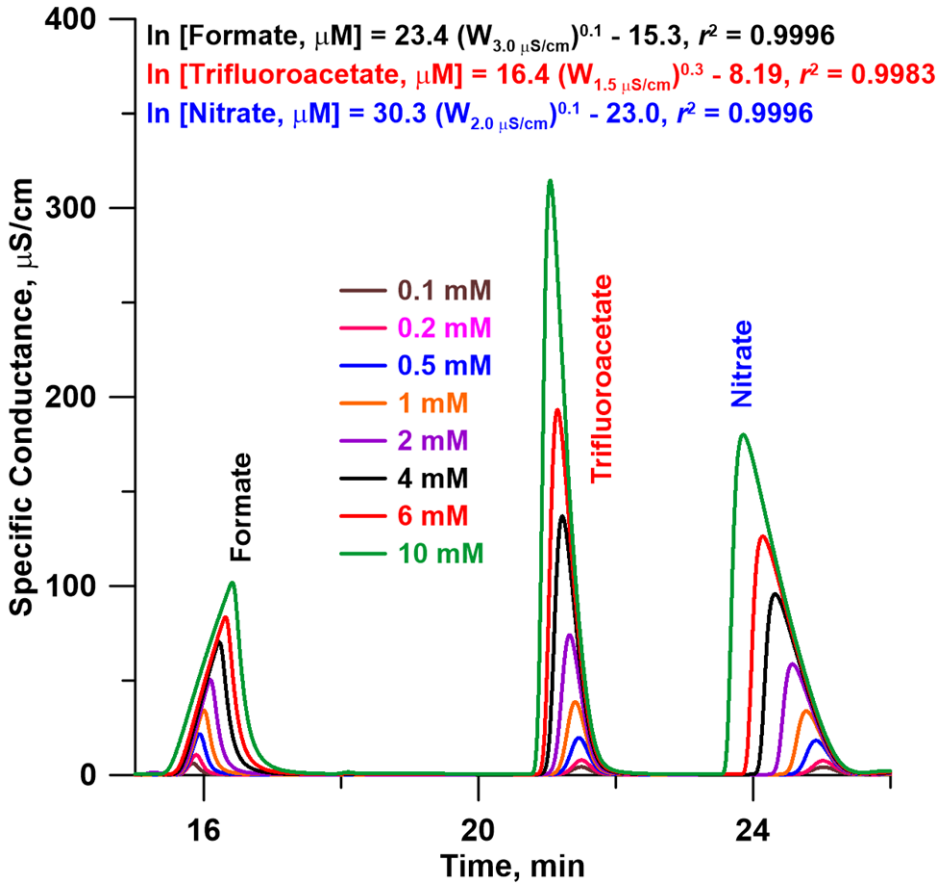

Figure 6.4. Formate, Trifluoroacetate and Nitrate eluted under a specific gradient condition show extensive tailing and/or fronting. Experimental setup as in Figure 6.3, except for KOH eluent gradient: (0.3 mL/min) 0-10 min, 2.0 mM; 10-15 min, 2.0-10 mM; 15-32 ,min, 10 mM. Injection volume 10 μL. Width was measured at 3.0, 1.5, and 2.0 μS/cm for formate, trifluoroacetate and nitrate, respectively, substantially above the baseline noise levels but still below the height of the lowest concentration peak in each case. Width-based calibration equations appear atop.

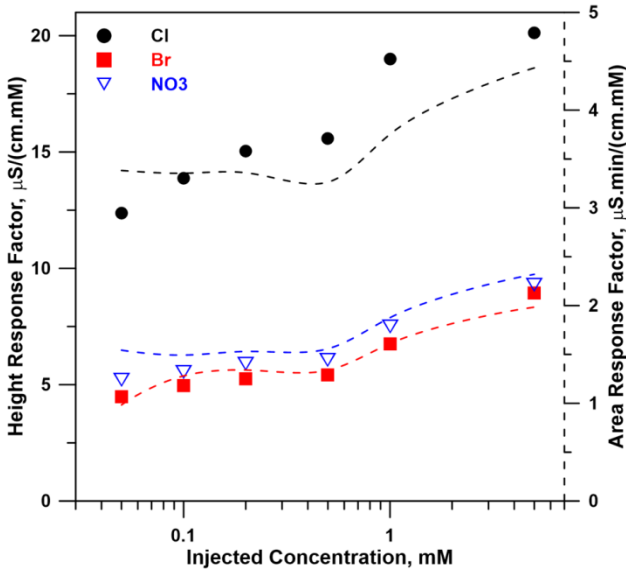

Figure 6.5. Sensitivity plots for area and height for chloride, bromide and nitrate for the chromatograms shown in Figure 6.3. In all cases WBQ pertained to the height domain near the lowest concentration and in all cases, this was the region showing the least variation of sensitivity with concentration. With significant nonuniformity across the whole range, in all cases, in unweighted regression, WBQ outperformed height and area.

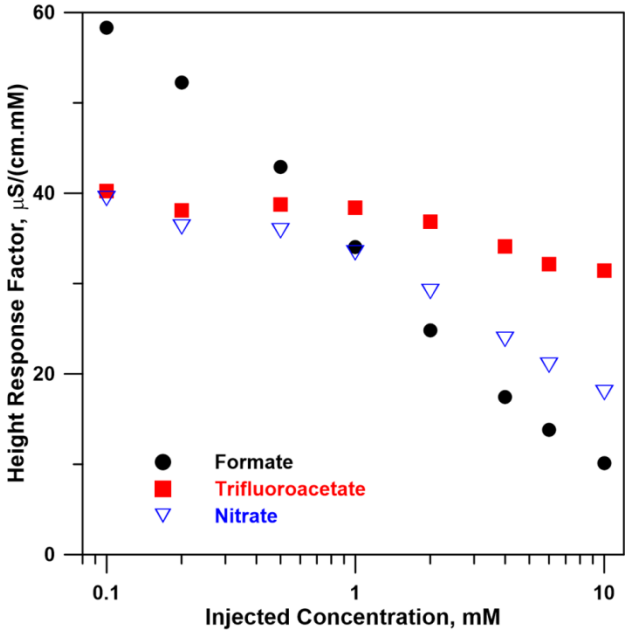

Figure 6.6. Sensitivity plots for area and height for formate, trifluoroacetate and nitrate for the chromatograms shown in Figure 6.4. In all cases WBQ pertained to the height domain near the lowest concentration and in all cases, this was the region showing the least variation of sensitivity with concentration. With significant nonuniformity across the whole range, in all cases, in unweighted regression, WBQ outperformed height and area.

CHAPTER SEVEN: Choice of Height for Width Measurement for Real Chromatographic Data

Considerations for quantitating a single idealized peak were outlined earlier. In real separations, the upper limit of $\boldsymbol{h}$ in generating a single width-based calibration curve covering the entire span will generally be limited to about 0.9 $\boldsymbol{h_{max}}$ of the lowest concentration in the calibration curve. Within this upper limit, is there any benefit to choose a lower $\boldsymbol{h}$ to measure the width? Results for the data in Figure 6.3, processed at multiple heights, are shown in Table 7.1**.** The highest height at which the width can be measured depends on the analyte, whereas a height of 0.5 μS/cm can be used readily for chloride at the lowest concentration (50 μM) in the calibration set; this choice of height eliminates the lowest concentration calibrant for nitrate and bromide. With the caveat that even the lowest $\boldsymbol{h}$ examined here was considerably above baseline noise, there was no consistent or monotonic change of r^2 or % RMSRE with $\boldsymbol{h}$. However, there may be other reasons for generally choosing as high a $\boldsymbol{h}$ as possible, short of entering a nonlinear response range. The use of a low $\boldsymbol{h}$ will suffer from noise and influence of adjacent peaks. Regarding the latter, if the analyte peak of interest is overlapped dominantly on one side, WBQ is advantageously performed with half-width of the peak on the non-overlapped side.

Chloride			Bromide			Nitrate		
Height for Width Msmt, μS/cm	**Eq 14 Best fit r^2**	**%RMSRE**	**Height for Width Msmt, μS/cm**	**Eq 14 Best fit r^2**	**%RMSRE**	**Height for Width Msmt, μS/cm**	**Eq 14 Best fit r^2**	**%RMSRE**
0.10	0.9997	2.6	0.08	0.9979	7.1	0.09	0.9977	7.1
0.20	0.9995	3.4	0.11	0.9980	7.2	0.13	0.9970	8.3
0.30	0.9998	2.2	0.14	0.9984	6.4	0.17	0.9985	5.9
0.40	1.0000	0.9	0.17	0.9988	5.4	0.21	0.9985	6.0
0.50	0.9997	2.7	0.50[a]	0.9984	4.7	0.50[a]	0.9987	4.9

Table 7.1. Errors as a Function of the Height Chosen for Width Measurement. [a]n =6 in all cases except for nitrate and bromide at $\boldsymbol{h}$ = 0.5 μS/cm, the lowest (50 μM) datum cannot be included due to insufficient height; in this case n=5.

CHAPTER EIGHT: Situations where WBQ is effective while Height/Area-based Linear Calibrations Fail

8.1 WBQ with Peak Maximum in Nonlinear Response Regime

With nonlinear/saturated detector response, area- or height-based quantitation has obvious limitations. Figure 8.1 shows nitrate chromatograms with absorbance extending to the nonlinear region. $\boldsymbol{ln\ C}$ could be expressed as:

$$\boldsymbol{ln\ C} = \mathbf{31.6} * (\boldsymbol{W_{50\ mAU}},\ \text{min})^{\mathbf{0.10}} - \mathbf{23.0},\ r^2 = 0.9935 \quad ...(15)$$

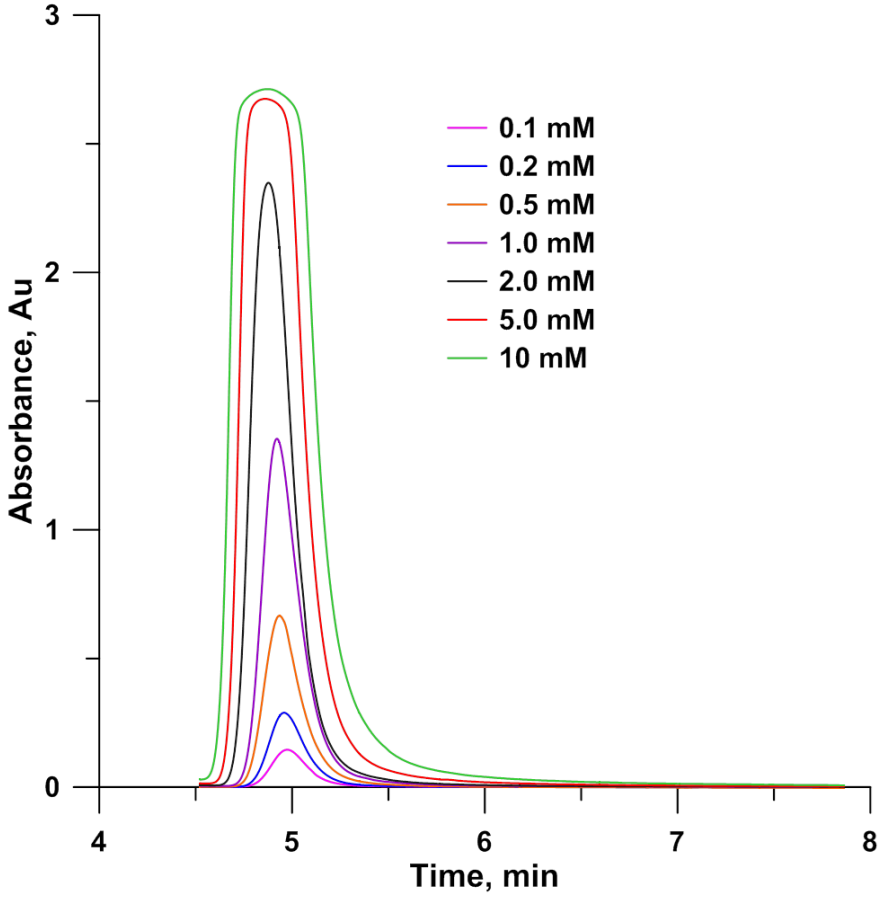

Figure 8.1. Nitrate peak in chromatogram detected at 200 nm on a Dionex AD 20 detector. Chromatographic details: AG11 (2 x 50 mm)+ AS11 (2x 250 mm) columns. ASRS-Ultra II anion suppressor in external water mode. 12.5 mM NaOH isocratic at 0.3 mL/min; injection volume, 10 µL.

with 11.4% RMSRE in comparison to 373% and 1130% RMSRE for area and height based unweighted regression. The quantitation errors in the three paradigms (height- area- and width-based) are shown in Table 8.1; WBQ outperforms area and especially height-based quantitation in both unweighted and $1/x^2$-weighted regression. Height-based quantitation, most affected by nonlinearity, shows the highest error. WBQ is not significantly affected by weighting, it outperforms the others, especially in the unweighted mode.

	% RMS Errors, unweighted			%RMS Errors, $1/x^2$ weighted		
	Area	Height	Width	Area	Height	Width
Nitrate	373	1130	11.4	23.2	40.2	11.5

Table 8.1. Weighted and unweighted calculated % RMS Errors of Area, Height, and Width based quantitations of figure 8.1.

Although an RMS relative error of 11.4% may seem high, this needs to be judged in perspective to errors that result in conventional methods. In part the error arises from a change in the peak shape; this is readily apparent at the highest level. It is instructive to consider instead caffeine, a well-behaved model analyte in reverse-phase liquid chromatography and also as an absorbance standard.

8.2 Response Non-Monotonic with Concentration and/or Truncated

Many fluors undergo self-quenching at higher concentrations. An interesting use has involved a fluorescent eluent in the quenched domain to generate positive signals in indirect fluorescence detection[43] but mostly it limits the use of fluorescence detection at higher concentrations. If the peak apex of a fluorophore is in the quenched domain, an $\wedge$-shaped response results. In altogether other situations, a $\vee$-shaped response is possible. For example, IC relies on conductometry. But very weak acids barely ionize and are undetectable. We have been exploring determination of strong to very weak acids by adding a base post-suppression as a PCR.[44,45,46-51] Following base addition, the principal conductive species is OH^-. An eluting acid reacts as $HX + OH^- \rightarrow H_2O + X^-$, the highly mobile OH^- is replaced by less conductive X^-, producing a negative response. Reducing the PCR

concentration decreases the background and associated noise, improving LODs.[44] However, when the analyte concentration exceeds the base background, the response is truncated. As in a strong acid-strong base conductometric titration, on the leading edge of the eluite acid peak, conductivity decreases until the base is neutralized, then conductivity increases until the peak apex (unless truncated by detector/data system) and the process reverses on the trailing edge creating a **W-** (Figure 8.2) or center-truncated **W** (Figure 8.3a). For a very weak acid like silicate (pK_a 9.3), the response is considerably more complicated due to multiple factors: insufficiently high pH to cause complete ionization of silicate, buffer formation and poor to no ionization of the excess silicic acid (Figure 8.3b). In performing WBQ for formate and silicate in Figure 8.3, the parameters in eq 14 are fit to obtain the lowest RMSRE; over a 0.1-6 and 0.1-10 mM concentration span the RMSRE were 5.0 and 5.7%, respectively. Given the unusual peak shapes, this is remarkable.

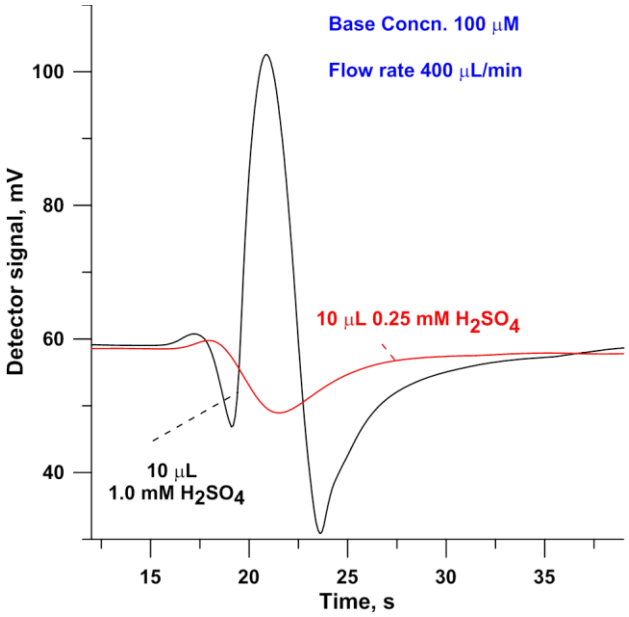

Figure 8.2. Two different concentrations of H_2SO_4 are being injected into a 100 μM strong base carrier. At lower injected concentrations, a negative peak results (red trace). When the acid concentration at the peak exceeds the base concentration, a W-shaped peak results (black trace). Note that if a fluorescent substance was injected into a nonfluorescent carrier and the resulting signal monitored with a fluorescence detector, an M-shaped peak will result if at the peak the fluorescence is in the self-quenched domain. Both belong to a general case where the response is not a single-valued function of the concentration.

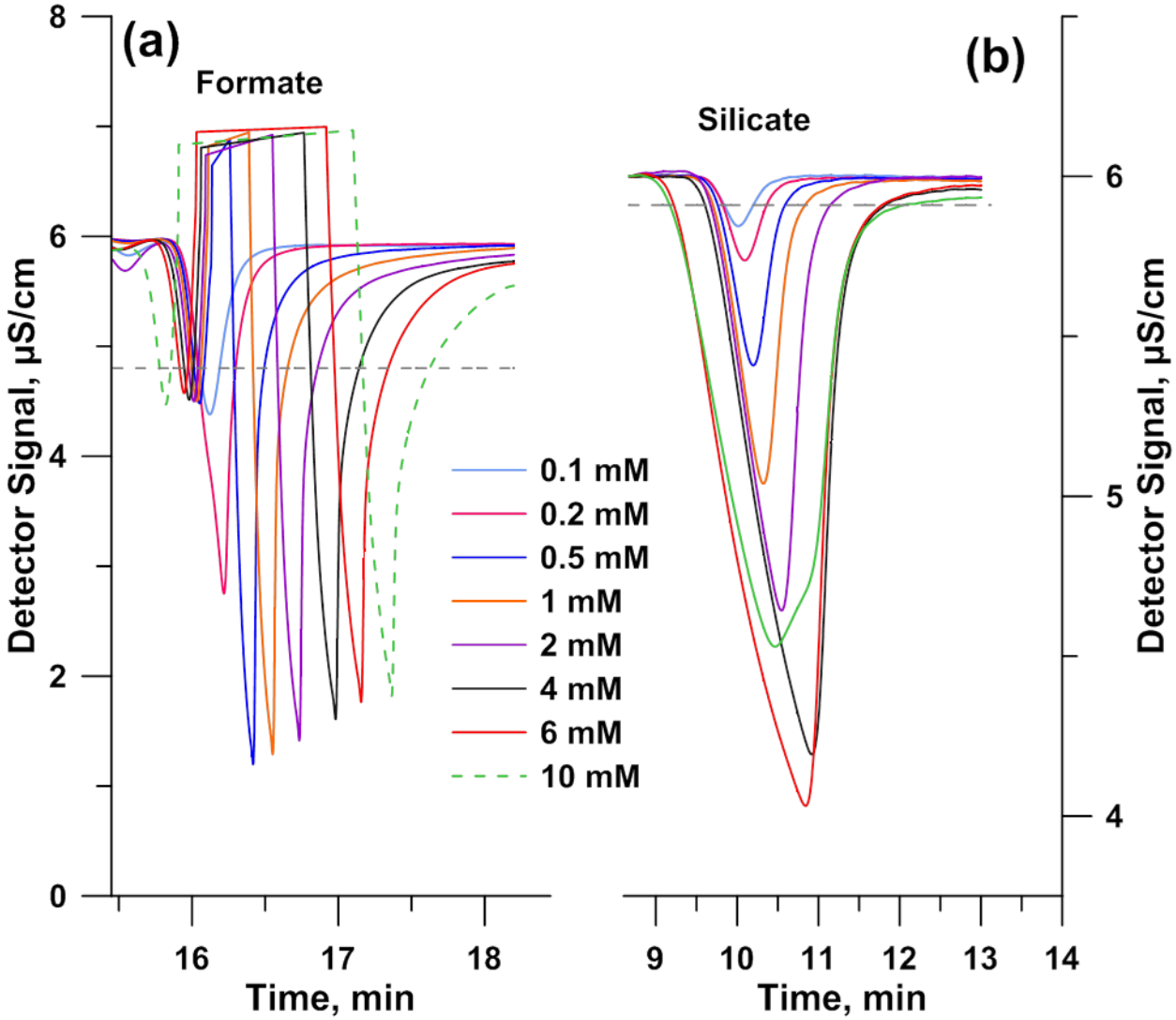

Figure 8.3. Conductometric responses of two (a) formate (b) silicate, each over two orders of magnitude, to a detection system using a permeative amine introduction system (PAID) which introduces diethylamine to detect acids.[52] Electrogenerated KOH eluent at 0.30 mL/min was used with AG11 (2 x 50 mm)+ AS11 (2x 250 mm) columns as follows: Time, min (Concentration, mM): 0(2.0), 10(2.0), 15(10.0), 32(10.0), 33(2.0). Injection volume 10 µL. The horizontal dashed lines indicate where width was measured in each case. Quantitation equations: Formate (0.1-6 mM): $ln\ C = 5.64\ \boldsymbol{W_h}^{0.43} + 2.18$, RMSRE = 4.98%. If extended to 10 mM the equation alters significantly and RMSRE increases to 8.18%, mostly because of peak shape alteration due to overloading. Silicate (0.1-10 mM) is quantitated using $ln\ \boldsymbol{C} = 13.1\ \boldsymbol{W_h}^{0.16} - 6.45$, RMSRE = 5.71%.

Asymmetry at $1/\bar{h}$ = 0.05 and 0.10 are typically cited. These cannot describe *overall* symmetry. Our love for symmetry[53,54] affects visual perception; this is rarely objective (Figure 9.1).

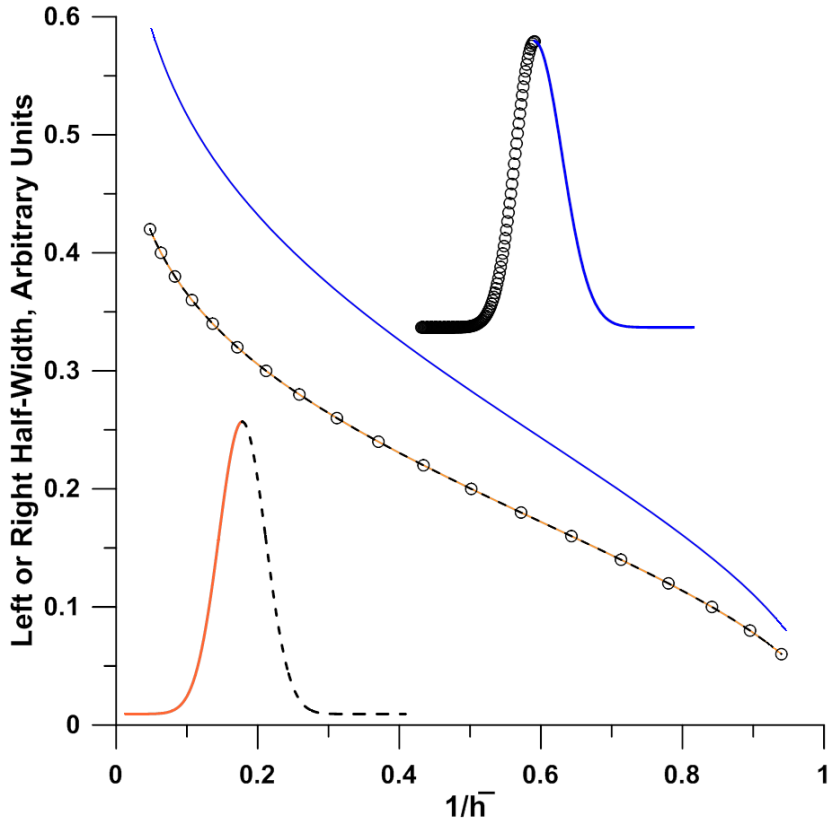

Figure 9.1. The peak on bottom left is a perfectly Gaussian peak that obeys the equation $h = \exp(-t^2/0.058)$ where the peak is centered at $t = 0$. The orange solid trace and the dashed black trace in the main plot respectively shows the left and right half width for this peak as a function of $1/\bar{h}$ ($\bar{h}$ being h_{max}/h). As the two halves are mirror images, the half-width traces are superimposed. The peak on top right has Gaussian left and right halves but the right half has a squared standard deviation term that is twice that of the left half: $h = \exp(-t^2/0.116)$. As the left halves of the top and bottom peaks are identical, the circles representing the leading half of the top peak superimposes the previous half-width vs. $1/\bar{h}$ traces. The right half of the top peak, however, provides a very different half-width vs. $1/\bar{h}$ trace. This figure illustrates that peak symmetry (or lack thereof) is much easier to ascertain in left half-width and right half-width vs. $1/\bar{h}$ plots than visually examining the chromatographic peak.

Plots of left- or right half-width vs. time have been beautifully explored by Baeza-Baeza et al.[55] for many purposes. However, for any peak, it would be obvious that $W_{h,l} = t_R - t$ and $W_{h,r} = t - t_R$. As such, plots of $W_{h(l,t)}$ vs. t are merely inverted triangles version of the peaks. Plots of $W_{h(l,t)}$ vs. $1/\bar{h}$ offers a different perspective, as shown in Figure 9.1 for simulated Gaussian peaks and in Figure 9.2 for several previously discussed real chromatographic peaks with large variations in symmetry.

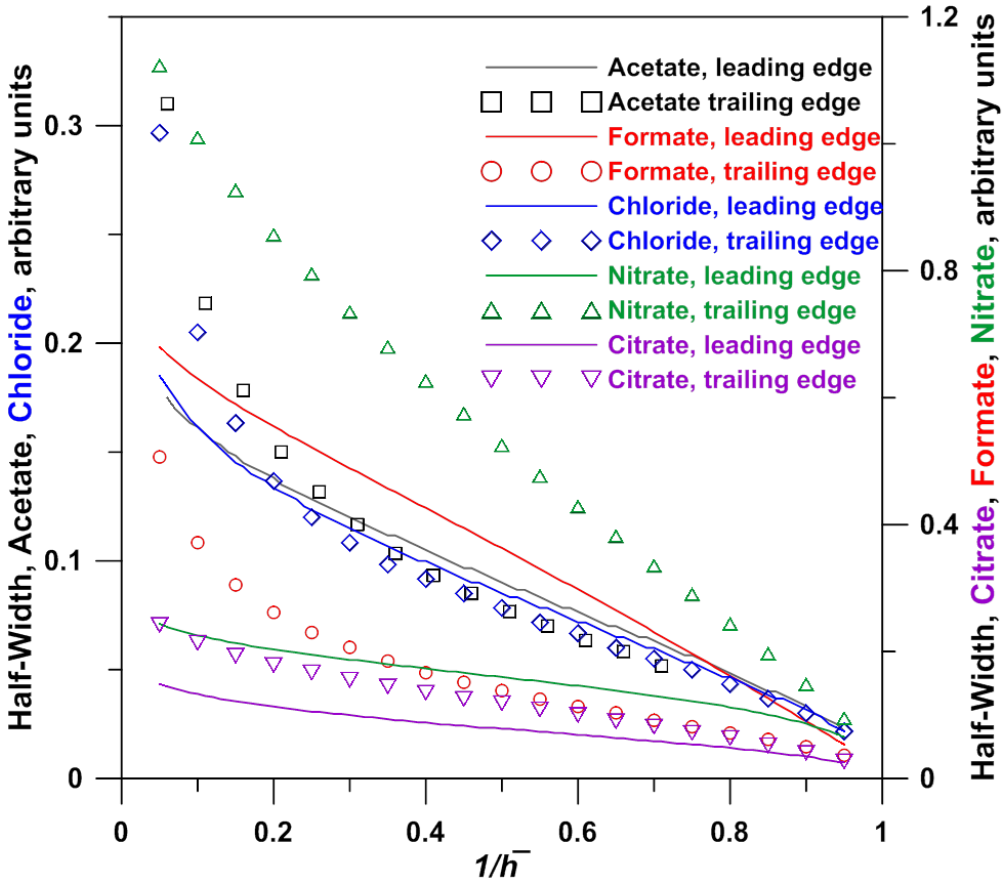

Figure 9.2. Left (leading) and right (trailing) half-width vs. $1/\bar{h}$ plots for acetate, formate, chloride, nitrate, and citrate. The original chromatograms can be seen above. Note that while generally the trailing half is wider than the leading half, it is the reverse for the formate peak which fronts strongly. For chloride and acetate, the two halves are very close to each other at high $1/\bar{h}$ but the trailing half becomes wider towards the base (classic tailing). The absolute value of the width is dependent on the standard deviation of the peak and the injected concentration.

These depict not only how each half behaves comparatively, but also fronting and tailing. If chromatographic peaks were perfectly Gaussian, a single parameter, specifying the SD will be sufficient. As this is not the case, one has the choice of remaining within the strict Gaussian paradigm and assuming that is not a constant. It can be readily computed at all points in the peak from $s = |t|/\sqrt{(2 \ln \bar{h})}$ and examined as a function of the relative height or time. Figure 9.4 plots s vs. $1/\bar{h}$ for caffeine over a 300-fold range of concentration. Figure 9.5 shows s vs. $|t|$, providing slightly different information.

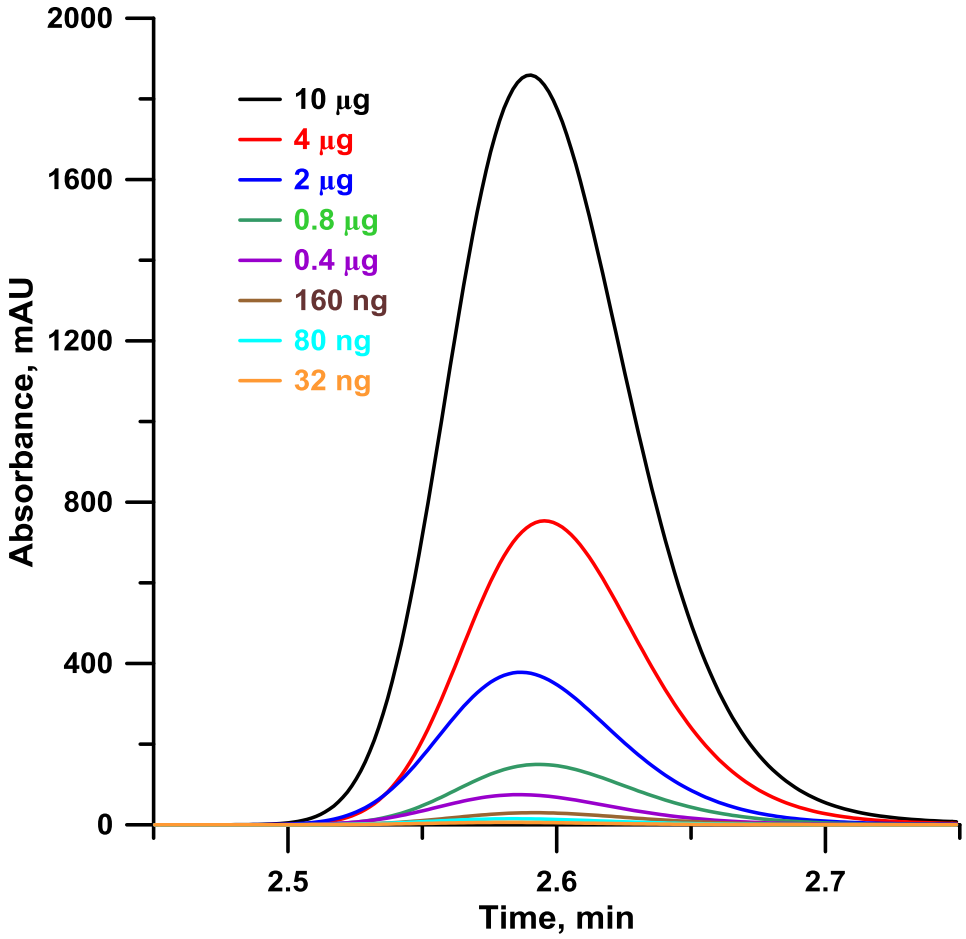

Figure 9.3 Caffeine chromatograms at 272 nm, 32 ng -10 µg injected. Chromatographic conditions given in Experimental Section.

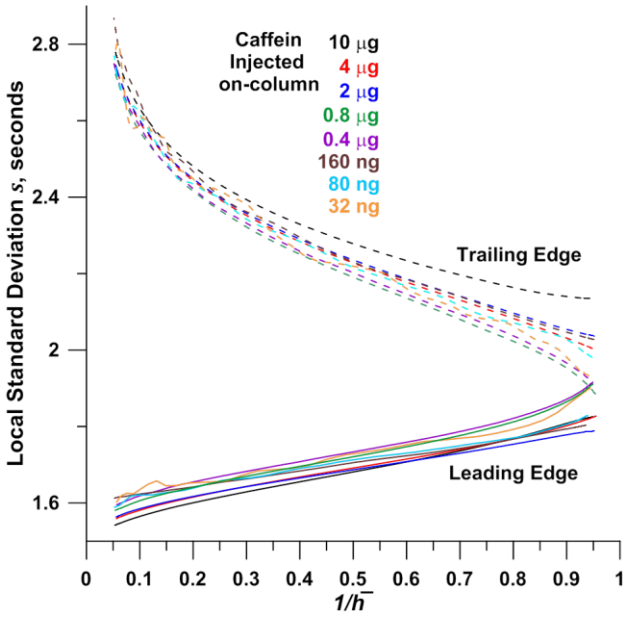

Figure 9.4. Local standard deviation for caffeine injected over a 300 fold mass range are plotted in terms of $1/\bar{h}$ within the bounds of 0.05-0.95 (the same bounds are used in all other similar plots as conformity to the GGDM is best observed within these limits. The data plotted was within the linear range of the detector. A true Gaussian would have had constant across the peak, a flat horizontal trace. The original chromatograms appear in Figures 9.3. At the lower height end the lowest mass injection trace (orange) perceptibly shows the effect of noise and at the highest mass injection trace (black) clearly has greater standard deviation than the rest. It is interesting to note that such a plot clearly shows that the biggest effect of such overloading occurs near the highest concentration on the trailing edge and not just at the tail of the trailing edge as is often thought.

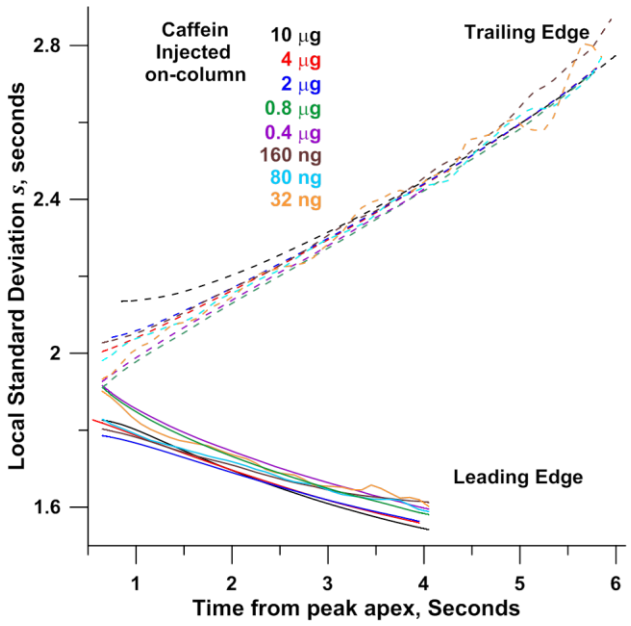

Figure 9.5. Local standard deviation for caffeine injected over a 300 fold mass range are plotted vs. time from the peak apex (X-axis bounds $1/\bar{h}$=0.05-0.95). The data plotted was within the linear range of the detector. The original chromatograms appear in Figures 9.3. At the lower height end the lowest mass injection trace (orange) perceptibly shows the effect of noise and at the highest mass injection trace (black) clearly has greater standard deviation than the rest both near the peak and near the tail. Compared to Figure 9.4, this plot more clearly indicates increase in standard deviation at the tail end.

Whereas ***s*** varies considerably across a peak, its constancy as a function of concentration is remarkable. Figure 9.2 may provide a holistic view of variance across the peak but a complete description still requires the dependence of s with $\boldsymbol{1/\bar{h}}$ or ***t*** to be specified. If we adopt the GGDM (eq 7) instead of the strict Gaussian paradigm, such a description is self-contained. Figure 9.6 shows $\boldsymbol{\ln W_{h(l)}}$ or $\boldsymbol{\ln W_{h(t)}}$ vs. $\boldsymbol{\ln(\ln \bar{h})}$ plots for chloride nitrate and citrate including the slope, SD (calculated from the intercept), and r^2.

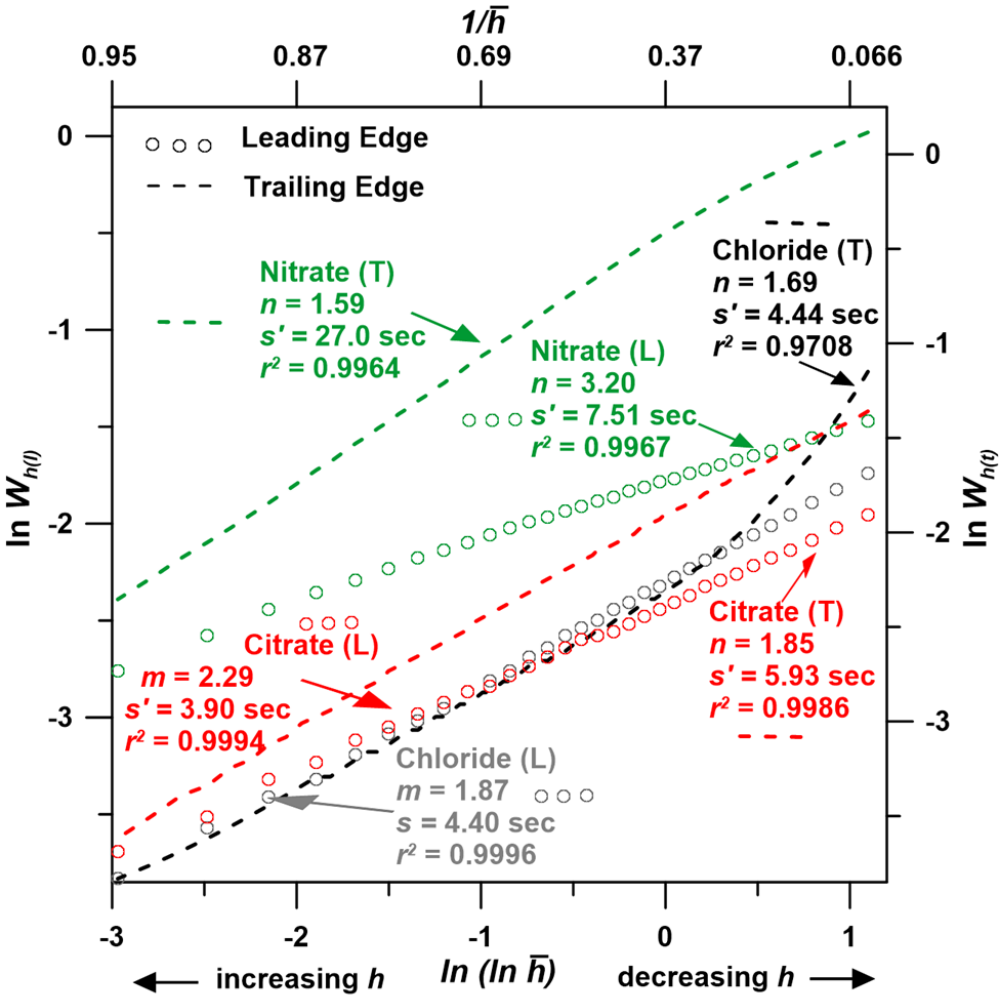

Figure 9.6. Circles: leading edge (L), dashed lines: trailing edge (T). The leading edge always fits GGD better, albeit for nitrate and citrate the difference is insignificant. The standard deviation is also always greater for the trailing half although the difference is minor for chloride. The value for an ideally Gaussian peak for ***m*** or ***n*** is 2. The leading edge of the chloride peak and the trailing edge of the citrate peak are very nearly true Gaussians. For all the others, except for the leading edges of nitrate and citrate, ***m*** or ***n*** is <2. All traces are highly linear (high r^2) throughout except for the trailing edge of chloride there is departure from linearity towards the base of the peak (below $\boldsymbol{1/\bar{h}}$ = 0.30).

For all three, the plots are essentially linear (except for the tail of the chloride peak. The slope and the SD then (for each half of the peak) provide a more complete description than any presently available. The r^2 values serve as a quality assurance for the model. Conventional asymmetry can be estimated at any value of $1/\bar{\boldsymbol{h}}$ from these specifications (reliability depending on r^2). WBQ relies on peak shape being concentration-independent. A change in shape brought about by concentration-dependent ionization or chromatographic overloading is not accommodated. Unlike the fully/uniformly ionized situation in Figure 9.6, except for the leading edge of the acetate peak, these are obviously nonlinear. However, it is still possible to specify $1/\bar{\boldsymbol{h}}$ limits within which the peak fits the GGDM.

CHAPTER TEN: Impurity Detection

If the impurity and analyte differ in exact retention and/or peak SD, the eluting band shape will differ in principle from that of the pure analyte. Consider both the analyte (concentration $\boldsymbol{C}$) and impurity (concentration 0.1$\boldsymbol{C}$) to have Gaussian profiles (Figure 10.1) eluting at identical retention times ($\boldsymbol{t_R}$). We assume analyte peak SD to be unity. If the impurity peak SD were the same, the overall response would be the same as the response of an analyte peak of concentration 1.1$\boldsymbol{C}$.Chromatographic theory assumes column efficiencies to be analyte-independent but in reality SDs are rarely identical even when retention times are. Consider impurities with SDs of 1.41 and 0.71. Applying WBQ at $1/\overline{\boldsymbol{h}}$ = 0.9 in either case will result in 1.1 $\boldsymbol{C}$ as concentration ($\boldsymbol{C_{pred}}$). But applying WBQ at $1/\overline{\boldsymbol{h}}$ = 0.2 will lead for *s*=0.71 to 1.1$\boldsymbol{C}$>>$\boldsymbol{C_{pred}}$ ~>$\boldsymbol{C}$ and for *s*=1.41 to $\boldsymbol{C_{pred}}$ >>1.1 $\boldsymbol{C}$. When analyte and impurity $\boldsymbol{t_R}$'s are identical, $\boldsymbol{C_{pred}}$(high $1/\overline{\boldsymbol{h}}$)>$\boldsymbol{C_{pred}}$(low $1/\overline{\boldsymbol{h}}$) if $SD_{analyte}$> $SD_{impurity}$ and *vice-versa*. Figure 10.2 presents $\boldsymbol{W_h}$ vs $\boldsymbol{h}$ plots for the Figure 10.1 data with the same conclusions.

In the more common case where the impurity/analyte differs in $\boldsymbol{t_R}$, impurity contribution towards the bottom vs. top width increases with $\Delta\boldsymbol{t_R}$. For the Figure 10.1 situation, the results of increasing the impurity (*s*=0.71) $\boldsymbol{t_R}$ by 0.5, 1.5, and 2 units. The impurity becomes more apparent as $\Delta\boldsymbol{t_R}$ increases. With $\Delta\boldsymbol{t_R}$ =0.5, $\boldsymbol{C_{pred,}}_{\text{low } 1/\overline{\boldsymbol{h}}}\approx 1.1\boldsymbol{C}$ but $\boldsymbol{C_{pred,}}_{\text{high } 1/\overline{\boldsymbol{h}}}$ will be much lower. With $\Delta\boldsymbol{t_R}$ =1.5 or 2, $\boldsymbol{C_{pred,}}_{\text{high } 1/\overline{\boldsymbol{h}}}\approx\boldsymbol{C}$ while $\boldsymbol{C_{pred,}}_{\text{low } 1/\overline{\boldsymbol{h}}}$>>1.1$\boldsymbol{C}$. Even when the analyte does not exactly obey the GGDM, the WBQ-based $\boldsymbol{C_{pred,}}_{\text{low } 1/\overline{\boldsymbol{h}}}/\boldsymbol{C_{pred,}}_{\text{high } 1/\overline{\boldsymbol{h}}}$ ratio will increase in the presence of an impurity, increasingly so with increasing $\Delta\boldsymbol{t_R}$.

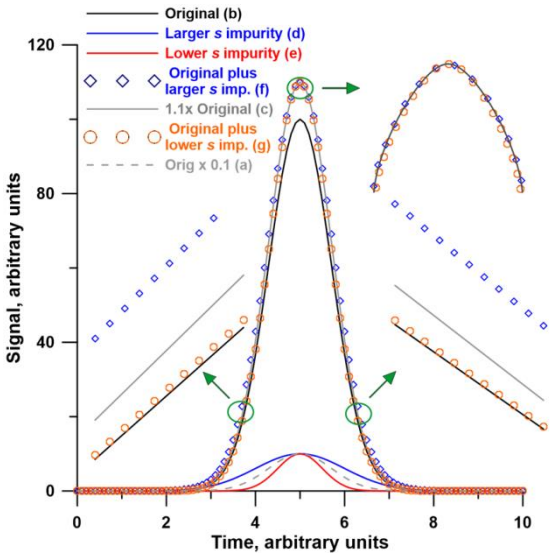

Figure 10.1. The original analyte (**a**) 10, (**b**) 100, and (**c**) 110 units amplitude are shown in dashed gray, solid black and solid gray traces; they are all centered at t = 5 and have a SD of 1 time unit. Thus **a + b = c**. The impurities themselves are shown in the solid blue (**d**), and solid red (**e**) traces, both are centered at t = 5 and have an amplitude of 10. The respective SDs are 1.41 and 0.71 units. The dashed blue (**f**) and dashed orange traces (**g**) respectively equal **d + b**, and **e + b**. Indicated circled areas in magnified views: all four traces are seen: the outermost is **f**, the innermost is **b**, with **g** running very close to **b**, and **f** considerably beyond **c**. Near the top, however, trace **b** is so much lower than the rest that it is below the span of the magnified plot. Both traces **f** and **g** run extremely close to **c** near the top. It would be obvious that WBQ for either **f** or **g** at $1/\overline{h} \approx 0.9$ will predict an amplitude (and concentration) close to that of **c**. Conversely, applying WBQ to **f** and **g** respectively near $1/\overline{h} \approx 0.2$ (near the circled areas) will produce a concentration prediction considerably beyond **c** and close to but slightly beyond **b**, respectively.

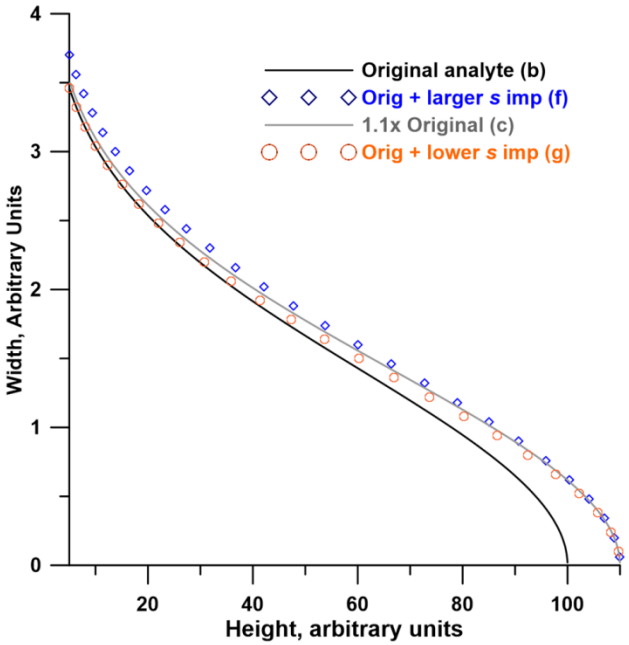

Figure 10.2. The widths relevant to the case discussed in Figure 10.1 is presented in a different manner, as the width plotted as a function of height covering approximately $1/\overline{h}$ = 0.05-0.95. This rendition makes it easier to observe that at high height both **f** and **g** are very close to **c** but at low heights, **g** becomes close to **b** (C_{pred} decreases) while **f** goes beyond **c**, (C_{pred} increases).

10.1 Impurity Diagnostics When a Pure Standard is Unavailable

If a pure standard is not accessible or has not been characterized, the presence of an impurity can still be diagnosed, e.g., with dual wavelength absorbance ratiograms, a technique now 40 years old. This relies on the ratio of the extinction coefficients of the analyte and the impurity being different at the two wavelengths.[56] Changes in composition of the solvent, as during gradient elution, can be a problem.[57] Two structurally similar species, difficult to separate chromatographically, are also often spectroscopically similar. Other substantially more complex and computationally intensive approaches such as iterative target-transformative factor analysis,[58] evolving factor analysis (EFA),[59] fixed-size moving-window EFA,[60] never became popular. Ratioing with orthogonal serial detectors must correct for dispersion between detectors, a generally unsolved problem.[47]

Even without a known standard shape, an inability to fit the GGDM may potentially signal the presence of an impurity. While these cannot be used for truncated peaks because the apex cannot be located, the approximation represented by eq. 1-9 (reproduced below in a different form) is applicable

$$\boldsymbol{W_h}^{\boldsymbol{k}} = \boldsymbol{jln}(\overline{\boldsymbol{h}}) \quad ...(15)$$

or

$$\boldsymbol{W_h}^{\boldsymbol{k}} = \boldsymbol{u} - \boldsymbol{jln}\,\boldsymbol{h} \quad ...(16)$$

where

$$\boldsymbol{u} = \boldsymbol{jln}(\boldsymbol{h_{max}}) \quad ...(17)$$

and thence

$$\boldsymbol{u} = \boldsymbol{r} + \boldsymbol{jln}\,\boldsymbol{C} \quad ...(18)$$

$\boldsymbol{r}$ being $\boldsymbol{j} * \boldsymbol{ln}\,\boldsymbol{p}$ and $\boldsymbol{C} = \boldsymbol{ph_{max}}$. eq 18 does not require $\boldsymbol{h_{max}}$ to be known. Best fit values for $\boldsymbol{k}, \boldsymbol{u}, \boldsymbol{j}$ can be obtained by nonlinear least square routines, e.g., Microsoft Excel Solver™. The goodness of fit (linear r^2 or better, RMSRE) is an indication of the validity of the model. If chromatographic data are available for multiple concentrations (even if some

peaks at higher concentrations are truncated), and ***h*** is within the linear response range, eq 18 states that the respective intercepts (***u***) for each fit at individual concentrations will be linearly related to ***ln C*** in the absence of impurities.

Width at multiple height data can be used to test their conformity to eq 16. If the procedure is repeated for a set of serial dilutions, a second test, which examines if a linear relationship exists between the respective intercepts and *ln* ***C***, can be performed as further evidence of conformity. We test this with the chloride data in Figure 4.1. Figure 10.3 plots the relevant data in the form of eq 16. Figure 10.4 shows that the linear relationship of the intercepts in Figure 10.3 with *ln* ***C*** also holds for this pure peak.

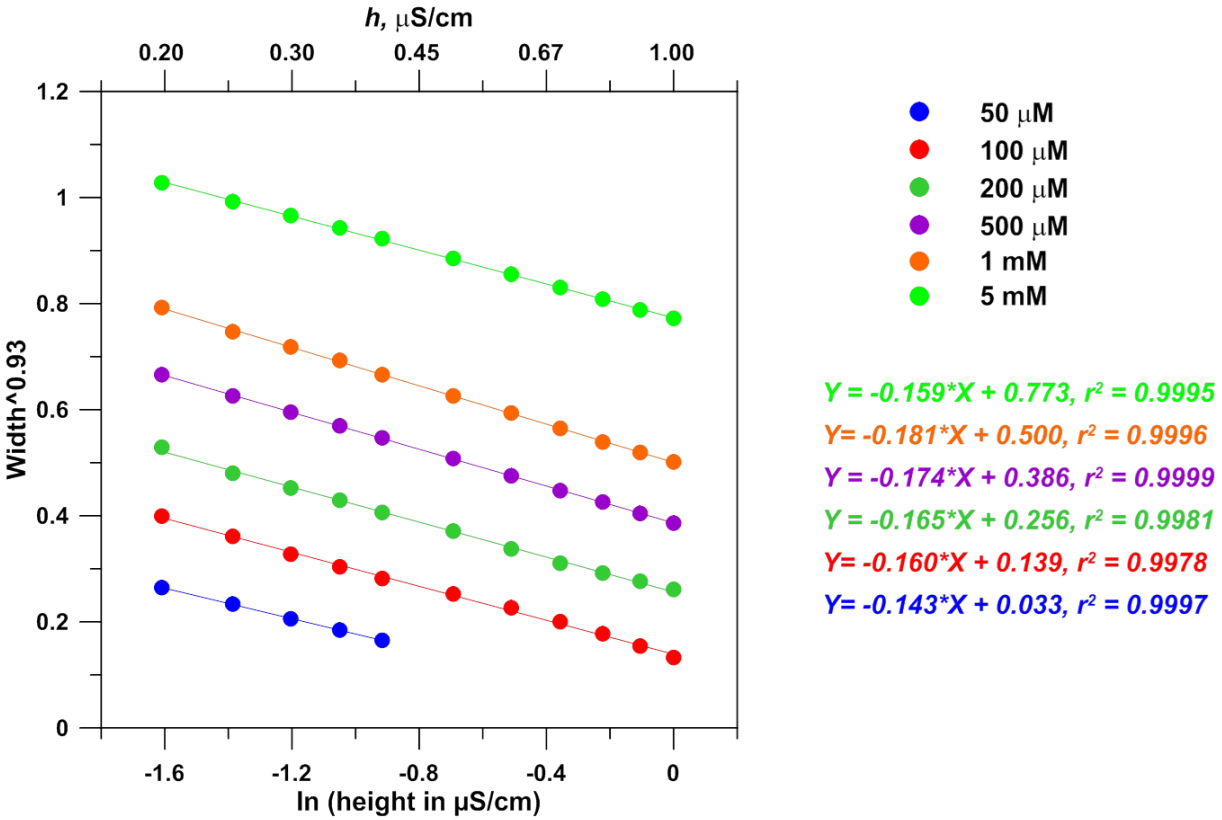

Figure 10.3. The chloride data in Fig 4.1 is plotted in the form of eq. 16, a linear plot results throughout. In addition, the intercept ***u*** in Eq. 16 should be linearly proportional to *ln* ***C*** provided that all measurement heights are within the linear response domain. Figure 10.4 shows the plot of ***u*** vs. *ln* ***C***.

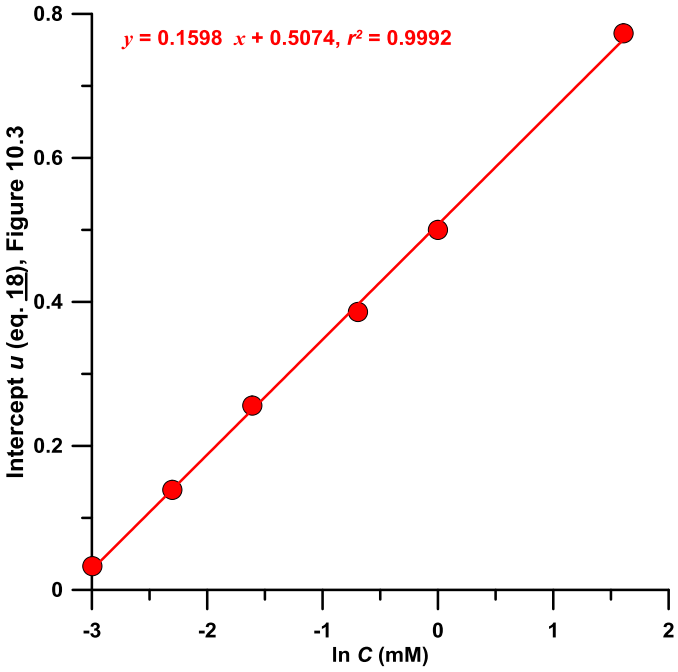

Figure 10.4. A plot of the intercepts for the chloride data in Figure 10.3 vs. ***ln C*** shows an excellent linear correlation.

Chromatographic data for caffeine provided an opportunity to explore conformity to a GGD model over a large range using plots as in Figures 10.3, 10.4. Importantly, for the raw chromatographic data, *there was no indication of an impurity in any of these chromatograms*. We were disappointed that linear plots were *not* observed (Figures 10.5 and 10.6 cover 2-400 ng injected caffeine, similar to the data for chloride in Figures 10.3, 10.4 spanning two orders of magnitude). Note that these caffeine concentrations result in absorbance peak maxima of 0.4-30 mAU, sufficiently above noise but far below possible detector nonlinearity onset. Initially, we took this as failure to conform to the GGDM. However, the nonlinearity occurred especially in the high ***C***-low ***h*** sector. This becomes even more obvious for the data at even higher concentrations (Figure 10.6). This is the same effect expected from an impurity. Therefore we examined both edges of each caffeine peak at high magnification. While the presence of an impurity is barely discernible on the tailing edge of the 400 ng peak, for the 100 µg injection, the magnified view makes the presence of the impurity obvious (Figure 10.5 inset). It is remarkable that although the impurity contribution to the overall absorbance at any concentration level was so little that

height- or area-based linearity studies were unaffected, the discovery of the co-eluting impurity originated solely in the nonconformity of the peak to the GGDM.

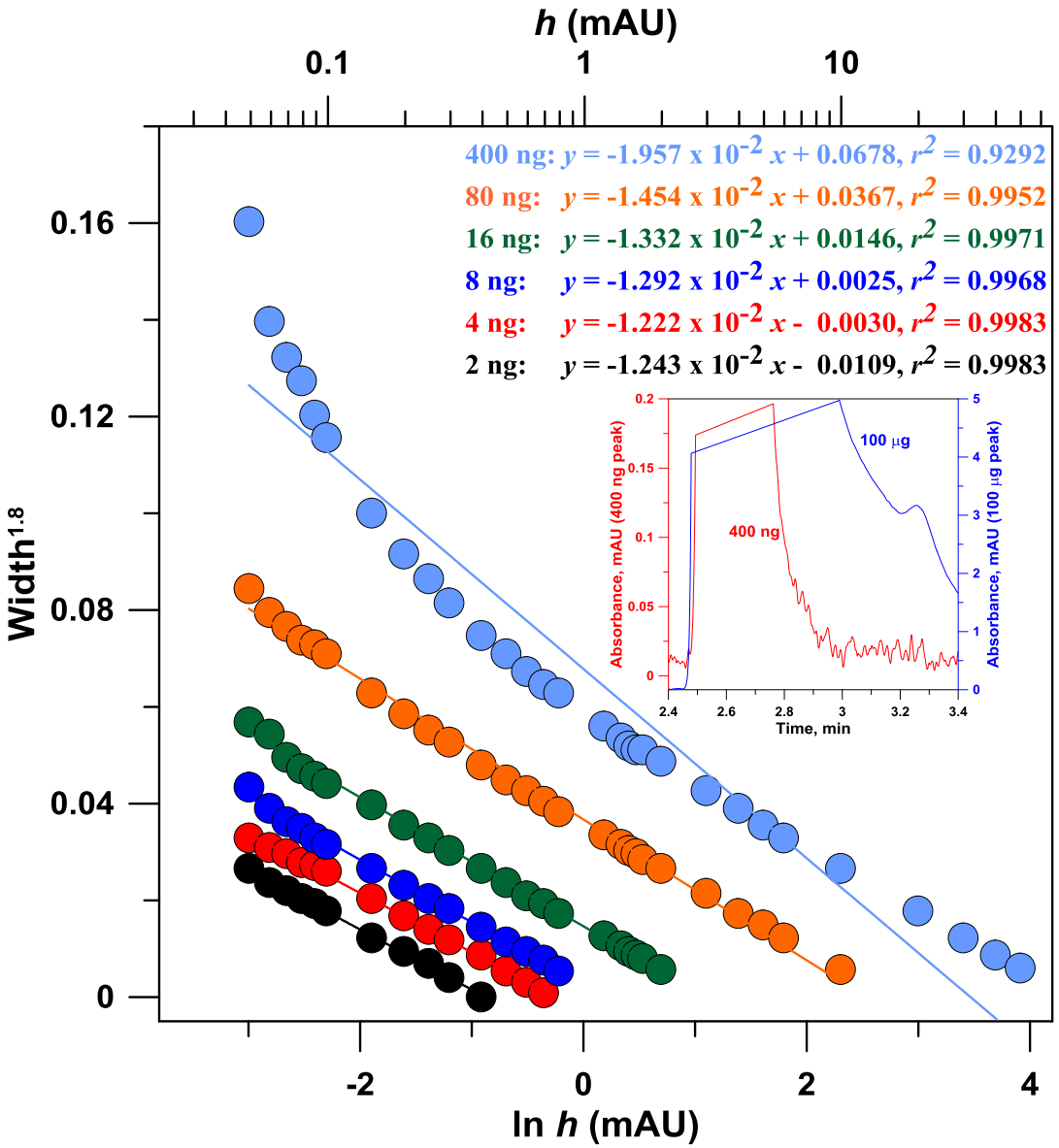

Figure 10.5. Caffeine chromatographic data for 2-400 ng injected amounts plotted in the form of Eq. 16. See Experimental Section for chromatographic details. See also Figure 10.6 for a plot of the intercepts vs logarithm of the amount injected for departure from linearity at the high concentration end.

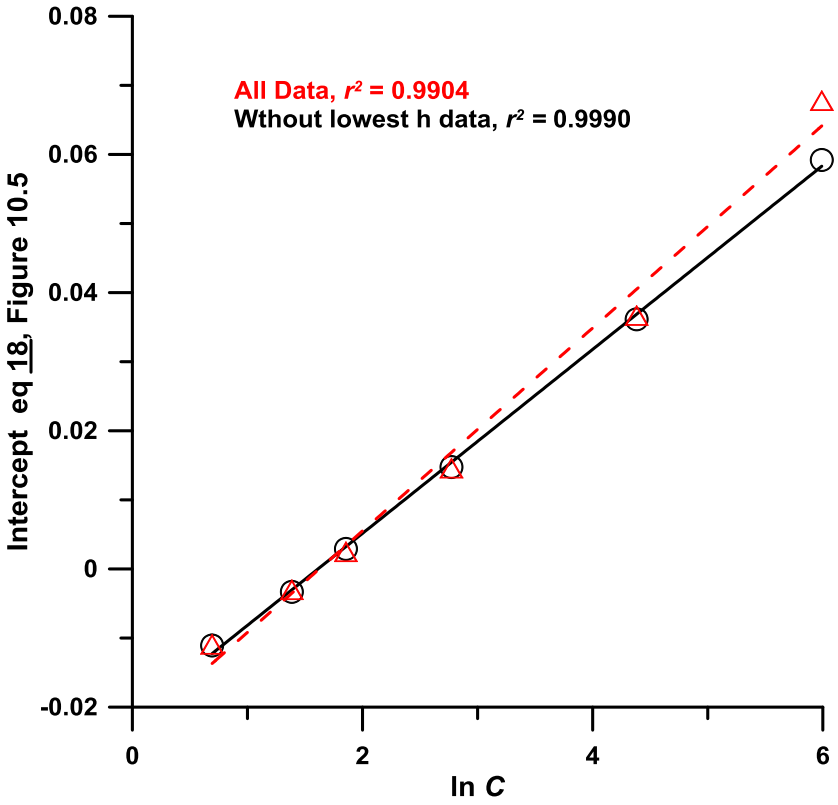

Figure 10.6. This plot for caffeine is similar to that for chloride in Figure 10.4. When all the data (red triangles) are used in the regressions done in Figure 10.5, deviation from linearity at the higher concentration end is evident.

10.2 Impurity Diagnostics when Pure Standards are Available

We examine quantitatively how the presence of an impurity changes the shape. Qualitatively, by definition, an *impurity* contributes a smaller portion of the overall peak response compared to the main component. An impurity therefore affects the peak-width differently at the bottom vs. the top. Therefore WBQ applied to an impure peak that is based on calibration by pure standards will predict different concentrations using lower vs. higher ***h*** calibrations. Impurity diagnostics can be based on a significant increase in variance (e.g., F-test) of the predicted concentrations from width-based calibrations at multiple heights of the suspect peak vs. that for standards at the same heights.

Also, ratios of widths at various heights can be used as shape indices. The change in this shape index may indicate the presence of impurities. For a Gaussian peak, it is readily derived:

$$W_{h1}/W_{h2} = \sqrt{\frac{ln\,\bar{h}_1}{ln\,\bar{h}_2}} \quad ...(19)$$

For example, $W_{0.2}/W_{0.8}$ for a Gaussian peak is readily calculated to be 2.686. For a peak defined by two independent GGDs, as in eq. 7, widths at minimally three heights are needed to compute a numerical constant.

For any peak obeying eq 4, the terms $\frac{ln\frac{W_{\bar{h}_1}}{W_{\bar{h}_2}}}{ln\frac{W_{\bar{h}_2}}{W_{\bar{h}_3}}}$ or $\frac{ln\frac{W_{\bar{h}_1}}{W_{\bar{h}_2}}}{ln\frac{W_{\bar{h}_3}}{W_{\bar{h}_4}}}$ are constants readily derivable from the specific values of $\bar{h}_i$ chosen. From three W_h measurements, j and k (eq 16) can also be computed. Even when a peak does not exactly follow eq. 7, we find that $\frac{ln\frac{W_{0.2}}{W_{0.4}}}{ln\frac{W_{0.4}}{W_{0.8}}}$ or a similar parameter involving some other combination of W_h values of the examined peak can be compared with the corresponding value of a standard for impurity diagnostics, with conclusions based on statistical criteria.

Consider calibration curves are made with pure standards; during analysis of real samples, an impurity is suspected in the analyte peak. For a calibration curve of 200-2000 μM bromide (Figure 10.7), both height/area display excellent linear correlation with concentration but an intercept is present (Figures 10.8). Best practice of WBQ utilizes peaks that scalable with concentration; this is nearly seen (Figure 10.9), there is discernible improvement in scalability after proportional intercept correction.

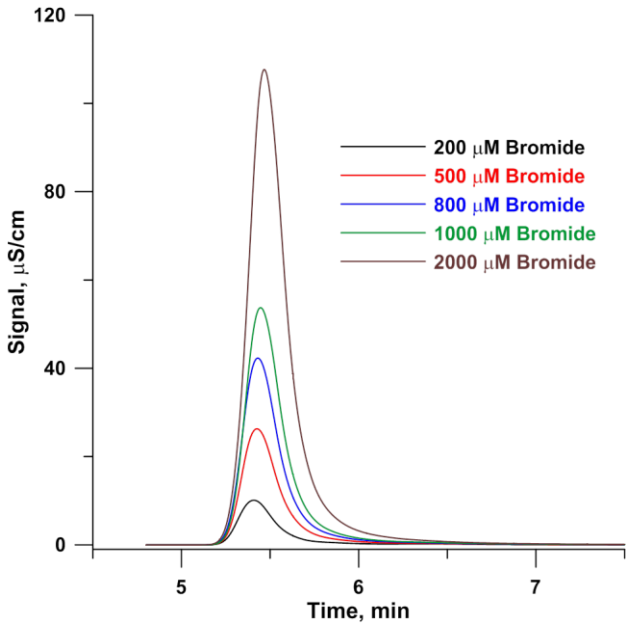

Figure 10.7. Suppressed ion chromatographic responses to different concentrations of bromide. Chromatographic conditions: ThermoFisher Dionex ICS-5000 system, AG20 (2 x 50 mm) + AS20 (2 x 250 mm), Electrogenerated KOH eluent 8.0 mM, 0.25 mL/min, Dionex AERS 500 2 mm suppressor. Compare with Figure 10.10 which contains the same samples but with 20 µM nitrate as impurity.

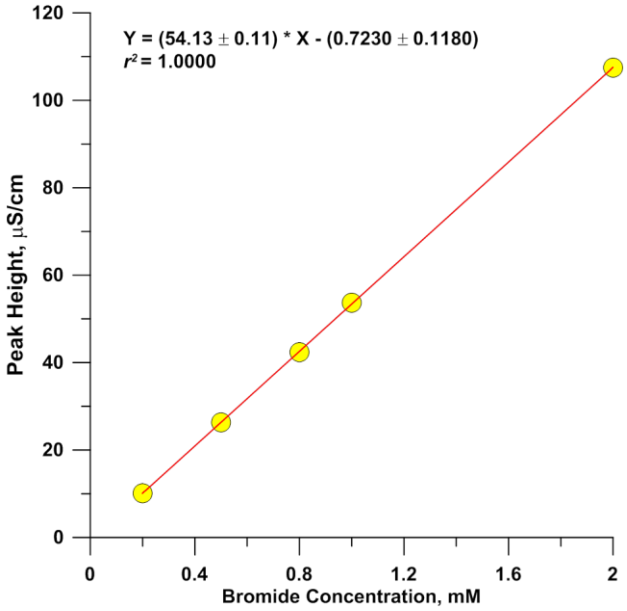

Figure 10.8. Height based calibration plot for the data in Figure 10.7 exhibits excellent linearity but has a significant negative intercept

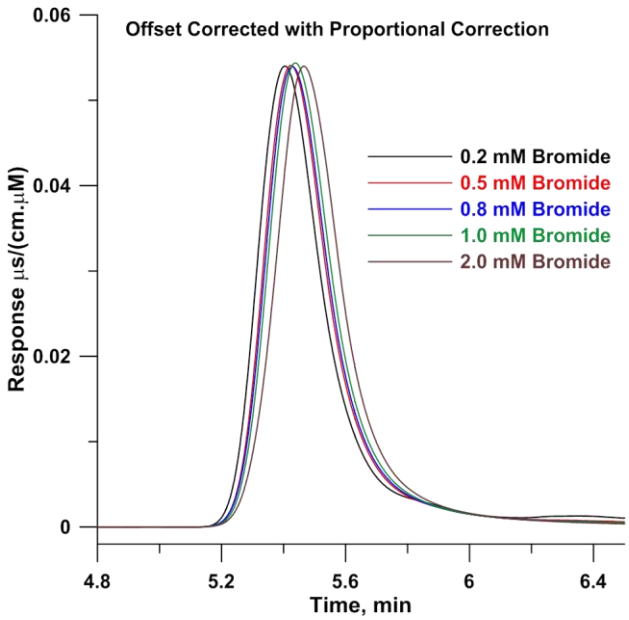

Figure 10.9. Offset correction can be performed by applying a proportionate correction for each chromatogram: Plotted ordinate value = (original value - zero intercept/$\bar{h}$)/injected concentration. An appropriately corrected plot shows good shape conformity. The amplitudes all match albeit minor shifts in the peak retention time can be observed.

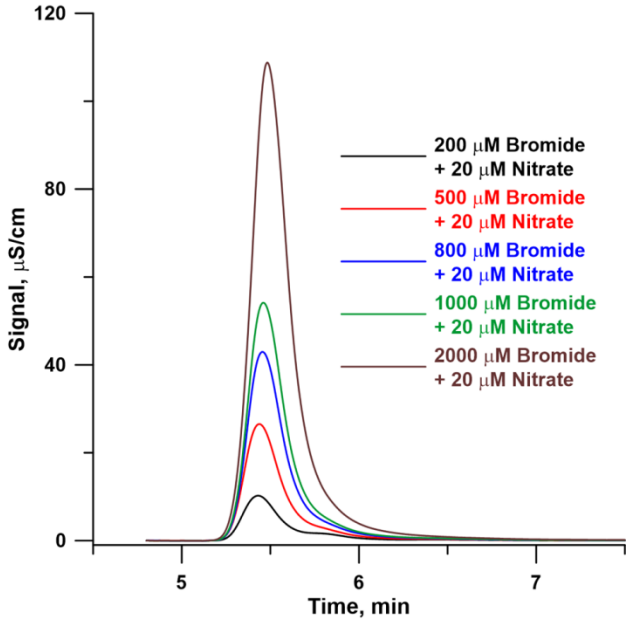

Figure 10.10. Injected responses to bromide containing a smaller amount of nitrate (1-10% relative on a molar basis). Elution conditions given in Figure 10.7 (which shows the same responses without any nitrate) were deliberately so adjusted as to cause co-elution. With or without reference to the pure bromide peaks in Figure 10.7, a cursory observation does not readily reveal the presence of an impurity, except perhaps for the lowest bromide concentration.

Figure 10.10 shows the same bromide samples each now containing 20 μM nitrate. The relative impurity amount is thus 1-10%.Except perhaps for the 10% case, the impurity is not readily discernible. We had outlined two approaches to impurity diagnosis: (a) checking equivalence of quantitation using calibration at multiple heights (at least one high, one low, within the realm of the examined peak) and (b) examination of ratio of log (width ratio) parameters for a putatively impure peak vs. standards. Both are examined below.

The data in Figure 10.7 were used to generate nine separate calibration curves at up to 9 different heights ranging from 2 to 43 μS/cm. The various $\boldsymbol{W_h}$ values for the standards were processed by the corresponding calibration equations to generate the $\boldsymbol{C_{pred}}$ values (blue triangles, Figure 10.11). The best fit through these are shown as dashed lines. The $\boldsymbol{C_{pred}}$ values are essentially height-independent (RMSRE 0.7 -2.2%). In contrast, in all cases for the impurity containing peaks, $\boldsymbol{C_{pred}}$ at the various heights differed much more. $\boldsymbol{C_{pred}}$ variances for all but the 200 μM case are higher for the impure samples at the $p<0.001$ level. $\boldsymbol{C_{pred}}$ variances for the 200 μM impure sample case differed from the standard at the $p<0.005$ level, largely because of a smaller n. (We note that the predicted concentrations generally decrease with increasing $\boldsymbol{h}$ but where the relative amount of the impurity is smaller, a monotonically decreasing trend of predicted concentration with $\boldsymbol{h}$ is only observed at $1/\overline{\boldsymbol{h}} > 0.1$.)

Given current computing power, automated quantitation predictions at multiple heights is not an onerous task. But should we limit ourselves to just the highest and lowest $\boldsymbol{h}$ predictions, the $\boldsymbol{C_{pred,}}_{\text{low } 1/\overline{\boldsymbol{h}}} / \boldsymbol{C_{pred,}}_{\text{high } 1/\overline{\boldsymbol{h}}}$ ratios are 1.01(1.14), 1.00(1.50), 0.98(1.25), 0.97(1.19), and 1.01(1.07)%, respectively, for the 200-2000 μM standards(impure samples in parentheses). Based on the standard deviations observed in duplicate analyses in all of the above, all these ratios were statistically different at the $p<0.001$ to $p<0.05$ level for the standards vs. the impure samples.

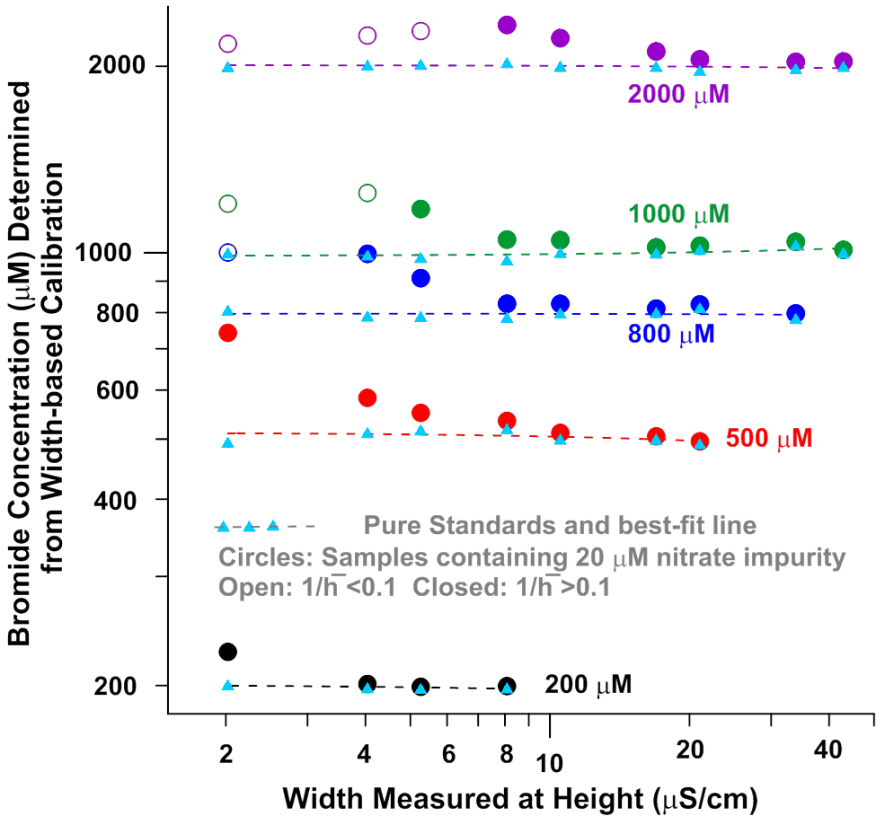

Figure 10.11. Impurity diagnostics based on concordance of quantitation conducted using calibration curves at multiple heights. Note logarithmic axes were used to adequately cover the large range of the parameters plotted. A logarithmic axis visually minimizes large differences while smaller differences are not as affected. The small blue triangles indicate the concentrations predicted from calibration equations for the standards and the dashed lines indicate the best-fit (these are essentially flat, the RSDs for 200 through 2000 μM standards, respectively: 0.65% (n=4), 2.2% (n=7), 1.2% (n=8), 1.1% (n=9), and 0.6% (n=9)). The circles indicate concentrations interpreted from the same calibration curves for impurity-bearing samples. These differ markedly when determined at different heights, respective corresponding being RSDs: 6.5%, 15.8%, 8.8%, 7.2%, and 2.9%. If determined at heights $1/\bar{h}$ >0.1, the predicted concentrations also decrease monotonically with increasing ***h***, confirming the presence of an impurity.

Impurity diagnosis based on the ln ($W_{0.2}/W_{0.4}$)/ln($W_{0.4}/W_{0.8}$) parameter is presented in Table 10.1. This approach detected a statistical change ($p<0.05$) in peak shape (and hence an impurity) in all but the three cases where the impurity concentrations were the lowest (in the 1-2% range). The confidence limits can be tightened by running more standards. Alternatively, $W_{0.1}$ being more susceptible to an impurity than $W_{0.2}$, changing

the test parameter to ln ($W_{0.1}/W_{0.4}$)/ln($W_{h0.4}/W_{h0.8}$), the remaining three cases are also identified as statistical outliers ($p<0.05$). Note also the remarkable constancy of the shape parameter across a large concentration range of the pure standard.

Standards	$W_{0.2}$	$W_{0.4}$	$W_{0.8}$	ln ($W_{h0.2}/W_{h0.4}$) / ln($W_{h0.4}/W_{h0.8}$)	ln ($W_{h0.2}/W_{h0.4}$) / ln($W_{h0.4}/W_{h0.8}$)	suspects	$W_{0.2}$	$W_{0.4}$	$W_{0.8}$	ln ($W_{h0.2}/W_{h0.4}$) / ln($W_{h0.4}/W_{h0.8}$)
Concn, mM ID					95% Confidence range	Concn, mM ID				
0.2 a	0.3648	0.2589	0.1248	0.4699	0.4590 - 0.4928	nom 0.2 a	0.3812	0.2585	0.1231	**0.5236**
0.2 b	0.3656	0.2583	0.1256	0.4818		nom 0.2 b	0.3833	0.2603	0.125	**0.5276**
0.5 a	0.3666	0.2593	0.1263	0.4814	0.4742 - 0.4964	nom 0.5 a	0.3775	0.2619	0.1261	**0.5002**
0.5 b	0.3688	0.2599	0.1271	0.4892		nom 0.5 b	0.3764	0.2613	0.1263	**0.5020**
0.8 a	0.3692	0.2611	0.127	0.4807	0.4762 - 0.4901	nom 0.8 a	0.3757	0.2616	0.1275	**0.5037**
0.8 b	0.3698	0.2611	0.1275	0.4856		nom 0.8 b	0.377	0.2627	0.1277	**0.5008**
1.0 a	0.3715	0.2624	0.1265	0.4765	0.4672 - 0.4961	nom 1.0 a	0.3776	0.2634	0.1274	0.4959
1.0 b	0.3708	0.2619	0.1282	0.4867		nom 1.0 b	0.3769	0.2631	0.1279	**0.4983**
2.0 a	0.3789	0.2655	0.1264	0.4792	0.4778 - 0.4822	nom 2.0 a	0.3836	0.2671	0.1259	0.4813
2.0 b	0.3789	0.2655	0.1267	0.4808		nom 2.0 b	0.3842	0.2675	0.1261	0.4814
0.3 a	0.3626	0.2580	0.1254	0.4722	0.4621 - 0.4931					
0.3 b	0.3640	0.2588	0.1278	0.4831						
0.6 a	0.3634	0.2579	0.1256	0.4767	0.4748 - 0.4775					
0.6 b	0.3640	0.2587	0.1261	0.4757						
0.9 a	0.3650	0.2584	0.1259	0.4804	0.4782 - 0.4849					
0.9 b	0.3668	0.2596	0.1269	0.4828						
1.5 a	0.3695	0.2606	0.1262	0.4814	0.4759 - 0.4840					
1.5 b	0.3706	0.2618	0.1267	0.4786						

Standards	$W_{0.1}$	$W_{0.4}$	$W_{0.8}$	ln ($W_{h0.1}/W_{h0.4}$) / ln($W_{h0.4}/W_{h0.8}$)	ln ($W_{h0.1}/W_{h0.4}$) / ln($W_{h0.4}/W_{h0.8}$)	suspects	$W_{0.1}$	$W_{0.4}$	$W_{0.8}$	ln ($W_{h0.1}/W_{h0.4}$) / ln($W_{h0.4}/W_{h0.8}$)
Concn, mM ID					95% Confidence range	Concn, mM ID				
1.0 a	0.4848	0.2624	0.1265	0.8414	0.8255 - 0.8737	nom 1.0 a	0.5173	0.2634	0.1274	**0.9292**
1.0 b	0.4835	0.2619	0.1282	0.8583		nom 1.0 b	0.5166	0.2631	0.1279	**0.9354**
2.0 a	0.4955	0.2655	0.1264	0.8408	0.8364 - 0.8497	nom 2.0 a	0.5130	0.2671	0.1259	**0.8677**
2.0 b	0.4962	0.2655	0.1267	0.8455		nom 2.0 b	0.5127	0.2675	0.1261	**0.8650**

Table 10.1.Detection of Impurity based on Shape Criterion ln ($W_{h0.2}/W_{h0.4}$)/ln($W_{h0.4}/W_{h0.8}$)

Within the linear response range, a chromatographic peak is scalable; the shape is concentration-independent. The presence of an unresolved impurity in a peak subtly alters its shape. Based on eq 16 ($\boldsymbol{W_h^k = u - jln\ h}$), the width at a fixed height $\boldsymbol{h}$ to a certain power $\boldsymbol{k}$ should be linearly proportional to the natural log of $\boldsymbol{h}$. The same relationship could be applied to half widths (meaning fronting half or trailing half). Figure 11.1 and 11.2 are peaks from Figure 10.10 showing 2000 µM and 500 µM bromide samples each containing 20 µM Nitrate. The relative impurity amount is thus 1 and 4% on a molar basis; the impurity is not readily discernible.

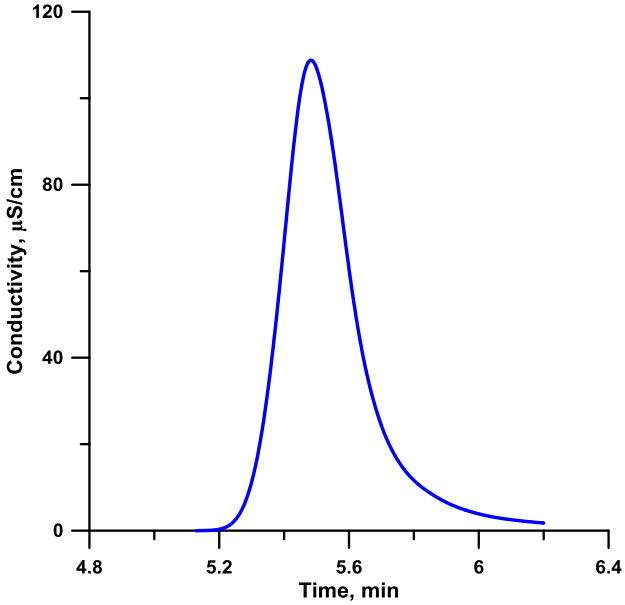

Figure 11.1. 2000 µM Bromide containing 20 µM of Nitrate (1% relative on a molar basis).

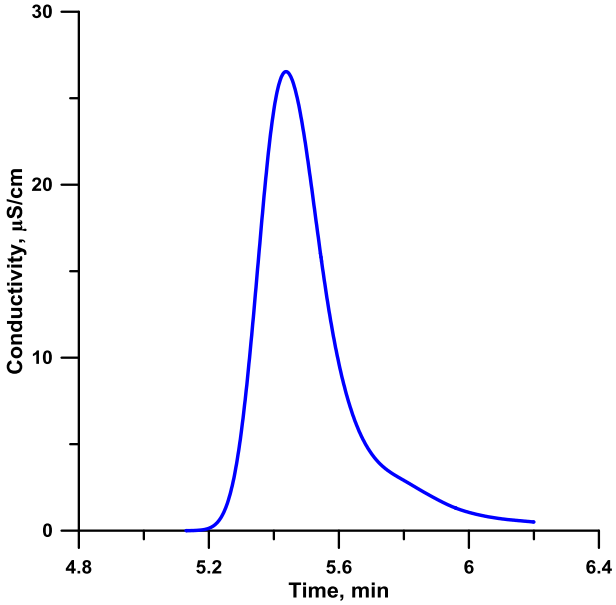

Figure 11.2. 500 µM Bromide containing 20 µM of Nitrate (4% relative on a molar basis).

Let's first take a look at the trailing width vs ln ***h***, without considering the ***k*** power, for the peaks in Figure 11.1 and 11.2, see Figure 11.3 and 11.4.

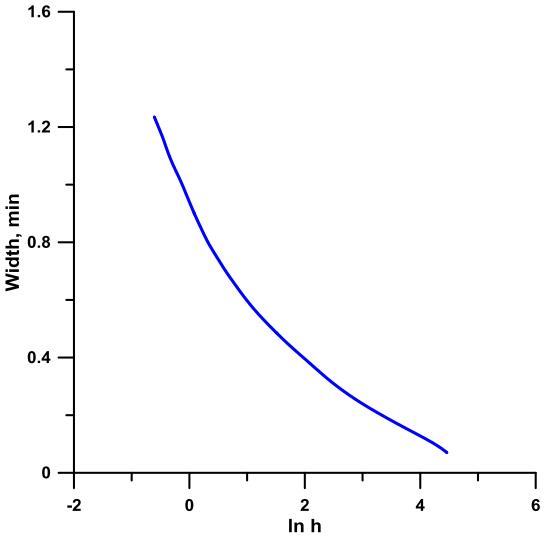

Figure 11.3. Trailing width vs ln ***h*** of Figure 11.1, 0.2 < ***h*** < 87

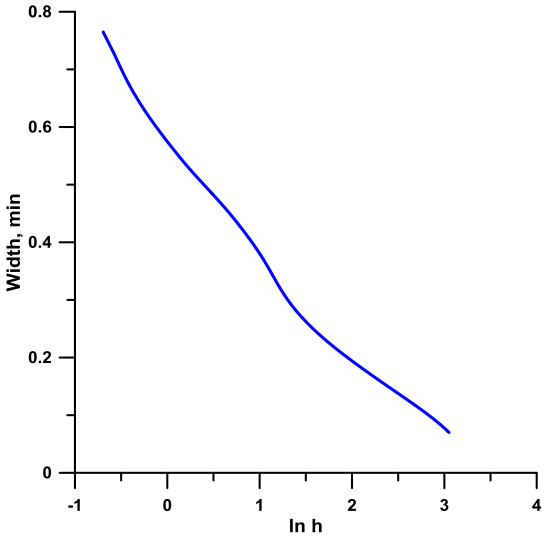

Figure 11.4. Trailing width vs ln ***h*** of Figure 11.2, 0.2 < ***h*** < 21

The presence of an impurity creates a disturbance of the trend, more obvious in Figure 11.4 than Figure 11.3. ***k*** is obtained by choosing a set of an interval of ln *h* values and width values before the disturbance, then ask Solver (a Microsoft Excel add in) to find the best ***k*** value possible such that $\boldsymbol{W_h}^{\boldsymbol{k}}$ vs. $\boldsymbol{ln\ h}$ is linear (or change ***k*** until r^2 reaches its maximum value). Once ***k*** is obtained, the predicted ln ***h*** for the entire set of data is calculated based on the slope, intercept and ***k*** values obtained in the process of choosing the best ***k*** value. The predicted ln ***h*** is what we assume would be without the perturbation of the trend (or simply put without the impurity). See Figure 11.5 and 11.6.

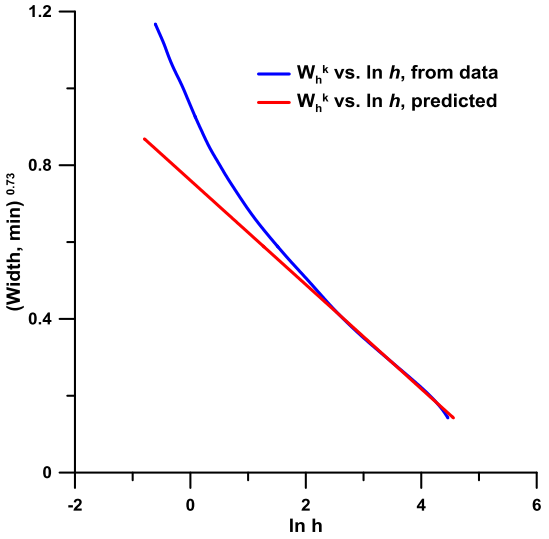

Figure 11.5. W_h^k vs. $ln\ h$ of the actual data and also that of the predicted one from Figure 11.1, 0.2 < *h* < 87

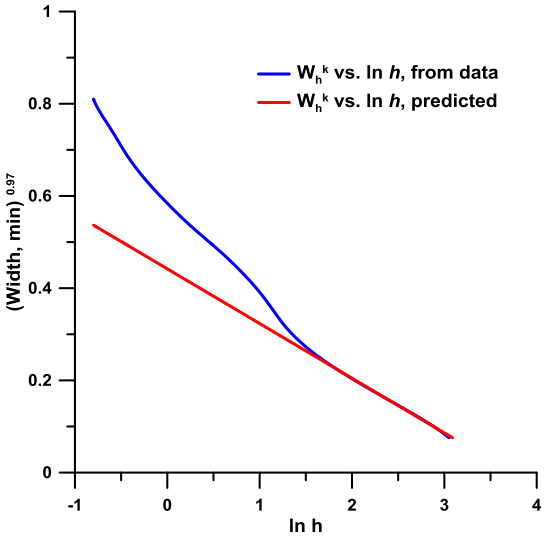

Figure 11.6. W_h^k vs. $ln\ h$ of the actual data and also that of the predicted one from Figure 11.2, 0.2 < *h* < 21

From the predicted ln ***h***, the signal of the pure peak is calculated. The signal of the impurity is calculated by subtracting the predicted pure signal from the original which gives us the impure peaks. Figure 11.7 and 11.8 are the complete plots of the original peaks and their components.

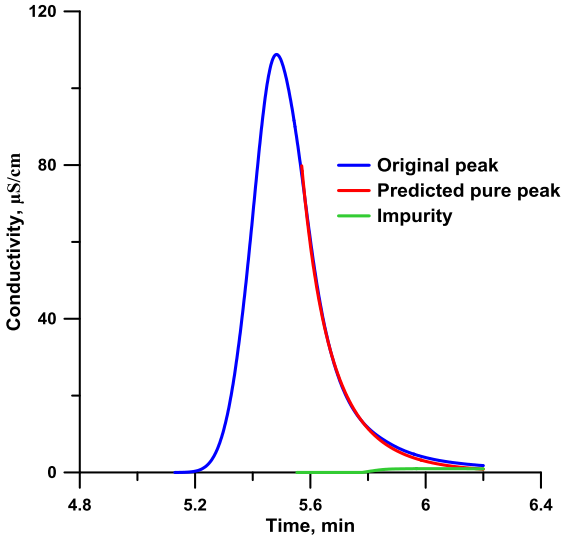

Figure 11.7. Deconvoluted Figure 11.1 peak

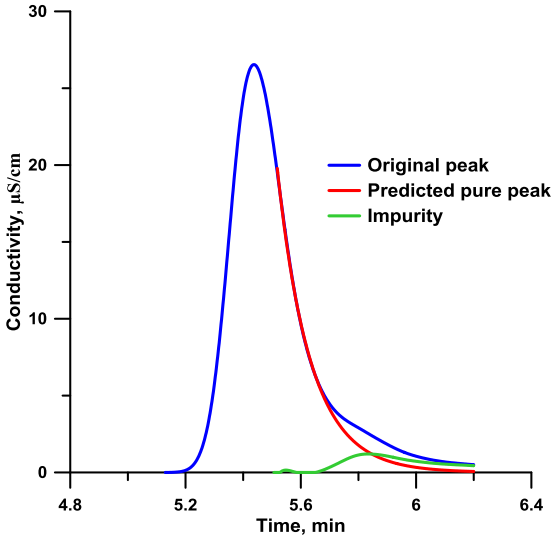

Figure 11.8. Deconvoluted Figure 11.2 peak

The percent (impurity/ main signal) based on the Areas are 1.18 % for Figure 11.1 peak and 4.91 % for the Figure 11.2 peak. These values are not far off the respectively 1.89 % and 4.69 % calculated from the pure peak available data.

CHAPTER TWELVE: Summary and Conclusion

Quantitative chromatographic analysis is long established and is of such practical importance that claims of unturned stones hiding valuables on the road do not ring true. It surprised us that the simple GGD models can describe a variety of chromatographic peaks so well when each side of the peak, at least the majority of it ($1/\overline{\boldsymbol{h}}$ = 0.05-0.95), are considered independently. This is the key to WBQ being generally applicable to both Gaussian and non-Gaussian peaks with the unanticipated merit that the resulting RMSRE values become comparable to those using height or area cased quantitation using weighted regression. Perhaps this is a timely finding: the resolution and hence the uncertainty of WBQ would not have been competitive with height- or area-based quantitation without high-speed high-resolution data acquisition. We suggest WBQ not as a panacea but as an adjunct: quantitation can be height-based at the low-end, width-based at the high end (where detector saturation/nonlinearity may set in) and if needed, area-based at intermediate concentrations.

Research in chromatography has in great part been about improving efficiency in separations: faster separations, creation of new columns (different particles chemistries). This often involves the improvement of the hardware. Little attention is given to the data processing share. Rightfully, the hardware (better column, appropriate solvent and other conditions) are crucial for an efficient separation, but also investing in improving data processing of the chromatograms could make things even better. This could open a lot of door to great innovations, easier analysis and better identifications.

ACKNOWLEDGMENTS

We gratefully acknowledge financial support from the US National Science Foundation through Grant CHE-1506572 and Agilent Technologies through University Relations and External Research Gift #3819, the latter program also permitting the participation of KGK. We thank Mrinal Sengupta and Kannan Srinivasan for some provided data.

Appendix A:

Evaluation of Amount of Blood in Dry Blood Spots: Ring-Disk Electrode Conductometry

Akinde F. Kadjo, Brian N. Stamos, C. Phillip Shelor, Jordan M. Berg, Benjamin C. Blount[≠] and Purnendu K. Dasgupta

Analytical Chemistry. **2016**, 88, 6531-6537

A.1 Introduction

The diagnostic use of dried blood spots (DBS) dates to 1963; DBS was first used to screen for Phenylketonuria in infants.[61] Typically a small amount of a blood sample (heel prick in infants, finger prick in adults, tail prick in animals) is collected on a paper filter and is archived or sent for analysis. DBS analysis is widely used for screening neonatal metabolic disorders.[62] Relative to whole blood or plasma, DBS presents several advantages in sampling, storage, and transport. No centrifugation is needed. The lifetimes of many biomarkers are extended by months to years[63] while facilitating robust and compact storage. It is particularly suited for screening infectious agents; it has made a major difference in diagnosing infant human immunodeficiency virus (HIV) infection and subsequent care in resource-poor areas.[64] Dried blood is not considered a biohazard and small sample volumes reduce risks. This helps sampling, storage and transportation.[65] DBS sampling and archival is thus becoming increasingly popular in large scale clinical and other field use.

Originally introduced for qualitative screening, DBS is being used for quantitative analysis, thanks to advances in liquid chromatography-(tandem) mass spectrometry.[66] DBS sampling and analysis have been widely validated in situations where only whole blood/plasma was used. The applications range from HIV-1N diagnosis to pharmacokinetic and toxicokinetic studies.[67-70] Sample sizes are typically 10–20 μL (most commonly 15 μL) but volumes down to 3.3 μL have been used.[71] The blood is directly placed onto a filter card, usally S&S 903 (now Whatman 903) filter paper. [71,72] Typically the cards are catalogued and stored at temperatures from ambient to –20 ^{o}C.

For analysis, an area of the spot (most commonly 3-3.2 mm ϕ)[71] is punched out, and extracted in water or water/(m)ethanol mixtures. Quantitative analysis requires the exact volume of blood in the punch. One recommendation is to follow a strict protocol where the exact amount of blood being spotted is known.[73-75] This is inconvenient in collecting samples in the field and also makes it difficult to envision someday subjects mailing out finger prick DBS samples for routine analysis. One would want to cleanse an area, and soak up by the filter whatever blood is elicited by a prick, without having pipet an exact volume.

However, even when fixed volumes are spotted, varying hematocrit levels result in different viscosities and the spot area varies.[76,77] Further, for the same blood sample, the speed of dispensing to the filter can affect the spot size. Reportedly hydrophilic monolithic porous polymer sheets produce more uniform spot sizes from the same volume of blood than paper filters.[78,79] However, analyte distribution may not be radially uniform across the spot;[80] using any media that promotes chromatography-like differential retention may make this worse. Also, while strict protocols may be adequate for self-contained studies, hospitals sharing patient samples may use different collection methods. Moreover, strict protocols have rarely been followed in the past. DBS sampling is used in forensic archival. Determination of a victim's age from a DBS sample is often sought; high accuracy quantification of biomarkers would greatly aid in this task. The ability to nondestructively quantify the blood volume represented by an extract will thus be of benefit in many cases.[81,82]

Rather than relying on the combination of (a) spotting a known volume, (b) producing a fixed spot size and (c) assuming spatial uniformity, the weight of the punched-out spot has been measured. The success of this strategy is limited by uniformity of the substrate and hematocrit constancy. Presently the recommended method is to use the sodium level as an "internal standard", typically measured by flame photometry.[80] For determination of trace constituents in a DBS, the extract volume is small, typ. ~100 μL. With such a small sample, any destructive sub-analysis is undesirable. We propose that nondestructive conductivity measurement can serve the same purpose as measuring sodium. We further propose that a small ring-disk electrode (RDE) dip probe is particularly well suited for making such measurements. We believe this to be the first report to use conductance measurement to quantitate the amount of blood in a DBS punch and also the first to provide *a priori* the minimum liquid depth necessary to obtain reproducible results with a RDE type conductance probe.

A.2 Perspective

Electrolyte concentrations in human blood are remarkably constant. Osmolarity in humans is regulated through the Renin-Angiotensin-Aldosterone pathway.[83] The predominant ion in blood, Na^+, has been shown to lie within the 120-150 mM range in 99.5% of > 111,000 blood samples studied.[84] Assuming normal distribution, the normal (95%) limits will be given by 135 ± 10.8 mM, a variation of ± 8.0%. Most standard compilations state much tighter bounds, for example, the normal range for Na^+, K^+, HCO_3^- and Cl^- are stated[85] to be 141±6, 4.25±0.75, 25±3 and 100±5 meq/L. Ionized Calcium and Magnesium normal ranges respectively span 2.4±0.2 and 1.65±0.25 meq/L.[86] Although chloride concentration less than that of sodium, 50% higher mobility makes it the largest contributor to conductivity. Based on infinite dilution equivalent conductance (λ^0) values, the relative contributions are: Cl^-: 46.7%, Na^+: 43.2%, HCO_3^-: 6.8%, K^+: 1.9%, Ca^{2+}: 0.9% and Mg^{2+}: 0.5% and the overall conductance is approximately equivalent to that of 130±4 mM NaCl. However, note that at concentrations >~2 mM, the concentration-conductance relationship becomes nonlinear and the applicable λ values are less than the λ^0 values. A typical DBS extract (a 3 mm ϕ DBS punch, approximately representing 5 μL of blood, into 100 μL extract) represents a dilution factor of ~20 and an equivalent NaCl concentration of ~6.5 mM.

Regardless of nonlinearity, if calibrated in an appropriate range of electrolyte concentration, electrical conductivity measurement of the DBS extract should indicate blood volume present in the DBS punch. The RDE represents a two-dimensional sensing surface that is easily made in a miniature form. The RDE is used extensively in voltammetric applications (often in a rotating format); this geometry has been widely used for amperometric measurements in a wall-jet configuration. The RDE geometry has also been used in sensing capacitance of soils[87] or liquids,[88] and electromigrative injection from a small loop in capillary electrophoresis,[89,90] etc. The use of the RDE geometry for conductivity measurement is scant;[91] in a related geometry a cylindrical electrode (outer surface area active) with a small diameter wire (only tip active) protruding beyond the outer cylinder terminus was shown to be especially tolerant of suspended solids and

floating debris.[92] An obvious problem of RDE conductometry is that a cell constant cannot be readily calculated; it depends on the depth of the liquid below the RDE making it impossible to calculate the solution specific conductance (σ) from the measured conductance (G). Nevertheless, the geometry is particularly conducive to measuring conductance in small volumes. Indeed, the only conductometric capillary electrophoresis system ever commercialized used an RDE.[93]

A.3 Principles and Approach

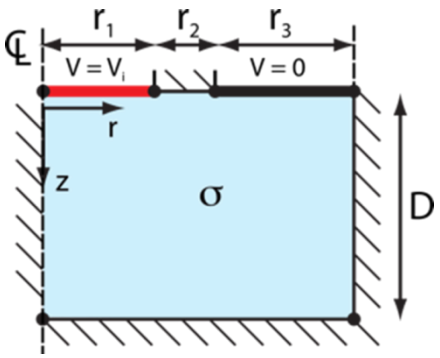

Figure A.1. Electrode configuration and model variables. The top left corner is the center of the RDE; only one half of the RDE is shown. The behavior of the complete electrode assumes cylindrical symmetry. The diameter of the central electrode (red) is $2r_1$, the width of the gap between the two electrodes is r_2 and the width of the outer electrode is r_3. Below the electrode is a homogeneous conducting medium of specific conductance σ that extends to a depth D. In calibration experiments, the arrangement was upside down.

The basic configuration of the model system is shown in Figure A.1. The central disk has a radius of r_1, the insulating ring separating the disk and the outer ring electrode has a width of r_2, and the outer ring electrode is bounded by radii r_2 and r_3. In a practical system (including our model comparison experiments) there is an outer insulator of finite thickness, so the conducting electrolyte extends to the side beyond r_3. Further, in use when such an electrode is *dipped* into a measurement solution in a vial, there will not only be solution extending to the sides, the liquid meniscus will be above the sensing plane, around the insulated outer wall. These factors have not been considered in the model.

The sample specific conductance, σ, is related to the measured conductance, G by the relationship

$$\sigma = GK \quad \ldots(A1)$$

where K is the probe cell constant. In most conductivity cell designs, the solution to be measured is contained in the space between the two electrodes; to a first approximation, the electric field is wholly contained within this volume. Presence or absence of solution beyond this space has little effect on the measured conductance. With an RDE, this is not the case: it is intuitive that the measured conductance will be greater if the depth D of the solution layer extending from the sensor surface is substantial, rather than infinitesimal. It follows that the "cell constant" is not a constant but depends on the solution depth. Experiments and numerical simulations bear out the intuitive expectation that G would keep increasing with D. But as the field dissipates with distance, increasing D beyond a certain value will have diminishing returns. G will thus asymptotically approach a limiting value G_∞ as D approaches infinity. Conversely, K will decrease with increasing D and also asymptotically approach a limiting value K_∞ as D approaches infinity. Solutions to similar problems have previously been advanced by finite element[87,88] or similar "annular patch subdomain"[94] methods for capacitance probes. The only extant analytical equation for conductometry with interdigitated planar electrodes is applicable solely to a solution of semi-infinite boundaries.[95]

An infinite solution depth is obviously not practical. We propose that the depth at which 99% of the limiting value of G is reached, D_{99}; as a more usable index, where:

$$G(D_{99}) = 0.99\ G_\infty \quad \ldots(A2)$$

For any conductance measurement with sample height greater than or equal to D_{99}, representing $G_{(D > D99)}$ as $G_{\geq D99}$, G_∞ can be estimated as

$$G_\infty = 1.005\ G_{\geq D99} \pm 0.5\% \quad \ldots(A3)$$

Likewise K_∞ may then be taken as $0.995 \pm 0.005\ K(D_{99})$. To avoid the need to know the sample volume (depth) precisely, and to reduce conductance variations due to

variations in depth, if the sample depth is chosen to be $\geq D_{99}$, K and G will be insensitive to further variations in D. If we can *a priori* know/estimate D_{99} from the sensor dimensions, one can ensure accurate results by ensuring that sufficient liquid is taken for the liquid depth below the probe to be $\geq D_{99}$. Herein we simulate and model the RDE conductance sensor to estimate D_{99} from the RDE dimensions. Thence one can operate comfortably above D_{99} and obtain an accurate estimate of K_∞ from the measurement of a solution of known σ.

We assume that the applied voltage to the sensor is small enough such that heating due to the passage of current is insignificant. The electrical potential and resulting current densities can be described by Laplace's equation. Finite-element software of considerable power is available to solve Laplace's equation for complex geometries and boundary conditions; however, the learning curve to use such specialized programs is steep. We have chosen therefore to take a hybrid approach. We first simulate and model using the commercial finite-element package COMSOL Multi-physics (hereinafter COMSOL) for a number of RDE dimensions and sample depths. The COMSOL simulation results for D_{99} and G_∞ were validated by experimental measurements and stored in a spreadsheet, from which values for intermediate geometries may be estimated by interpolation.

The convergence of the model to compute D_{99} was tested by ascertaining that the sensitivity of the computed value of G to further changes in D has become sufficiently small. We define a term dimensionless *sensitivity*, $S_D^G(D)$ as the ratio of the relative change in G resulting from a relative change in the depth.

$$S_D^G(D) = \frac{dG}{G} \cdot \frac{D}{dD} \approx \frac{\Delta G}{G} \cdot \frac{D}{\Delta D} \quad \text{...(A4)}$$

From simulation results we observed that D_{99} corresponds to $S_H^G(D_{99}) \approx 0.05$. Note that if the functional form of $G(D)$ is modeled as

$$G(D) = G_\infty(1 - e^{-kD}) \quad \text{...(A5)}$$

with k being a fitting parameter, then an explicit form for D_{99} is readily derived as

$$D_{99} = -(\ln 0.01)/k \approx 4.605/k \quad \text{...(A6)}$$

As will be seen, eq A6 does closely describe the experimental conductance measurements. In this case, the value of the sensitivity function at D_{99}, $S_H^G(D_{99})$, is readily calculated to be ~0.0465, consistent with that observed in the simulations.

Figure A.2 shows the potential field contours around the electrode surface as simulated by *COMSOL* for one of the RDE probes.

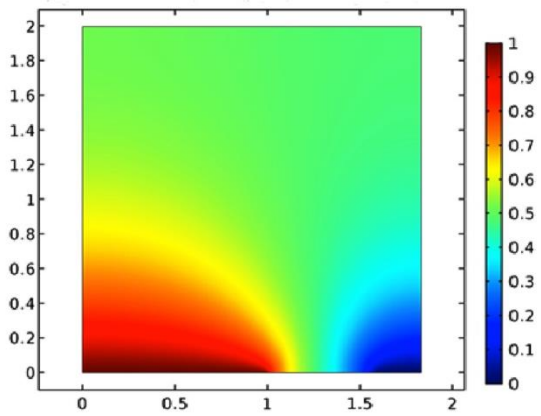

Figure A.2. Results of COMSOL simulation for Probe C. All units are nondimensional. The ordinate and abscissa are, respectively, the depth below the electrode surface and the radial coordinate, each divided by r_1.

A.4 Experimental Section

Blood Spotting and Processing. Unidentified adult human blood samples (finger prick) were collected from volunteers. As previously stated, a 3-3.2 mm ϕ punch, (representing on an average ~ 5 μL of blood) is typical.[71] This volume was therefore approximately at the middle of the range of volumes (0, 1, 2, 4, and 8 μL) used for spotting. As errors and uncertainties increase with smaller spotted volumes and spotted volumes as low as 3.3-3.4 μL have been used.[71,96], the majority of our spotted volumes were ≤ 4 μL, to provide the worst case scenario. In one experiment, 0-8 μL samples from one of the authors were alternately pipetted into prewashed and dried 1.5 mL micro-centrifuge tubes or spotted on prewashed and dried Whatman No 3 filters.[97] The samples in the vials were diluted respectively with 100, 99, 98, 96, and 92 μL water, capped, allowed to sit for 20 min, vortexed for mixing and conductance measured within 5 min using probe A (*vide*

infra). The filters were allowed to dry. One-fourth inch (6.3 mm) diameter disks[71] were punched out with a stainless steel punch under dust-free conditions. This punch area was chosen because it was large enough to completely contain the largest amount of blood (8 μL) spotted. The punch was transferred to a prewashed and dried 1.5 mL micro-centrifuge tube, 100 μL of water added, the vial capped and allowed to remain for 20 min. After vortex mixing, the conductance was measured with Probe A without removal of the filter. In another experiment, after proceeding exactly as above, extraction was carried out with 50:50 methanol:water, and the conductance measured. In yet another experiment, extraction was carried out with pure methanol and the conductance measured. Following this, the methanol was evaporated in a gentle stream of N_2, the residue re-extracted in 100 μL water[66] and the conductance measured again. Ion Chromatography was conducted on these extracts, all equipment was from www.thermofisher.com. In still another experiment, 2 μL blood samples from 12 volunteers were spotted on filters and then processed as above. All experiments throughout were done minimally in triplicate.

Conductivity Probe Construction and Measurements. Ring disk electrodes are available from virtually all electrochemical equipment vendors but are generally too large for present use. As the basic construction (solid conductive rod surrounded by an insulator tube, then a metal tube then another insulating tube) is very simple to fabricate, we made our own. Several RDE probes, differing in dimension, were constructed and are referred to as Probes A, B, and C, respectively. The center and outer insulators were PTFE tubes. The r_1-r_2-r_3 values for probes A, B, and C respectively were: 400-300-215, 355-400-800, 1485-800-350 μm. Probe A was used in all actual DBS/blood measurements; to protect from corrosion in high chloride DBS extracts, the electrodes were electroplated with gold before covering the outside.

Calibrations were conducted at 22 °C. Probes B and C were inserted upside down into the bottom of a well drilled into an acrylic block such that the snug-fit probe acted as a stopper. The cavity was filled with a known volume of a KCl solution of known σ. The conductance was then measured with a Dionex CDM-1 Conductivity Detector. Aliquots of the solution

were then removed in 0.5 µL steps, thus changing the liquid height above the probe and the conductance was measured in each step.

A.5 Results and Discussion

Electrode Corrosion and Measurement Conditions. Probe A was provided with an external union with male nuts, the union terminus sits on the lip of the vial (see Figure A3 and A4) making it convenient to position it reproducibly (this is not critical as long the electrode touches the extract and the liquid depth below is $\geq D_{99}$). Some corrosion of the stainless steel electrodes was observed on prolonged use in high concentration chloride solutions with the excitation conditions used (square wave, 3 kHz, 5 V p-p); the need for frequent electrode polishing to maintain reproducibility was eliminated by electroplating both electrodes with gold. Rapid vertical insertion of the probe into the liquid was avoided so as not to trap air bubbles at the interface.

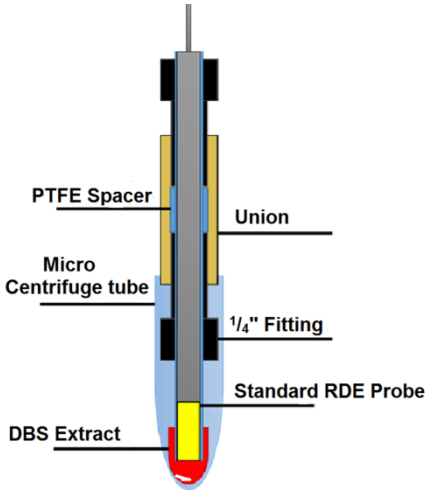

Figure A3. Construction of probe A to maintain constant blood immersion depth

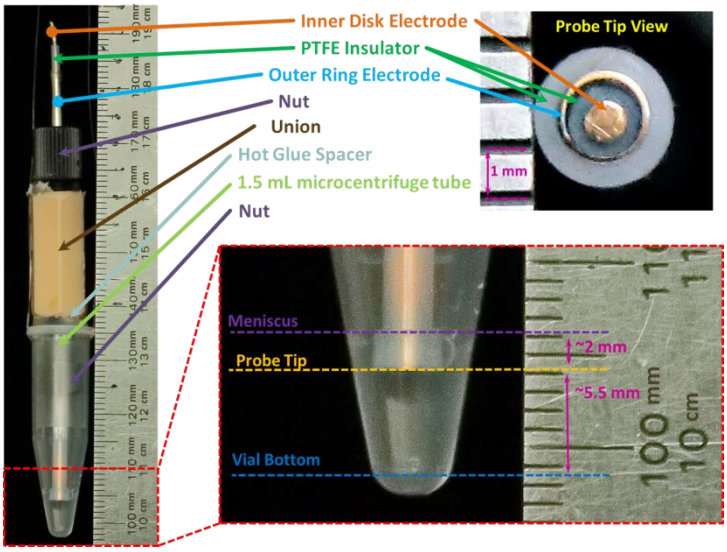

Figure A.4. Photographs of the standard probe being dipped in 100 µL of water (left image). A blown up image of the tip is shown in the lower right photo. The tip extends approximately 2 mm below the meniscus of the water. The tip lies about 5.5-6 mm above the microcentrifuge bottom. An end-on view is provided in the upper right corner where the disk and ring electrodes as well as PTFE insulators can be clearly seen.

Liquid Depth vs. Conductivity. Experiment vs COMSOL Simulation. Figure A.5 compares the *COMSOL* simulation results for probe C as a function of sample depth D with the actual experimental results for 500 μM KCl solution. Simulations were carried out up to D = 2400 μm while the measurements extended to ~1700 μm. The fit of the experimental data for $D \geq 500$ μm to an exponential dependence of G on D (eq A5) is indicated by the dashed line. The projected G_∞ values are 42.2 and 41.1 μS for the experimental vs. simulation data; the simulated value is 2.6% lower (note, however, the simulated value is directly proportional to the assumed value for σ). The computed D_{99} value was 1.66 mm, compared to 1.42 mm determined experimentally. Consideration of similar data for the probe B for the same solution (see Figure B.6 in the Supporting Information) shows an even closer match. Using the asymptotic fit (eq A5 and A6) we compute D_{99} to be 920 vs 926 μm, respectively for the experimental data and the COMSOL simulations, in excellent agreement. The simulated value for G_∞ was ~<1% lower than the value projected from the experimental data. The predicted D_{99} value for the probe A is only 0.6 mm. For a 100 μL sample using probe A in the vials described, the tip is immersed to a depth of ~2 mm below the meniscus and the liquid depth below the tip is ~ 6 mm, an order of magnitude greater than needed according to the calculated D_{99} value. An extract volume of 100 μL in a typical 1.5 mL micro centrifuge tube thus provides sufficient liquid depth to stay comfortably above D_{99} for any of RDE sensors described here.

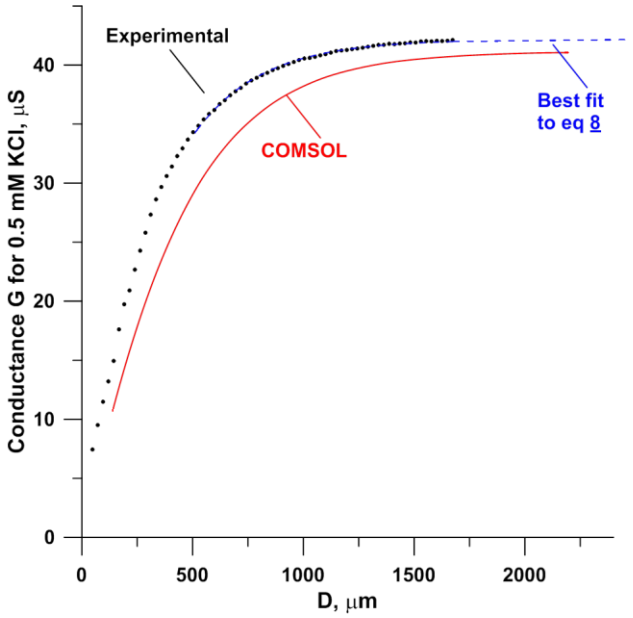

Figure A.5. Comparison of experimental and simulation results for probe C, conductance versus sample depth for a 500 μM KCl solution. The blue dashed line is the best fit to eq. A5.

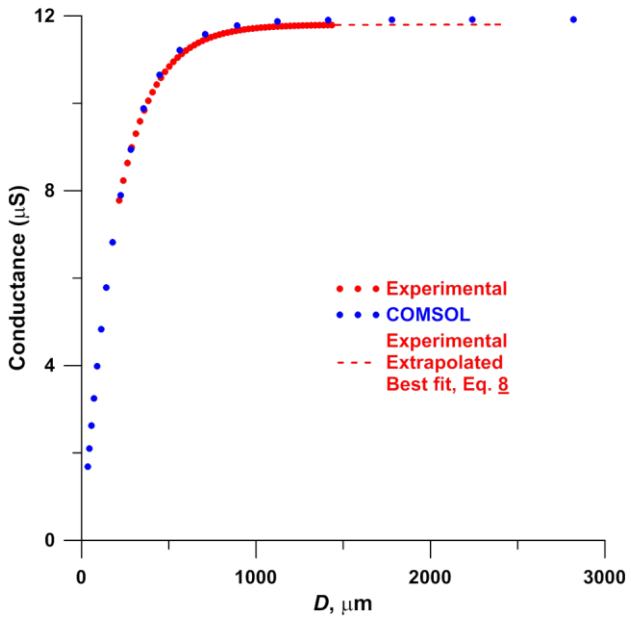

Figure A.6. Comparison of experimental and simulation results for conductance measured by probe B versus sample depth.

Two other aspects of the simulation vs. experimental data are noteworthy. For probe C, experimental data were collected down to very low values of D. At $D \leq 500$ μm, especially at $D \leq 200$ μm, the nonplanarity of the liquid meniscus due to surface tension effects becomes significant; the model in contrast assumes a flat liquid surface. The poorer agreement between the model vs. experimental data at small D values can be thus explained; however, this has no effect on determining D_{99}. Second, the G vs. D curve is shifted to somewhat lower D values experimentally compared to that computed leading also to a slightly lower experimental D_{99} value. This likely arises from the probe having an outer insulating shield of appreciable thickness, leading to a significant amount of solution extending in the radial dimension beyond the electrode, whereas the model assumes no peripheral solution.

For calculating D_{99} and G_∞ for any RDE probe, we have provided an Excel calculator; it uses r_1, r_2, r_3 and σ as the input parameters and calculates G vs D. To provide these values over a range of geometries, we solve all cases on an 11 x 11 logarithmic grid. The radial

measures are given in dimensionless parameters (in units of r_1 and are denoted as $\bar{r}_i$ ($\bar{r}_i = r_i/r_1$). Therefore, by definition $\bar{r}_1$ is 1 and in Figure 3, $\bar{r}_2$ and $\bar{r}_3$ are each varied from 0.1 to 10 in logarithmic steps of $10^{0.2}$. Figure A.7 shows the results for $\bar{D}_{99}$ (= D_{99}/r_1).

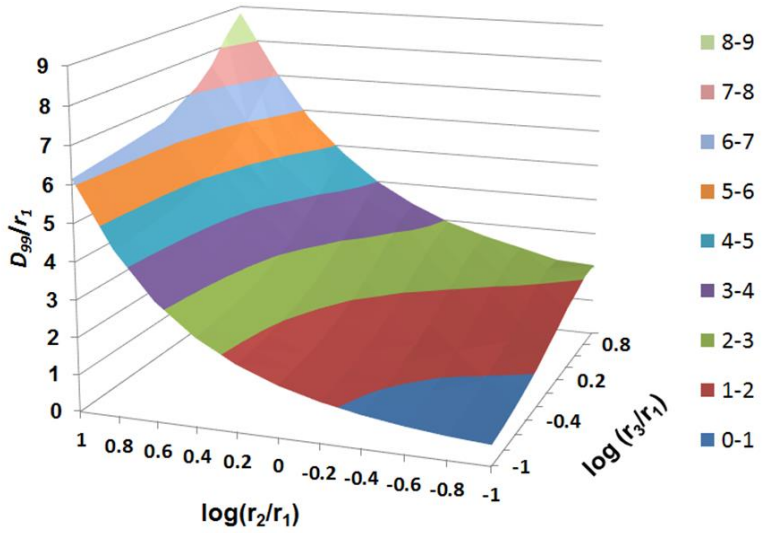

Figure A.7. Dependence of $\bar{D}_{99}$ as a function of $\bar{r}_2$ and $\bar{r}_3$.

For most practical situations involving conductance measurement, one rarely relies on the cell constant computed from absolute dimensions/spacing of the electrodes; rather, the cell is calibrated with standards of known σ. While the COMSOL model predicts the measured conductance value well, the most useful outcome is a good prediction of D_{99}. After ensuring that the solution depth below the electrode surface will significantly exceed D_{99}, we would presume that the user would then calibrate the measurement system at the operating temperature with conductance standards or NaCl standards. The latter do not have to be purely aqueous, if for example extraction is conducted with pure methanol, methanolic NaCl solutions can be used for calibration.

Real Samples.

Does the DBS Extract Reflect A Complete Extraction of Blood Electrolytes?

It was of interest to determine how whole blood directly put in the extraction solvent compares with the same amount of blood put on a filter, dried and extracted. Figure A.8 shows that these values are virtually identical, indicating that the electrolyte is

efficiently extracted. The conductance variance of the diluted blood samples ranged from 3.7-9.1% (mean±sd 5.4±1.9%); that for the DBS extracts were slightly higher at 2.0-12.1% (mean±sd 7.4±4.2%). Neither variance showed a consistent pattern with the amount of blood taken. A paired t-test indicated at 90+% confidence levels the two sets of values are statistically indistinguishable. More aggressive extraction conditions (sonication, extended vortexing during extraction) are typically used in actual DBS extractions, which can only further enhance the completion of the extraction. As the data in Figure A.8 would suggest, the presence of the filter remaining in the solution or any debris therefrom made no difference in the measured conductance; this was also independently verified by removing the filter.

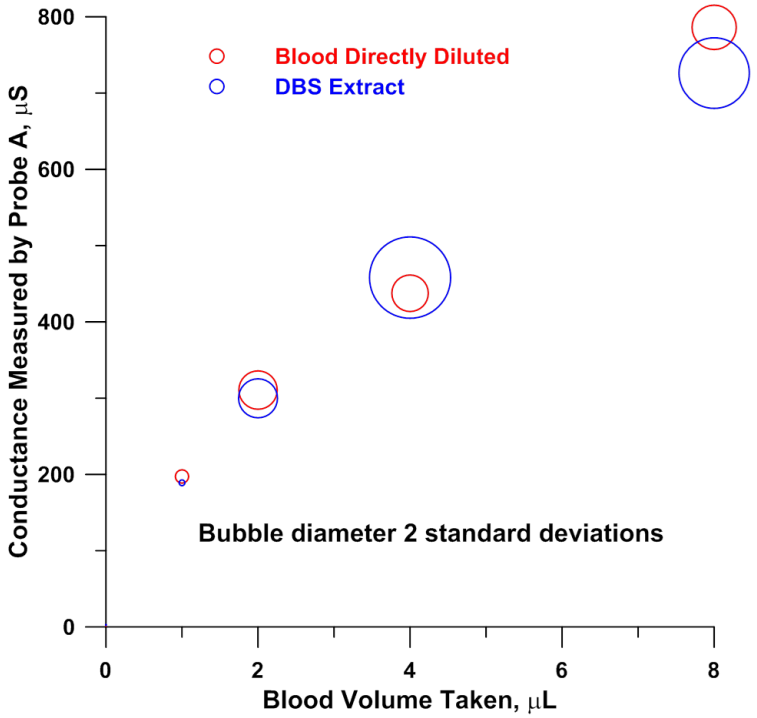

Figure A.8. Measured Conductance values for x = 0-8 µL blood samples diluted with (100-x) µL of water (red circles) or the same blood samples spotted on filter, dried, extracted with 100 µL water and conductance measured (blue circles). Measurements were made with triplicate samples in each case and the diameter of each circle represents two standard deviations

Relating to NaCl Equivalents Present in the Sample. In principle, all data can be interpreted by the absolute conductance measured by a given probe in a given laboratory but comparability across probes and laboratories require calibration. We presently calibrated the standard probe with 0, 0.1, 0.5, 4.0, 8.0, and 10.0 mM aqueous NaCl, the measured conductance values were linearly correlated with the tabulated specific conductance values for these concentrations (r^2 = 0.9992, Figure A.9, A.10). The relationship between the NaCl concentration and the conductance in this domain is nonlinear but is satisfactorily described by a quadratic relationship (r^2 = 0.9998, Figure A.11). Our experiments were conducted in an open laboratory environment in the presence of CO_2. When measured directly at the outlet of a deionized water system, the conductance measured by the standard probe is essentially zero but by the time the same water is transferred to a vial and measured with probe A, due to CO_2 intrusion this becomes 1.6-1.7 μS within the first two minutes. For a calibrant like 0.1 mM NaCl, this blank correction is significant. If the vial is not washed, impurities contributed by the vial (which are labeled as sterile but not apparently electrolyte free) also contributed, in the batch we used the unwashed blank conductance was ~5 μS. For real DBS extracts, the conductance is, however, several hundred μS and blank correction has little to no impact. Blank filter punches, if unwashed, were also found to contribute an insignificant amount to the extract conductance.

At 25°C the solubility of NaCl in pure methanol and pure ethanol are >250 and >10 mmol/L, respectively, compared to ~6.5-7 mmol/L expected from extracting a ~5 μL blood spot into 100 μL solvent. Conductance measurement in pure alcoholic solvents should therefore be just as practical as shown in Figure A.12 but conductance calibration in the specific solvents must be carried out.

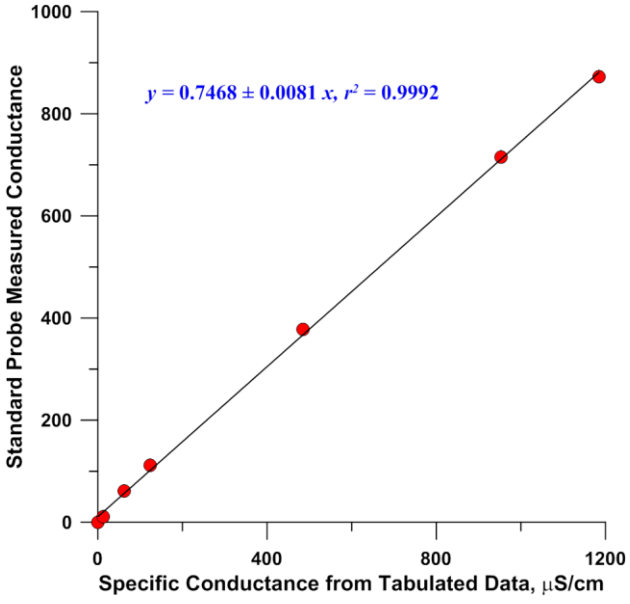

Figure A.9. Probe A response to 0, 0.1, 0.5, 1.0, 4.0, 8.0 and 10.0 mM NaCl vs. tabulated data on specific conductance at these concentrations. The values for 0.1, 4.0 and 8.0 mM NaCl were interpolated from extant data.

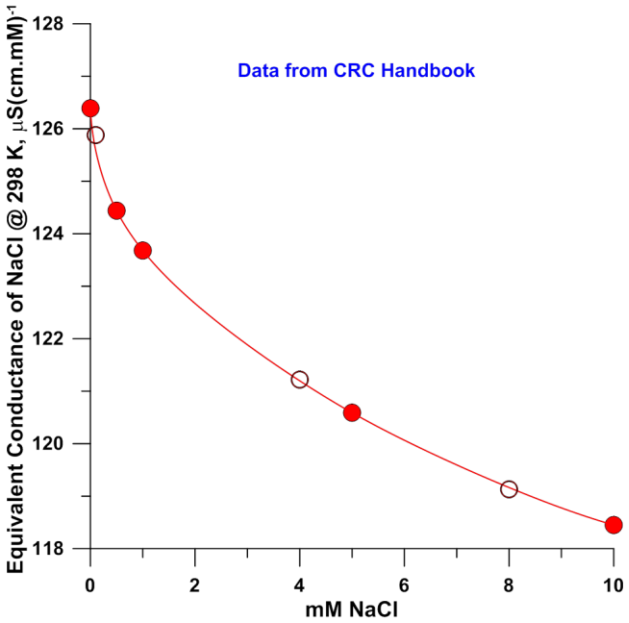

Figure A.10. The solid circles are from tabulated data, the line drawn is a spline fit and the open circles are interpolated values at 0.1, 4.0, and 8.0 mM NaCl. For a web-based source of the tabulated data, see http://sites.chem.colostate.edu/diverdi/all_courses/CRC%20reference%20data/equivalent%20conductivity%20of%20electrolytes.pdf

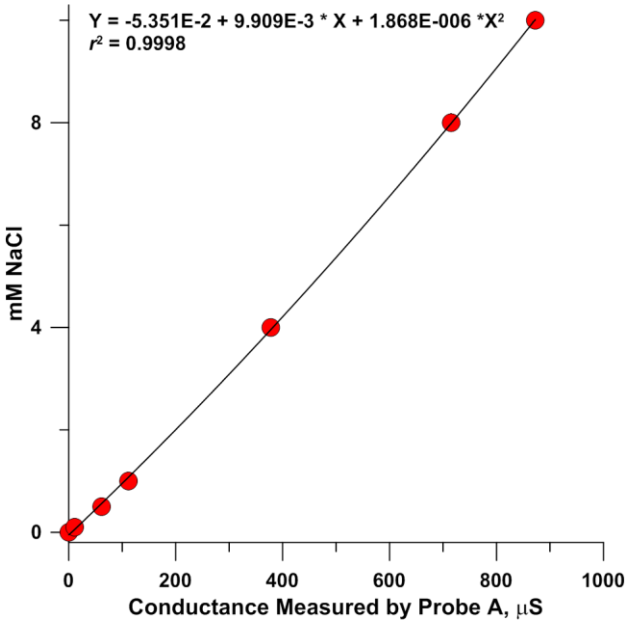

Figure A.11. The best quadratic fit for the relationship between the conductance measured by probe A and the NaCl Concentration. Traditional x-y roles are reversed to permit facile calculation of the NaCl concentration.

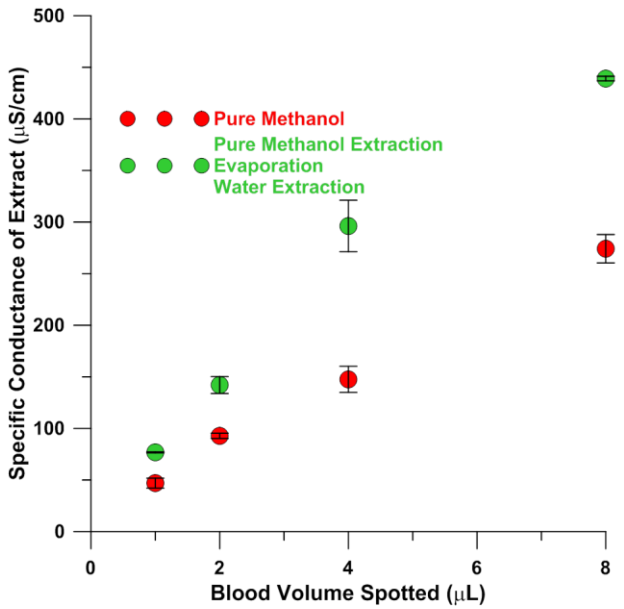

Figure A.12. Specific conductance measured for different volumes of blood extracted on a 6.3 mm ϕ filter disk into (a) 100 μL methanol: red symbols, and (b) the same extract as in a, then evaporated in a slow stream of N_2 and re-extracted in 100 μL water : green symbols.

Variations in Real Samples

Triplicate 2 μL samples were taken from 12 volunteers (ranging in age from 20-66, 9 male, 3 female). Within-subject variance, which includes effects of operator skill and thence reproducibility in pipetting/spotting,etc. ranged from 2.6-12.2% (mean±sd 6.5±2.7%) while between-subject variance was 17.9% (Figure A.13). Granted that this is a very limited number of subjects and the present researchers have no prior experience in sampling and spotting blood, these data provide an indication of the degree of accuracy in quantitating the amount of blood taken in a DBS punch one may expect by the proposed approach of conductance measurement.

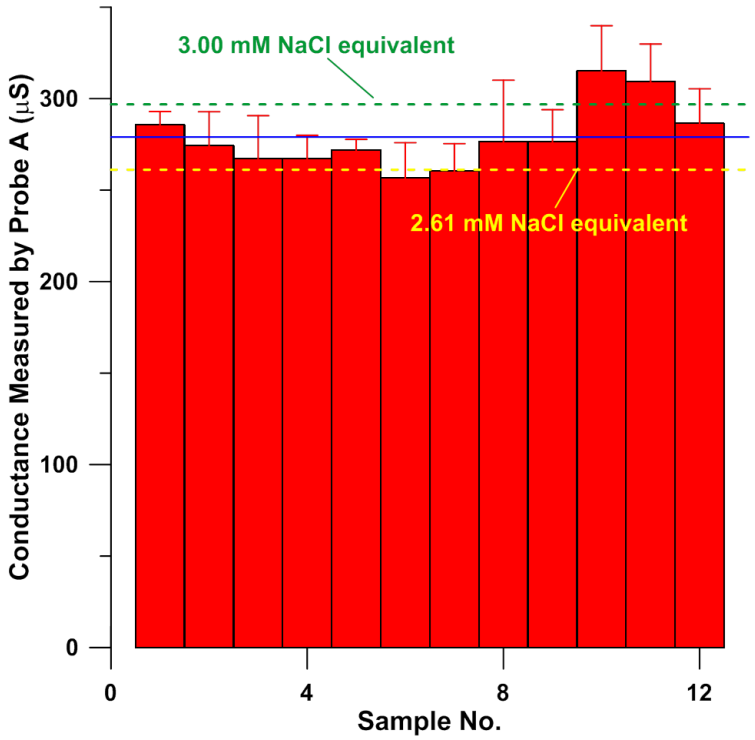

Figure A.13. Conductance measurements of 2 μL blood spot extracts (100 μL water) of 12 healthy individuals. Error bars (1 standard deviation) for each individual (triplicate samples) are indicated. The blue line is the sample set mean while the dashed lines depict +/- 1 standard deviation boundaries.

Effectiveness of Normalization by Conductance. Figure A.14 shows suppressed conductometric anion chromatograms of (HPLC grade) methanol extracts of a filter/solvent blank, and DBS samples containing 4 and 8 μL blood from a researcher. Although many peaks are identifiable in this chromatogram, by far the major component is chloride and compared to the sample chromatograms, the blank chloride level is negligible. Sulfate on the other hand poses a challenge in accurate quantitation, it is present as a trace constituent and good quantitation is made difficult by the fact that it essentially appears on the tail of a broad carbonate peak and the blank value is significant. Based on the respective calibration plots the blank corrected values of chloride for the nominally 4 and 8 μL DBS samples (n=5) are respectively 6.47± 0.53 and 12.1 ±0.6 μM and the corresponding values for sulfate are 18.6±2.8 and 34.1±2.5 μM respectively, factors of 1.87 and 1.83. When divided by the specific conductance of the methanolic extract (Figure A.12), the

chloride and sulfate values differ by 0.8 and 1.3%, respectively, testifying to the merits of conductance normalization.

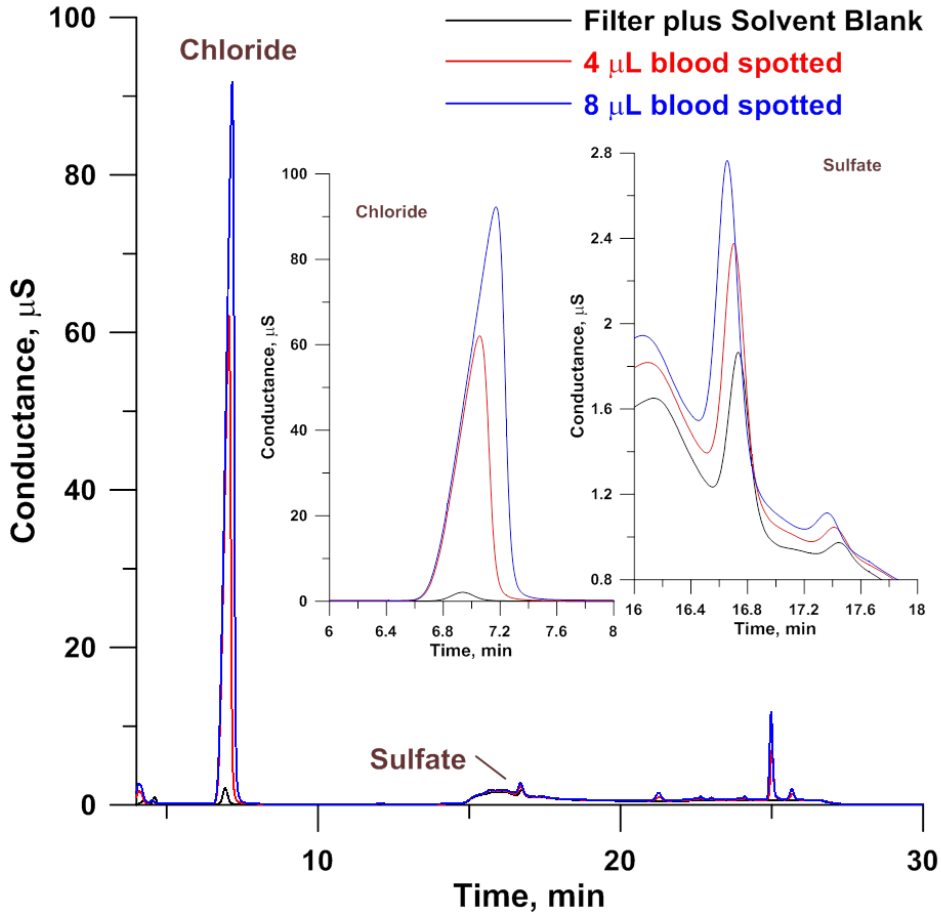

Figure A.14. Ion chromatograms of DBS methanol extract. ICS-5000, 2x50 +2x250 mm AG-11 + AS11 columns, ERS-500 suppressor. Electrogenerated KOH eluent, 0.25 mL/min. Eluent Program: t (min), mM KOH : 0, 5; 5, 3; 11,10; 18, 20; 20.9,50; 23, 50; 23.1, 3; 30, 3. Black trace: Filter/Solvent blank; Red trace: 4 μL blood spot: Blue trace: 8 μL blood spot. Insets show the magnified views of the chloride and sulfate peaks.

A.6 Conclusions

A ring-disk electrode geometry was modeled to determine minimum immersion depth to obtain results accurate to within 1% and found to correlate well with experimental data. Applicability towards quantitation of the amount of blood represented in a DBS punch by nondestructively measuring the conductance of an aqueous extract of

the DBS punch was shown. There are presently no comparable data on the uncertainties of similar quantitation via sodium measurements. While we cannot draw conclusions as to comparability in this regard, there is no reason to believe that the results will not be equivalent. The conductance measurement approach with a small RDE probe has the considerable advantage of zero sample consumption. For chromatographic analysis, an injection loop consisting of metallic tubes separated by an insulating union may permit on-the-fly conductivity measurement with conventional geometry.

The caveat to conductance-based normalization is that the data we presented pertain to normal healthy subjects. The approach cannot work if the subject has abnormal electrolyte levels, which can occur in certain diseases. Of course, normalization with sodium levels also fails if sodium levels are abnormal.

Acknowledgements

This work was supported partially by NSF (CHE-1506572), ThermoFisher/Dionex, the CDC Foundation and the Hamish Small Chair Endowment at the University of Texas at Arlington.

Appendix B:

Temporal Ion Analysis of Shallow Groundwater in an Area of Unconventional Oil and Gas Drilling

Akinde Kadjo, C. Phillip Shelor, Zacariah L. Hildenbrand, Stephanie Korlie, Kevin A. Schug, and Purnendu K. Dasgupta

B.1 Introduction

Development of new unconventional drilling (UD) techniques such as horizontal drilling and hydraulic fracturing have allowed extraction of oil and gas from low permeability formations that were previously not economically feasible.[98] While exact methods differ by region, a several km deep well is typically first drilled. The drilling is then directed horizontally to follow underground shale formations.[99] Once drilling is complete, a mixture of water, proppants (sand or similar particulate material that help keep fissures open), and chemical additives are pumped in at pressures up to 20,000 psi. The rock fractures under the high pressure, releasing the valuable hydrocarbons.[99] The fluid used to fracture the rock is returned often termed "flowback" or "produced water". This fluid is rich in salts, chemicals, heavy metals, and naturally occurring radioactive materials.[100,101] Shale gas generates 42,000-250,000 gallons of produced water per fracture with 10-16 fractures per individual well.[102] In 2007, the U.S. generated more than 880 billion gallons of produced water (35% in Texas alone);[103] UD activities have significantly accelerated since then. The produced water is commonly disposed of in underground injection wells[103] or stored in closed tanks. Sometimes they are put in open containment pits till the water evaporates.[104] There is increasing concern about possible contamination of ground and surface waters with produced water from UD operations.[99,105,106]

Studies of groundwater in the Marcellus shale, where significant UD activity has taken place have shown elevated levels of methane,[107] stray thermogenic gas (natural gas produced by thermal degradation of organic matter and hydrocarbons),[108] brine contamination,[109] and consequently elevated chloride and bromide levels.[110] Analysis of groundwater in the Barnett Shale at the height of UD activity showed elevated concentrations of arsenic, selenium, and strontium that were inversely related to distances from the drilling locations.[111] These studies did not, however, have baseline measurements available prior to UD activities; making it more difficult to draw definitively conclusions about the impacts of UD activities. The need for groundwater quality measurements before, during, and after UD cannot be overstated.[98,101,112]

Herein we look at the temporal changes in the anion profiles of private water wells in a region where UD has recently begun and has been accelerating over a 13 month period.

Such time dependent data will help more definitively assess the impact of UD, if any, on groundwater quality.

B.2 Experimental Section

Sampling. Samples were collected from 42 privately owned water wells from 3 contiguous counties in West Texas between December 2012 and January 2014. The exact geospatial coordinates were recorded for each well but are not cited here to protect the privacy of the well owners. All the wells draw from the Edwards-Trinity aquifer. The area lies on the eastern shelf of the Permian Basin that spans 86,000 square miles over 52 counties in Texas and New Mexico. While this region has seen a significant amount of conventional drilling in the past, a dramatic increase in UD has occurred since 2012 with new techniques for extraction oil and gas from carbonate rock formations. The drilling locations and operation dates are available from publicly available resources (for example, www.fracfocus.org). The private water well samples were collected in four phases over the 13 month period to document any changes in the groundwater anion profile as the UD activity increased. The sampling date and number of private water wells sampled during each phase were as follows: Phase 1 (12/14/2012)-50 water wells; Phase 2 (07/28/2013)-50 water wells, Phase 3 (10/27/2013)-18 water wells, and Phase 4 (01/25/2014)-26 water wells. Each water well was sampled at least in two of the above four phases. Information on age and depth of the water wells was generally not available; however, the majority are believed to be >60 years old and ~200 feet deep.

The number of UD wells within a 5 km radius of each water well was calculated to assess the density of unconventional drilling in the area. During phase 1 sampling, there was only one unconventional drilling well located within 5 km of any water well. While the first sample therefore cannot serve as a true baseline without any UD activity, it can still serve the purpose of determining the effects of further drilling activities.

Samples were collected by one of the authors as near the wellhead as possible to bypass any downstream treatment or filtration systems. Water was purged from the wellhead until the readings from a multiparametric probe (temperature, conductivity, DO, pH; Professional Plus MPP, www.ysi.com). Samples were then collected in 200 mL dark high density polyethylene bottles. Two bottles were completely filled at each location

leaving no headspace. The samples were put on ice in a cooler before arrival at our laboratories at the University of Texas at Arlington (UTA) within <48 h. For quality assurance, field blanks and randomized duplicates were also taken. For the samples analyzed here by ion chromatography (IC), to a 990 μL portion sample aliquot, 10 μL of a 0.5% v/v aqueous chloroform solution was added to prevent microbial degradation of organic acids. The samples were then frozen until analysis.

Analysis. The IC analysis protocol used an IC-25 isocratic pump with an EG40 electrodialytic eluent generator (EG), 2 mm bore AG20/AS20 guard and separation column sets housed in a LC30 temperature controlled oven (30 °C), ASRS-Ultra II anion suppressor in external water mode, and a CD-25 conductivity detector, all from ThermoFisher/Dionex. An electrogenerated KOH gradient at 0.25 mL/min was conducted as follows: 0-3-15-19-27-27.5-30 min; 4-4-10-40-40-4-4 mM KOH, all concentration change segments involving linear ramps. Gradient generation, electrodialytic suppression, autoranging conductivity detection and data acquisition were all conducted under software control (Chromeleon Ver. 6.8). A Thermo Finnigan Surveyor Autosampler performed sample delivery and injection (2 μL); all above components were from www.thermofisher.com.

Mixed standards containing the following were prepared: fluoride (10-500 μM), acetate (10-200 μM), formate (10-200 μM), bromide (10-200 μM), chloride (10-1000 μM), chlorate (10-200 μM), nitrate (10-500 μM), sulfate (10-1000 μM), chromate (10-200 μM), and perchlorate (10-200 μM). All data were interpreted in terms of a 5-point calibration with check standards run daily. Any sample falling outside the calibration range was reanalyzed after appropriate dilution. Only fluoride, chloride, sulfate, and bromide were detected frequently enough to be tested for statistical significance.

B.3 Results and Discussion

Choice of Ion Chromatography as the diagnostic tool for judging impact. It was not our purpose here to make value judgments on whether UD activities are affecting groundwater composition in a harmful manner; rather we wished to assess if major constituent composition in groundwater is being affected and the relationship of any changes with the proximity and density of UD activities. While methane concentration changes in groundwater have been much studied,[107,108] special care is needed for the

collection/storage/transport of samples containing gases under pressure. There is little data on other substances, especially major ionic constituents. While in terms of health-related concerns, certain contaminants in hydraulic fracturing or "fracking" fluids (FFs) or decomposition products thereof may be of greater interest, FF compositions vary greatly. There is no universally agreed upon benchmark identifier of fracking induced contamination. Additionally and importantly, some of the compositional changes that may take place originate from disturbances in the geologic strata resulting in the release of previously sequestered material therein and may have nothing to do with any direct contamination from FF derived material. Arsenic for example is a very common crustal element (20th in abundance) and in many regions, perturbing subsurface layers may result in elevated levels of As in groundwater through mobilization. This has already been observed.[111] Halides, sulfate, nitrate, etc. nearly universally constitute the major anions in groundwater. If the concentrations of these significant constituents increase markedly, this would be a clear indication of a significant impact, whether through direct FF contamination or crustal disturbance, whether or not any of these reach concentrations to be of concern for health reasons. Ion chromatography, a relatively simple, inexpensive and highly robust technique can not only analyze inorganic anions, it can also look at trace organic ions simultaneously and samples can mostly be directly analyzed without further preprocessing.

Sampling Locations and History. Figure B.1 is a representation of the sampling region and process. The following analyses looks at the variation in concentration of these inorganic anions from one sampling phase to the next statistically as well as the relative changes as a function of the distance to the nearest UD well. While the actual coordinates of the wells are not given, the scaling in Figure B.1 is accurate.

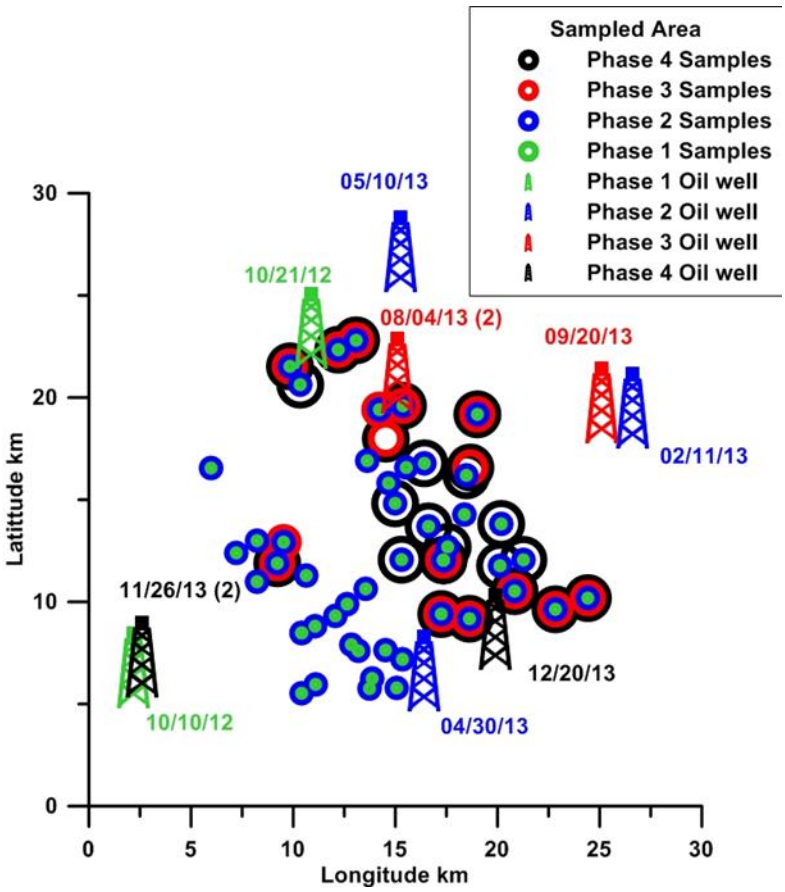

Figure B.1. Sampled wells at each phase; only UD sites within 5 km of a sampling well are shown. The dates indicate initiation of the UD activity on the indicated UD site and the number of main bores at each site are given in parentheses. All groundwater wells sampled during phase 1 were sampled during phase 2. In phase 3, some new ground water wells were sampled along with some previously sampled during phase 1/2. In phase 4, no new wells were sampled, only the ones newly sampled during phase 3 and some previously sampled ones in phase 1/2 were sampled.

Drilling Activity in the Area. At the time the first samples were collected in Phase 1 (December 2012), there were a total of 298 UD sites in the tri-county area. Phase 1 samples were collected within 2 months of the first UD well (Figure B.1, asterisked green derrick) being erected in the area. Samples were collected from 50 groundwater wells 515-9586 m distant from the UD well. By Phase 2 (July 2013), the total number of UD wells in the tri-county area had increased to 383, with 6 new UD wells located within 5 km of one or more groundwater sampling wells in the region depicted in Figure B.1 (blue derricks). Note that horizontal drilling allows a single platform /bore site to create new horizontal wells/fractures in different directions and at different depths (different strata)

that may be initiated on same or different dates. In phase 2 the groundwater wells sampled ranged 515-9328 m in distance from the nearest UD site. By Phase 3 (October 2013), the number of wells in the tri-county area had increased to 420; 5 of the new wells were now located within 5 km of a sampled water well which ranged 108-9328 m in distance from the nearest UD well. By phase 4, the total number of UD wells in the tri-county area had increased to 435 (nearly 50% over Phase 1). Three of the newly stimulated UD wells now within 5 km of a sample well, making a total of 15 UD wells within 5 km of one or more of the sampled water wells. Water samples collected in phase 4 were from wells that ranged 108-8940 m in distance from the nearest UD well.

	Phase 1 Water Samples(12/14/2012) n=50				Phase 2 Water Samples(07/28/2013) n=50			
	Mean ± S.E.	Median	Range	≥ MCL	Mean ± S.E.	Median	Range	≥ MCL
Conductivity (mS/cm)	0.7 ± 0.2	0.5	0.4–6.1	N/A	0.6 ± 0.0	0.6	0.4–1.4	N/A
pH	7.4 ± 0.03	7.3	6.8–8.1	0	8.7 ± 0.09	8.8	7.2–9.3	74
Fluoride (mg/L)	0.5 ± 0.05	0.4	0–1.3	0	0.5 ± 0.05	0.4	0.1–1.1	0
Chloride (mg/L)	37.6 ± 7.8	19	0.02–207.3	0	34.1 ± 6.7	18.9	4.8–220.9	0
Bromide (mg/L)	0.18 ± 0.08	0.16	0.08–0.31	6*	0.26 ± 0.11	0.22	0.17–0.30	3*
Nitrate (mg/L)	5.8. ± 1.1	4.4	0–31.5	0	4.6 ± 1.0	**2.9 a,d**	0–27.2	0
Sulfate (mg/L)	39.4 ± 4.1	35.7	0.6–106.9	0	41.4 ± 3.8	40.8	8.6–91.9	0
	Phase 3 Water Samples(10/27/2013) n=18				Phase 4 Water Samples (01/25/2014) n=26			
	Mean ± S.E.	Median	Range	≥ MCL	Mean ± S.E.	Median	Range	≥ MCL
Conductivity (mS/cm)	0.7 ± 0.1	0.7	0.4–1.5	N/A	0.7 ± 0.04	0.6	0.4–1.5	N/A
pH	7.9 ± 0.08	8	6.8–8.1	0	7.4 ± 0.03	7.4	7–7.7	0
Fluoride (mg/L)	0.3 ± 0.1	0.2	0–1.6	0	0.6 ± 0.07	**0.5 c,d**	0.1–1.6	0
Chloride (mg/L)	31.3 ± 11.4	**13.3 b,d**	2.1–225.4	0	48.2 ± 9.9	**26.6 c,d**	5.5–286.4	3
Bromide (mg/L)	0.09	-	-	1*	0.23 ± 0.07	**0.1 c,d**	0.1–2.0	16*
Nitrate (mg/L)	5.6 ± 1.9	2.1	0–28.5	0	8.5 ± 1.6	**6.2 c,d**	0–31.9	0
Sulfate (mg/L)	38.9 ± 6.3	29.5	9.1–129.5	0	58.7 ± 8.7	**49.7 c,d**	6.6–196.5	0

Table B.1. Ion Analysis Summary Table

a = significant difference from Phase 1 with a t-test, **b** = significant difference from Phase 2 with a t-test
c = significant difference from Phase 3 with a t-test , **d**= significant difference between 0-5 km data and >5 km data with a t-test
* =number of wells bromide was detected in. All t-tests were performed at 95% confidence

Major Inorganic Anions, Specific Conductance and pH Potable well water ion analysis. The concentrations of F^-, Cl^-, Br^-, SO_4^{2-}, NO_3^- as well as the sample conductivity

and pH are summarized in Table B.1. The *t*-test was used to determine if a significant difference existed at the 95% confidence level between the ion concentrations between specified phases. Along with formate and acetate, which were quantifiable in a minority of the samples, up to 10 unidentified peaks, most likely other organic acids, were also found some of the samples. The frequency of which these occur was tracked as well.

Casing failures[106,113]or improperly/inadequately lined waste storage pits[98,99,101]have been suggested to be the most likely route to contamination of shallow aquifers. Gases and water from the deep formations are not likely to percolate up to the surface, and in any case, the impact from such a process would not be observed in the short term.[106] The well casing is a cement tube that extends down through the ground water layer(s) and in principle prevents contamination from drilling activities. A recent study suggests casing failure may be as high at 6.2%.[113] This is especially alarming considering that much of the produced water is pumped into older oil and gas wells to stimulate production[103] and such older wells are more likely to have damaged casings. In any case, whether contamination occurs from a breach in the casing or from the flowback pit that is located near the wellhead, such contamination is likely to be maximum close to the well. Only if contamination occurred by fluids from UD sites entering groundwater over larger areas as through off-site disposal would a more diffuse pattern of contamination emerge. We sored sampled wells in two groups: those that were located within 5 km of one or more UD site and those that were at longer distances.

The 50 water wells were analyzed in phase 1 were situated at an average distance of 5.6 km from the nearest UD well. Chloride, Fluoride, Nitrate, Sulfate concentrations were all below the Maximum Contaminant Level (MCL) in all of the samples. Bromide was present in only 6 samples (0.1-0.3 mg/L). 5 samples contained 2 unknown peaks (we designate them A, B, C, etc. in the order of retention times) in total, C (n=3) and D (n=2), 2 of these 5 samples were the only ones containing measurable levels of formate (0.1 mg/L) and acetate (0.1 - 0.2 mg/L).

When the same 50 water wells were resampled in phase 2 (3 new UD wells being added), the average distance of the sampled wells to the nearest UD well had decreased to 4.8 km. No MCL exceedances were seen; three samples had detectable amount of Bromide (0.2-0.3 mg/L).The difference in concentrations between Phase 2 and Phase 1 was

statistically significant only for nitrate; the nitrate increase was also more pronounced for sampled wells that were closer to an UD well. Although groundwater nitrate concentrations can be influenced by agricultural runoff;[112,114] the sampled region has relatively sparse agricultural cultivation. The occurrence and number of unknown peaks increased as well. Up to 6 different unidentified peaks were 13 samples: A (n=1), B (n=10), G(n=3), H(n=2) , J (n=4), I (n=2); interestingly, neither formate nor acetate was detected in these samples.

In phase 3, the average distance of a sampled well to the nearest UD well decreased to 4.5 km. As in the previous 2 phases, no MCL exceedances were observed. Only one sample had a detectable concentration of Bromide (0.1 mg/L). Chloride concentrations increased from phase 2 to phase 3 at a statistically significant level. The absolute change in the chloride concentration between phase 2 and phase 3 were higher for the sample wells within 0-5 km of an UD well compared to those at a distance >5 km from the nearest UD well at a statistically significant level. There were no unknown peaks were in the phase 3 samples but a much smaller number of samples (18) were available on this round.

The 26 sampled wells in phase 4 were located at an average distance of 3.8 km. There were 3 MCL exceedances for chloride. Bromide was detected in >60% of the samples (0.1-2 mg/L). Natural groundwater bromide concentration is usually very low.[115] While aquifer contamination can occur through the use of agricultural soil fumigants[116], potassium mining and pesticide contamination.[114] The only agricultural practice in the study area is ranching and there are no mining activities. As such these sources can be ruled out. In contrast, bromide concentrations in produced water are generally high; indeed, following bromide concentrations in groundwater has been suggested as a possible means of detecting FF contamination or brine migration.[109] Phase 4 Chloride, Fluoride, Nitrate and Sulfate concentrations were all higher at a statistically significant level relative to any other phase. For all four ions, the 0-5 km distance sample well group had a statistically significant higher concentration than those the >5 km group. Up to 7 unknown peaks were detected in 11 samples: A (n=1), B (n=1), C (n=1), G (n=1), F (n=3), E (n=3) and J (n=1).

Additionally, if the relative change in concentration in going to phase 4 from phase 3 was plotted vs. the distance from the nearest UD well, all four ions exhibited a good inverse

correlation with the distance. This can be seen overleaf in Figure 2 where the relative change in concentration from phase 3 to 4 is plotted as a function of the distance of the test well from the nearest UD well in phase 4. This provides compelling evidence that UD activities are indeed affecting the groundwater major anion composition. What is also remarkable that in regression plots of the percent change vs. reciprocal distance the slopes for fluoride, chloride, and nitrate (1400±400, 1000±200, and 1400±300) are statistically identical indicating a common source and mechanism of dispersion. The corresponding value for sulfate is significantly lower but the much larger background concentration of sulfate initially present puts it in a different category. It is not yet possible to determine whether the increases are due to produced water entering the water table. The sheer volume of water that is used to stimulate new wells may itself affect the local water table leading to changes in the anion concentrations. Further analysis will be needed to verify the presence of chemicals unique to hydraulic fracturing to determine whether produced water contamination may be at play.

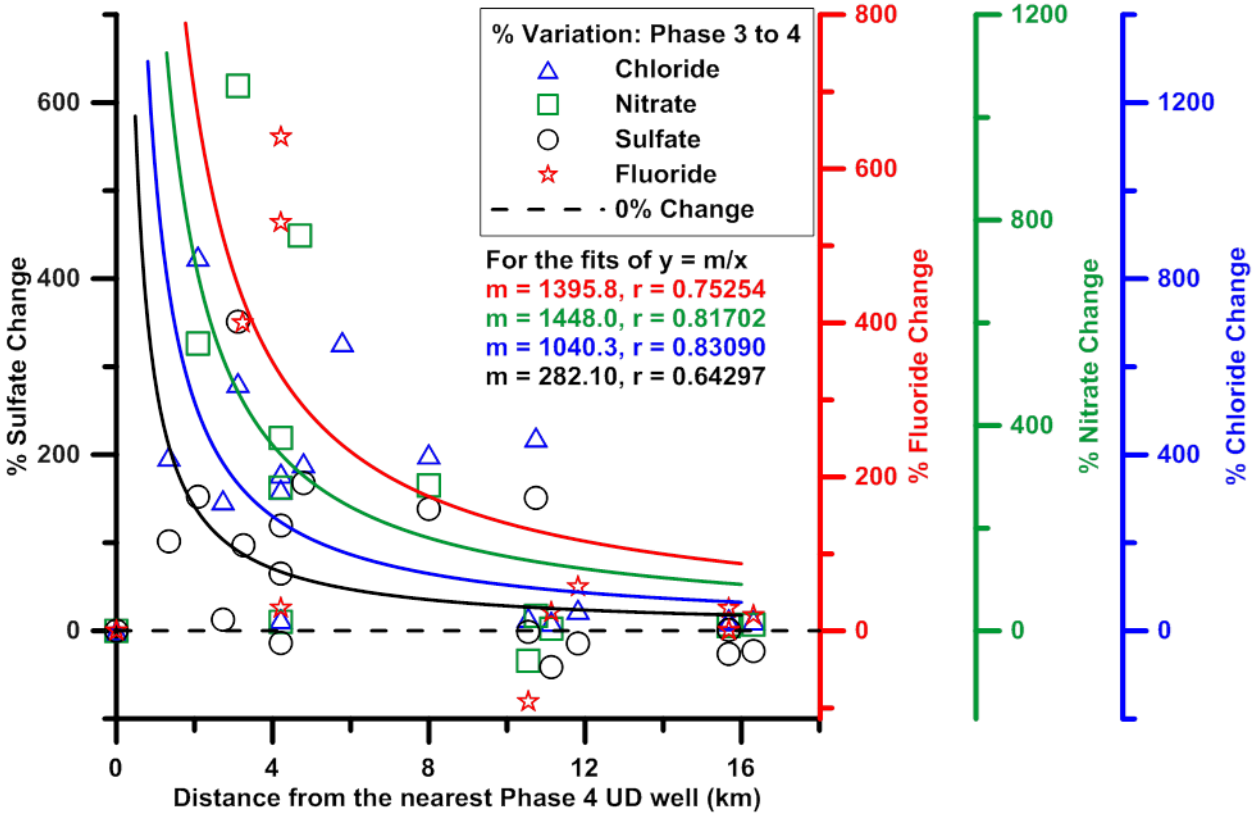

Figure B.2. Percent change in the concentration of an ion in a particular well in going from phase 3 to phase 4 vs. distance from the nearest UD well. See text for details.

B.4 Conclusions

The temporal major anion profile indicates a definite change from phase 3 to phase 4. The trend in the relative change vs. distance is the same for the major anions; therefore the contamination is occurring from the same source and mechanism. Ingraffea[113] demonstrated that between 2010 and 2011, Marcellus Shale well casings failed at a rate of 6.2%. Casing failure of one or more the UD wells (all in the same location) put in phase 4 can account for the abrupt change in major change in anion concentrations in the water wells in proximity and diffusion/passive fluid migration can account for the inverse distance relationship.

Appendix C:

Comment on 'Rapid visual Detection of Blood Cyanide' by C. Männel Croisé and F. Zelder , Analytical Methods, 2012, 4, 2632

Akinde F. Kadjo, Purnendu K Dasguptai, and Gerry R Boss

Analytical Methods. **2015**, 7, 5707-5711

Cyanide poisoning from Inhaled HCN is all too common in victims of smoke inhalation in fires. While the toxic effects arise primarily from its inhibitory effects on *cytochrome c oxidase*, the majority of the cyanide binds to methemoglobin (metHb) in the blood. It can be considered as the detoxification mechanism: one of the antidotes used earlier was nitrite which primarily works by converting hemoglobin to metHb (normally present to the extent of ~1% of the total hemoglobin). Cobinamide ($OH(H_2OCbi^+$) binds up to two moles of cyanide per mole and with a greater affinity than metHb and hence functions as an attractive antidote. Judicious dosage of this or any antidote requires a knowledge of the total blood cyanide levels and for this reason rapid determination of blood cyanide is needed in emergency situations. Cyanocobinamide ($CN(H_2O)Cbi^+$) has emerged in recent years as an excellent colorimetric reagent for measuring cyanide. Männel Croisé and Zelder (Anal. Methods, 2012, 4, 2632) have advocated direct addition of ($CN(H_2O)Cbi^+$) to blood samples and isolating the colored measurand $(CN)_2Cbi$ on a solid phase extraction cartridge. While they demonstrated attractive rapid measurement of cyanide in spiked blood samples, we believe that this is not a practically usable procedure. Cyanide bound to metHb dissociates too slowly for a 1 min reaction to work as suggested – we believe for reasons unknown (eg., metHb levels in their blood samples unusually low), cyanide added to their blood samples did not (have time to) bind to metHb and these samples may not resemble real situations where significant amount of the cyanide will be bound to metHb.

Männel Croisé and Zelder published an attractive method for rapid visual detection of blood cyanide in this journal.[117] There has been considerable valuable work done by these authors on the use of corrinoids for the colorimetric detection of cyanide.[118-122] The preferred reagent of choice that has emerged is cyanoaquocobinamide ($CN(H_2O)Cbi^+$, see e.g., ref [123] for relevant structure and nomenclature of these compounds closely related to vitamin B12. Independently, Boss et al. have been interested in hydroxoaquocobinamide ($OH(H_2O)Cbi^+$) as an antidote for cyanide poisoning,[124-125,126,127,128,129,130] and Boss et al. independently[131-133] or in collaboration with Dasgupta et al.[134-136] have used cobinamide based reagents for the colorimetric determination of cyanide. Spectrally ($CN(H_2O)Cbi^+$ is very similar to ($OH(H_2O)Cbi^+$) while $(CN)_2Cbi$ is very different. It was thus somewhat of a mystery as to how traces of cyanide can be detected with an excess of $OH(H_2O)Cbi^+$ as $CN(H_2O)Cbi^+$ will presumably be formed. We jointly solved the puzzle:[137] the reason is kinetic and not thermodynamic: $CN(H_2O)Cbi^+$ is much more rapidly attacked by CN^- to form $(CN)_2Cbi$; any $CN(H_2O)Cbi^+$ formed from $OH(H_2O)Cbi^+$ is rapidly converted to $(CN)_2Cbi$ in preference to more $CN(H_2O)Cbi^+$ being formed from $OH(H_2O)Cbi^+$. The preferred reagent will therefore be $CN(H_2O)Cbi^+$ as Männel Croise and Zelder have previously used; it leads to approximately twice the sensitivity as the amount of $(CN)_2Cbi$ formed is twice as much when one starts from $CN(H_2O)Cbi^+$ rather than $OH(H_2O)Cbi^+$.[135]

In the paper of present concern,[117] Männel Croisé and Zelder propose measuring cyanide in (spiked) blood samples by (a) adjusting the pH to 9.6 with CHES buffer, adding (b) $CN(H_2O)Cbi^+$ to the blood sample (c) allowing 60 s for $(CN)_2Cbi$ to be formed, (d) putting the mixture through a C-18 based solid phase extraction cartridge where the $(CN)_2Cbi$ is retained, (e) washing the cartridge with 3 mL of water to remove any adherent blood, (f) quantitating the cyanide visually by the extent of the red-violet coloration at the top of the column, or removing the top 2 mm of the sorbent layer and examining it by diffuse reflectance spectroscopy, or for the most accurate results, eluting the $(CN)_2Cbi$ with 400 μL of methanol, making up to 500 μL and measuring the product by solution phase absorbance measurements at 583 nm. In most other previous efforts in blood determination involving cobinamide or derivatives,[131,133,135,136] HCN had to be first released from the cyanide bound to blood by strongly acidifying the sample, prior to capturing the

gaseous HCN and measuring the resulting cyanide. In fact, it was pointed out[117] that a paramount advantage of the proposed approach, regardless of the technique or reagent used, is that this release of HCN along with a matrix isolation step (e.g., microdiffusion/microdistillation), common to all other approaches, is not necessary.

While we agree that a direct determination of cyanide without the need for microdistillation etc. is indeed attractive, there are several aspects of the proposed approach that are of concern to us, some of which we had communicated to the authors. While it may seem late to offer a critique in 2014 to a paper published in 2012, we deemed repeated experimental verification is needed to offer written criticism of the work of an esteemed colleague.

Previous work on blood cyanide determination without prior liberation of HCN. The sole exception (to previous approaches using microdistillation) cited by Männel Croisé and Zelder[117] is the work of Lacroix et al.[138] These authors spike the blood sample with an internal standard containing $^{13}C^{15}N$ and after deproteinization and centrifugation add Taurine and naphthalenedialdehyde (NDA) and allow it to react for 10 min at 4 °C to form the 1-cyano-2-alkyl-benz[f]isoindole derivative and quantitate the same by LC-isotope dilution MS/MS. The authors achieve a limit of detection of 10 ng CN/mL (0.4 μM). In comparison, cobinamide based colorimetric methods have been shown to provide an LOD as good as 8 nM; indeed even with portable analyzers for cobinamide-based blood cyanide, LODs were equal to or better than the Lacroix et al approach despite the fact that these authors used relatively large volume sample injections (100 μL on 2.1 mm ϕ columns) and the well-known high response of benz[f]isoindoles in ESI-MS. A likely possibility that one can surmise is that very little of the derivative is actually formed under the conditions used by Lacroix et al., albeit there may not be major quantitation errors because of the use of isotope ratio measurements. The use of NDA and Taurine to measure blood cyanide can be traced back to the work of Sano et al.[139] and Chinaka et al.[140] Both these authors state that ~83 % of the added cyanide is recovered after 30 min of reaction time at room temperature. If the formation proceeded at a first order rate, the putative first order rate constant would be 9.8×10^{-4} s^{-1}.

It is also not correct that cobinamide based approaches have been carried out only with prior HCN release. Dasgupta coauthored efforts to measure cyanide in which cyanide was spiked to whole blood, cobinamide was then added, allowed to react for 5 min and then the plasma, containing $(CN)_2Cbi$, was separated for spectrophotometric measurement[126] or visual estimation.[133] These approaches were abandoned because we subsequently realized that how much of the cyanide actually binds to the blood may depend on the time allowed for the cyanide to react with blood and conversely how much of the bound cyanide can be extracted by cobinamide depends on the time allowed for the cobinamide to react with the spiked sample.

Intrinsic concerns. Reagent amount and thermodynamic limitations. The final concentration of the $CN(H_2O)$ Cbi^+ reagent, which reacts with CN^- on a 1:1 molar basis to form $(CN)_2Cbi$, in the proposed method, is 42 μM prior to reaction with any cyanide present. The blood sample (0.5 mL) taken is spiked with up to 100 μM CN^-; with a final volume of 1 mL, in the absence of any reaction the cyanide concentration will be 50 μM, in addition to endogenous cyanide already present in any blood sample (this is typically in the low single digit μM level[136]). Regardless of the value of the equilibrium constant of the reaction

$$CN(H_2O)Cbi^+ + CN^- \rightleftharpoons (CN)_2Cbi \quad \ldots(C1)$$

Obviously there is not enough reagent present to react with all the cyanide present at the high end of the spike level and suggesting a straight line response through the entire 0-100 μM range is misleading. The equilibrium constant for reaction 1 is given by Männel Croisé and Zelder[117] to be 1.7×10^6 M^{-1}, based on their own as well as other prior work. While this may seem a large enough binding constant to provide for quantitative binding, at the levels involved, it is not so. Even with only 1 μM total cyanide (at which point the reagent is certainly present in large excess), it is easily calculated that 98.6% of the cyanide will react and the response will of course get steadily lower with increasing cyanide levels. Even in the absence of any competing ligands (notably metHb in blood), the reaction will not result in quantitative formation of $(CN)_2Cbi$ and by ~30 μM total CN^- in final solution,

the difference with the initial response slope will become apparent (Figure C1). If in fact a completing ligand such as MetHb is present, the reaction will be substantially less complete.

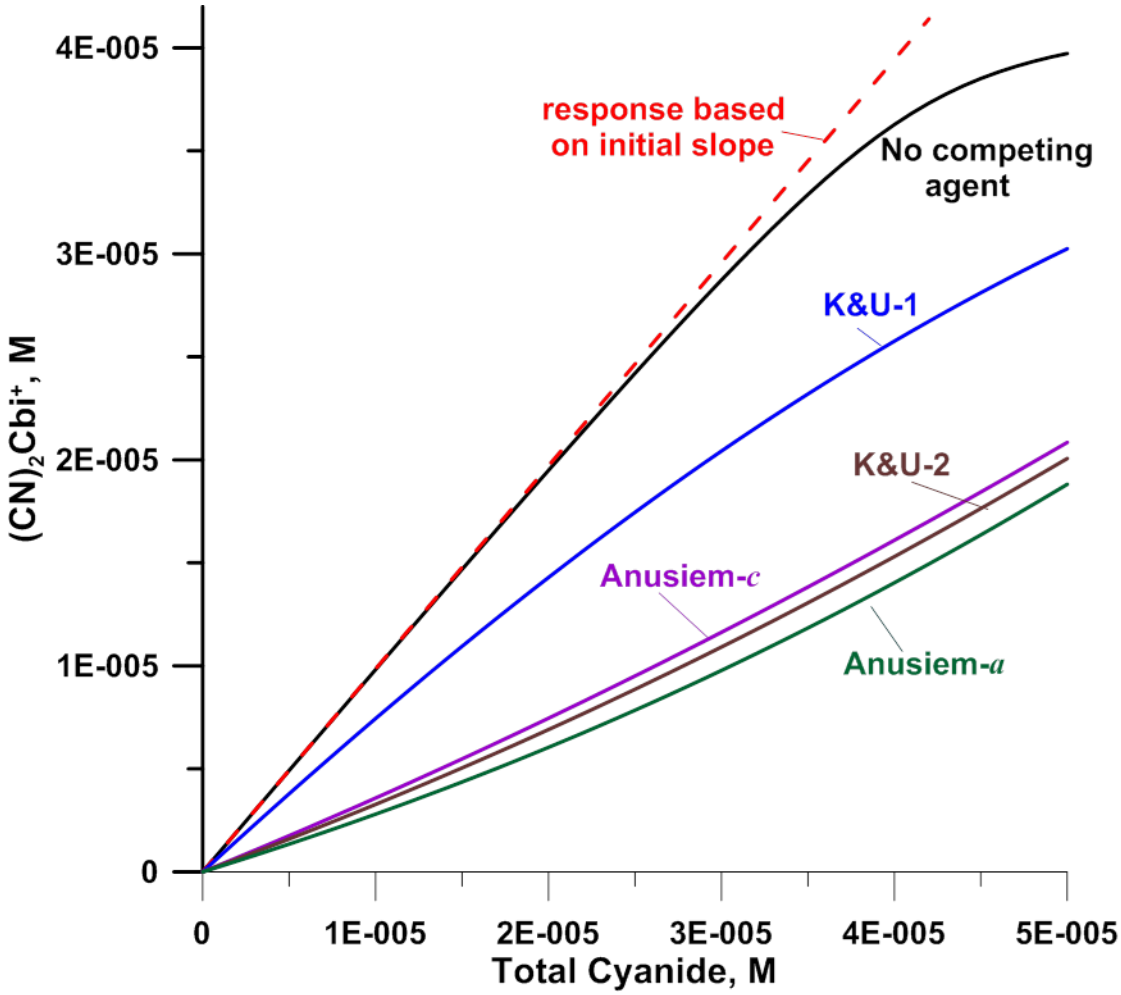

Figure C.1. Computed equilibrium $(CN)_2Cbi$ concentrations vs. total cyanide concentration initially present, total $CN(H_2O)Cbi^+$ added 42 μM. Solid black line: in the absence of competing agent: Dashed red line: hypothetical case where the initial linear slope observed at very low added cyanide levels is maintained throughout. Other traces represent computations that take into account competition of metHb present (45 μM) using different sets of metHb-CN binding constants from Klapper and Uchida[147] (K&U-1 and K&U-2) and by Anusiem et al.[148] for metHbA and metHbC (Anusiem-a and Anusiem-c). The computations are based on thermodynamic data, i.e., infinite reaction time is presumed.

Methemoglobin (metHb) is the primary cyanide binding agent in blood.[141,142] The normal range of metHb is 0.5 -2% of the total hemoglobin, often taken to be 1% of the total hemoglobin[143] the normal range for which is 120-175 g/L.[144] Although metHb typically is in the form of a tetramer in solution, it is customary to express the molarity in terms of molarity of the iron;[145] we assume here an average concentration of 1.5 g/L or 90 μM assuming an MW of 16,700 for the monomer. It is to be understood that metHb concentrations may be quite different in the animal blood samples with which Männel Croisé and Zelder as well as we experimented (in addition, there is some evidence that metHb concentration may increase some during storage[146] - these authors report a mean MetHb concentration of 1.6% in 312 banked fresh blood samples); however, ultimately the interest is in determining cyanide in human blood. After the addition of an equal volume of buffer, reagent etc., the metHb concentration will be 45 μM. The binding constant of MetHb with CN^- is given in two sources, one due to Klapper and Uchida[147] suggests that there are two binding sites with respective association constants of 0.45×10^6 and 3.5×10^6 M^{-1}. Figure C.1 also shows traces K&U-1 and K&U-2, that respectively represents these two binding constants. Obviously the formation of $(CN)_2Cbi$ is expected to be much less if the complexation by metHb is taken into account.

In fact there is an earlier study by Anusiem et al. that looks at cyanide binding to both metHbA and metHbC. [148] Because it provides an extensive data set (it reports the binding constants both as a function of temperature and pH, these data are used more often (see e.g., ref. [149]). The data does not extend to pH 9.6. By extrapolating the data given for pH 7.0 to 7.8 for metHbA (Table 13, reference 148), and that given for pH 7.6 to 7.8 for metHbC (Table 14, reference 148), we estimate the respective binding constants to be 4.5×10^7 and 3.0×10^6 M^{-1} at 20 °C. Two further traces, Anusiem-*a* and Anusiem-*c* are shown also in Figure 1 that respectively assumes these binding constants and an average metHb concentration of 45 μM in the final solution being measured, to complete the picture. It should become clear that at the level of reagent added, based on available thermodynamic data in the literature, it is extraordinarily unlikely that a quantitative linear response in the range of blood cyanide concentrations explored in this paper will be expected *a priori*, especially with the amount of reagent used.

Kinetic Considerations. The kinetics of the reactions involved is perhaps even more troubling aspect is kinetics. Klapper and Uchida[145] provide a second order rate constant of 180 M^{-1} s^{-1} (k_f) for the forward reaction

$$MetHb + CN^- \rightarrow MetHbCN \quad ...(C2)$$

The rate constant k_r for the reverse reaction, the dissociation, that must take place before cobinamide can bind to cyanide, is readily calculated from the overall binding constant, equal to k_f/k_r. For the range of binding constants discussed above (4.5×10^{-5} to 4.5×10^{-7} M^{-1} k_r is calculated to be in the range of 4×10^{-4} to 4×10^{-6} s^{-1}, corresponding to half-lives of ~30 min to 2 days; if any of the above literature data are to be trusted, it is simply not possible for the cyanide bound to metHb to significantly react with cobinamide in 1 min, much less do so quantitatively.

One plausible explanation is that due to whatever reason, the cyanide spiked into the blood samples in the experiments of Männel Croisé and Zelder did not have enough time to bind to the metHb. To test this hypothesis, we experimented with both bovine and porcine blood in an identical fashion to that described in the paper[117] with the sole difference being that we waited 0.5, 5,10, 20, 30, and 60 min between spiking cyanide to the extent of 50 μM and adding CN(H_2O) Cbi^+ to the extent of 42 μM and interpreting the results in terms of a calibration curve done in the 3.8% citrated water in place of blood, with the C18ec cartridge eluted by methanol and spectrophotometric measurement at 583 nm. The results are shown in Figure C2, along with a best fit line describing the disappearance of the recoverable cyanide with time to some final equilibrium value as a first order process. The best fit rate constants are 5.5×10^{-4} and 1.8×10^{-3} s^{-1}, respectively.

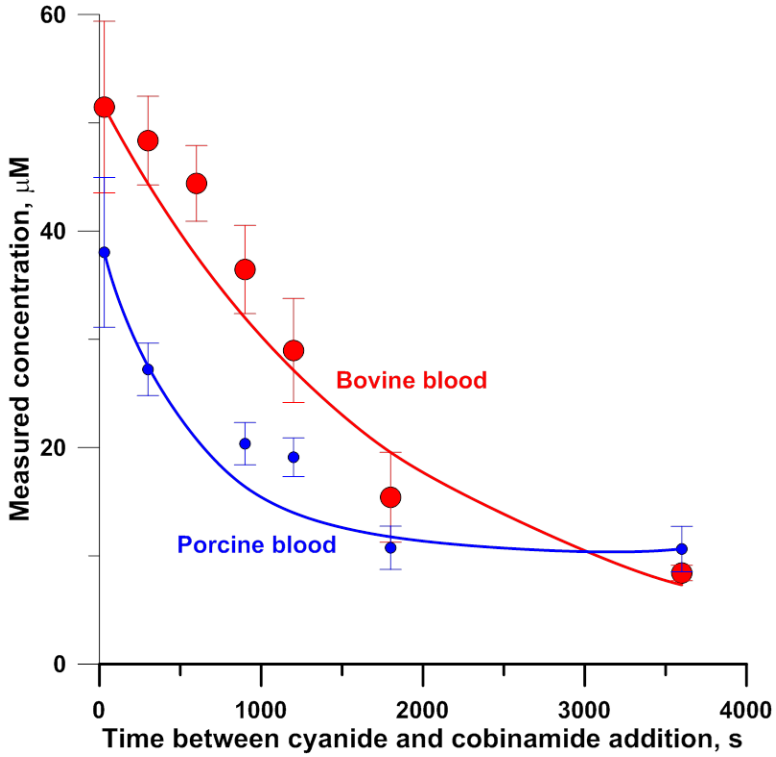

Figure C.2. Measured concentration of $(CN)_2Cbi$ vs. the incubation time of CN^- in Bovine and Porcine blood.

In a real situation with a human how much of the cyanide intake is already complexed with metHb will depend on the exact exposure scenario and duration but there is little doubt that a significant if not a major fraction can already be bound to metHb and this cannot be measured by the proposed method.

Acknowledgement

This work was funded in part by Jenkins Garrett Professorship funds at UTA and by the CounterACT Program, Office of the Director, National Institutes of Health and the National Institute of Neurological Disorders and Stroke, Grant # U01NS058030

Appendix D:

Enigmatic Ion Exchange Behavior of Myo-Inositol Phosphates

C. Phillip Shelor, Hongzhu Liao, Akinde Florence Kadjo, Purnendu K. Dasgupta

Analytical Chemistry. **2015**, 87, 4851-4855

D.1 Introduction

Ion exchange retention is commonly thought to be governed by electrostatic interactions. Both electrostatic and hydrophobic interactions control retention, the latter often being dominant: the hydrophobic monovalent ion ClO_4^- often elutes after divalent SO_4^{2-} or even trivalent PO_4^{3-}. True electrostatic selectivity can be achieved only with hydrophilic columns and hydroorganic eluent modifiers.[150] For a given subset of molecules of similar hydrophobicity, however, electrostatic interactions govern the elution order; an increase in charge results in an increase in retention.

There is presently considerable interest in *myo*-inositol hexakisphosphate (phytate, $InsP_6$, the primary P storage form in many living systems). Phytate is known to form many metal chelates[151-156] and was earlier considered an antinutrient because it sequesters calcium,[151] but now its antioxidant and anticancer properties are of greater interest. Phytate chelates iron and prevents it from initiating oxidative damage; it may potentially help prevent Alzheimer's and other neurodegenerative diseases.[152] We recently reported on the determination of phytate in Açaí berry extracts by hydroxide gradient IC.[157] Phytate will have a -12 charge[156,158] in a strongly alkaline eluent; elution of an ion with a -12 charge is thought to be essentially impossible. Yet we found it to elute shortly after citrate on several anion exchange columns using relatively mild eluent concentrations.

Hydroxide eluent IC determination of phytate has been reported by only one other group[159,160] using up to 110 -130 mM NaOH containing isopropanol on a multifunctional anion exchanger. IC methods more commonly use concentrated strong acids such as HCl (0.5-0.95 M),[161-163] CH_3SO_3H (1.5 M),[164] or HNO_3 (0.155 M)[165] as eluents to suppress ionization for anion exchange separation of InsP's. Ammonium acetate/acetic acid[166] (75 mM, pH 4.0) and Citrate buffer[167] (1 M, pH 5.0) are only able to elute up to $InsP_3$ and $InsP_4$, respectively. Complete class separation (no isomeric separation) of $InsP_1$-$InsP_6$ was possible with a 0.01 M methylpiperazine buffer (pH 4.0) with a salt gradient up to 0.5 M $NaNO_3$.[168] Postcolumn reaction absorbance detection with $Fe(ClO_4)_3$ is typically used; few other analytes can be sensitively detected in this mode.

Having successfully separated phytate by gradient hydroxide IC, we attempted to separate the variously phosphorylated InsP's ($InsP_{0-6}$) and were surprised to find that $InsP_4$'s and $InsP_5$'s apparently elute after $InsP_6$.[169] It is not logical that $InsP_4$'s and $InsP_5$'s have so much greater hydrophobicity than $InsP_6$ that it even overcomes the considerable differences in the net charge of -12 for $InsP_6$ to -8 for $InsP_4$. Here we unravel reasons for this unusual behavior.

D.2 Experimental Section

Phytic acid was acid hydrolyzed according to the method of Cosgrove[170] to produce $InsP_0$ to $InsP_5$. Aliquots were taken from the solution kept at 110° C every 30 min for the first 14 h, and at longer intervals (6-12 h) thereafter until 48 h; details are given in the supporting information (SI). The equipment and details of ion chromatographic studies of InsP's are also given in the SI. An electrogenerated KOH eluent gradient ramped to 55 mM was used with an AG24/AS24 column permitting analysis. An NMe_4OH –NaOH concentration and composition gradient was used with AG11HC/AS11HC columns, details appear in the SI. For Ion chromatography -mass spectrometry, a TSQ Quantum Discovery Max electrospray ionization (ESI) MS/MS system with a heated ESI probe (www.thermoscientific.com), two different IC systems were used.

D.3 Results and Discussion

Separation of Inositol Phosphates. The optimized separation of InsP species is shown in Figure D1 for selected hydrolysis times between 0.5 – 40.5 hours; the production of intermediate and finally lower InsP's is clearly visible. The 12.5 hour hydrolysate (selected for its relatively even distribution of all components) was analyzed by MS to identify specific zones (Figure D2): 5-8, 17-22, 30-40, and 40-50 min elution windows corresponded to $InsP_1$, $InsP_2$, $InsP_3$, and $InsP_4$ - $InsP_5$ respectively. $InsP_6$ eluted at 42 min. The ultimate product of InsP hydrolysis, inositol and phosphate were detected eluting in

the void volume and 15 min, respectively. The rate of phosphate appearance can be used to determine the rate of the reaction at any given time.

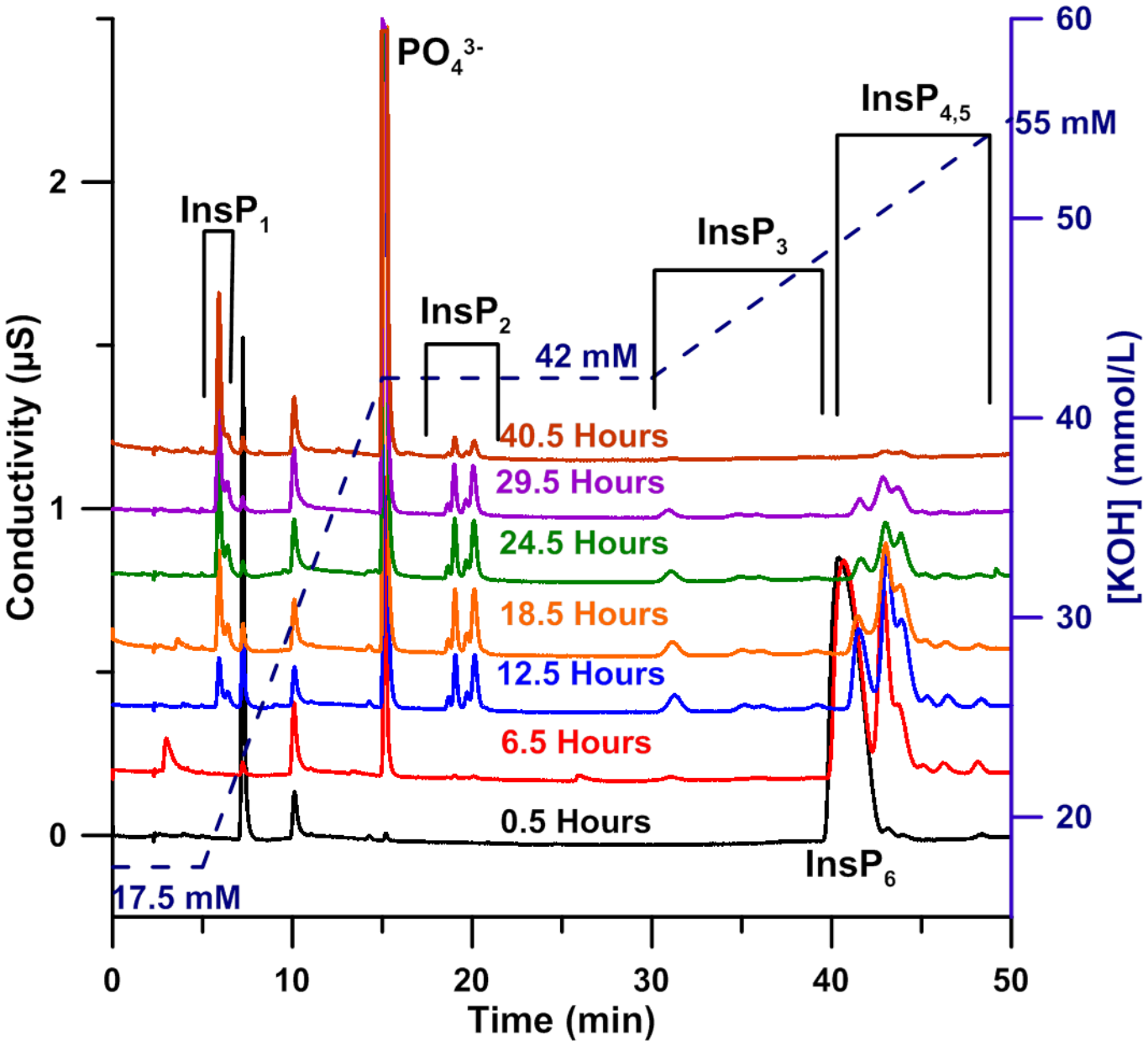

Figure D.1. Ion Chromatograms of phytate Hydrolysates from 0.5-40.5 hours. The dashed blue line is the KOH gradient concentration. Regions of elution for the InsP's are marked.

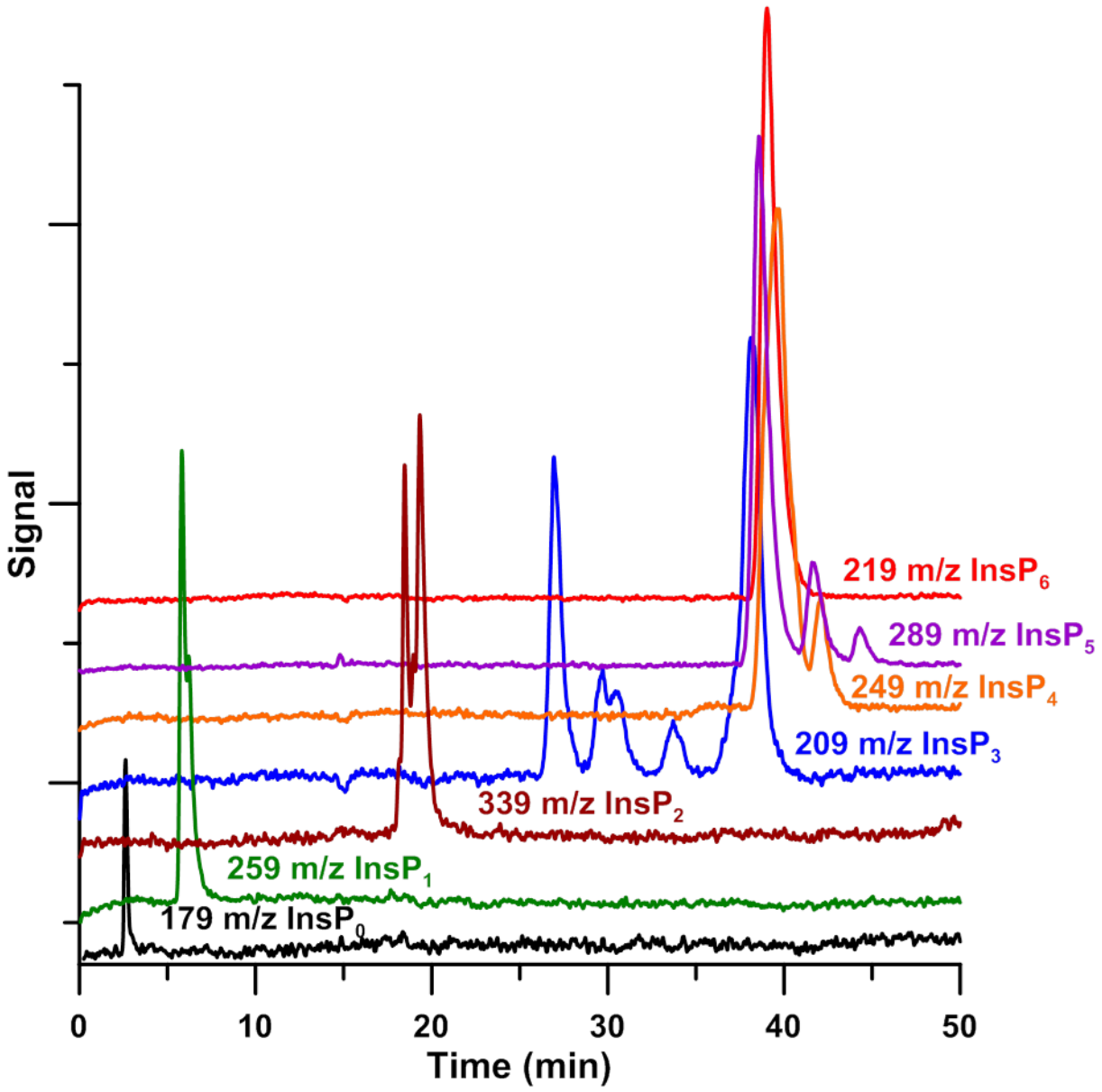

Figure D.2. Single ion monitoring traces, 12.5 h hydrolysate. Chromatograms have been offset and scaled differently for clarity.

Figure D1 indicates (as interpreted by MS analysis, see below) that $InsP_1^{2-}$, PO_4^{3-}, $InsP_2^{4-}$, $InsP_3^{6-}$ elute in the order of their charge but $InsP_4$ – $InsP_6$ do not follow this trend: $InsP_6$ elutes before the majority of $InsP_4$ and $InsP_5$ isomers. The close elution/coelution (Figure D2) of these isomers clearly fails the charge-retention predictions. The hydrolysis of $InsP_6$ can theoretically result in 6, 15, 20, 15, and 6 (62 total) possible geometric isomers

for $InsP_1$-$InsP_5$ respectively. However, Ins has a plane of symmetry and 4, 12, 16, 12, and 4 of the above positional isomers make up half as many (24 total) enantiomeric pairs which cannot of course be resolved on achiral columns. This makes a total of 40 possible chromatographic peaks including Ins and $InsP_6$. Of these, only 2, 4, 5, 2, and 3 isomers are visually apparent in Figure D2.

Mechanism of Phytate Separation. Plausible explanations for the retention behavior of $InsP_4$ – $InsP_6$ may include: (a) $InsP_4$ – $InsP_6$ anions do not carry the assigned formal charges, the final protons do not ionize, (b) On a molecular scale, the stationary phase cationic site density is not sufficient to fully interact with all charges on the highly phosphorylated InsP's and (c) the rigid inositol skeleton can at best orient 4 phosphate groups toward the stationary phase, any phosphate groups not interacting with the stationary phase increases eluophilicity (see below).

Successive K_a values for $InsP_6$ have been extensively studied.[156] The pK_a of the final proton varies from >13 in 0.17 M Et_4NClO_4 to 8.29 in 3 M $NaClO_4$. In media closest to our eluent conditions (0.1 M KCl) pK_{12} was reported to be 10.24. The lowest concentration KOH (40 mM) we used for isocratic elution has a pH of ~12.6, sufficient to fully ionize $InsP_6$. Hypothesis (a) must therefore be discarded.

For a hydroxide eluent, the slope of a log (capacity factor (*k*)) - log [OH^-] equals the charge on the eluite ion.[171] For $InsP_6^{12-}$, the slope should be -12. Figure D3 shows such plots for KOH elution on both AS11HC (exchange capacity 140 μeq) and AS24 (290 μeq) columns. Note that within experimental error both columns produced the same effective charge (EC) of -10 with the KOH eluent, given the >2x exchange capacity difference, hypothesis (b) must also be wrong. A closer examination of the log [OH-] – log *k* plots suggest, however, that a linear model may be inadequate (see Fig. D4 for a plot of the residuals). In Fig. D3, the slope between two adjacent data points was plotted vs. the geometric mean of the OH^- concentration as dashed lines. Here, the EC is seen to decrease with increasing KOH concentration. This also suggests the invalidity of hypothesis (a), especially as it is known that increasing ionic strength actually enhances the dissociation of phytic acid.[156] On the other hand at the lowest eluent concentration, the EC determined for

$InsP_6$ was -11 for the lower capacity column, suggesting strongly that the theoretical -12 will be approached at still lower eluent concentrations, and there is no insufficiency of the resin capacity: hypothesis (b) is untenable.

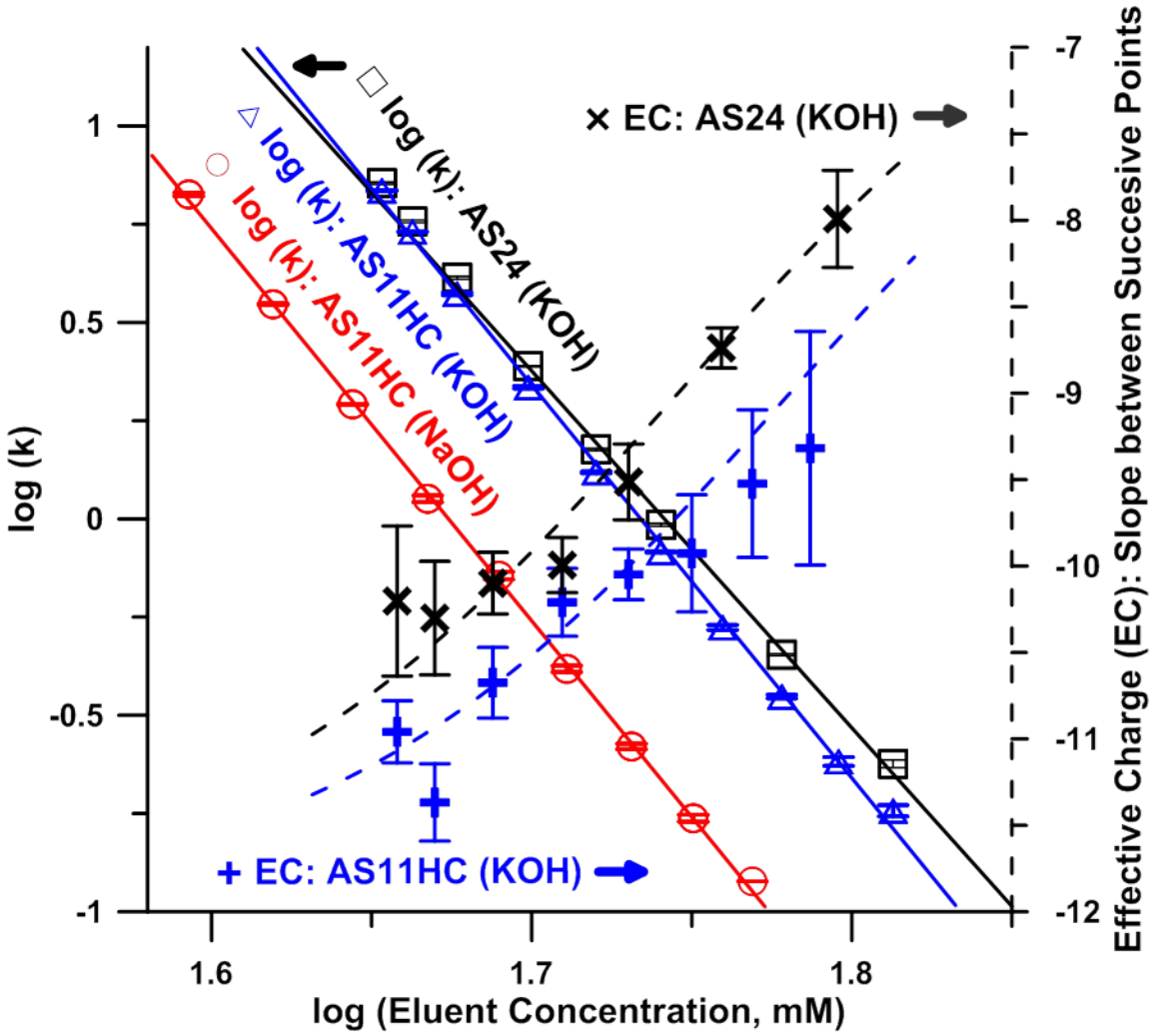

Figure D.3. Log [OH^-] vs Log k for $InsP_6$ anion elution on AG/AS11HC columns using (a) NaOH and (b) KOH; and (c) AG/AS-24 columns using KOH. The slope generally indicates the effective charge of $InsP_6$; this ranges between -9.3 and -10 in these plots. The respective slopes and linear correlation coefficients are: (a) -9.98 ± 0.05, r^2 = 0.9994, (b) -10.00 ± 0.08, r^2 = 0.9982, and (c) -9.34± 0.10, r^2 = 0.9977. The interpoint slopes (with ± 1 SD error bars) are plotted vs the log of the geometric mean of the hydroxide concentration. The effective charge of phytate decreases with increasing KOH. The dashed lines are the predicted charge states based on the fits of the complexation constants.

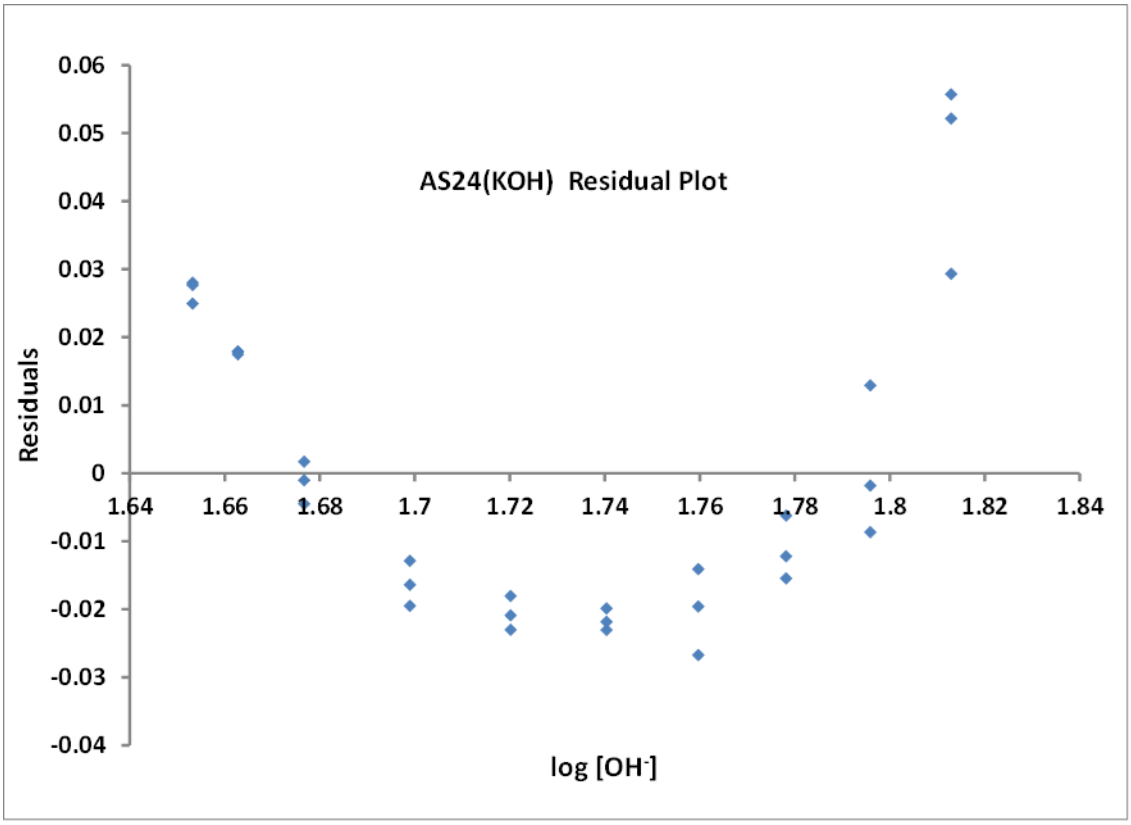

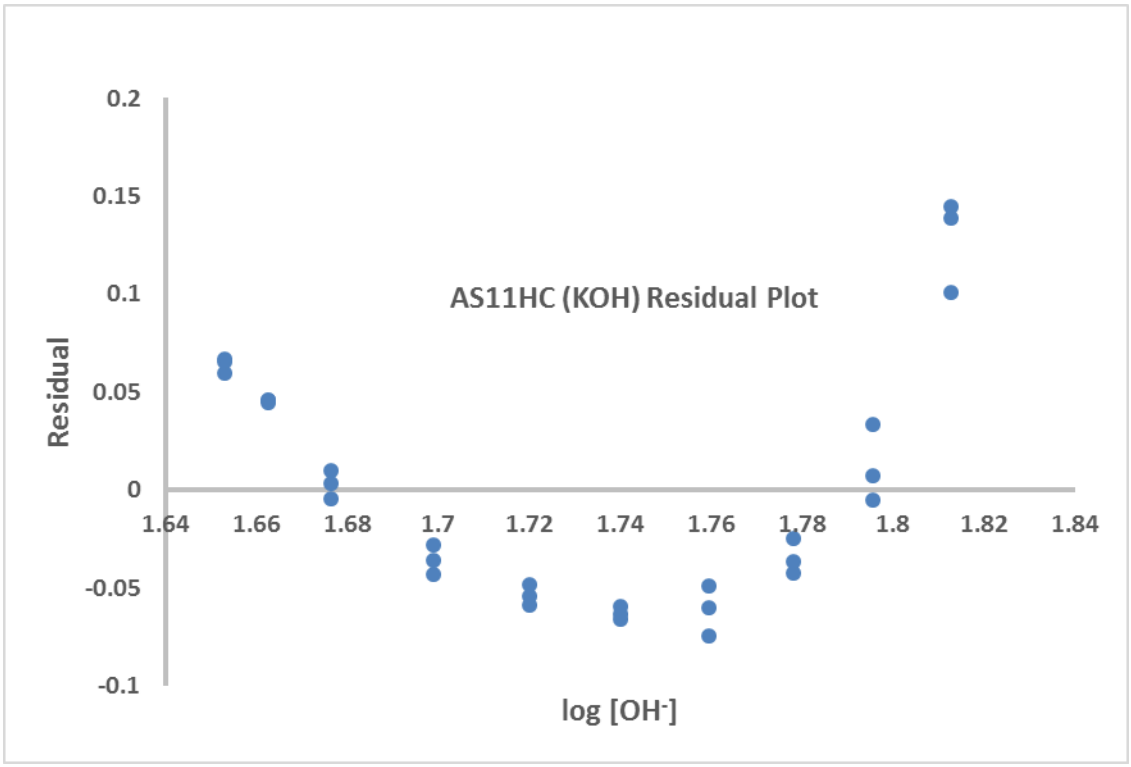

FigureD.4. Residual plots, KOH eluent regression plots in Figure D3

Alternative (c) suggests that the charges on a multiply charged rigid molecule are sterically arranged on opposite sides, the solvation affinity of charged sites not bound to the stationary phase will lead to an eluophilic effect. For stainless steel open tubular columns bearing anion exchange sites, Mo reported that while 2,6-naphthalenedisulfonate elutes after 2-naphthalenesulfonate as expected, 1,3,(6 or 7)-naphthalenetrisulfonate elutes in between the two.[172] While this may provide an explanation for the elution behavior of $InsP_{4\text{-}6}$, this cannot explain why there is such a large difference in retention behavior of $InsP_6$ between the same concentrations of KOH and NaOH as eluent and why the EC magnitude of phytate is perceptibly lower with NaOH than with KOH. Indeed our confusion was compounded when we experimented with NMe_4OH: Compared to NaOH or KOH, even a much higher concentration (0.1 M) of NMe_4OH could not elute phytate from either column in 1 h.

The Role of the eluent Cation. Determining Complexation Constants from Effective Charge. The literature indicates significant alkali metal complexation by phytate. The complexation constants are not available in a straightforward manner. Essentially all the data are reported as potentiometric measurements of the successive K_a values of $InsP_6$ in the presence of various concentrations of NaCl, KCl, etc. and assumptions are made as to charge states that the present experiments will clearly indicate to be invalid. Although direct quantitative comparison with our data is not therefore possible, qualitatively the complexation follows the charge density order $Li^+ > Na^+ > K^+ > Cs^+ >> NR_4^+$.[153,154,156] As eluent cations Na^+ or K^+ will form adducts with phytate, this will reduce EC and increasingly so as the eluent concentration is increased. This is depicted in the dotted line traces (right ordinate) in Figure D3. The change in EC with $[M^+]$ ($[M^+]$ being the same as the eluent concentration) can be used in a simple manner to determine the stepwise complexation constants. If we express the equilibria much like the dissociation of a polyprotic acid, $M_{12}L$ (L being $InsP_6^{12-}$) losing M^+ stepwise to eventually form L^{12-}, the stepwise dissociation constants being K_1 through K_{12}:

$$M_nL^{(12-n)-} \rightleftharpoons M^+ + M_{n-1}L^{(12-(n-1))-} \quad ...K_{13-n} \quad (n = 12\text{-}1) \quad ...(D1)$$

Much as with polyprotic acids, we express the fraction of the total concentration of each L-bearing species as α-values (K_0 is 1, has no physical meaning, for mathematical convenience)

$$\propto_{M_nL^{(12-n)-}} = \frac{[M^+]^n K_0 \ldots K_{12-n}}{\sum_{n=12-0} [M^+]^n K_0 \ldots K_{12-n}} \quad \ldots(D2)$$

EC is then simply the charge-weighted sum of the α-values:

$$EC = -\sum_{n=12-0} (12-n) \propto_{M_nL^{(12-n)-}} \quad \ldots(D3)$$

The analyte concentration is so small relative to the eluent concentration that even if 12 M^+ ions were bound to a single ligand molecule, there will be no perceptible change in the nominal [M^+] concentration stated. We have the value of EC as a function of [M^+] but in a given set of experiments, all of the twelve equilibria are not going to be important. For example, in our experiments with KOH with the AS11HC column (Figure D3, dashed black trace), EC ranged from -7.4 to -11. Only equilibria involving K_7 through K_{12} play a significant role; if we have *at least* 6 EC values as a function of [M^+], the best fit values for K_7 - K_{12} can be calculated by any nonlinear least squares algorithm, e.g. Microsoft Excel Solver™.[173,174] The respective best fit values (and their uncertainties from the jackknife approach[175]) are reported in table D1 (although the formalism above were for dissociation constants, it is customary to report metal-ligand equilibria in terms of association constants) for -log K_7 through –*log* K_{12} as measured with the AS11HC column. The values are consistent with greater binding of Na^+ relative to K^+ by phytate.[153-156] To our knowledge, this is the first illustration of measurement of successive metal-ionic ligand binding constants through chromatographic measurement of changes in the effective charge on the adduct.

Eluent Cation	*-log* K_7	*-log* K_8	*-log* K_9	*-log* K_{10}	*-log* K_{11}	*-log* K_{12}
K^+	6.08±0.35	3.12±0.12	2.44±0.11	1.20±0.04	-0.93±0.02	-4.60 ±0.04
Na^+	6.69±0.02	2.97±0.00	2.31±0.00	1.15±0.00	-0.96±0.00	-4.60±0.01

Table D.1. Formation Constants for phytate alkali complexes of sodium and potassium

In the only other examples known to us where both the eluent cation and anion play a role in anion exchange separations, the cation provides retention to the analyte ion via adsorption on neutral sites on the stationary phase; this can be a tetralkylammonium ion being adsorbed on a nonpolar phase[176] or alkali cations being adsorbed on a cryptand column.[177,178] A typical gradient run may involve the gradual change from a more to a less adsorbed cation (e.g., NPr_4^+ to NEt_4^+ or Na^+,[176] or Na^+ to Li^+,[177,178] thus leading to reduced column capacity as the gradient progresses. Here, the situation is fundamentally different, the column capacity is unaffected by the eluent; increases in either the cation or anion concentration helps elute the analyte anion. It is also possible to view the effect of the metal ion the same as that of the effect of pH in anion exchange separations, decreasing the pH and converting the analyte to a lower charged form decreases the retention. Variation of the eluent cation in ion exchange chromatography is rarely studied, aside from the alkali metals, the use of Ca, Ba, or quaternary ammonium ions may prove useful in separations between large, highly charged structurally similar ions separated by suppressed conductometric IC.

Experiments were carried out to try and elute phytate with $Ca(OH)_2$ or $Ba(OH)_2$ as well. The poor solubility of $Ca(OH)_2$ allowed only concentration of 20 mM to be tested, and phytate could not be eluted under these conditions. However, it is possible to dope Calcium in an eluent largely containing KOH and the addition of even 100 μM $Ca(OH)_2$ into 50 mM KOH showed a remarkable decrease in retention time from 30 min down to 8 min (Fig D5-D7). However such a system takes substantial time to stabilize. Perhaps more importantly, considerable loss of efficiency and hence sensitivity are observed; the phytate peak broadens either due to kinetic limitations of the complexation process itself or in interphase mass transfer. Similar results were obtained for $Ba(OH)_2$ (Fig. D8); as with Li^+ Vs. K^+, the effects of Ba^{2+} were less than a comparable concentration of Ca^{2+} albeit $Ba(OH)_2$ has much greater solubility and can be used at higher concentrations. It may be possible to determine the complexation constants of the alkaline earth metals (not including Mg^{2+},$Mg(OH)_2$ is not sufficiently soluble) by the present approach but in terms of chromatographic utility, the interaction of phytate with Ca^{2+} and Ba^{2+} is too strong to be of much practical value.

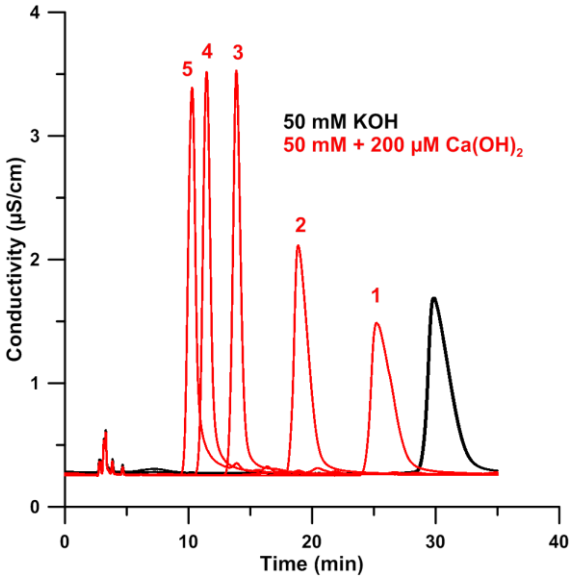

Figure D.5. Elution of 25µM phytate using 50 mM KOH (shown in triplicate) and 50 mM KOH + 200 µM $Ca(OH)_2$. Sequential injections are shown of Phytate elution after addition of $Ca(OH)_2$ and numbered accordingly. After addition of $Ca(OH)_2$ the system is slow to equilibrate. Phytate is seen eluting earlier and earlier. Initially an increase in peak height is observed due to the earlier elution, but the peak then begins to tail more heavily after a while.

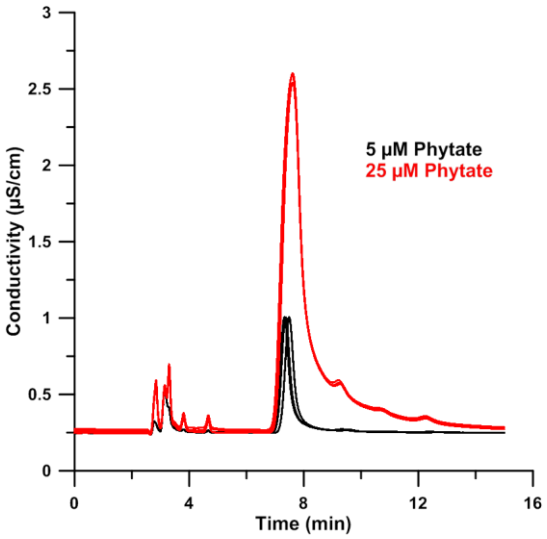

Figure D.6. Elution of phytate in 50 mM KOH and 100 µM $Ca(OH)_2$. The system was allowed to equilibrate overnight before testing. Considerably more tailing is observed when 25 µM phytate is injected compared to 5 µM. At 25 µM, phytate is essentially complexing enough calcium to reduce the availability in the solution which results in a higher effective charge and a greater net retention for the less complexed phytate. Lower inositol phosphate impurities are clearly visible on the tail of the 25 µM peak. Such separation was not achieved when just a KOH eluent was used. Repeat runs are shown.

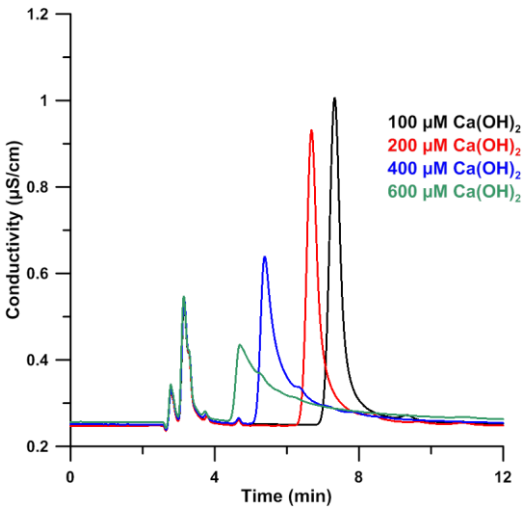

Figure D.7. Elution of phytate in 50 mM KOH containing different amounts of $Ca(OH)_2$. The system was allowed to equilibrate for 45 minutes between injections. A loss in efficiency and sensitivity occurs at higher concentrations of $Ca(OH)_2$. Conversely, use of too little $Ca(OH)_2$ limits the range at which phytate can be measured as shown in Figure D6.

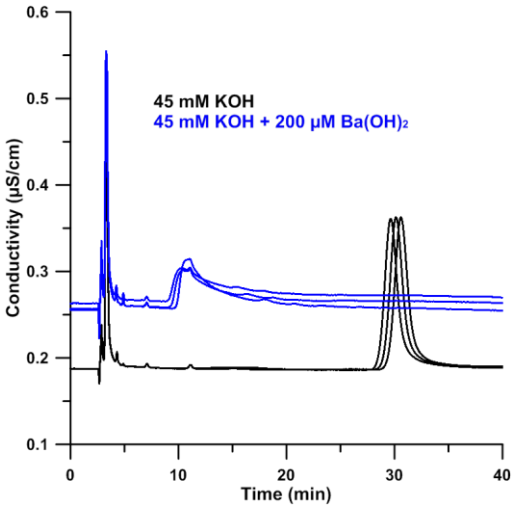

Figure D8. Elution of 5 µM phytate with 45 mM KOH and 45 mM KOH + 200 µM $Ba(OH)_2$. The $Ba(OH)_2$ contains some impurities which accounts for the elevated background. Upon addition of $Ba(OH)_2$ phytate retention decreases but the peak height also decreases and the peak becomes wider. Repeat runs are shown.

Practical Consequences. Because there is a significant difference between the degrees to which different cations are complexed by phytate, in particular the inability of even 0.1 M NMe_4OH to elute phytate in 1 h, whereas even much lower concentrations of NaOH eluted it readily (Figure D3), this can be exploited to achieve an extended range of gradient strength in the separation of InsP isomers via an NMe_4OH-NaOH (or even LiOH)

gradients. As the cation is entirely removed in a suppressed system, a low conductivity MS-compatible background will still be attained.

Figure D9 shows such a separation of the 12 h phytate hydrolysate with mass spectrometric eluite identification (for comparison, an electrodialytic KOH gradient chromatogram is also shown in Figure D10). The first 15.5 minutes uses only an NMe_4OH gradient (see Table D2). Then NMe_4^+ is replaced with Na^+ while $[OH^-]$ is held at 65 mM. As the phosphate groups have little affinity for $N(Me)_4^+$, separation is initially purely driven by $[OH^-]$; $InsP_1$'s elute at essentially the same time with KOH or NMe_4OH eluents. While $InsP_2$'s elute after PO_4^{3-} with either KOH or NMe_4OH the retention is less with NMe_4OH, likely because anionic impurities, notably carbonate, in the manually made eluent, the NMe_4OH eluent was also marginally lower in concentration (with a quartic vs quadratic dependence on $[OH^-]$ for the elution of $InsP_2^{4-}$ vs. $InsP_1^{2-}$).

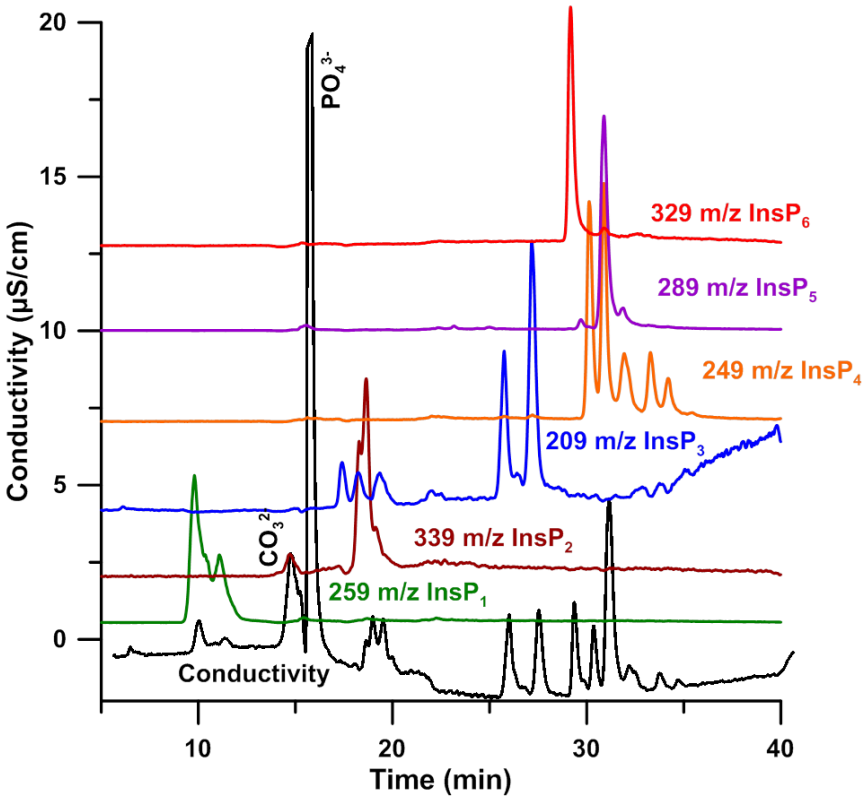

Figure D.9. NMe_4OH and NaOH gradient separation of 12 hour hydrolysate. MS chromatograms have been rescaled for clarity.

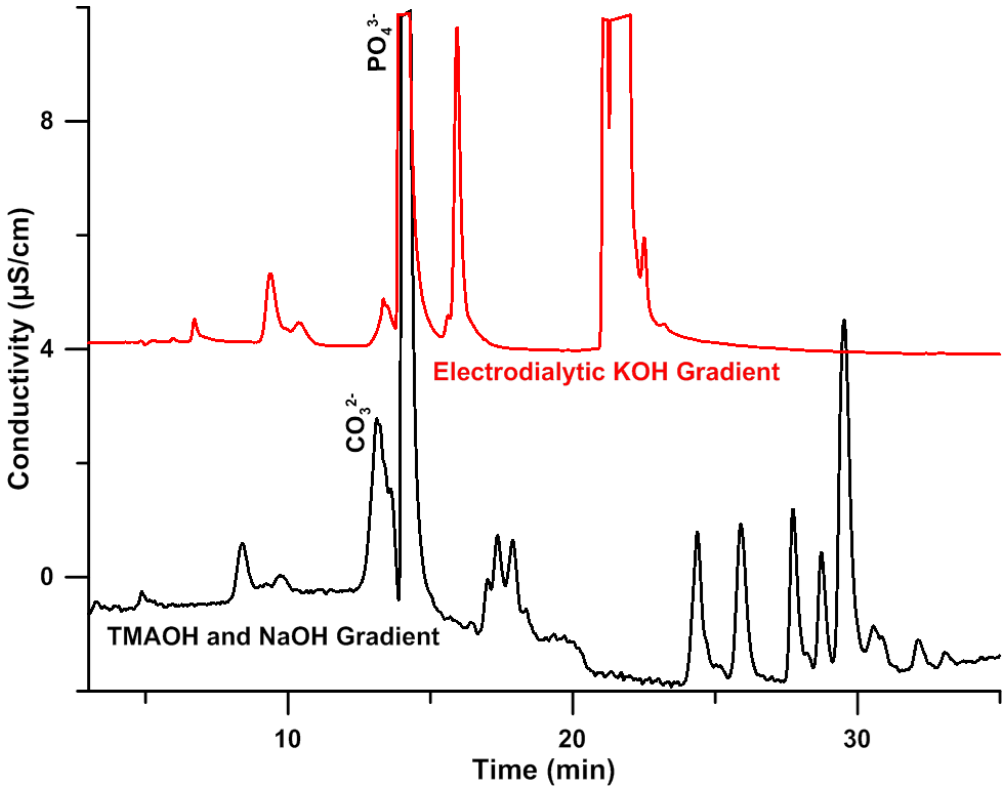

Figure D.10. Separation of 12 h phytate hydrolysate. The black traces is the TMAOH and NaOH gradient. The red trace is the same hydroxide based gradient but uses entirely KOH. The red trace has been deliberately delayed by 2.2 minutes to compensate for the volume associated with the gradient mixing chamber. The apparent later elution of $InsP_1$ in the red trace is an artifact of this.

Time, min	TMAOH, mM	NaOH, mM
0	6	0
7	6	0
7.5	35	0
14.5	35	0
15	65	0
23	35	30
30	0	65
33	0	65
33.5	6	0
40	6	0

Table D.2. Mixed Hydroxide Elution Program for AG/AS11HC Columns

Although it is not apparent from the conductometrically monitored chromatograms, selected ion monitored MS clearly show $InsP_3$'s elute in two regions. The first group (with at least 3 isomers) elutes with the $InsP_2$'s. Note that higher InsP's can be fragmented to lower ones during electrospray at higher voltages, we have carefully examined the effect of the electrospray voltage and used very low electrospray voltages to minimize this possibility. In any case, during electrospray InsP's can only degrade to a lower phosphorylated state and the earliest eluting $InsP_3$ elutes before any of the $InsP_2$'s (Fig. D9). The second $InsP_3$ group elutes only after NaOH is introduced as an eluent. $InsP_3$ has the largest number of structural isomers and spans the largest elution region (also with KOH, see Fig. D1). In the NMe_4OH-NaOH gradient however, the InP_3's eluting in the first group likely has 2 phosphate groups on one side of the inositol ring while the third is on the other and the eluophilic behavior of the latter is leading to equal or less retention than $InsP_2$'s. The remaining $InsP_3$'s do not elute with NMe_4OH up to the maximum concentration of 65 mM used and elute only after incorporation of Na^+ in the eluent.

The separation of $InsP_4$ – $InsP_6$ elute after $InsP_3$; $InsP_6$ eluting before any of the $InsP_4$'s or $InsP_5$'s indicating the eluophilic behavior of the largest number of phosphate groups that must remain unbound to the exchanger at a given time. Binding to the exchanger is tantamount to binding with a metal ion and the affinity of the free phosphate groups for complexation must be lower. $InsP_4$ and $InsP_5$ can respectively have 2-4 vs. 3-4 phosphate groups on a single face of the inositol ring, resulting in a narrower elution window for $InsP_5$'s. The NMe_4OH-NaOH gradient clearly provides better separation than a KOH gradient (Fig. D9 vs. Figs. D1 and D2). In Fig. D9, 18 peaks are distinguishable in 40 min compared 16 in 60 min using a KOH gradient. With selected ion MS detection and the NMe_4OH-NaOH gradient, the total number of detectable $InsP_{1\text{-}6}$ peaks are 3, 3, 6, 6, 3, 1, respectively accounting for 22 of the 40 possible separable isomers. It is possible to deconvolute the composite responses observed, assuming Gaussian peaks (phytate as a pure compound produces a nearly perfect Gaussian peak) and the maximum number of isomers possible. However, within each class $InsP_n$, the concentration of individual isomers may not be the same; it is possible that some of them are negligibly formed. (Figures D12-D16).

Cation chromatography is routinely conducted with chelating eluents where the analyte cation is complexed by the eluent anion. The obverse, where the eluent cation is complexed by the analyte anion is rarely used. Indeed, cation interaction is often ignored in anion exchange chromatography, but may play a critical role in improving separations of highly charged analytes.

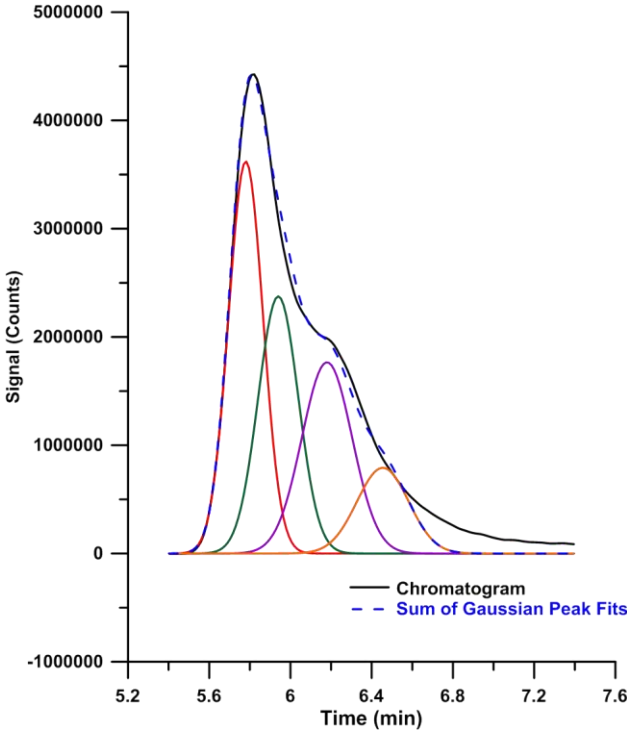

Figure D.12. Gaussian peak to $InsP_1$. 4 isomers are possible

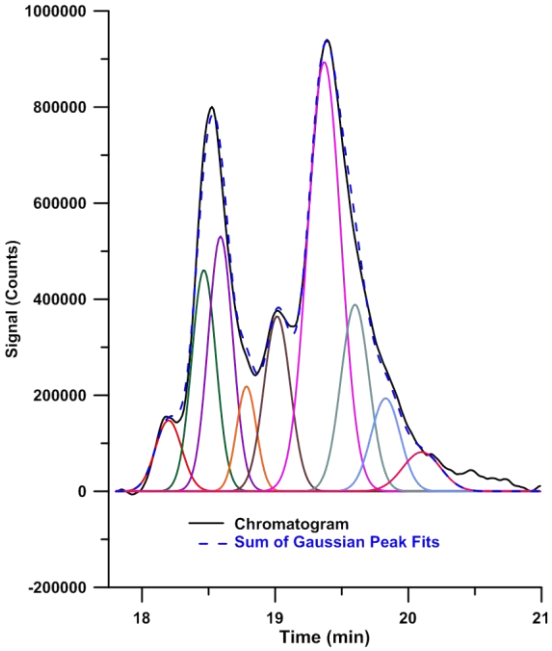

Figure D.13. Gaussian peak to $InsP_2$. 9 isomers are possible

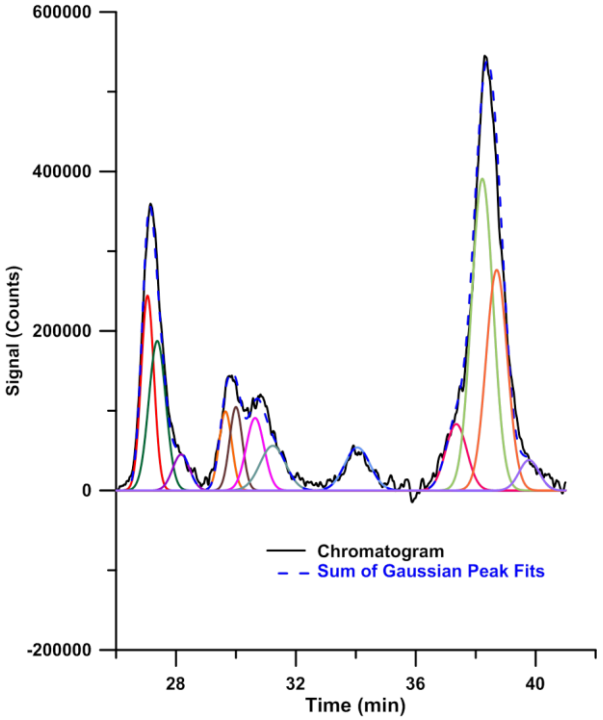

Figure D.14. Gaussian peak to $InsP_3$. 12 isomers are possible

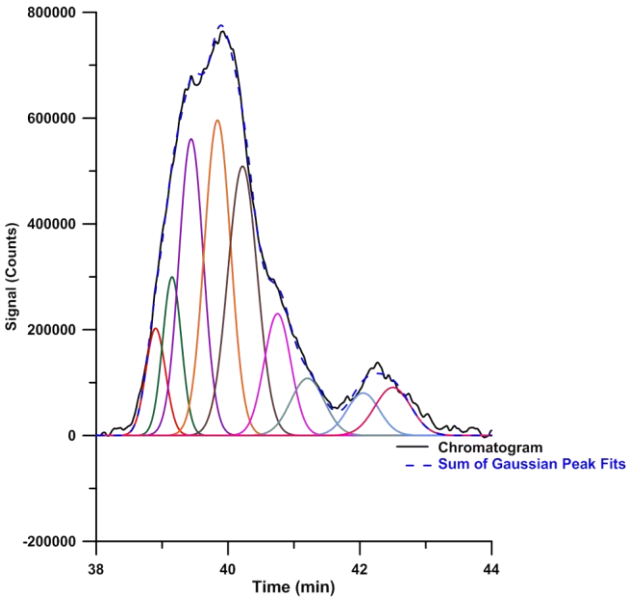

Figure D.15. Gaussian peak to $InsP_4$. 9 isomers are possible

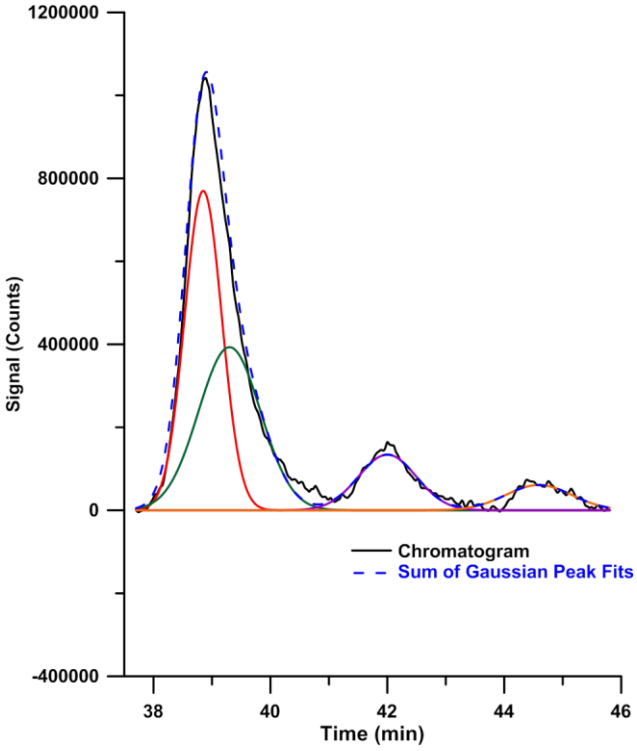

Figure D.16. Gaussian peak to $InsP_5$. 4 isomers are possible

ACKNOWLEDGMENT

We thank Christopher A. Pohl for valuable discussion. We thank an anonymous reviewer for the suggestion to explore the effect of Calcium. This research was supported by a grant from Thermo-Fisher Dionex.

My contribution was to provide data analysis support by de-convoluting the composite responses observed by assuming Gaussian peaks and the maximum number of isomers possible. Microsoft Excel Solver was used to fit a series of Gaussian curves to the MS traces. For each InsP SIM-MS trace, the maximum number (n) of geometric isomers was fit according to eq D4:

$$F_t = \sum_i^n \alpha_i \, e^{\frac{\left(t_i - t_{ri}\right)^2}{2\sigma_i^2}} \qquad \text{(D4)}$$

F_t is the sum total signal produced from each curve i at time t in the chromatogram. The constants α, σ, and t_r represent the peak height, width, and retention time respectively. Optimization of these parameters through Excel Solver was carried out using a least squares approach according to eq D5:

$$M = \sum_t \left(F_t - S_t\right)^2 \qquad \text{(D5)}$$

Where S_t is the background subtracted signal of the SIM trace at time t. The parameters α, σ, and t_r were iteratively adjusted to minimize M. It was necessary to constrain the peak width parameter σ to produce fits with widths no larger than the largest observable peak. Figures D12-D16 show the fits for $InsP_1$ – $InsP_5$.

Appendix E:

Concurrent High Sensitivity Conductometric Detection of Volatile Weak Acids in a Suppressed Anion Chromatography System

Hongzhu Liao, Akinde Florence Kadjo, Purnendu K. Dasgupta

Analytical Chemistry. **2015**, 87, 8342-8346

E.1 Introduction

Suppressed conductometric ion chromatography (SCIC) has become the benchmark technique for anion analysis. It cannot, however, measure weak (and especially very weak) acids. Karu et al.[179] have recently reviewed extant strategies to determine such analytes by modified SCIC approaches. In their view, the most promising approach is to introduce a base at a constant concentration to the SCIC effluent and measure the conductivity again. Eluting acids (HA) react with OH^- as follows: $HA + OH^- \rightarrow H_2O + A^-$; the replacement of highly conducting OH^- by lower mobility A^- results in all acid analytes with $pK_a<10$ showing up as negative peaks.[180] But mixing in a high conductivity base solution at a low flow rate to a principal flow steam requires a compromise between good mixing (to reduce baseline noise) and minimum band dispersion (that decreases peak height and deteriorates chromatographic resolution). The best case baseline noise with typical background conductivities (~25 μS/cm) is ~10 nS/cm.[181]

Among weak acid anions, sulfide and cyanide are of special interest. Both derive from the corresponding highly toxic volatile acids that play important roles in diverse areas ranging from biological cell signaling[182] to corrosion in petrochemical plants[183] to mine wastes[184] to wastewater treatment.[185] Hydrogen sulfide is known to be involved in a number of specific physiological processes; there is much interest in slow *in-vivo* H_2S-releasing pharmaceuticals.[186] A large number of fire mortalities stem from HCN inhalation; developments in cyanide determination methods have been recently reviewed.[187] There are numerous colorimetric methods for both these analytes; recent examples include nitroprusside-based determination of sulfide (limit of detection, LOD, 0.2 μM[188]) and cobinamide-based determination of cyanide (LOD 0.03 μM, 50 cm liquid core waveguide cell[189]).

While specific photometric approaches can be attractive with some sample types, interferences are possible and multiple analytes cannot be determined. Chromatographic separation and detection methods applicable to multiple analytes are therefore preferred. The dominant technique to measure sulfide and cyanide by IC has been pulsed amperometric detection (PAD): “sulfide or cyanide and pulsed amperometry”

produces ~1000 citation hits. While PAD is sensitive, and more robust and reproducible compared to standard amperometry, it requires special sample preparation steps: The most cited article on the topic[190] emphasizes the necessity of "deep deoxygenation of the sample for at least 10 min" to achieve optimum results. For insufficiently alkaline samples, volatile analyte losses can occur with such procedures.

In the present paper, we provide a robust conductometric approach that uses the previously utilized[2] principle of reacting HA with OH^- and measuring the signal that results from the difference in mobilities of A^- and OH^-. But there are important differences: (a) no liquid mixing: volatile analyte acids transfer into the base stream through a nonpolar membrane; this reduces baseline noise by two orders of magnitude and makes the technique selective to only sulfide, cyanide and carbonate; (b) the base receiver stream has a flow rate much lower than the donor chromatographic effluent stream, leading to analyte enrichment. Compared to previous conductometric techniques,[2,3] these attributes improve LODs by $\geq$ 100x.

E.2 Experimental Section

. An ICS-5000 ion chromatography (IC) system (one analytical scale and one capillary scale chromatograph), both configured for anion analysis (Figure E1, Figure E2 gives further details). Chromatography was carried out on 2x50/2x250 mm AG11HC/AS11HC guard/analytical columns using an electrogenerated KOH gradient (0.3 mL/min). The receptor LiOH flow rate was in the range of 10-100 μL/min to permit analyte enrichment. Volatile analyte loss through the membrane suppressor used (2 mm ERS-500) was examined in comparison with a 2x50 mm packed column suppressor (400 mesh H^+-form Dowex 50wX8 resin). Water was pumped by the capillary pump (10 -100 μL/min) through the LiOH generator to produce ~0.1-0.2 mM LiOH. This stream flowed through the central lumen of the volatile analyte transfer device (VATD) to a second conductivity detector (D2) while the effluent from the suppressed conductivity detector (D1) flowed through the outer, annular channel of the VATD, with the two flows being in the same direction (cocurrent). Three membrane devices were used. The first was a commercially

available capillary scale Carbon dioxide Removal device (cCRD). The holdup volumes in the inlet/outlet tees of this device, intended for a different application, is larger than the optimum for the present purpose. We therefore constructed and tested two other devices where these volumes are minimized; one with an effective membrane length (L_{eff}), smaller (5 cm, hereinafter VATD-5) than the cCRD (7.5 cm), the other being significantly greater (24 cm, hereinafter VATD-24). All three devices use the same type of membrane tube (courtesy ThermoFisher Dionex). The VATD design is similar to a previously described[3] tubular membrane mixer except for both inlet and outlet connections to the annulus. Detailed design and dimensions are in Figure E3).

Data collection (10 Hz) and analysis were performed using Chromeleon ver. 7.1; all above were from ThermoFisher Dionex. Standards were prepared with reagent grade chemicals.

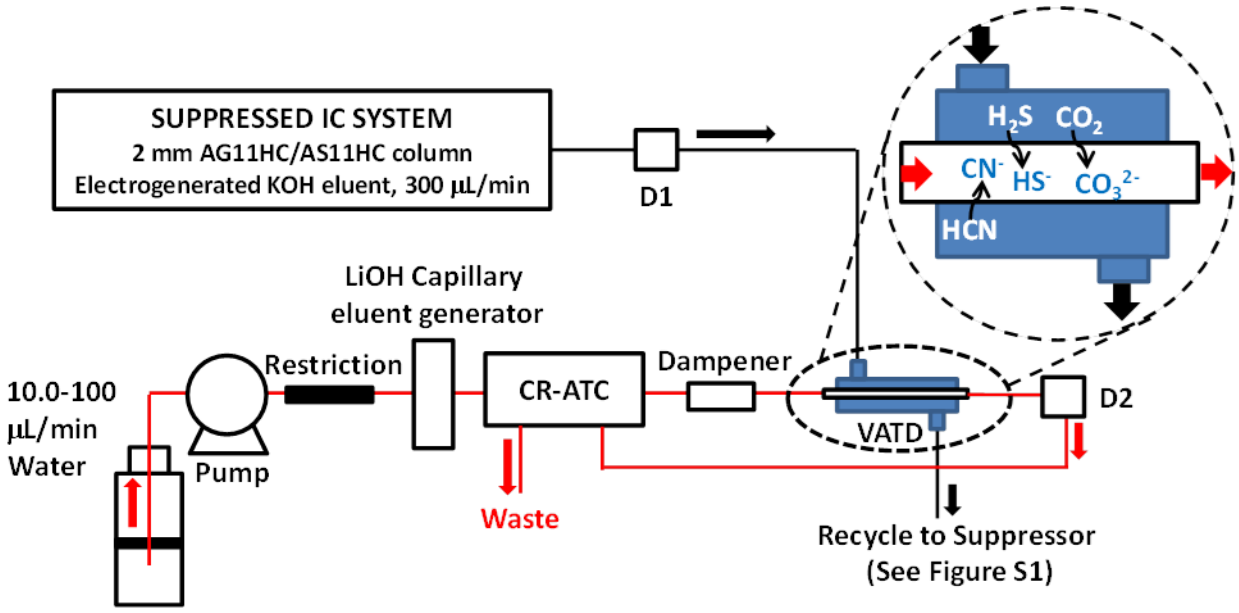

Figure E.1. The macroscale IC effluent flows through its detector D1 into the volatile analyte transfer device (VATD) to waste. Downstream of the capillary pump a restriction capillary (25 µm i.d.; 6.0-25.0 cm long depending on flow rate (100-10 µL/min)) is used to provide some backpressure for proper operation. To further reduce pump pulsations, a PEEK tubing (0.76x600 mm) is added after the capillary scale continuously regenerated impurity anion trap column (CR-ATC) that follows the LiOH generator.

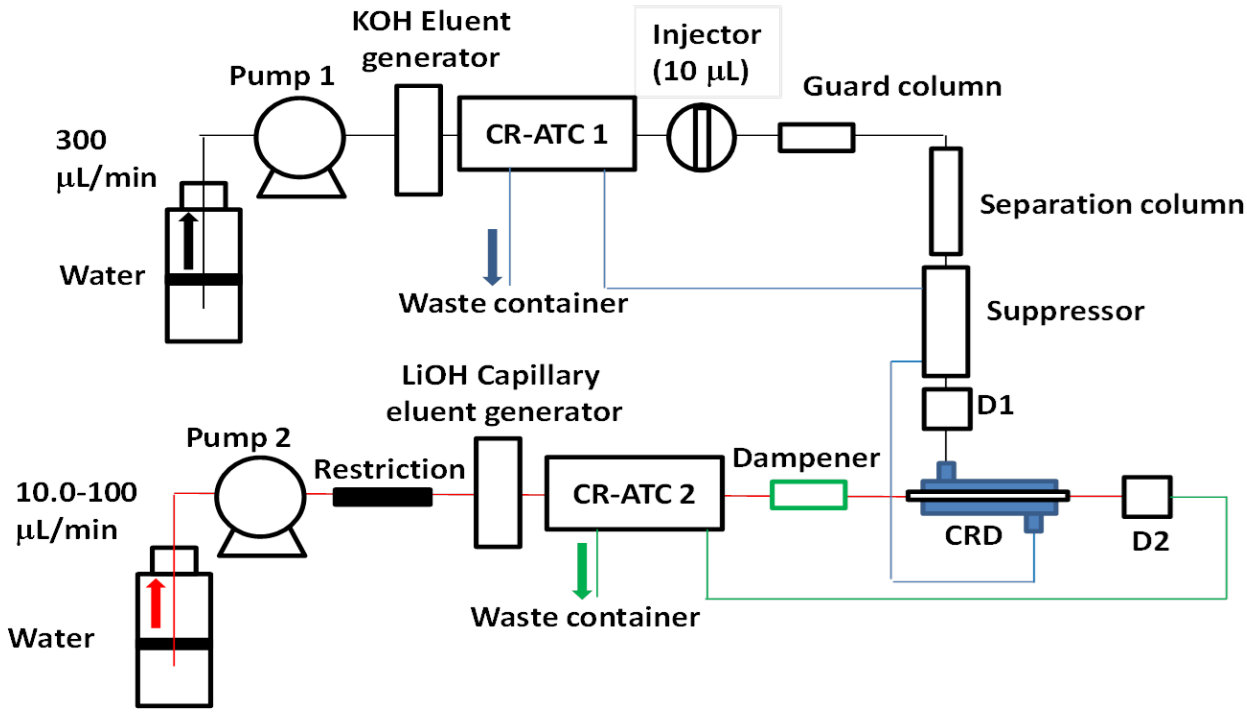

Figure E.2. Detailed experimental configuration. A restriction capillary (25 µm i.d.; 6.0-25.0 cm long depending on flow rate (100-10 µL/min)) is used before the capillary LiOH generator to provide some backpressure to Pump 2 for proper operation. To reduce pump pulsations, a PEEK tubing (0.76x600 mm) is added after the capillary scale continuously regenerated anion trap column (CR-ATC2). The similar macroscale device is labeled CR-ATC1.

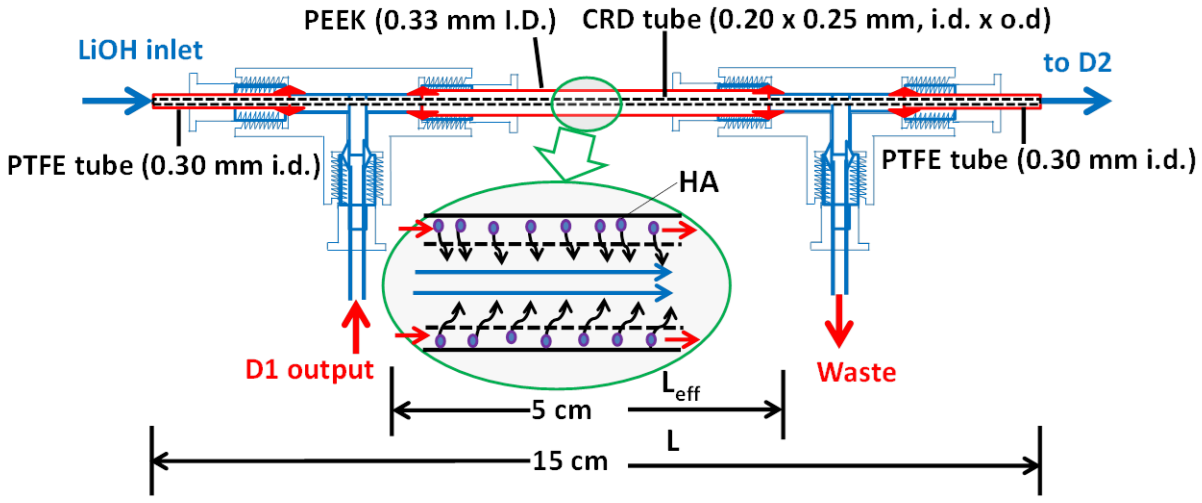

Figure E.3. The design of the in-house fabricated volatile acid transfer device (VATD). Compared to the capillary CRD, the annular space is smaller. The drawing is not to scale.

E.3 Results and Discussion

High Selectivity for Cyanide and Sulfide.

Figure E4 shows a gradient ion chromatogram containing 12 anions, including sulfide, cyanide and carbonate, anions derived from volatile weak acids. While sulfide and carbonate responds some in D1 because they ionize partially (pK_1 ~6-7), the response is poor and highly nonlinear, characteristic of a very weak acid. Cyanide is derived from an even weaker acid (pK 9.3) and cannot essentially be seen in D1. All three respond selectively and sensitively in D2, which responds only to undissociated volatile acids. At concentrations used in Fig. E4, formate, acetate, sulfite, etc. responds at the 5-10 nS/cm level, imperceptible in the ordinate scale of Fig. E4. The pK_a is simply not high enough for significant amount of the unionized acid to exist at levels of analytical interest, in addition the Henry's law solubilities (see below) are high.

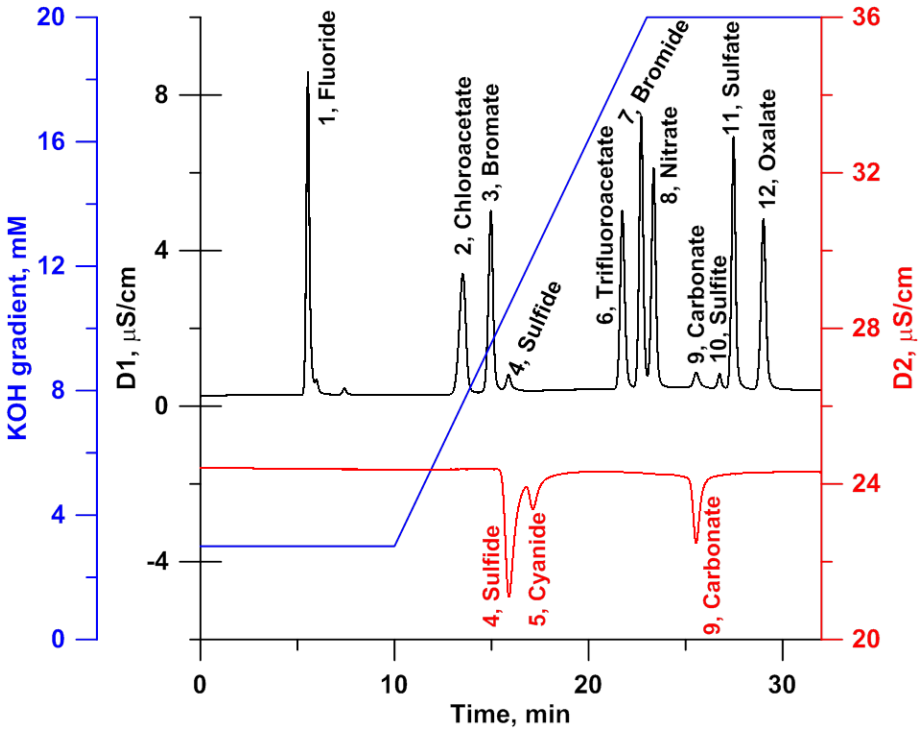

Figure E4. Illustrative application of VATD-5. Dual conductometric detection. 10 µL injection of 100 µeq/L for each ion; 0.1 mM LiOH flow. Carbonate results from CO_2 intrusion. Sulfite is an impurity in the sulfide standard used.

Strong acid analytes are fully ionized; D2 signal was neither expected nor observed. Overall the transport is proportional to $\alpha_0 C_x P/K_H$ where α_0 is the unionized fraction of the total concentration C_x, P is the permeability coefficient (product of solubility and the diffusivity of the analyte in the membrane), and K_H is the Henry's law constant for the gas. Since $pK_{a,HCN} >> pK_{a1,H2S}$, $\alpha_{0,HCN} \geq \alpha_{0,H2S}$ but HCN produces a significantly lower response; there is a great difference in the respective K_H values ($K_{H,HCN} \simeq 100\ K_{H,H2S}$)[191,192].

Volatile Acids. Extent of loss in Suppressors and Transfer in the VATD.

In much the same way a volatile analyte goes through the VATD membrane to the receptor, it can be lost through the suppressor membrane in the IC system. This has been exploited for example in removing CO_2 from carbonated drinks by passage through a Nafion tube prior to IC analysis.[193] The exact loss of volatile weak acids in membrane suppressors have never been quantitated but is of obvious interest in the present application. We measured this by using both (a) a packed column suppressor, and (b) the membrane suppressor. To the suppressor effluent a 100 μL/min stream of LiOH was added to reach a final concentration of ~0.2 mM (Figure E5). The difference in the area signal (a-b) then gives a direct indication of the loss through the suppressor (the peak area is immune to broadening differences in the two suppressors). Figures E6/E7 shows the extent of the loss for H_2S/HCN. In the 50-2000 μM injected analyte concentration range, ~10-25% of the H_2S is lost through the membrane suppressor. The pattern of the H_2S loss is unexpected: greater loss is observed at lower concentrations. The loss through the membrane is augmented by a zero order loss in the suppressor from oxidation. This is discussed in more detail in the supporting information (Figure E8). Over the same concentration range, HCN loss is relatively constant at 9.5-12%, with no discernible dependence on the injected concentration. The difference between HCN and H_2S in the extent of the loss is likely due to the greater intrinsic solubility (K_H) of molecular HCN.

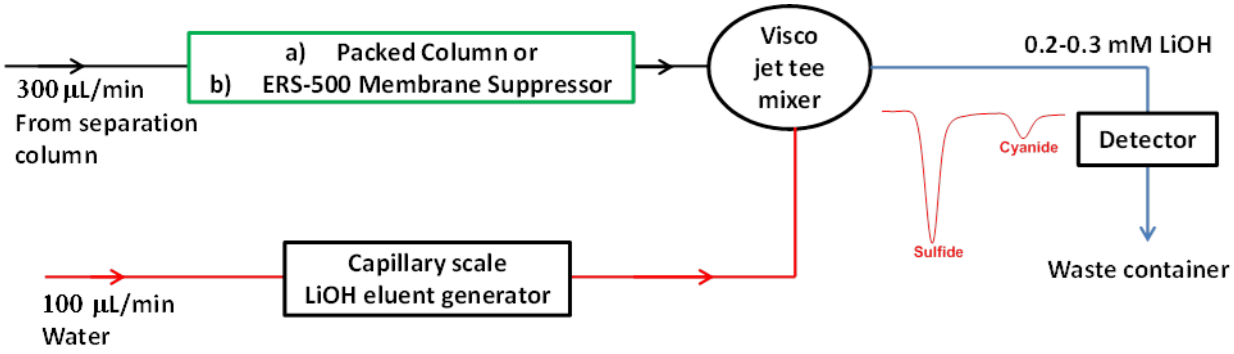

Figure E.5. Experimental configuration for measurements of loss of volatile acid analytes in membrane suppressor.

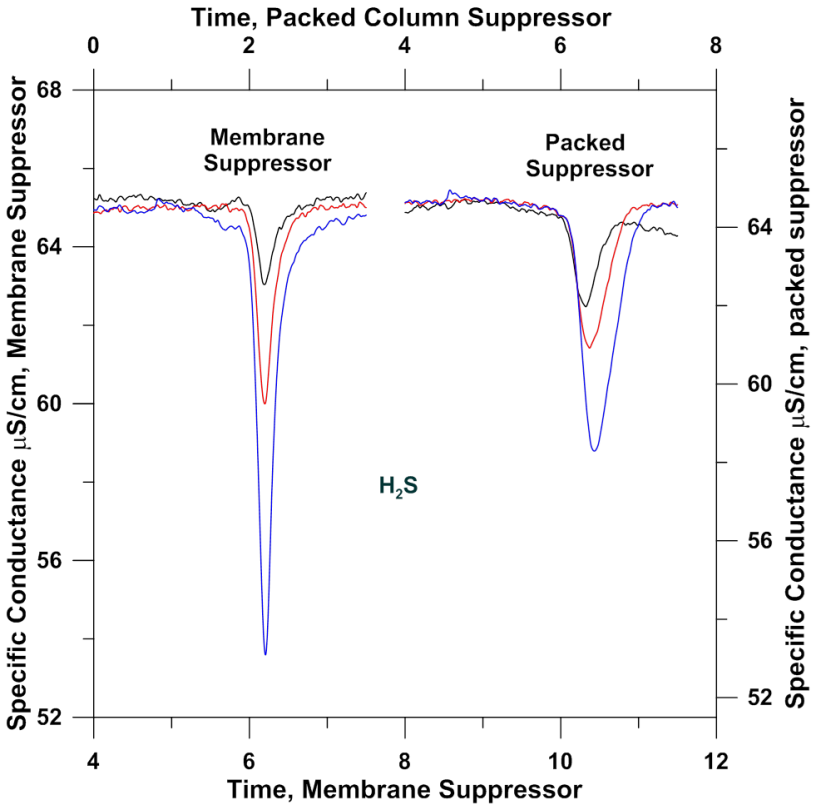

Figure E.6. Measurements of loss of H_2S in membrane suppressor. Blue traces, 2.00 mM H_2S; red traces, 1.00 mM H_2S, black traces, 0.50 mM H_2S.

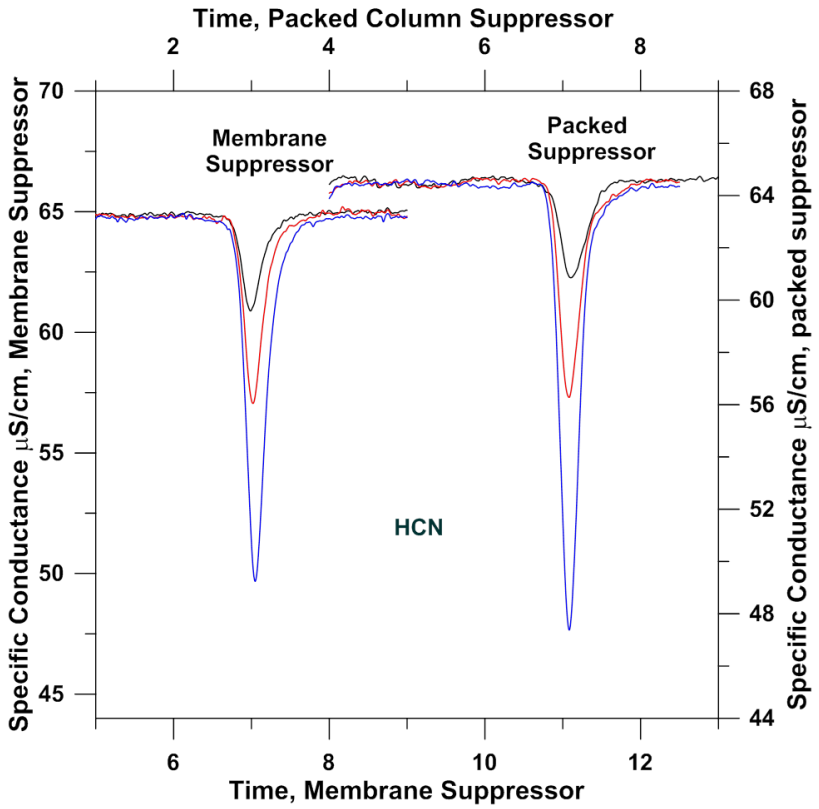

Figure E.7. Measurements of loss of HCN in membrane suppressor. Blue traces, 2.00 mM HCN; red traces, 1.00 mM HCN, black traces, 0.50 mM HCN.

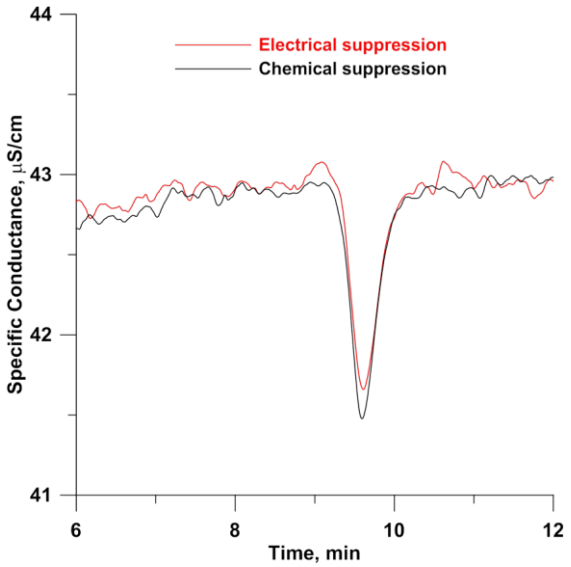

Figure E.8. Loss of sulfide due to redox reaction in electrodialytic membrane suppressor. Chromatographic response to 0.50 mM sulfide using VATD-5 device. KOH eluent isocratic concentration, 5.0 mM; receptor 0.2 mM LiOH @ 10 µL/min. The black and red traces were obtained with power to the suppressor turned on and off.

Once the loss in the suppressor is accounted for, the amount transferred to the receptor in a VATD can be determined from theoretical considerations from known ionic mobilities as outlined in the supporting information. In the analyte concentration range investigated, ~18/58% of the H_2S is transferred in VATD-5/24. In contrast, 7/33% of HCN is transferred in VATD-5/24. The actual responses appear in Figure E9. There is clearly considerable room for improvement here, especially for HCN. In principle the extent of transfer should increase if the absolute pressure on the donor side is increased, e.g., by putting a restriction tubing at the VATD jacket outlet within limits of pressure tolerance of the suppressor; this was not presently investigated.

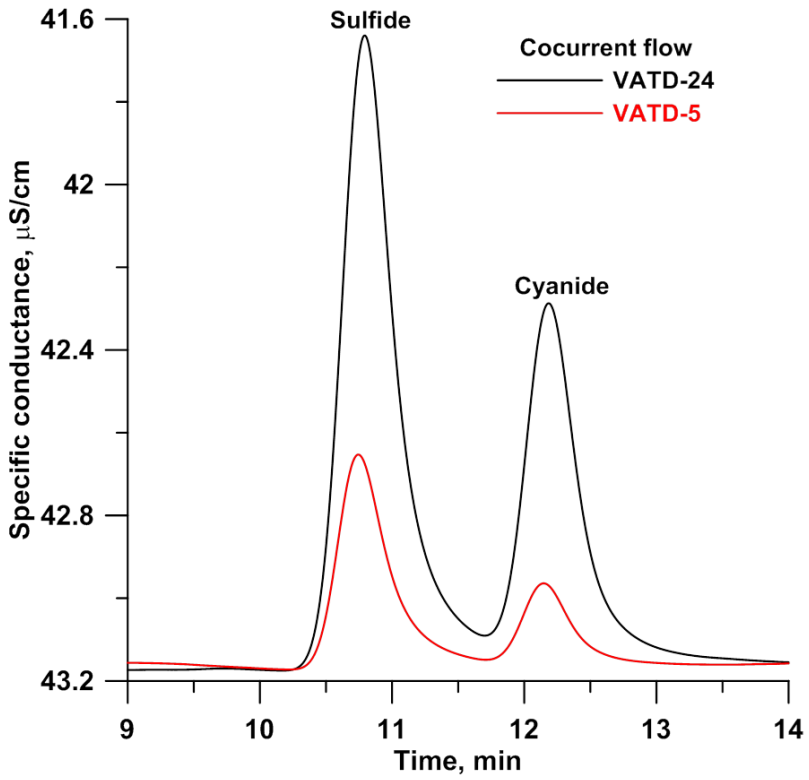

Figure E.9. Chromatograms of 50 µM of sulfide and cyanide using VATD-24 and VATD-5. KOH eluent isocratic concentration, 5.0 mM; LiOH concentration, 0.2 mM; LiOH flow rate, 40 µL/min. The peak resolution is 1.96 vs 2.11 for VATD-24 vs. VATD-5.

Cocurrent vs. Countercurrent Flow in the Transfer Device. Band Dispersion vs. Mass Transfer.

Typically the donor and receptor flows are countercurrent in membrane systems to maximize transport. For H_2S, without boundary layer stagnation, at the receptor (pH $\geq$10) undissociated H_2S concentration will be essentially zero. Thence its concentration gradient should solely be controlled by the donor concentration and its VATD residence time, the transfer extent should be flow-direction independent. For HCN (pK_a 9.3), however, with 0.1/0.2 mM LiOH, some 17/9% of the permeate will remain unionized (and any boundary layer stagnation will make this worse). In countercurrent flow a greater amount of fresh receiver is encountered; greater transfer is expected.

The results do indeed show that while the sulfide response does not change significantly between flow directions (peak area changes by ~5%, 0.767±0.008 vs. 0.731±0.006 area units), the cyanide response is discernibly higher (by ~15%, 0.453±0.007 vs. 0.391±0.024 area units) in countercurrent flow (Figure E10a).

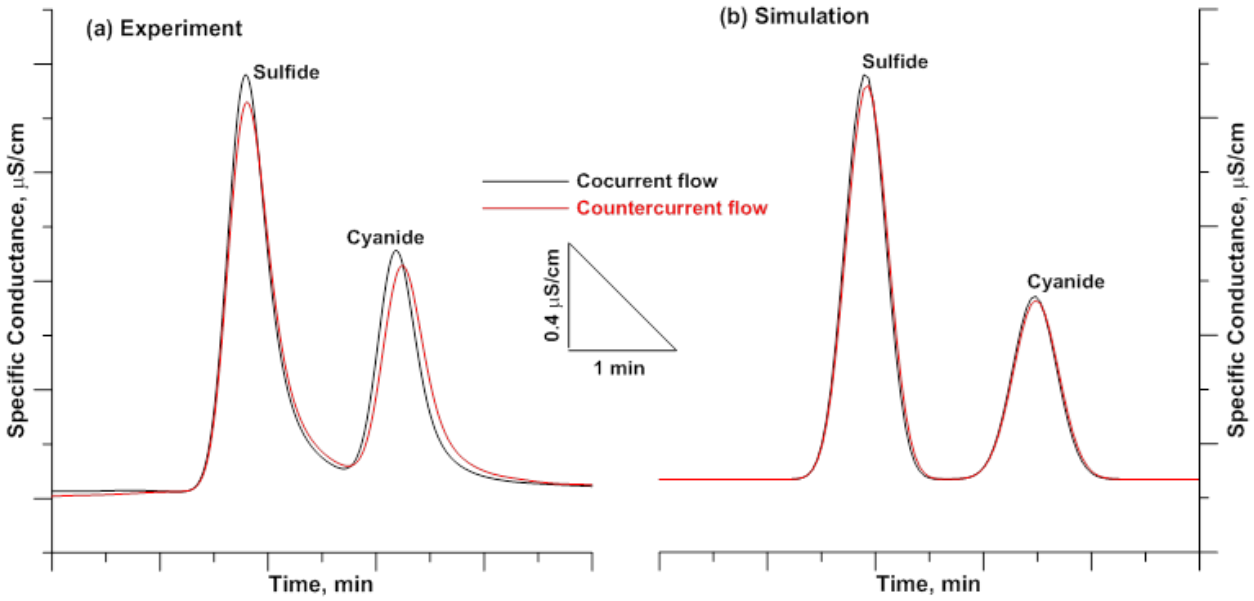

Figure E.10 (a) Experimental (b) Simulated comparison between cocurrent flow and countercurrent flow in VATD-24. Chromatograms of 50 µM sulfide and 50 µM cyanide. 5.0 mM KOH eluent @ 300 µL/min; VATD receptor 0.2 mM @ 40 µL/min.

It is intuitive that if the donor and receiver are moving in opposite directions, the permeated analyte band will spread across a greater volume. The sulfide-cyanide resolution in Figure E10a is 1.87 in countercurrent flow vs. 1.96 in cocurrent flow. While with cyanide, there is gain in mass transport with countercurrent flow, the peak height increase is marginal. The increase in transport is offset by added dispersion and thence poorer resolution makes accurate quantitation at low levels increasingly difficult. Cocurrent flow was henceforth used.

Mass Transfer as a Function of Device Length.

Let the fraction collected by the VATD be denoted by *f*. Much like transmitted light, the transmitted fraction 1-*f* is expected to follow an exponential pattern and hence be expressible as

$$1-f = \exp(-aL) \quad \ldots(E1)$$

where *a* is the extinction coefficient and L is the length. For L = 24 cm, f = 0.579 and 0.329, respectively for H_2S an HCN, the respective *a* values are computed to be 0.0360 and 0.0166 cm^{-1} for H_2S and HCN, respectively, a_{H2S}/a_{HCN} being 2.17. Predictions for *f* using L = 5 cm using these α values predict removal efficiencies of 0.165 and 0.080 in for H_2S and HCN in reasonable agreement with observed values of 0.185 and 0.074. Although empirical, if *f* is known for a certain membrane length, the results suggest that reasonable estimates can be obtained for other lengths. Given comparable permeabilities, the *a* values should be related to K_H; the relevant mass transfer equations[26,27] suggest a_{H2S}/a_{HCN} should be related to log ($K_{H,HCN}$ /$K_{H,H2S}$). The latter has a value of ~2 and the theoretical expectations are met. A first principles approach to estimating collection efficiencies is also possible and is discussed in the Supporting Information.

Effect of Receptor Flow Rates. Dispersion will be minimum when both the donor and receiver are moving cocurrent isokinetically and the characteristic transmembrane transfer time is small relative to VATD residence time. For VATD-5/24, the annular/central volume ratio is 1.16:1; best dispersion and resolution is expected at this flow ratio.

However, a larger donor:receptor flow ratio (DFR) greatly improves the signal and hence the LOD (Figure E11). The amount of analyte transferred is independent of receptor flow rate in the range studied as indicated by the constancy of the peak area if the abscissa is expressed in volume units, also suggesting there is no lack of LiOH due to boundary layer stagnation. While peak resolution decreases some with decreasing receptor flow rate, a flow rate of 40 µL/min (DFR 7.5) still provides baseline resolution of sulfide and cyanide.

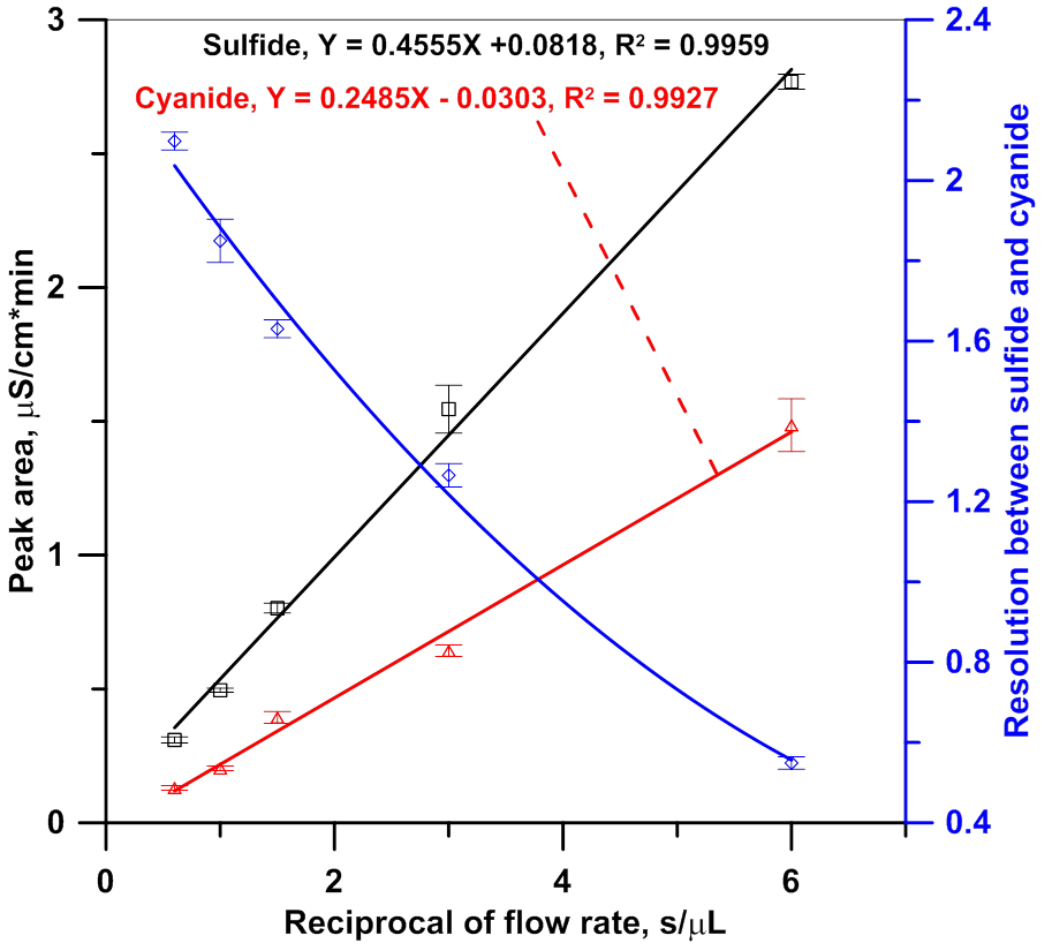

Figure E.11. Chromatographic conditions, separation of 50µM of sulfide and cyanide using VATD-24 device. KOH eluent isocratic concentration, 5.0 mM; LiOH concentration, 0.2 mM; LiOH flow rate varied from 10 to 100 µL/min. (b) Relationship between peak area and peak resolution of chromatograms as a function of LiOH receptor flow (±1 SD error bars are shown, n=3). Black trace, peak area of sulfide; Red trace, peak area of cyanide; Blue trace, resolution between sulfide and cyanide.

Simulation of Cocurrent and Countercurrent Transport. Spreadsheet software (e.g., MS Excel™) not only allows numerical simulation of the transport process and numerous other parametric effects, e,g., the length of the device, residence time, the effects of flow direction, etc. it can also provide pedagogically valuable quantitative understanding of such processes as well as predictive capabilities that allow for *in-silico* experiments.[194] Referring to Figure E12 as an illustrative example in cells A1:B22 we depict the HCN (approx. A1:A11) and H_2S (approx. B12:B22) bands exiting the suppressed detector, with 4 bit blue and red color gradation to indicate concentration magnitude. In reality both are of course present in the same flowing column (say B) but we distinguish between the separate chemical entities by putting them in separate columns. Similarly on the receiver side we designate column C for HCN and Column D for H_2S, although both are present in reality in the same column. A 20-row long membrane is present, indicated by the heavy line running between columns B and C, rows 22 through 41. The simulation begins by (a) transferring a fixed fraction (say 10% for H_2S and 5% for HCN) of the concentration difference in each row across the membrane and (b) then transferring contents of both columns B and C down one row and repeating the process. This process is repeated until the input bands are out of the system. The subsequent panels in Figure E12 depicts the progression of this process.

The full simulation (see Supporting Information) differs from the illustrative simulation above in that it uses conditions from the real system: (a) the input band width for H_2S is estimated from the small but finite first detector signal and that for HCN is estimated from the known retention time difference between sulfide and cyanide and assuming the same efficiency as sulfide; (b) the simulation for the 24 cm membrane is assumed to span a 60-row length; this means that the donor and receptor (B and C) cell volumes are ~0.15 and ~0.13 μL, respectively; (c) the DFR being >1, during each iteration step the donor column moves a larger number of steps than the receptor: for donor:receptor flows of 300 and 40 μL/min, respectively the donor moves down 51 rows while the receptor moves down/up (cocurrent vs. countercurrent) 8 rows, the step duration representing 0.0251 min; (d) while sulfide is essentially completely ionized, for the [HCN] gradient, the computation takes into account that ~91% ionization will occur in

0.2 mM LiOH; (e) The fraction transferred values are adjusted so simulated transferred peak areas correspond to that observed; and (f) axial diffusive redistribution is applied to the receptor cells (a fixed fraction of the concentration difference is redistributed in the cell above and below) to simulate axial dispersion. Figure E13 shows the simulation vs. experimental data for the sulfide cyanide separation. Further detailed discussion is in the SI and Figures E10 compares simulation vs. experimental results for the cocurrent vs. countercurrent case.

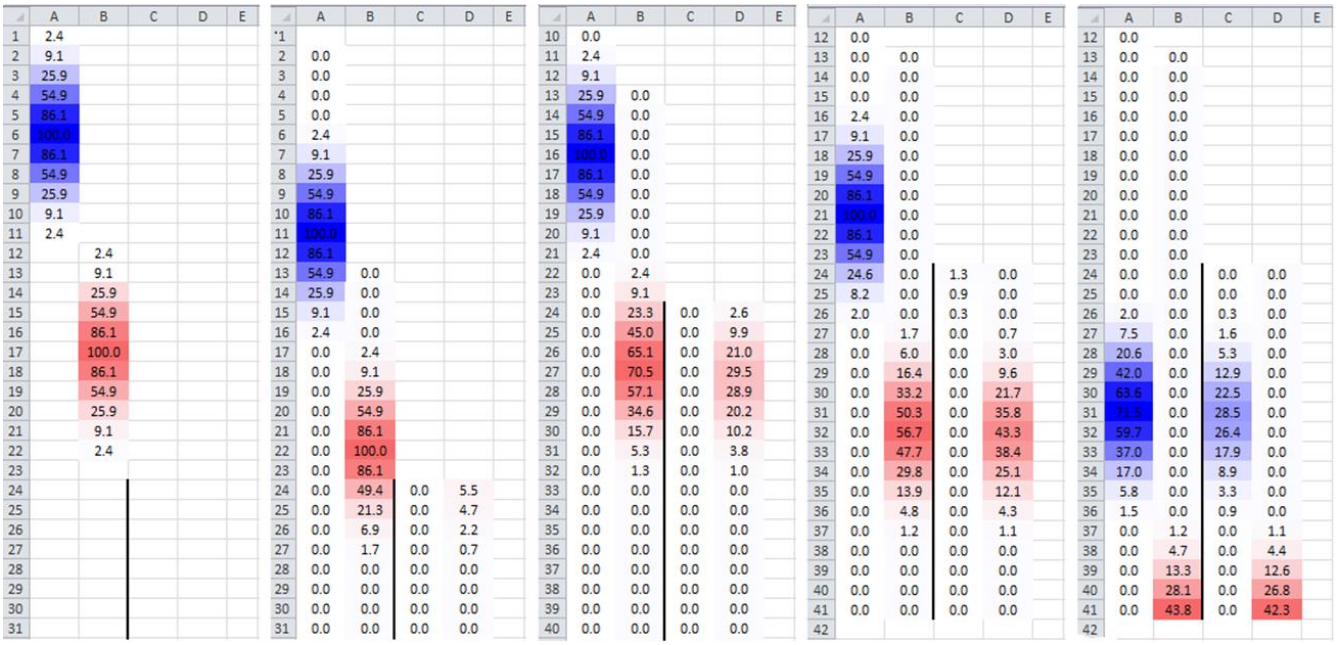

Figure E.12. Screen output for Excel Simulation A, B: donor columns for HCN, H_2S; C, D: receiver columns for HCN, H_2S; heavy solid line represents membrane. The panels depict snapshots after 0, 5, 10, 15, 20, and 25 iterations. See text for details.

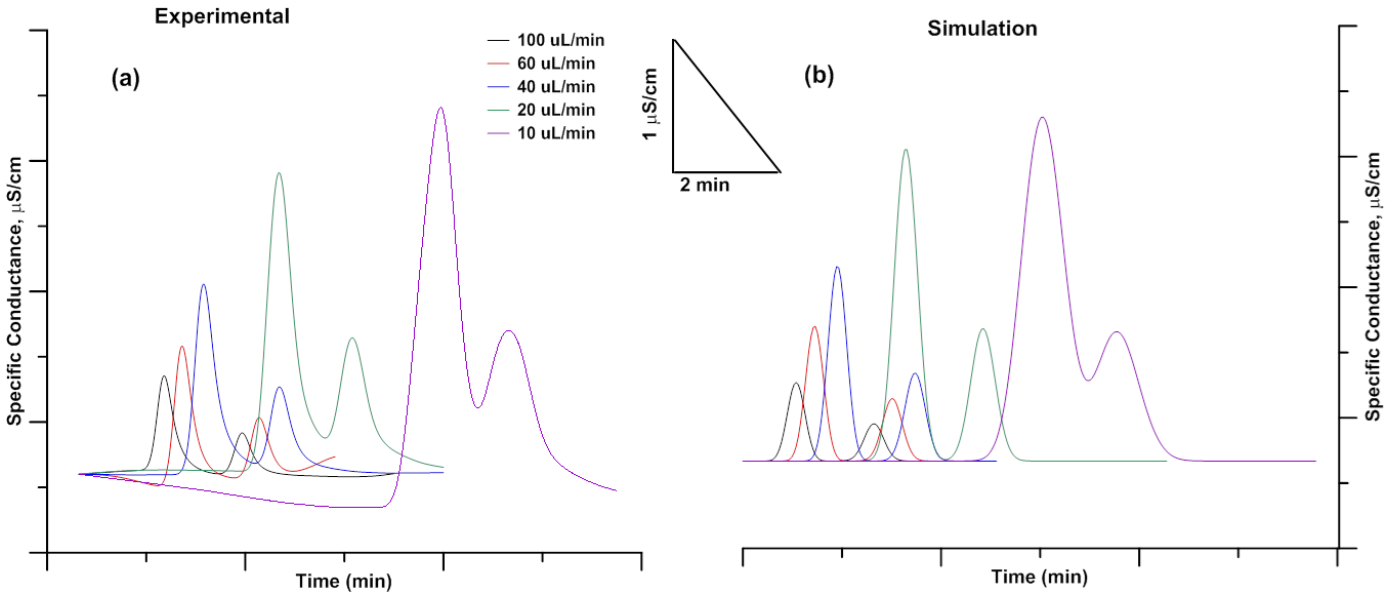

Figure E.13. (a) Experimental (b) Simulated response of 50 µM each sulfide and cyanide in VATD-24 eluent flow 300 µL/min, 0.2 mM LiOH VATD receptor @ 10-100 µL/min. See Figure 4 for other conditions.

Performance of Different Devices. The performances of VATD-5, the cCRD (inlet and outlet fittings were replaced with two 0.50 mm bore 10-32 threaded PEEK tees) and a 2 mm CRD were compared under chromatographic conditions. The results (Figure E14) indicate that the 2 mm CRD still exhibits too much dispersion to be attractive. The VATD-5 exhibits the least dispersion albeit the cCRD provides marginally higher signal for HCN.

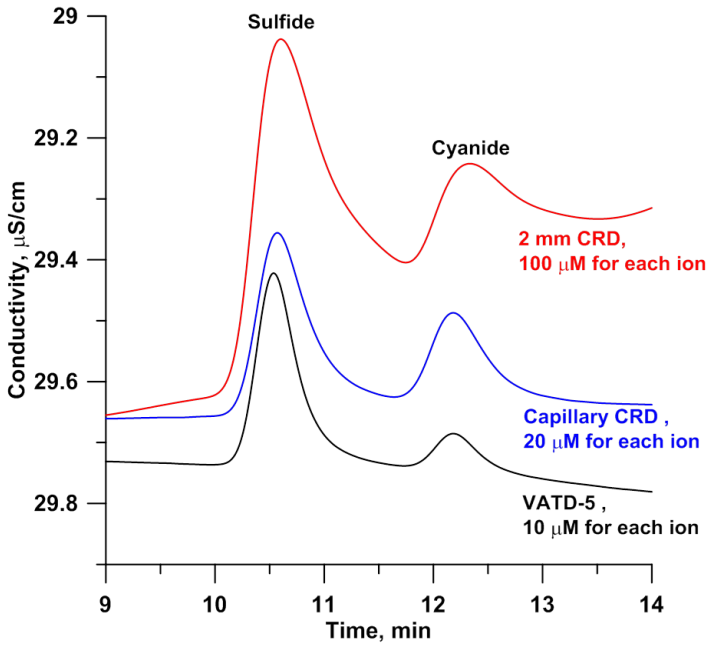

Figure E.14. Comparison of VATD-5, 2 mm CRD, and capillary CRD under chromatographic conditions. KOH eluent isocratic concentration, 5.0 mM; LiOH concentration, 0.1 mM; LiOH flow, 10 µL/min for VATD-5 and capillary CRD, and 100 µL/min for 2 mm CRD. The y axis is descending.

Both the VATD-5 and the cCRD were tested with a series of concentrations of sulfide and cyanide. The short term peak to peak noise level with 0.1 mM LiOH background was <0.1 nS/cm, comparable to the suppressed detector (D1) noise levels. Note that the base cation (Li^+) plays no role in the detection process but only contributes to the baseline conductance. For this reason, we use LiOH rather than KOH as the base, Li^+ has half the mobility of K^+. At 500 nM concentration, sulfide elicited a D2 response with an S/N >100 (Figure E15). However, at 100 nM (the LOD is estimated to be somewhat lower), the area response is much less than $1/5^{th}$ of this. The principal reason is the oxidative loss of sulfide in the system some of which seems to proceed on a zero order basis (see Figure E8). At sub-µM levels, some oxidative loss may also be occurring during standard preparation. The LOD for cyanide is ~50 nM on the same device.

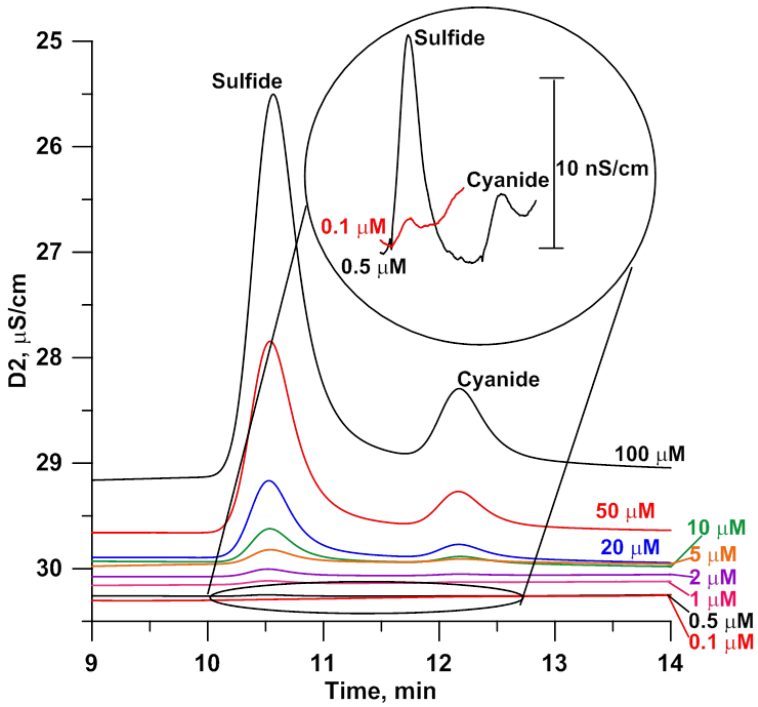

Figure E.15. Chromatograms of a series of concentrations of sulfide and cyanide using VATD-5. KOH eluent 5.0 mM @300 μL/min; VATD receptor 0.1 mM LiOH @ 10 μL/min

Calibration curves are shown in Figure E16. For both sulfide and cyanide, good linear relationships between concentration and D2 peak area were observed. The sensitivity of sulfide detection with VATD-5 is 1.5-2 orders of magnitude more sensitive due both to the enrichment in the VATD from the high donor/receptor flow ratio as well the difference in the degree of ionization in D1 vs. D2 (~11% and ~100%).

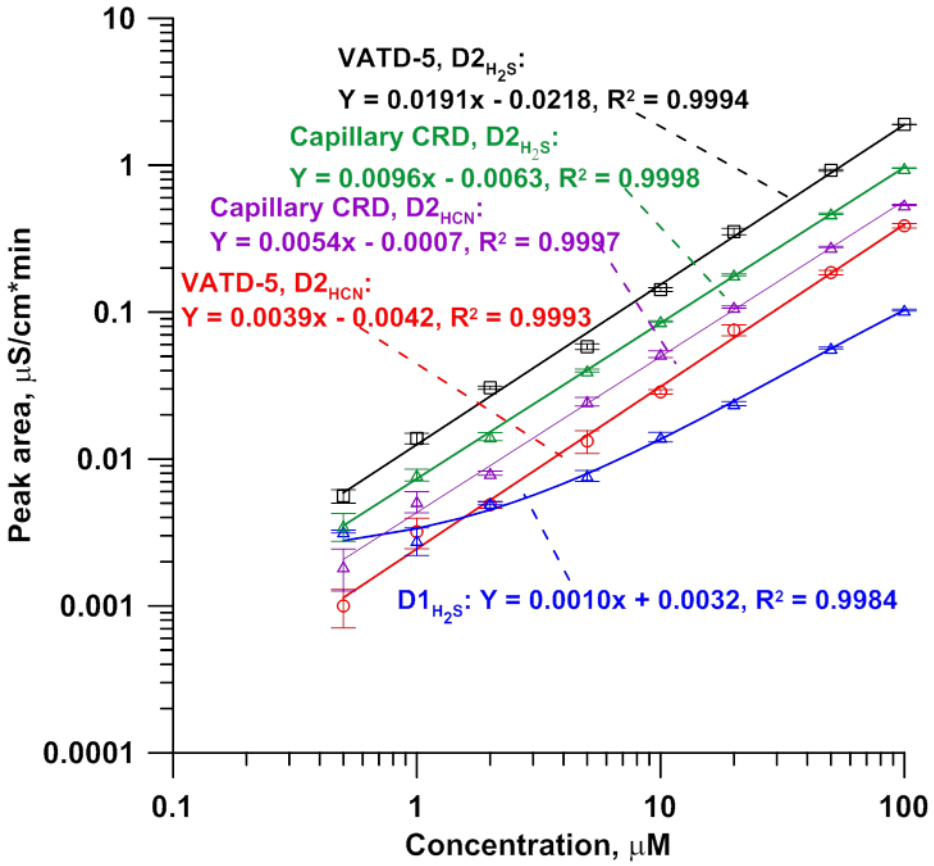

Figure E.16. Calibration curves of sulfide and cyanide using VATD-5 and Capillary CRD. Quadruplicate measurements; ±1 SD error bars are shown. KOH eluent concentration, 5.0 mM; LiOH concentration 0.1 mM @10 µL/min.

E.4 Conclusions

The VATD is a robust low-noise device permitting highly sensitive, wide dynamic range conductometric detection of volatile weak acids like cyanide and sulfide, without the maintenance requirements of amperometric detection systems. The principle should be extendable to volatile weak base analytes such as amines in a cation chromatography system with an acid receptor; this application area spans a greater range of analytes. Operation at an elevated temperature and increased backpressure on the VATD is expected to improve transfer efficiency and limits of detection for all analytes. Concentration through favorable donor/receptor flow rate ratios have generally not been practiced as a postcolumn detection enhancement; with the advent of electrodialytic ion isolators,[195]

there are further avenues of general enhancement of detection sensitivities. The speciation of metallocyanides is normally quite difficult. If these are separated with a saline eluent (Na_2SO_4), suppression will produce an acid environment for the liberation of HCN from acid dissociable cyanides and the more stable ones can also be similarly determined postcolumn after passage through a UV reactor that may do double duty as the VATD: a UV transparent tubing, e.g., FEP-Teflon® or quartz tubing can be used as the jacket with the device is coiled around a pen-lamp type UV emitter.

Appendix F:

Sampling frequency, response times and embedded signal filtration in fast, high efficiency liquid chromatography: A tutorial

M. Farooq Wahab, Purnendu K. Dasgupta, Akinde F. Kadjo, Daniel W. Armstrong

Analytica Chimica Acta. **2016**, 907, 31-44

F.1 Introduction

The goal in analytical chromatography is to obtain baseline separations with maximum peak capacities per unit time without sacrificing detection sensitivities (and hence detection limits) and reproducibility. While the last parameter is largely governed by the fluid handling system, all the foregoing benefit from better chromatographic efficiencies. Achieving high efficiencies may be dependent on the column technology but actually visualizing this is also demanding of the detection and the data acquisition system. Efficient columns generally require smaller sample volumes. Ever smaller analyte amounts passing through the detector at ever faster flow rates creates a challenge for the detection system as well.

In the context of HPLC, the terms "fast", "ultrafast", etc. are yet undefined. However, a survey of the current literature suggests that both these terms imply sub-minute separation.[196,197,198,199] The efficiencies attainable by present separation media can only be realized if the rest of the system does not pose limitations. History suggests that the development of the rest of the instrumentation often lags behind advancements in column technology.[197-200,201] As early as the 1970s, Halàsz showed that while a baseline resolution of two components on a well-packed 5 μm silica column could be achieved in under 2 minutes, the existing HPLC hardware had to be modified to reduce extra-column effects.[200]

In the last two decades, rapid developments have taken place in liquid chromatography. Smaller particles have enabled faster analyses by allowing shorter column with the same efficiency as previous 25 cm benchmarks. The early 2000's saw a rapid increase in separation speed. For example, 7 analytes were separated in 24 s in reversed phase liquid chromatography,[202] whereas 8 anions were separated under 30 seconds on monoliths in the ion-pairing mode.[201] The performance bottleneck was often the detection technology. With present well-packed core-shell silica columns, reduced plate heights (h) ≤ 2 are becoming common, even in columns of 5 cm length.[198-203] Such separations are characterized by very narrow peak widths, very fast elution times and relatively low back-pressures. The core-shell morphology is often the preferred choice for HPLC/UHPLC instruments since it allows column efficiencies comparable to sub-2 μm fully

porous particles while permitting the use of conventional HPLCs and column hardware. Recently, enantiomeric separations were reported on 3-5 cm long columns packed with 2.7 μm core-shell bonded chiral selectors in 4-15 s (h = 1.6-2.0) on a modified state-of-the-art UHPLC.[198]

With high-speed separations and sub-2 h values, detector/data system parameters can significantly affect the observed results. Even today's state of the art high performance instruments can potentially limit the "true" performance of a chromatography column. In our experience as well as that of others,[204,205] even current generation instrumentation can contribute as much as 30-60% to peak variance for short narrow bore columns. Remedial focus is often on injection ports and connection tubings as these are easily changed. The influence of the choice of detector/data system parameters such as response time/time constant and data sampling/acquisition rate is often ignored. Few chromatographic publications discuss these and the chosen parameters are often not even stated despite the well-recognized importance of sampling frequencies and time constants in signal processing over the years (Table F1). However, there is no consensus on mathematical approaches and/or goals. Thus the focus of different individuals ranged from accurately rendering peak heights[206,207] or areas[208] to the minimum number of points needed to describe a Gaussian peak.[209]

Herein we focus on the nuances associated with detector settings, namely, the data sampling frequency, the so-called detector response time, and the effect of embedded filters using three illustrative current generation HPLC instruments. Real and simulated examples are shown and recommendations are made.

Data Sampling Suggestion	Comments	Ref
20 data points per peak	Suggestion as “generally accepted rule” for the smallest peak in the chromatogram	244
100 data points per peak	Moment analysis; 100 points/peak are suggested for accurate peak areas	206
$\frac{\sigma_G}{t_s} > \frac{n}{\pi}$; The ratio $\frac{\sigma_G}{t_s}$, determines the minimum number of sampling points	Fourier analysis; t_s is sampling interval (s), σ_G = standard deviation of the narrowest Gaussian peak, n is harmonic component of the Fourier series.	210
1 data point per σ_G	Uses Nyquist's criterion; Comments that 6-7 points are sufficient for describing a Gaussian function	211
10 data points across 2.355 σ_G	Provides a "good guideline" for fast peaks	241
8 data points across baseline width of a Gaussian $8\sigma_G$	No criterion provided	212
36 data points per peak	Approximation derived from the inverse relationship between standard deviation of the Gaussian function and its Fourier transform	209
14 data points per peak	Analysis based on allowed maximum error (0.001%) in the peak height	207
sampling frequency $= \frac{CQ\sqrt{N}}{4V_o(1+k)}$	C= no. of data points desired per peak, Q= volumetric flow rate, N = plates, V_o= void volume, k= retention factor	213
Real time oversampling (MHz) and data averaging	Shows the advantage of oversampling points into one recorded data and averaging to improve the signal to noise ratio	231
15 data points for a Gaussian peak	15 data points for < 0.1 % error in peak area; Simpson’s rule: 6 x base width	208
Data acquisition rate does not affect peak width	Shows an example of "hidden features" in the software causing peak distortion	233

Table F.1. Analysis of the suggestions given by various authors on the sampling frequency for chromatographic purposes

F.2 Theory

F.2.1 Sampling frequency

The overall observed variance of a chromatographic peak σ^2, calculated by the second statistical moment, is composed of the following contributions:

$$\sigma^2 = \sigma^2_{column} + \sigma^2_{injector} + \sigma^2_{tubing} + \sigma^2_{detector\ volume} + \sigma^2_{detector\ electronics} \quad \text{(F1)}$$

Equation (F1) assumes that the variances are independent of each other. Typically, the user has some control over the first three components and less commonly, one can occasionally choose a particular detection cell but not the detector electronics and or any embedded signal processing algorithm. The user is generally not even aware of the latter, even though the consequences of this can be profound. For example, detectors based on aerosol generation (light scattering, charge detection, etc.) used in HPLC have a limited linear dynamic range (LDR), the signal being less than linear at higher analyte concentrations. The firmware commonly applies a power function to the signal S and the output is S^y where $1 < y < 2$. This results effectively in a greater LDR and has the (un)intended consequence of making the chromatographic peaks to appear more efficient than they really are.[214,215,216] For the more commonly used optical absorbance detectors, the available choices in detector electronics typically allow a user to choose a particular data sampling rate (a.k.a. sampling frequency in Hz) and a response time or a time constant. The variance contributions from detector electronics can have a large impact on the peak (height, width and asymmetry) and retention time (see below).

All signal generation and acquisition is subject to the sampling theorem, which is known by various names. Whittaker first mathematically addressed the sampling theorem in 1915 for frequency band limited functions.[217] In 1926, Nyquist pointed out the importance of data sampling frequency but did not elucidate theory of the minimum sampling frequency. In 1933, Kotelnikov formally applied the theorem to communication engineering and Shannon investigated the sampling problem in detail in 1948. For an interesting history and citations to the original literature, the reader is referred to Luke.[218]

Shannon[219] states in "*Communication in the Presence of Noise*": "*If a function $y(t)$ contains no frequencies higher than f cycles per second (Hz) it is completely determined by giving its ordinates at a series of points spaced $\frac{1}{2f}$ seconds apart.*" This theorem is exact and not an approximation. This implies that if a signal is collected for a period t, $2ft$ points will completely describe the signal.

In the chromatographic context, the choice of a sampling frequency by an analyst then requires knowledge of the highest frequency component in a chromatogram that carries information (i.e., as opposed to noise), this will generally be associated with the narrowest peak in the chromatogram. As a first approximation, with present-day columns, most eluite peaks can be represented by a Gaussian function:

$$y(t) = \frac{1}{\sigma_t\sqrt{2\pi}} e^{-(\frac{t}{\sqrt{2}\sigma_t})^2} \quad \text{(F2)}$$

Where t is the time and σ_t is the standard deviation in time, the peak half width being given by $2\sqrt{2\ln 2}\,\sigma_t$ or $2.355\sigma_t$ and a peak efficiency of $(t_r/\sigma_t)^2$, where t_r is the retention time of the peak. The frequency components (f) in the Gaussian peak are given by the Fourier transform of the Gaussian, $H(f)$:[220]

$$H(f) = e^{-(\frac{t}{\sqrt{2}\sigma_f})^2} \quad \text{(F3)}$$

where the standard deviation of the Fourier transform in terms of frequency, σ_f, is given by:

$$\sigma_f = 1/(2\pi\sigma_t) \quad \text{(F4)}$$

The inverse relationship between standard deviation in the frequency domain σ_f and standard deviation in the time domain σ_t are both fundamental properties of Gaussian functions (see also Figure F1)[221]. *Undersampling* and *oversampling* then refers to sampling below or above the sampling frequency ($2f$) dictated by the Shannon theorem.

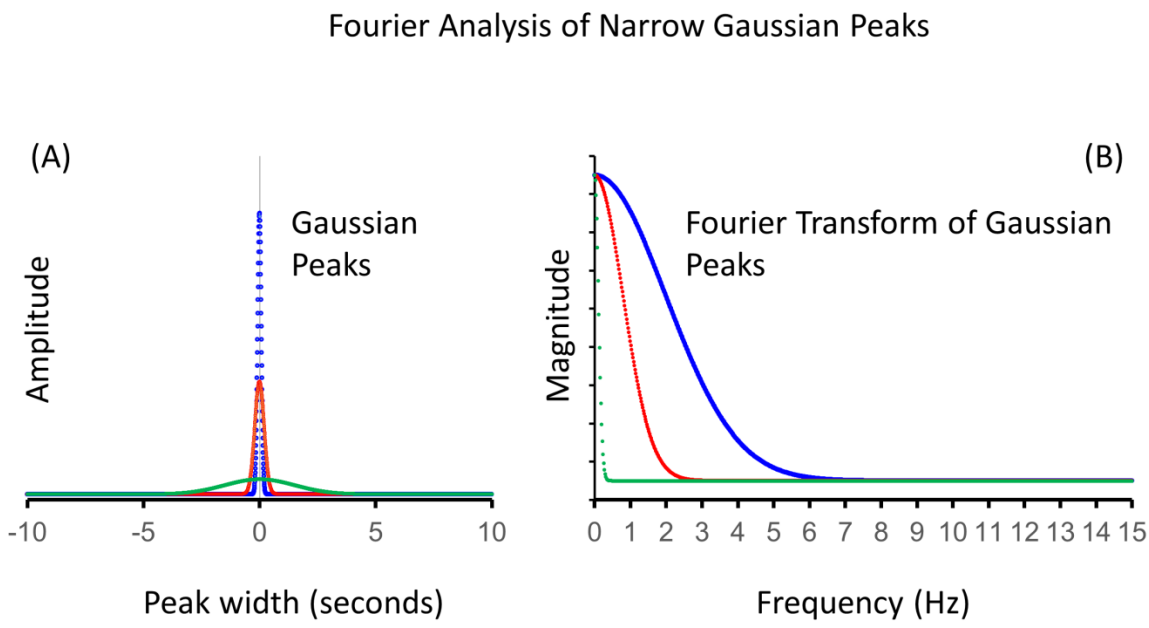

Figure F.1: Determination of frequency components in narrow Gaussian peaks by Fast Fourier transform (See experimental for the software details). (A) The Gaussian peaks are centered on zero for clarity. The standard deviations in time domain are as follows: blue =0.08 s, red =0.2 s and green 1.5 s. (B) FFT of the peaks in the frequency domain

F.2.2 Noise filtering by time constants and response times

The above discussion does not account for noise, present in any real signal. All present instruments seek to reduce the random noise, most commonly by digital filtering. Typically, the user can choose the time constant/response time from a list of available values; with some manufacturers, the choice of a response time results in automatic selection of a sampling frequency. When filtering is implemented in instrument firmware, it is relatively inflexible. When filtering is software implemented, it typically involves post processing and one has a choice of one or more filters, some common ones being Savitzky-Golay, moving average etc. (this feature of post-processing data is only available in few chromatography softwares). The specific digital filter implemented in firmware is rarely specified by a manufacturer. Volumes have been written on various types of filters and their designs. [222,223] Without knowing the nature of the specific filter present in the firmware, it is impossible to understand how a given system will respond to a step

function. The term *time constant* (τ) applies where an asymptotic approach to the final state is involved, as with a resistor-capacitor (RC) based filter or its equivalent; this *"e-folding time"* (the time it takes to reach 63.2% of the step function, $(1-\frac{1}{e}) = 0.632$, see Excel file in supporting information). "Time constant" has little or no meaning with other types of filtering. One major manufacturer for example uses a Hamming window filter to reduce noise,[224] whereas another uses a moving average filter (a.k.a boxcar filter/integrator) that includes a Gaussian weighting function.[225] It is rarely specified as to what a given manufacturer means by "response time" (a.k.a. the rise time), albeit the common interpretation is that it is the time required for the signal to rise from 10% to 90% in response to a upward step function. This is the ASTM definition[226] and we will use this definition of "response time" hereinafter. The exact output response will depend on the exact filter used, even if the 10-90% rise times are the same. Note also that some filters may be asymmetric; the 90-10% fall time observed with a downward step function may not be the same as the 10-90% rise time. For a RC type filter, the 10-90% rise time or 90-10% fall time equals 2.2 τ. Aside from the nature of the filter, there is the choice of sampling frequency. If a signal is severely undersampled, a faithful rendition is obviously impossible; gross oversampling with no changes in filter conditions on the other hand will lead to increased noise (see below). While we assume that a given detector hardware/firmware and the data system is faithfully recording the eluite profile exiting the column, it is actually so only if the sampling frequency and filter conditions are appropriate. As we illustrate below, the present practice of "fast" HPLC can certainly test the capabilities of the rest of the system.

As to noise, in any detection system, the fundamental root mean square (rms) noise limit is the shot noise given by the Schottky equation[227]

$$Shot\ noise\ (rms) = \sqrt{2Ie\Delta f} \qquad \text{(F5)}$$

where I is the photocurrent, e is the elementary charge on the electron, and Δf is the bandwidth. The response time is inversely proportional to the bandwidth.

$$t_{response} = \frac{constant}{\Delta f} \quad \text{(F6)}$$

The constant is typically between 0.3 - 0.5 and depends on the characteristics of the filter used. In chromatographic data acquisition, the lower bound of *f* is zero (DC) and the upper bound is dictated by the sampling frequency. If filtering does not bring in new noise sources, the rms noise increases with the square root of the sampling frequency. The Supporting Information provides simulation and brief explanation of three digital filters used by three different major manufacturers, namely, numerically simulated RC filter, boxcar averaging and Hamming window filter along with Excel sheets.

F.3 Materials and Methods

F.3.1 Simulations and Calculation Software

Simulations of chromatograms, RC low-pass and moving average filtering were performed in Microsoft Excel™ 2013; the Solver Add-in was often utilized.[228,229] Gaussian white noise[230] was added to the simulated chromatograms by using "Random Number Generation" function in Excel. Fast Fourier Transform (FFT) of Gaussian peaks and noise analysis was performed in OriginPro 2015 (Origin Lab Corporation, MA). For the Fourier analysis of the signal, the sampling interval and the raw response as a function of time seconds was used for FFT (Signal Analysis feature in OriginPro. The time data (simulated or real) were assumed to be in seconds. The FT output is depicted in the magnitude vs. frequency (Hz) format.

F.3.2 Chemicals

Uracil, phenol, and acetonitrile were purchased from Sigma-Aldrich (St. Louis, MO). Deionized water (18.2 MΩ) was produced by a Millipore Synergy 185 system (EMD, Billerica, MS, USA).

F.3.3 Instrumentation and Chromatographic Conditions

Brand names are not explicitly specified here, as it is not our purpose to exalt or impugn any particular instrument; however, detailed technical specifications for each instrument appear in the Supporting Information. All instruments were controlled and data acquired with the current generation of the manufacturer's software. We used three HPLC systems, all are current models. System 1 was a UHPLC system (manufacturer A, 120 MPa max), System 2 was a HPLC system (manufacturer A, 60 MPa max) and System 3 was a HPLC system (manufacturer B, 66 MPa max). All three instruments were equipped with diode array absorbance detectors recommended by the manufacturer for the particular instrument. Tubing and connections were minimized/optimized for the UHPLC as noted. Unless stated otherwise, injector-column and Column-detector connections were made with minimum possible lengths of 75 μm i.d. polyether ether ketone tubing using nanoViper fittings (Thermo Fisher Scientific) in chromatographic instruments. System 2, was used square wave experiments only (the software is same in the UHPLC and the HPLC). The third system was used as configured by the manufacturer.

All chromatographic experiments were conducted with a Poroshell-120 Column (120 EC-C18, 2.7 μm, 150x4.6 mm i.d., P/N 693975-902, Agilent Technologies. According to manufacturer certification, this particular column exhibited 38000 plates for their test chromatogram. We used isocratic elution with 80% acetonitrile and 20% water as eluent at a flow rate of at 1.8 mL/min (ΔP = ~36 MPa) for uracil and phenol at ambient temperature on system 1 and 3 (see supporting information for instrumental details).

F.3.4 Detector Response Time/Time Constant Experiments

Manufacturer A and B respectively refer to the choice of the response speed in their software as "response time" and "time constant". To test the effects of the choice of these parameters, we affixed a small surface mount red-orange (λ_{peak} 610 nm) light emitting diode (LED) on the light source side of the flow cell with tape and the cell was then

reinstalled in place. Lead wires soldered to the LED were connected to a function generator (5MHz, B&K Precision model 4011A) and driven by a square wave at 1.0 Hz.

F.4 Results and Discussion

For digital signals, the lower limit for sampling the signal is set by the sampling theorem, but there is no upper limit for the sampling frequency except as set by the capability of the analog to digital converters (ADC's)[231]. Such conversion capabilities presently extend to the several GHz range[232], clearly far beyond the needs of HPLC detection. We focus here mainly on the effect of detector settings chosen by the user (sampling frequency and response times) on present-day fast and narrow chromatographic peaks.

F.4.1 Revisiting the Sampling Frequency Concept

In Figure F1 we simulate three different chromatographic peaks of equal area but differing in peak widths (σ_t= 0.08, 0.2 and 1.5 s). A Fourier transform can identify what frequency components are present in such signals; this is also depicted in Figure F1. For the narrowest peak (σ_t = 0.08 s, half peak width $w_{0.5}$ = 120 ms), the FT is wide and conversely, the widest peak (σ_t = 1.5 s) has the narrowest frequency distribution, as predicted by the relation $\sigma_f = 1/(2\pi\sigma_t)$. Equation F4 thus provides the fundamental perspective why narrow peaks must be sampled at higher data collection rates.

Note that the Fourier transform of a Gaussian peak is also a Gaussian function;[221] the normally distributed amplitude in the frequency domain has its maximum amplitude at f = 0 (DC) and extends to $f = \infty$. It is readily estimated from standard distribution tables that 95%, 99%, and 99.9% of the information is then contained within f =1.64$_5$ σ_f, 2.33 σ_f, and 3.08 σ_f, or in terms of the half peak width, 0.62/ $w_{0.5}$, 0.87/$w_{0.5}$, and 1.15/$w_{0.5}$ (using the relation $w_{0.5} = 2.355\ \sigma_f$). An adequate sampling frequency (2f) for the different situations will range from 0.35 Hz for the widest peak while retaining 95% of the information content to

20 Hz for the narrowest peak with 99.9% information retention. The default sampling frequency seen in many instruments is 2.5 Hz, which is at least double the sampling frequency minimally needed to retain ≥95% of the information on peaks with half-width ≥ 1 s.

The above discussion clearly suggests a different conclusion compared to a recent publication that posits sampling frequency should not affect the signal and even when *undersampling,* the original chromatogram can be readily recovered.[233] This aside, the more important question is whether sampling at the minimally acceptable frequency according to the sampling theorem is adequate in the presence of noise. Noise is to be found in any real measurement and typically, the noise has components at higher frequencies than is present in the analytical signal. Data systems of course do not have any innate intelligence to distinguish noise from the signal, even when a particular incidence of spurious noise would be readily apparent to the user upon examination of the data. Consider a chromatographic peak recording which has had an incidence of a spike during the chromatogram due to whatever electromechanical reason or an errant bubble. Consider also that the spike occurred shortly before the peak apex and its magnitude was enough to put it above the peak apex. If the sampling frequency is high enough, the spike will readily appear for what it is, whereas in the case of an undersampled or just adequately sampled system, if the spike coincided with a sampled interval, this point would be considered the peak apex and both the perceived peak height and the retention time will be inaccurate. Granted that the some filters can circumvent this problem (the Olympic filter[234] for example removes the highest and lowest value within a chosen window), it is generally easier to distinguish the signal from noise as the sampling frequency is increased.

Now, let us consider a simulated chromatogram (Figure F2) with four high efficiency peaks (N = 13,000-15,000) with a total retention time < 1 min, realistically attainable on present-day short well-packed core-shell or sub-2 μm columns. The first peak at ~ 16 s represents a relatively weak signal, the second and third peaks are partially resolved, followed by a fourth peak at ~ 29 s. White Gaussian noise (mean zero, standard deviation 0.06 amplitude units) was added to the chromatogram. Panels A-D respectively depict the chromatograms as observed by sampling at 160, 40, 4, and 2.5 Hz, respectively, sampling

frequencies available in most present day HPLCs/UHPLCs. Note that the minimum sampling frequency for the widest ($w_{0.5}$ = 0.61 s) to the narrowest peak ($w_{0.5}$ = 0.31 s) would theoretically be 2-4 Hz for 95% accurate reproduction. Figures F2a and F2b thus represent oversampled chromatograms, F2c is just adequate according to the sampling theorem and F2d represents a sampling frequency that is nominally adequate for the widest peak but not for the narrowest. It is easy to see that in the last case, much of the information is lost or distorted, the first peak is nearly gone, resolution between peaks 2 and 3 is worse, and none of the peak apices is correctly registered. Undersampling compromises the peak height and areas. In contrast, by oversampling (160 Hz), the original signal is collected with high fidelity; no information is lost during the sampling process. However, Figure F2 makes it apparent that this is obtained at a cost of increased baseline noise.

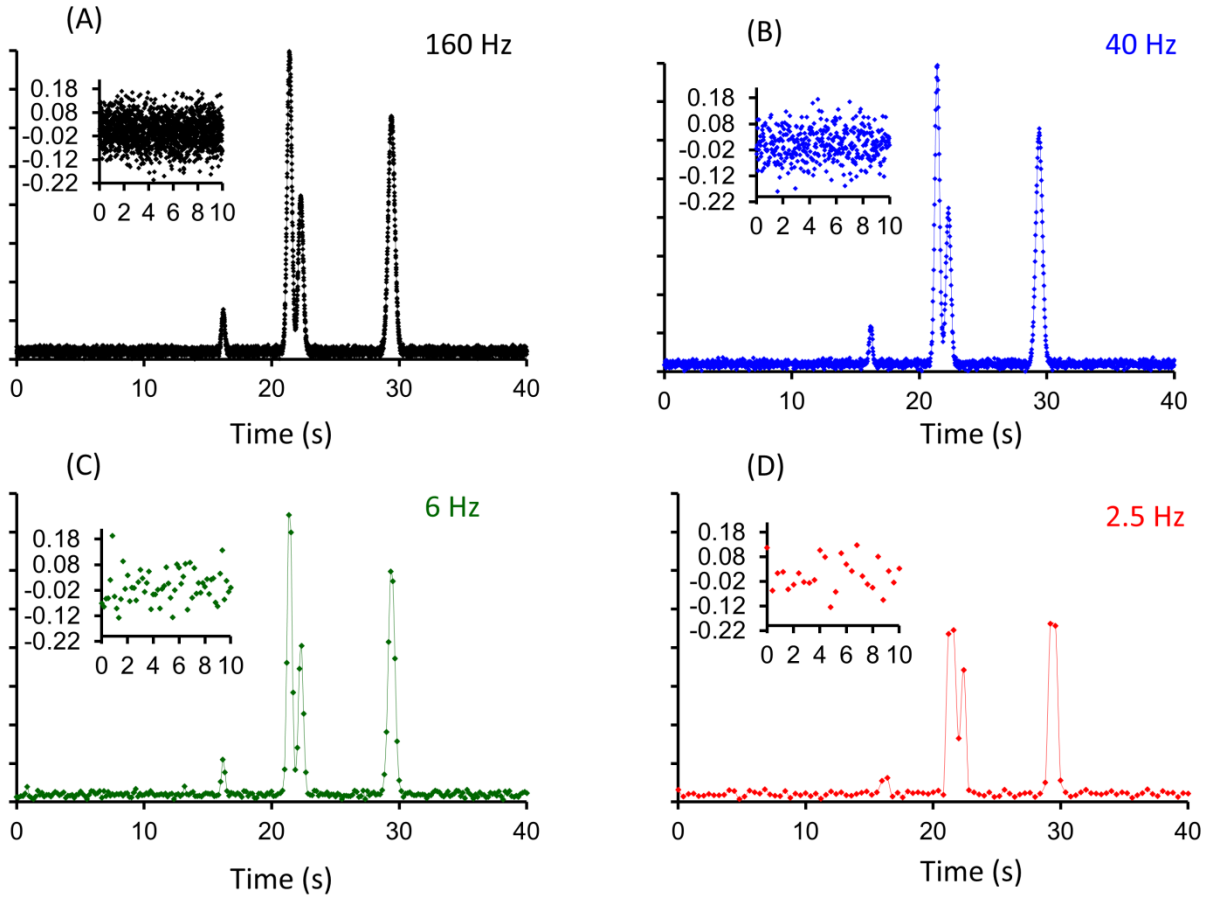

Figure F.2: Simulated ultrafast chromatogram showing the effect of sampling frequency (160, 40, 4 and 2.5 Hz) without any electronic effect on four peaks of different height, noise and resolution. White Gaussian noise has been added. The inset shows the noise level with sampling frequency. The efficiencies are set as follows for peak (1) 15,500, (2) 14,000 (3) 13,700, (4) 13,800 corresponding to standard deviations in the time domain σ_t of 0.13, 0.18, 0.19 and 0.25 s respectively.

The noise in the raw data is the same on the input signal in all four chromatograms. The inset in Figure F2 shows the local noise from 0 to 10 s. So what causes higher noise at the highest sampling frequency? This observation results from purely statistical reasons and the sampling theorem also predicts the same. The noise amplitude distribution is Gaussian, by increasing the sampling frequency; we increase the probability of picking the highest amplitude values. Statistics also suggests that had we considered a proportionately longer interval to consider the noise (such that the number of points in the evaluated window remains constant as a function of frequency), the noise would have been the same. Thus, an alternative perspective is that by lowering the sampling frequency, we exclude noise present at higher frequencies. However, the concept of *local noise* is important (this has been so invoked already in image processing[235]) because elution of a peak is a local event. The narrower the peak, the more localized it is in the time domain and more it is affected by *local noise*. The effect can be especially deleterious at low signal amplitudes and can clearly be seen for the first peak in the 160 Hz chromatogram. In an oversampled chromatogram, *assuming all electronic effects and data massaging are absent*, the lowest amplitude peaks are more likely to be affected by noise. At a sampling frequency of 40 Hz, the local noise level has decreased sufficiently that the earliest eluting peak is demarcated with less noise. At 4 Hz, the last peak height is lower compared to those obtained at higher sampling frequencies and at 2.5 Hz it is lower still. Figure F3 shows a magnified view of the first peak at different sampling frequencies. It is important to note that simulating sampling frequencies as represented here by picking every *n*th point from the raw data may not represent how the noise is affected by the sampling frequency choice in present data systems. This is a function of the nature of the ADC used (for a summary of principal types of ADCs see[236]). A Delta-Sigma ADC, the most common type used in data acquisition systems, intrinsically uses a fixed sampling frequency, the highest it is capable of. Rather

than picking every *n*th point, an *n*-fold lower requested rate results in integration/bunching of *n* data points with consequent lowering of the noise. Figure F3 also shows what the 40 Hz chromatogram is more likely to appear, where in a master 160 Hz data, every successive 4 point bunch has been averaged, resulting in a ~2-fold decreased noise compared to the original representation.

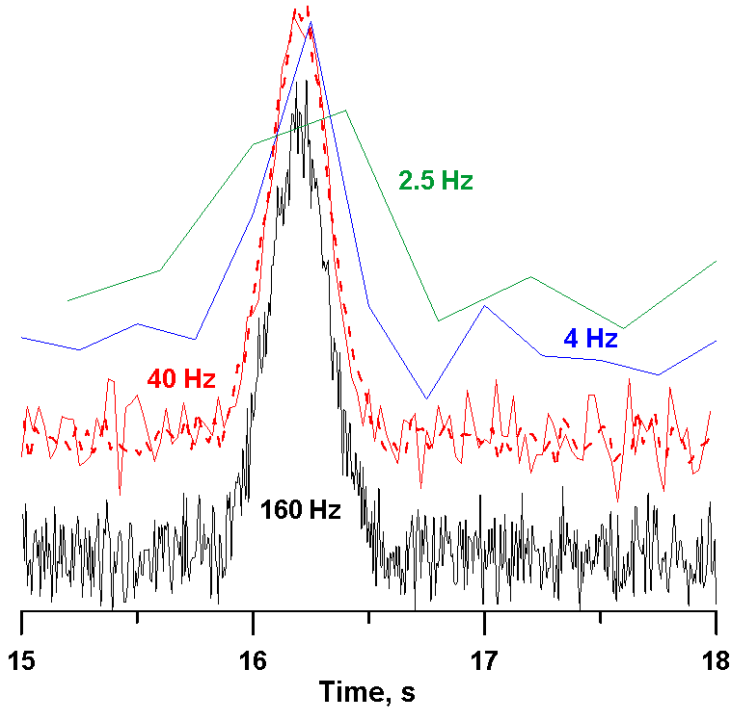

Figure F.3. Details of the first peak in Figure F2 as it would appear at different sampling frequencies. There is no data averaging except for the dashed line and all plots have the same ordinate scaling although they have been vertically displaced for clarity. The dashed red line shows what a real 40 Hz output may look like where every successive four data points have been averaged in an original 160 Hz sample. Note 2-fold decrease in noise.

Aside from noise, the sampling frequency also affects the computed peak efficiency by missing the peak apex. For the 4th peak for example at 29.4 s, there is loss of 7.7% loss in peak height (peak apex missed by sampling at 4 Hz) for Fig. F2b vs. F2c. The peak efficiency, the peak shape and the exact retention time and their reproducibility are important parameters to a chromatographer and all benefit from some oversampling compared to that minimally required by the sampling theorem. In locating a peak apex,

typically simply the highest point is chosen, there are no interpolations or fitting to some preconceived shape. The peak apex thus corresponds to a particular sampled point, whereas the real apex may be at a slightly different time. At a chosen sampling frequency of F Hz, the sampled points are $1/F$ s apart. It follows that the maximum error will be half the sampling interval or $1/2F$ s. Thus, sampling at 160 Hz, the worst-case scenario will give us a retention time uncertainty of ±3.1 ms whereas sampling at 2.5 Hz, the uncertainty is +/- 200 ms.

F.4.2 Real chromatograms

In Figure F4, we show four sub-minute high efficiency separations of uracil (peak 1) and phenol (peak 2). The chromatograms were obtained at a fixed τ = 0.01 s but at sampling frequencies ranging from 0.5 to 100 Hz. The highest efficiency is seen at the highest sampling frequency but the noise is also the highest. There is a consistent decrease in efficiency and noise with decreasing sampling frequency as depicted in the Figure. At 40 Hz, one observes perhaps the best compromise between efficiency and noise is realized although this is admittedly a subjective choice. Note that calculation of the peak efficiency has an uncertainty that also increases with decreasing sampling frequency, see the Supporting information for illustrative calculations. From >22000 plates at 100 Hz, if we sample at 6.25 Hz, which is twice the approximately the minimum sampling frequency putatively needed for a peak of 8.38 s half-width (sampling theorem requires 3.6 Hz as the bare minimum), the efficiency decreases to ~16,000 plates (Figure F4c). Sampling at even lower frequencies (Figure F4d) results in irreproducible chromatograms where both peak height and shape change from run to run.

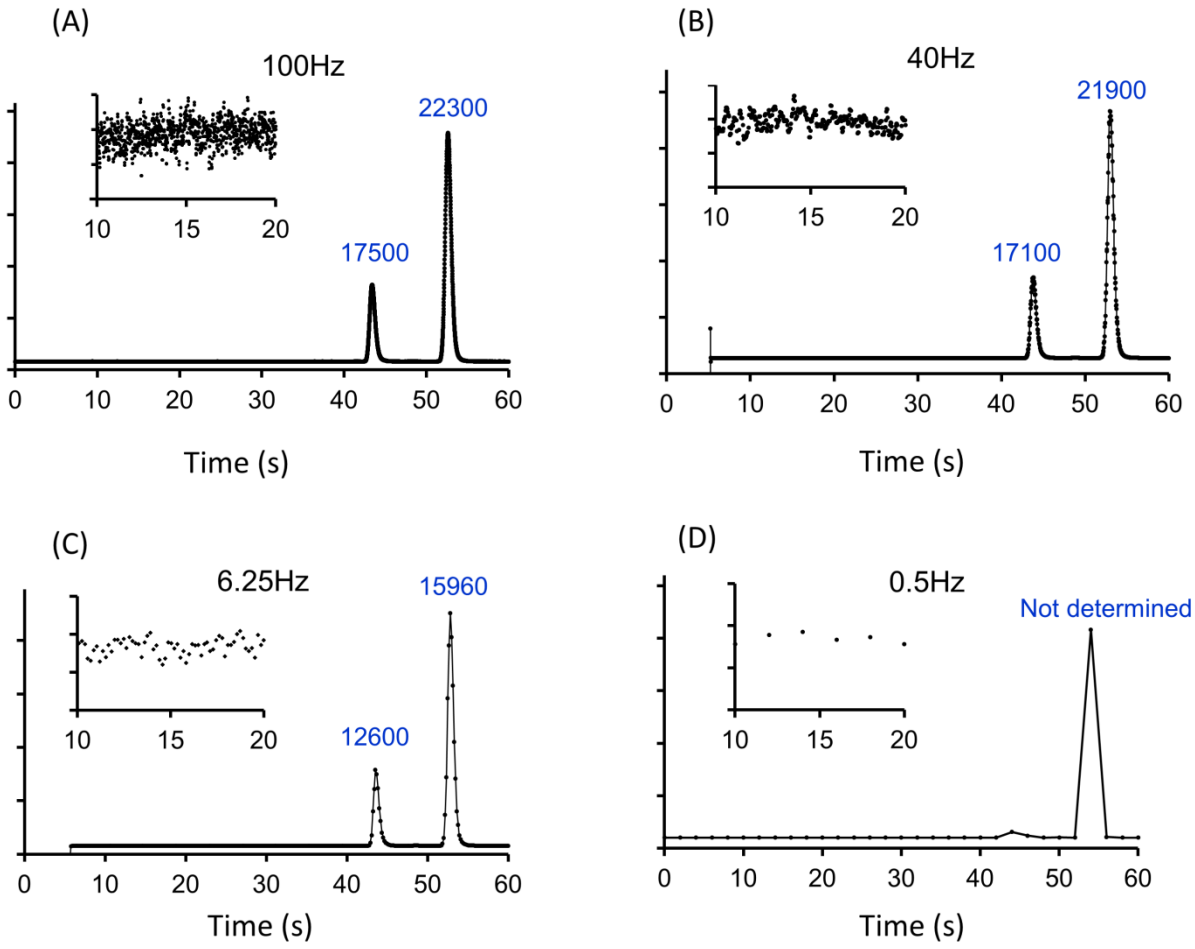

Figure F.4. Effect of sampling frequency on the efficiency and noise level in high efficiency chromatography. System 3, time constant fixed at 0.01s. The first peak is uracil and second peak is that of phenol. Injection volume 1 µL, mobile phase: 80:20 ACN:H_2O at 1.8 mL/min, detection wavelength 254 nm.

A detailed analysis of noise will indicate that the decrease in noise in real systems is not always exactly predictable. Referring to the 10-30 s period, the baseline standard deviation was 36, 12, 9.6, and 9.6 units at 100, 40, 4, and 0.5 Hz. The noise decreases by a factor significantly more than the expected amount in going from 100 to 40 Hz. This suggests that additional sources of noise appear at the higher frequencies (i.e., unlike our illustrative example it is not white Gaussian noise) and below 40 Hz, the noise actually decreases very little, if at all, suggesting there are non- random sources of noise (and/or drift; computation of noise as standard deviation counts drift as noise). Remember

however, τ was not nominally altered in the above experiments although when τ is smaller than the sampling interval (as in the case of the two lower sampling frequencies) has no real effect.

Given the drastic decrease that we observe above in the peak efficiencies, one may well wonder why a recent publication stated: "When the data acquisition frequency is too low, only a few points per peak are recorded. We will miss the peak apices,…, but *peaks remain as sharp as they were at the highest sampling frequency*" .[233] The reason is that these authors used a column with 2000-3000 plates only, and in such a case, indeed, it may not matter. The decision of the sampling frequency clearly will be dependent on the column performance level. A micrometer is not essential in measuring the height of an elephant; in the same vein, gross oversampling, while certainly technologically feasible, has few advantages and aside from increased noise, results in very large data files.

F.4.3 Effect of Noise Filters on the Signal

Noise is present with any real signal. As discussed, the choice of a high sampling frequency with an adequately fast response time provide the most efficient peaks, but with greater noise. Whenever the signal bandwidth is known to be smaller than the noise bandwidth, noise at frequencies greater than those occurring in the signal can be attenuated, by appropriate processing, also called *filtering a signal*. Butterworth famously stated (some 30 years before such filters were even attempted): "*An ideal electrical filter should not only completely reject the unwanted frequencies but should also have uniform sensitivity for the wanted frequencies*".[237] The simplest traditional filter used in analytical instrumentation is the RC filter where the output signal is connected to ground via a resistor (R) and then a capacitor (C) that are connected serially. The output signal is collected from the junction of the R and C elements (see Figure S1 in the Supporting Information). When R is in Ohms and C is in Farads, τ = RC and is in seconds. It can be readily changed by changing the values of one or both components. An RC filter does have an essentially flat response in the desired frequency domain but higher frequencies are not abruptly cut off. Rather, they are exponentially attenuated as the frequency increases.

Exactly how the output to input voltage ratio changes as a function of frequency is referred to as the *transfer function* of the filter. An RC filter is a "single-pole low-pass filter". For a short summary on filters and "poles" see reference. [238] A "pole" is so-called because if the transfer function is visualized at in the Laplace domain, imagining the response surface as a flat rubber sheet, it will stick up in a particular frequency region as if supported by a pole underneath. An audiophile is well acquainted with an "equalizer": A 24-band equalizer is simply a 24-pole filter where each of the poles in the 24 different discrete frequency domains can be raised or lowered. The marvel of digitization and consumer interest is such that such a 24-pole digital filter in the audio frequency range can be freely downloaded for various popular audio players; unfortunately, this is not the case for data in the frequency range of chromatographic interest). Much sharper cut-off at higher frequencies than the exponential *roll off* provided by a simple RC filter are possible and may be desirable in many cases.

Whereas hardwired electrical circuits with a multitude of elements were used in yesteryears, currently signal filtration is invariably carried out after digitization. The digitized data is typically processed by the desired mathematical algorithm implemented in instrument firmware; hence, they are called digital filters. Some digital filters may have a transfer function identical to a RC filter. In other cases, the simplest of digital filters, a "moving average" filter, is very easy to implement in the digital domain but not on a hardwired basis. In a simple *n*-point moving average filter (a function built into data analysis packages of common spreadsheets like Microsoft Excel™), the input is *n* successive points in the data array and the output is their average – the algorithm then simply moves down one row in the data array and repeats the process. The simplest of moving average filters is said to have a *rectangular kernel,* the rectangle represents the filter window while the flat top of the rectangle indicates that all the points are weighed equally in the averaging process. In other variants of the moving average filter, individual elements within the averaging window may be weighed differently, e.g., by a Gaussian function centered at the center of the averaging window. Running the signal through the same moving average filter multiple times is also possible. Running it twice through the same filter is essentially equivalent to a triangular filter kernel whereas 4 or more passes

results essentially in a Gaussian filter kernel. An excellent discussion of moving average filters appears in reference,[239] which also categorically states "*In spite of its simplicity, the moving average filter is optimal for a common task: reducing random noise while retaining a sharp step response. This makes it the premier filter for time domain encoded signals. However, the moving average is the worst filter for frequency domain encoded signals, with little ability to separate one band of frequencies from another.*"

For a simple moving average filter, if a data points are averaged in the window and the sampling frequency is $2f$ Hz it is easily verified that the response time is $0.4a/f$ s. It is interesting to note that running a moving average filter n successive times increases the response time by a factor slightly less than $\sqrt{n}$. A moving average filter can be implemented in a nested configuration. While the simple moving average filter is extremely fast in execution, modified moving average filters can be orders of magnitude slower in computational execution albeit they do a much better job in moving frequency domain noise.[239] Fortunately on an absolute scale even the highest sampling frequencies in current HPLC detectors is relatively low and implementing almost any filtering algorithm does not pose a problem with present microprocessors.

The effect of signal filtration on chromatographic or spectroscopic signals has been previously examined. [240,241] However, most of this literature in the analytical chemistry context is dated and sometimes contradictory.[231,241] Filters of yesteryears were invariably RC types and at best only, this type has been discussed. Hinshaw discussed for example artifact tailing that is observed if an inappropriately high τ is used. [241]

Presently we examined the effect of the chosen response time (manufacturer A) or time constant (manufacturer B) on our illustrative systems by using a LED source driven by a 1 Hz square wave, to simulate a sharp peak of 0.5 s "width", comparable to that of the narrowest peaks attainable from present high efficiency columns. Figure F5 shows the results; note that there was no additional superimposed noise and all sampling frequencies were well above the lower limit dictated by the sampling theorem to capture the repetition frequency (but not the sharp rising or falling edge of a square wave (which theoretically extends to infinity but because of the function generator limitations and LED capacitance is

likely to be several hundred kHz). Manufacturer A (system 2, panels A-D) picks the sampling frequency as soon as the response time is chosen, they cannot be independently chosen. At 80 Hz sampling frequency, the square wave is reasonably reproduced with 31 and 63 ms response times although rabbit ears (overshoots) begin to appear in the latter case at the edges but not very reproducibly (Figures F5a and F5b). At 40 Hz and 130 ms response time (Fig. F5c), the peak shape is distorted, is irreproducible and occasionally has minor asymmetry but at still lower sampling frequencies and slower response times (Fig. F5d) the signal is grossly over filtered; it regains symmetry, assumes a more Gaussian character and essentially appears as a sine wave. While the manufacturer does not state the specific filter used, a moving average filter with an appropriate kernel, or multiple passes of a moving average filter can reproduce this behavior (see Supporting Information).

The right panel of Figure F5 shows the behavior of system 3 for a similar experiment. In this case, the sampling frequency was maintained constant and τ was varied. With τ = 10 ms, the square wave was faithfully reproduced (Fig. F5e). At higher τ (ranging from 160 to 2000 ms) the choice of the sampling frequency was immaterial as the behavior is governed by the choice of τ. At 160 ms (Fig. F5f) the response has become seemingly asymmetric with a peak that is tailing. In reality, however, the rise and fall behavior are mirror images (along y-axis). Again with continued increase in τ, symmetry is regained and eventually a triangular wave of lower amplitude results (Figures F5g and F5h). This filter behavior is that of a classical RC filter and the manufacturer reference to “time constant” is thus appropriate.

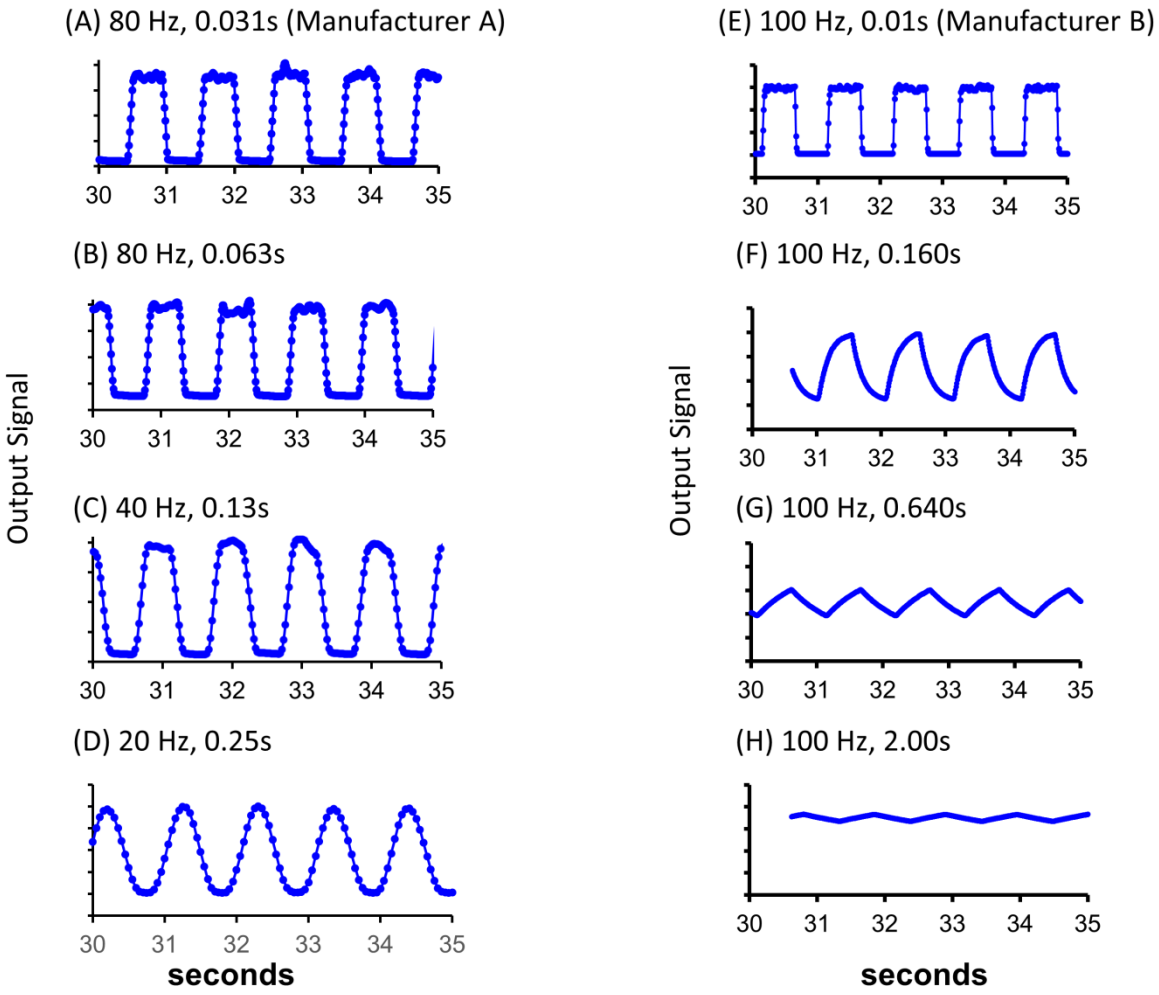

Figure F.5. Convolution of 1 Hz square wave by digital filtering on two different liquid chromatographs; System 3 (A to D), and System 1 1260 (E to H). The Shimadzu software uses "time constant" and Agilent uses a "response time". Wavelength of detection is 610 nm.

F.4.4 Effect of filtering parameters on fast chromatography

We assessed the effect of filter parameters on System 3, which allows the sampling frequency and the response time to be independently chosen. Several major manufacturers, (Dionex, Shimadzu, and Waters, to name a few) offer a similar choice and leave the user to make the judgment that a particular combination is judicious. In Figure F4, we had fixed τ at a very low value and gradually decreased the sampling frequency to a point where the latter became the limiting factor and were clearly not a judicious choice.

Presently we fix the sampling frequency at 100 Hz and vary τ over a wide range, using identical conditions to the experiment in Figures F5e - F5h. The results are shown in Figure F6. Predictably, baseline noise decreases monotonically with increasing τ but peak efficiency also decreases, as labeled in the Figure. The last two choices are again clearly not judicious. Peak asymmetry (in terms of tailing factor) also increases with increasing τ, respectively being 1.2, 1.2, 1.6 and 3.0 in Figures F6a - F6d for the second peak. Less apparent are the decreases in peak height (From Figure F6a to F6d the height has decreased by a factor of 66%) and the perceived retention time (peak apex) that shifts to larger values as the τ is increased. In a RC type low-pass filter, the relative width of the distorted peak depends only on the ratio of the τ to the original width of the peak.[240] At the highest τ chosen, the plate count for phenol has decreased to 600 from the original 17500 (Figure F6 a to d) accompanied by severe apparent tailing, both total artifacts brought about by the data system parameters. Instrument operation manuals often correctly suggest that a smaller τ be chosen if peaks are narrow, without specific recommendations as to what for example an appropriate ratio of the two should be. Such problems are compounded by popular tools that are supposed to simulate the behavior of an HPLC system. In the "HPLC Simulator",[242] an otherwise admirable tool, when the "time constant" is increased, the peaks simply broaden symmetrically. Obviously, that is not what will be observed if a RC type filter is present (which would be suggested by the use of the term time constant).

Meyer has suggested a method for choosing τ if retention time and efficiency are known beforehand, if θ is the allowed percent broadening of the peak width:[243]

$$Time\ constant\ \leq \theta\left(\frac{t_r}{\sqrt{N}}\right) \qquad \text{(F7)}$$

If 1% broadening of the peak width is acceptable, for the values for phenol in Fig. F6a (t_R =53 s; N = 17500), with peak efficiencies of 17500 and retention time of 53 s (phenol), the calculated time constant would be 0.4 s. In reality, even with a time constant of 0.025 s, we observed that N decreases to 16700 plates, representing a >2% increase in peak width. For a Gaussian peak, it is possible to predict how $w_{0.5}$ will change as a function

of $\tau/w_{0.5}$. Table F2 lists values the increase in $w_{0.5}$ and the peak asymmetry at 5% and 10% of peak height after processing through an RC filter as a function of $\tau/w_{0.5}$. Note that when we use the dimensionless parameter $\tau/w_{0.5}$ rather than the absolute value of τ, the effects on an initially ideal Gaussian peak becomes independent of the $w_{0.5}$. Alternative to using or interpolating values in Table F2, the Excel workbook RC filter Gaussian.xlsm given in the Supporting Information accepts $w_{0.5}$ for the raw peak (assumed to be Gaussian) as the input and provides the output for any time constant chosen, automatically generating all the peak parameters of interest listed in Table F2. Another version of the same program, *RC filter anydata.xlsm* allows inputting the actual *x-y* data array for a peak, which may not be Gaussian.

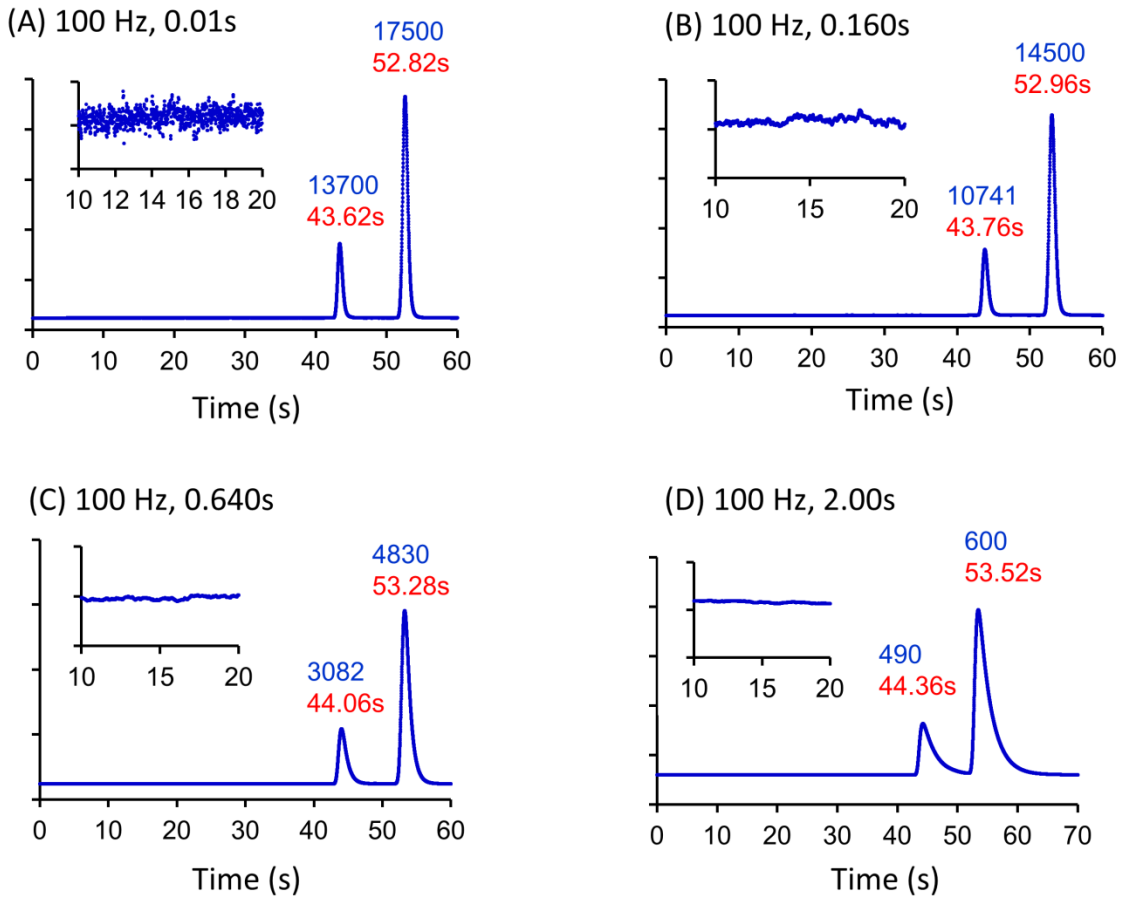

Figure F.6. Effect of the choice of the time constant on the efficiency and noise level. System 3 with a fixed sampling frequency of 100Hz. The first peak is uracil and second peak is that of phenol. Injection volume 1 µL, mobile phase: 80:20 ACN:H_2O at 1.8 mL/min,

detection wavelength 254 nm. The peak efficiency (average of 3 measurements) was calculated by the exponentially modified Gaussian method to account for tailing.

$\tau/w_{0.5}$	10-90% response time/$w_{0.5}$*	increase in $w_{0.5}$ (%)	decrease in (N) (%)	decrease in peak height (%)	asymmetry at 5% peak height	asymmetry at 10% peak height
0.0231	0.0507	0.1155	0.2308	0.1470	1.0007	1.0004
0.0462	0.1015	0.5389	1.0748	0.5767	1.0022	1.0017
0.0693	0.1522	1.2317	2.4483	1.2597	1.0066	1.0059
0.0924	0.2030	2.1170	4.1892	2.1559	1.0142	1.0121
0.1155	0.2537	3.1563	6.2129	3.2228	1.0261	1.0215
0.1386	0.3044	4.3495	8.5098	4.4208	1.0417	1.0344
0.1617	0.3552	5.6197	10.9236	5.7153	1.0607	1.0500
0.1848	0.4059	6.9669	13.4484	7.0774	1.0834	1.0687
0.2079	0.4567	8.3911	16.0780	8.4838	1.1089	1.0886
0.2309	0.5074	9.8152	18.6671	9.9158	1.1376	1.1111
0.3464	0.7611	17.4365	31.8327	17.0504	1.3150	1.2502
0.4619	1.0148	25.2887	44.1822	23.6305	1.5276	1.4192
0.5774	1.2685	33.2948	55.5042	29.4507	1.7523	1.6029
0.6928	1.5222	41.3010	65.5443	34.5416	1.9829	1.7938
0.8083	1.7759	49.4226	74.4193	38.9930	2.2146	1.9873

Table F.2. Effect of RC type filtering on chromatographic peak characteristics on an initial Gaussian peak.

F.4.5 Effects on best case performance

System 1 (UHPLC) was optimized with the smallest possible lengths of 75 μm i.d. connecting tubing between the injector and the column and the column to detector. We were able to attain 39000 plates compared to manufacturer's certification of 38000 plates minimum. As previously stated a choice of the response time in this system automatically results in a choice of the sampling frequency that ranges from (160 Hz to 0.31 Hz). A choice of 0.031 or 0.063 s as response time will automatically result in a sampling frequency selection of 160 Hz, a choice of 0.13 s, 0.5 s or 4.0 s response times will automatically result in sampling frequencies of 40, 10 and 1.25 Hz. This approach prevents the user from making a choice of an inappropriate combination but does not of course prevent the choice of an altogether inappropriate response time that has an equally inappropriate associated sampling frequency. The coupling of appropriate sampling frequencies and response times is specifically mentioned in the manuals of the manufacturer that does so. It is not a "hidden feature" as recently claimed,[233] (see Supporting Information for manufacturer details). The vendor emphasizes in its manuals that choosing a lower sampling frequency does not actually change the intrinsic sampling frequency but the output data are simply averaged/integrated in bunches (see previous discussion on Delta-Sigma ADCs).

Referring to Figure F7, based on the narrowest peak (Figure F7a, $w_{0.5}$ 0.619s; note that we also measured with a response time of 16.5 ms and a sampling frequency of 160 Hz, there was no discernible difference with Fig. F7a), all of the sampling frequencies used should be almost adequate, so the observed changes are due solely or dominantly from changing the response time. However, with such highly efficient peaks even the accuracy of determining time plays a role that is not often appreciated. To determine half-width, the temporal interval between two actually measured points will generally be taken and no interpolation used. In going from 80 Hz to 40 Hz, the uncertainty in locating each point goes from ±6.25 ms to ±12.5 ms. That for measuring an interval will be a factor of √2 higher: at 40 Hz the overall uncertainty is 17.7 ms. For the present parameters, (t_R = 52 s, $w_{0.5}$ = 0.619 s, an uncertainty of 17.7 ms results in uncertainty of ±2200 plates in the value of N! In comparing Figures F7a and F7b (39000 vs 37940), this needs to be borne in mind

that the small difference that exists can be due both to the increases in the sampling interval and the response time. In going to Fig. F7c, it is interesting to note that from between its 1% bounds, this peak comprises of 20 sampled points, a number often prescribed as adequate.[244] The sampling frequency may be adequate to describe the peak shape (sampling points 100 ms apart) but a response time of 500 ms is clearly inadequate for a $w_{0.5}$ only slightly higher than this and as a result, there is a near 50% loss in efficiency compared to the best case. The choice of sampling/response parameters in Figure F7d is simply a travesty to this highly efficient column. It essentially goes to show that a manufacturer may provide compatible combinations of response times and sampling frequencies but the determined analyst can always find a way to pick the most inappropriate combination!

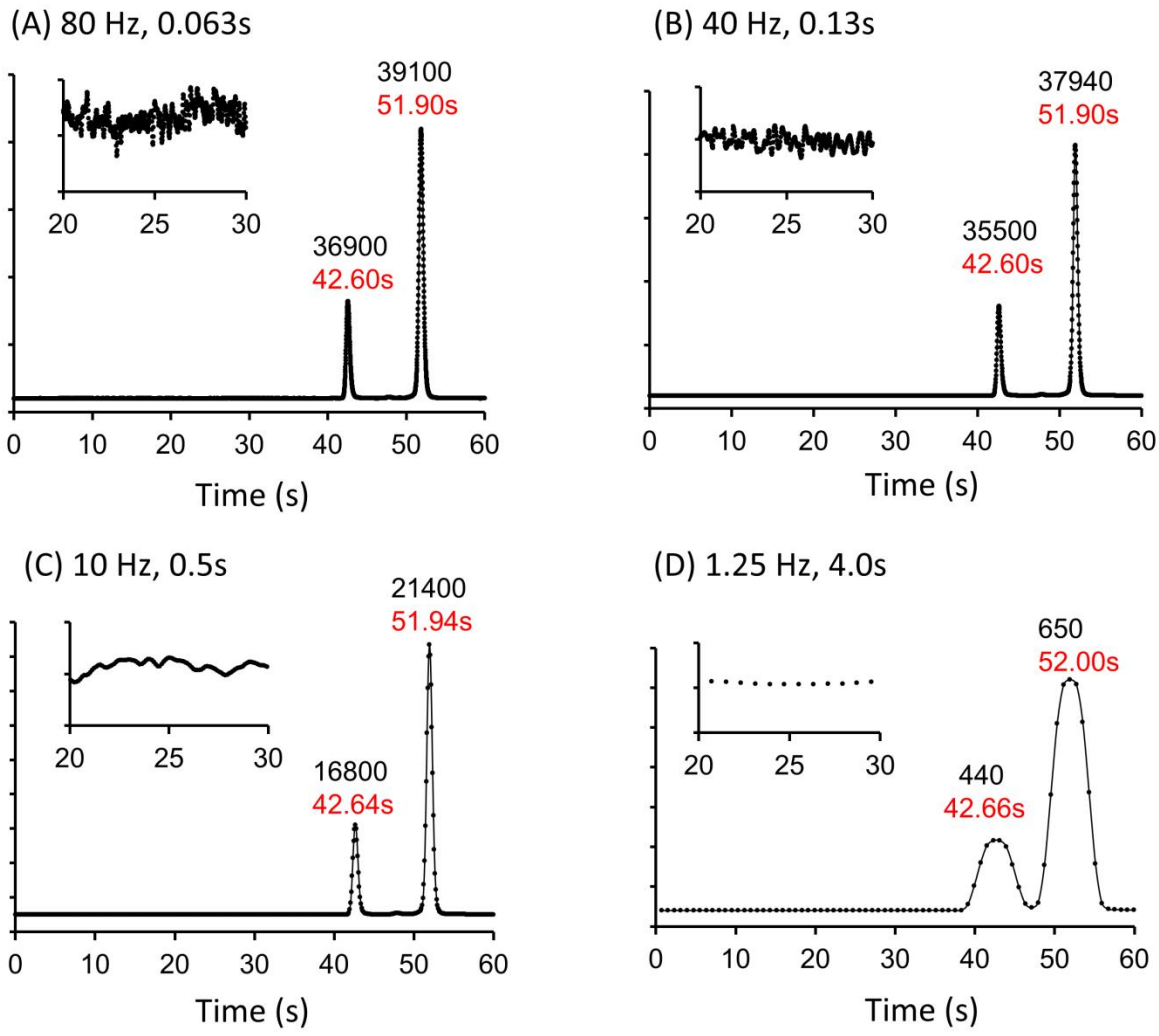

Figure F.7. Effect of coupled digital filtering and sampling frequency on the efficiency and noise level in high efficiency chromatography. System 1. The first peak is uracil and second peak is that of phenol. Injection volume 1 μL, mobile phase: 80:20 ACN:H_2O at 1.8 mL/min, detection wavelength 254 nm. The efficiency is an average of 3 measurements.

There are both commonalities and differences between the results in Figures F6 and F7. In both cases, as τ or response time increases noise decreases in a consistent fashion. However, unlike in Figure F6, the increase in t_R with increasing response time was minimal in Figure F7. Also unlike Figure F6, increases in the response times did not induce peak tailing. These results are consistent with the results of the previously described square wave experiment, and as stated therein, consistent with the use of a moving average filter.

F.4.6 Suggestions for practitioners and manufacturers

In modern HPLC instrumentation, details of detection and signal processing are largely black boxes to most users. Details of signal processing are rarely, if ever, available to the analyst. The choice of data acquisition and signal processing parameters within a given instrument and the choice of different signal processing techniques between different instruments can affect the chromatographic output data, especially for present day fast separations. Those engaged in stationary phase development and column-packing processes need to be aware that much as long lengths or larger bore tubing or dead volumes in connections at any point after the introduction of the sample, poor choice of detector/data acquisition parameters can have the same effect. The following is our suggestion to the practicing chromatographer:

(i) Use the test mixture, injection volume and chromatographic conditions used by the manufacturer to test the column efficiency. Use the highest sampling frequency and lowest value of τ or response time that your system will allow. Use a sufficiently high analyte concentration so that visualization of peaks or efficiency calculations are not affected by the baseline noise. If you do not get close to the manufacturer specified efficiency, minimize all connection tubing diameter and length after the injector and make

sure that connections themselves have no dead volume. This will be the best you can do. Run samples of your interest under appropriate chromatographic conditions that you have developed. If you are not bothered by the present noise level or the data file size of your chromatograms for your samples of interest, you can leave the data acquisition settings at their fastest but most noisy level.

(ii) Consider the half-width of the narrowest peak in your chromatogram. If you can afford to sacrifice some efficiency, estimate what increase in $w_{0.5}$ will not affect your quantitation (remember that efficiency will change with the square of the change in $w_{0.5}$, 1% and 10% changes in $w_{0.5}$ respectively connote a 2% and 21% change in efficiency. Table 2 will guide you to the τ, you might use. If your system uses response times, estimate on the basis that response time equals 2.2 τ. If your system choses the sampling frequency based on the chosen response time then no further action is needed. If you need to pick a sampling frequency, you can proceed in one of two ways. If the maximum error in retention time accuracy you can tolerate is x seconds, pick a sampling frequency of $1/2x$ Hz or higher. Alternatively, if you know the number of points (n) across the (narrowest) peak you are comfortable with (while 15-20 is commonly suggested for n, we prefer *at least* 30 if high precision retention time or efficiency information is desired) pick a sampling frequency that is no less than $0.5n/w_{0.5}$ Hz.

(ii) We suggest to the HPLC vendors to provide the user the ability to process different parts of the chromatogram with different filtering capabilities. It is common to have a "General Sensitivity Problem" analogous to the well-known "General Elution Problem" that while the chromatogram has some narrow tall peaks that are far above the noise levels it also has some broad low intensity peaks that are difficult to quantitate because of the noise. The post-processing the data can be readily done by exporting the data to a spreadsheet and applying different filters in selected regions of the chromatogram. The individual segments can be highlighted and different degrees of filtering (time constant/response time/bunching/variable kernels or number of passes of a moving average filter) can be chosen for each will be very valuable especially if that can be then incorporated into a particular "method". When that "method" is executed, this mode of

data processing will be automatically implemented and it will perform quantitation based on calibration that has been carried out using the same “method”.

(iii) Researchers need to be aware that while all instruments offer the choice of sampling frequency and some filtering parameters, the results of comparable manipulations may vary from one instrument to another. As was demonstrated, increasing τ or response time may lead to tailing in one case and symmetric broadening in another. While the term time constant decidedly implies the use of an RC or exponential decay type transfer function, the use of the term “response time” can be applied to any filter type and the nature of the filter used cannot be determined from this specification. As we have seen in Figure 4, it is not possible to predict how noise will decrease with the sampling frequency in real instruments as the nature of the noise in real system is not properly described by white noise or for that matter, any pre-specified noise spectrum. Our conservative recommendation for high fidelity recording will be to use a minimum sampling frequency equal to $2/\tau$ or 4.4/(response time)

(iv) To determine the time constant/ response characteristics of the detector, the ASTM suggests adding a UV absorbing component in the mobile phase and monitoring the response at various flow rates. Most detector configurations will allow the use of a simpler approach, the use of a small solid-state light source to provide a step function to the light received by the detector. This approach also reveals far more about the overall data processing method, which can reveal what is happening by changing the digital filtering times.

Acknowledgments

DWA thanks the Robert A. Welch Foundation (Y-0026) for support of this work. PKD acknowledges support from National Science Foundation through CHE-1506572 and from NASA through NNX11AO66G. We also thank the Advanced Analytical Instrumentation Center at the University of Texas at Arlington for the use of their facility.

Appendix G:

Transient Ion-Pair Separations for Electrospray Mass Spectrometry

Hanghui Liu, Lily Lam, Bert Chi, Akinde F. Kadjo and Purnendu K. Dasgupta

Analytical Chemistry. **2016**, 88, 2059–2064

G.1 Introduction

Ion-pair chromatography (IPC) has had a long and illustrious history in separations; Google Scholar produces ~2000 articles with this term in the title. While a pair of ions may be involved in IPC; an ion-pair is rarely involved. Bidlingmeyer suggested early that the technique be termed Ion Interaction Chromatography.[245, 246] Some of us adopted this nomenclature;[247] it is, however, still mostly called IPC. Terminology aside, the attractiveness of the technique lies in its ability to enhance the retention and separation of hydrophilic charged/ionizable species on reverse phase columns, arguably the most developed, most efficient, best characterized, and the most affordable of stationary phases. Traditionally it has provided an attractive option for a large class of analytes not well-separated by reverse-phase LC.[248] With the widespread use of electrospray ionization mass spectrometry (ESI-MS), the use of IPC has dramatically decreased; in 2014 only 30 articles bore that designation in the title. Most ion-paring reagents (IPRs) are both nonvolatile and natively ionic, thus depositing in the source and contaminating it, and/or causing serious ionization suppression. While true devotees may feel that despite obligatorily frequent source cleaning, nonvolatile reagent IPC is still worth it,[249] and granted that some ion source geometries are substantially more immune to contamination than others,[250] not many share this conviction. Limiting IPC-ESI-MS to either volatile acids (see [[251]] for a review of perfluorocarboxylic acids as IPRs) or weak bases that are protonated by using a volatile acid component[6] in the eluent severely restricts its horizons. While Hydrophilic Interaction Chromatography (HILIC) may have substituted IPC in some applications, at least one comparison finds IPC superior.[252]

It is not surprising then that despite the problems IPC has with ESI-MS, research has continued to attain the chromatographic blessings of IPC while minimizing ion suppression. How a number of different IPRs fare for the ESI-MS measurement of several analyte classes has been studied with different instruments/ion-source geometries.[6] IPC-MS has been proven useful in a variety of arenas for polar analytes.[8-254]

The major problem with IPC-MS is with the IPR during the detection stage. This problem is solved if the reagent is removed prior to that stage by exchanging for H^+ or

OH^- by using an appropriate ion exchanger,[255,256] borrowing from suppression concepts used in ion chromatography. Paradoxical only in the present use of the terms, the use of a suppressor here mitigates ion suppression in the MS detector. Suppressors have limited exchange capacities and/or must be rejuvenated. They cause band dispersion not compatible with present high efficiency columns; at the very least they represent an additional element. A volatile IPR can be used to avoid source contamination but ionization suppression is still a problem.

Here we introduce a novel approach: the IPR is simply not allowed to proceed to the detector. The eluent does not contain any IPR. The IPR is injected as a bolus some time before the sample, coats the column and helps separate the next injected sample components by interacting with the moving reagent zone. The chosen solvent gradient elutes the analytes of interest before the pairing reagent. Following analyte elution and measurement, the solvent composition is chosen to rapidly remove the IPR and the effluent is diverted to waste until the reagent is essentially removed. The only caveat is that the IPR must be more strongly retained than the sample components of interest even after their retention is increased through interaction with the IPR.

G.2 Experimental Section

Greater details are given in supporting information, only the essentials are stated here. Chromatographic separations were performed at 30°C and 0.75 mL/min on an Acquity UPLC HSS T3 column (2.1 x 50 mm, 1.8 μm particles, 11% carbon loading, www.waters.com) on an Agilent 1290 UHPLC system with a 6550 QTOF mass spectrometer with JetStream™ electrospray ion source (www.agilent.com).

For positive ionization MS, a binary eluent system of (A) 0.1% w/v HCOOH and (B) CH_3CN was used. For negative ionization mode, the A component in the binary eluent system was changed to 10 mM 4-methylmorpholine adjusted to pH 7.0 with HCOOH. Automated sample injection (5 μL) followed IPR injection (4 and 2 μL for positive and negative MS modes, respectively) by a fixed period (except as stated, programmed 1 min,

effectively 1.43 min). All data were collected at least in duplicate. The specific ions monitored in various experiments are given in Table S1 in supporting information.

The effect of experimental variables (amount of IPR injected, delay before sample injection, and the nature of the solvent gradient) on the retention, detector response, response reproducibility and linear dynamic range (LDR) were evaluated. In all cases, a high level of acetonitrile was used in the final stages to remove the IPR but the solvent program is referred to as gradient elution only if the solvent composition was changed during the analyte elution/detection period. IPR concentrations were 0.05 M except as stated.

For the separation of iodate and nitrate and iodide, a Raptor C18 column (2.1 x 100 mm, superficially porous 2.7 μm particles, www.restek.com) was used at a flow rate of 0.2 mL/min. The IPR was hexadecyltrimethylammonium chloride (www.fishersci.com).

G.3 Results and Discussion

Elution profiles of IPRs. The IPR elution profile is critical to exploiting TIPS and avoiding co-elution of the IPR. While other detection means could have been used, use of the intended detector will reveal the extent of detector response if and when the IPR reaches it. Admittedly while nonvolatile reagents can be tolerated by the ion source for a short duration without requiring cleaning,[5] this is not desirable. However, given the vast difference in the amount of IPR used in traditional IPC (a 10 min run with 10 mM IPR @0.75 mL/min equals 75 μmol IPR, compared to 0.10-0.75 μmol/injection presently used, we chose to follow the IPR elution in the initial studies by MS. In use, the IPR elution profile for the method will already be known and the column effluent would be diverted to waste before IPR elution.

Positive MS mode with anionic IPRs. Isocratic elution.

Figure G1 shows the elution profile of perfluoroheptanoic acid (PFHA). With a low initial eluent strength (10% ACN), 100-200 nmol PFHA does not elute from the column until a steep eluent gradient has been started. With ≥200 nmol PFHA, essentially column overloading occurs and becomes increasingly significant: the breakthrough time (t_b, when PFHA first appears in the column effluent with this eluent), is related to the logarithm of the amount injected (n) by the relationship

$$t_b = 20.3 \pm 0.6 - 5.53 \pm 0.25 \log n,\ r^2 = 0.9980 \quad \ldots(G1)$$

where n is the amount in nmol. However, the second term only applies if the column is overloaded, the second-term is not to be used if only a small amount is injected (there is indeed no difference in t_b between n = 100 and 200); this is consistent with the observation that if isocratic elution with 10% ACN is continued, breakthrough for n = 100 occurs at~23 min (Figure S1). It is to be noted that with a weak eluent like 10% ACN, the IPR zone moves through the column not as a plug but by broadening and extending the front edge of the reagent zone where the IPR concentration is the highest while the tail of the zone essentially decreases in magnitude rather than moves. The combination of the large capacity factor of PFHA, prolonged tailing, and the need for high acetonitrile content to wash the adsorbed PFHA out indicate that PFHA tended to form a "sticky" coating along the column. Eq G1 thus provides a guideline on the elution window available for resolution of the analytes and this window is shortened by increasing the acetonitrile content.

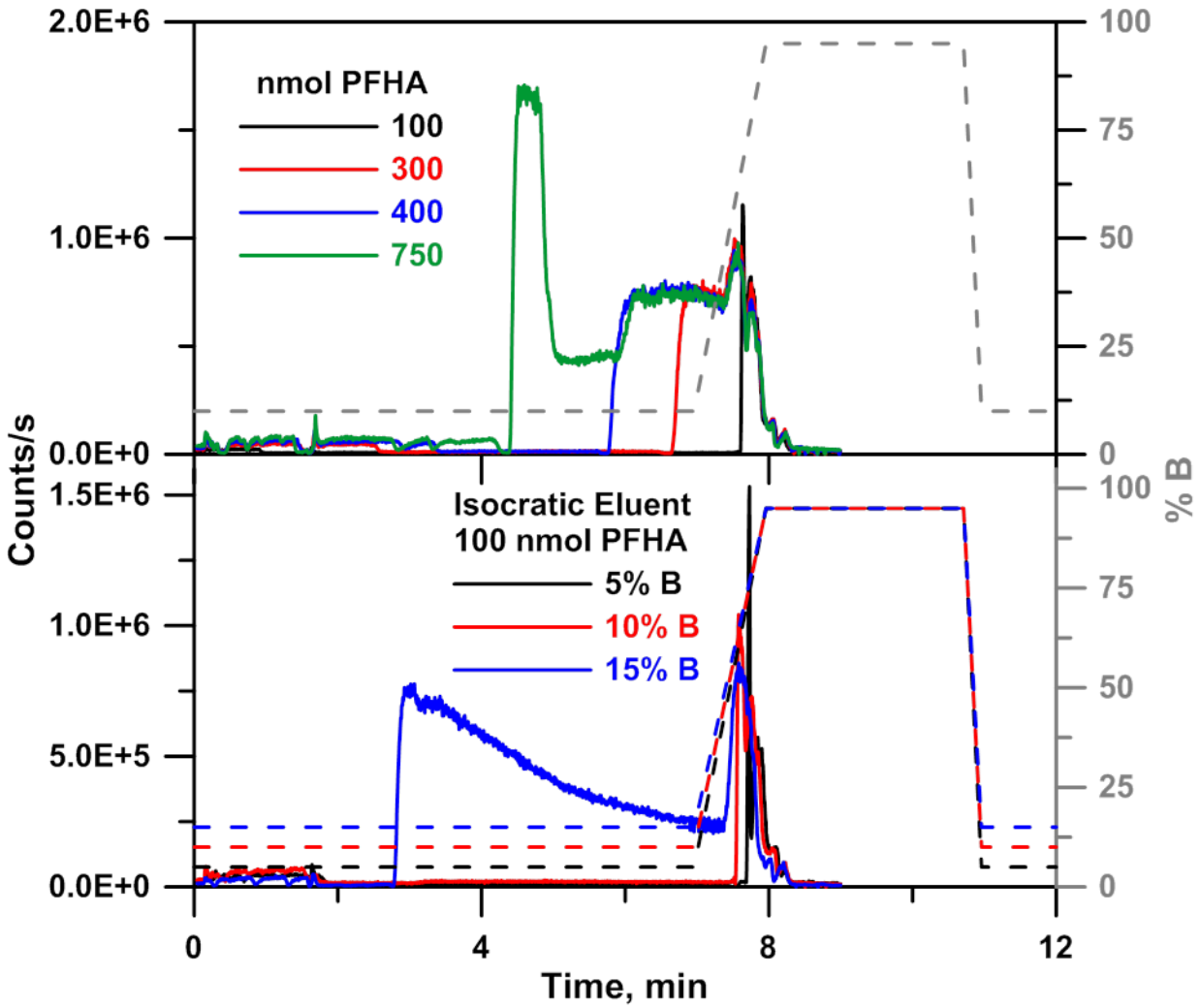

Figure G.1. Elution profile of PFHA injected as a transient IPR. The eluent composition is indicated by the dotted lines in the right ordinate. The time on X-axis begins from IPR injection. Top panel: results are indicated for different amounts of PFHA injected (200 nmol, not shown, produces virtually the same elution profile as 100 nmol). A and B eluent compositions are given the Experimental section. Bottom Panel: results for different isocratic eluent composition (5-15% B) with 200 nmol PFHA. If elution was continued isocratically at 10% B, first breakthrough of PFHA will occur at ~23 min and continue at a low, steadily diminishing level (see Figure S1). In the time scale shown, sample injection will normally be made at ~1.4 min.

Gradient elution. Positive MS mode with anionic IPRs and Negative MS mode with cationic IPRs

Figure G2 shows the elution profiles for various amounts of heptanesulfonic acid (HSA) and PFHA in the positive MS mode and those for tributylamine (TBA) and tetrabutylammonium hydroxide (TBAOH) in the negative MS mode under gradient elution conditions. In all cases t_b decreased consistently with increased IPR loading. For an IPR like HSA, t_b is unusably short at larger IPR amounts. We also experimented with 3-[(3-cholamidopropyl) dimethylammonio]-1- propanesulfonate (CHAPS) in both positive and negative modes under gradient conditions and in both cases it eluted in a relatively narrow band (base width < 1.5 min) even though the retention time was ~7 min (void time was 0.15 min, see Figures S2 and S3 in supporting information).

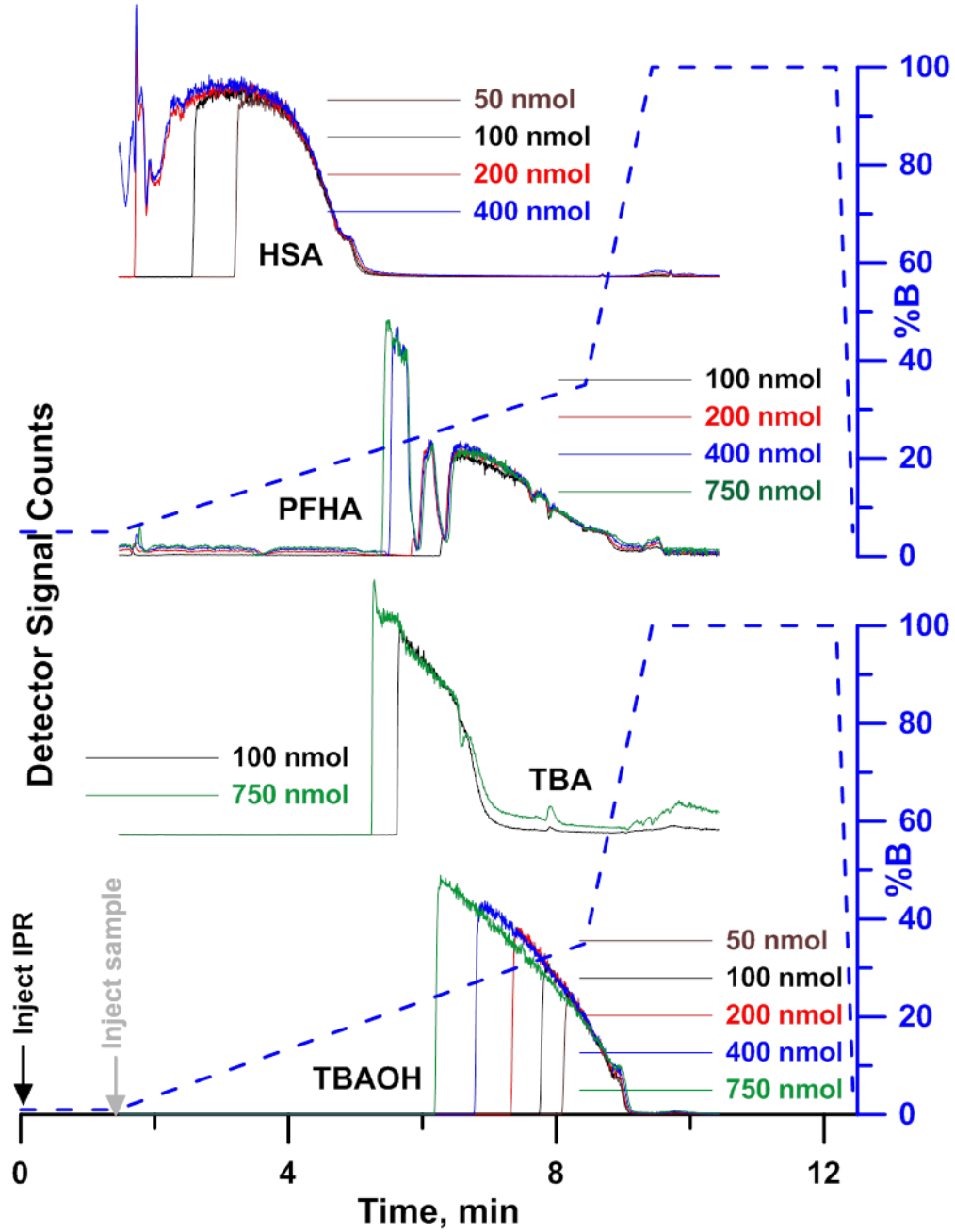

Figure G2. IPR elution profile under gradient elution conditions. Top: anionic IPRs PFHA and HSA. Bottom: Cationic IPRs TBA and TBAOH. Gradient profiles are indicated by the dashed line in blue (right ordinate. The typical time the sample will be injected is indicated by the light arrow. See Experimental section for composition of eluents A and B.

Effect of IPR amount on the retention and response of analytes

Positive ionization mode.

The retention of tyramine (TYR), norepinephrine (NOR), and mitoguazone (MGZ) were examined as analytes in the positive mode with various amounts of PFHA as IPR under both isocratic and gradient elution conditions (as described in Figures G1 and G2) as well as HSA under gradient elution; the results are summarized in Fig. G3 and Table S3. In all cases, the retention predictably increased monotonically with the IPR amount. (Although similar data for erythromycin (ERY) have been given, this compound is generally retained quite well without an IPR (often the retention time (t_R) was actually greater than the IPR breakthrough time (t_b) value) and the retention is not much influenced by the presence of an IPR.) The increase in log k (retention factor) was nearly linear with the IPR amount; certainly a quadratic fit provides excellent prediction ($r^2 > 0.99$, see Table S2). In many cases (especially with HSA as the IPR and under gradient elution conditions for both IPRs) the increase in analyte retention was so great that analyte t_R went into the unusable region where $t_R \geq t_b$ (these data therefore do not appear in Figure G3). As an IPR, HSA under gradient conditions was itself retained poorly; with amounts over 100 nmol HSA, analyte t_R exceeded the t_b values and HSA over 100 nmol was not useful as IPR. Structurally (see Supporting Information), tyramine is a relatively simple molecule with one phenolic –OH and one aliphatic amino group; norepinephrine is similar with an additional phenolic –OH and a benzylic –OH group. Mituguazone is entirely different in structure, a C5 aliphatic with multiple primary and tertiary amino as well as imino nitrogens. All are highly hydrophilic and none display chromatographically useful retention on a reverse phase column in the absence of an anionic IPR.

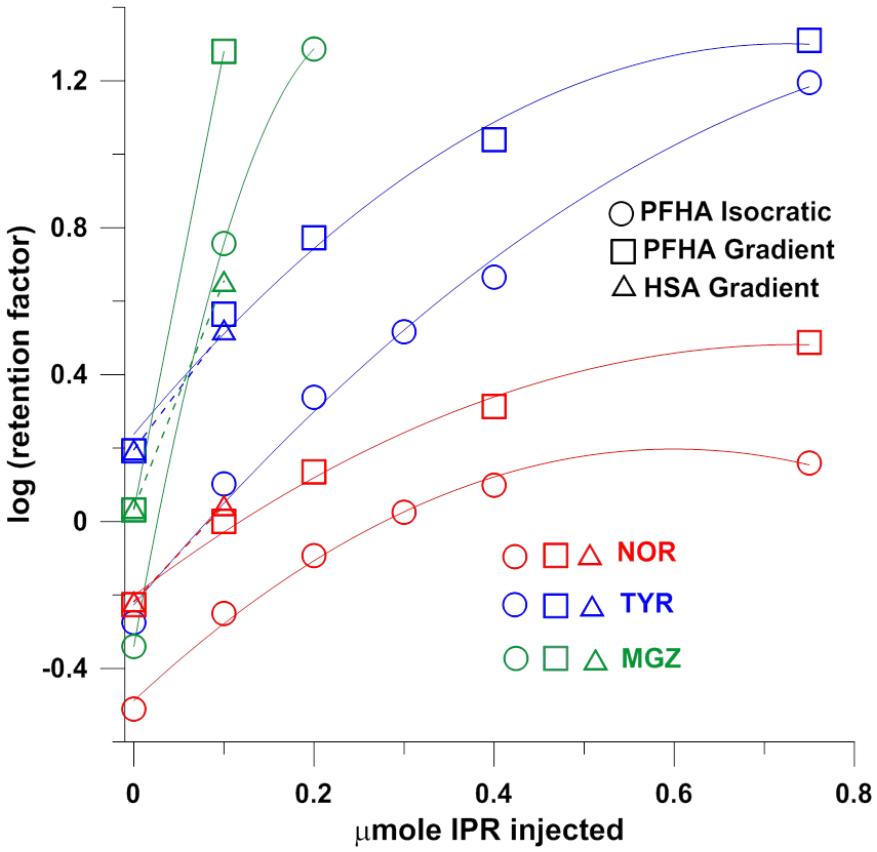

Figure G.3. The retention of three analytes of increasing structural complexity with different amounts of IPR injected on column. The circles reflect the behavior with PFHA as the IPR under isocratic elution conditions; the squares with the same IPR under gradient elution conditions. The triangles reflect the use of HSA under gradient elution conditions.

With multiple basic sites, despite its low retention MGZ tailed badly in the absence of an IPR (see Figure S4). In the presence of an IPR, MGZ peak shapes improved greatly and retention increased exponentially with the IPR amount, practical amounts being ≤200 nmol. For all analytes, improved retention in the TIPS mode was not associated with any loss of signal (peak area) from IPR-induced ionization suppression. It is important to note that while volatile IPRs like PFHA may not deposit in the ion source, they still may cause severe ionization suppression; see for example the data for MGZ in Fig. S4 for analyte t_R values > IPR t_b. In general, in the presence of the IPR, both retention and calculated theoretical plate numbers increased and peak area remained constant within experimental uncertainty until t_R exceeded t_b.

Negative ionization mode.

The effect of the amount of two cationic IPRs on the retention of four anionic analytes (uric acid (UA), Eosin Y (EY), Orange G (OG), and Orange II (OII)), determined in the negative ionization mode, is shown in Fig. G4 (with greater details in Figure S5, and Tables S4 and S5). TBA and especially TBAOH were primarily examined as the IPR. Predictably TBA had only a limited effect with a neutral pH eluent. As in the anionic IPR case, t_R increased while the peak area remained constant for cases with $t_R < t_b$. As indicated, TBA had a limited effect; with the intrinsically more retained analytes EY and OII, at higher levels of TBA, t_R actually decreased due to competition for the available stationary phase sites and limited ion-pairing effect. Indeed, although EY, OG, and OII exhibited a $t_R > t_b$ of TBA, the analyte signals were not significantly suppressed, as the TBA in the effluent was largely uncharged.

CHAPS did not increase retention significantly in positive mode of operation, but improved the retention of OG and EY in negative mode of operation that used different elution conditions.

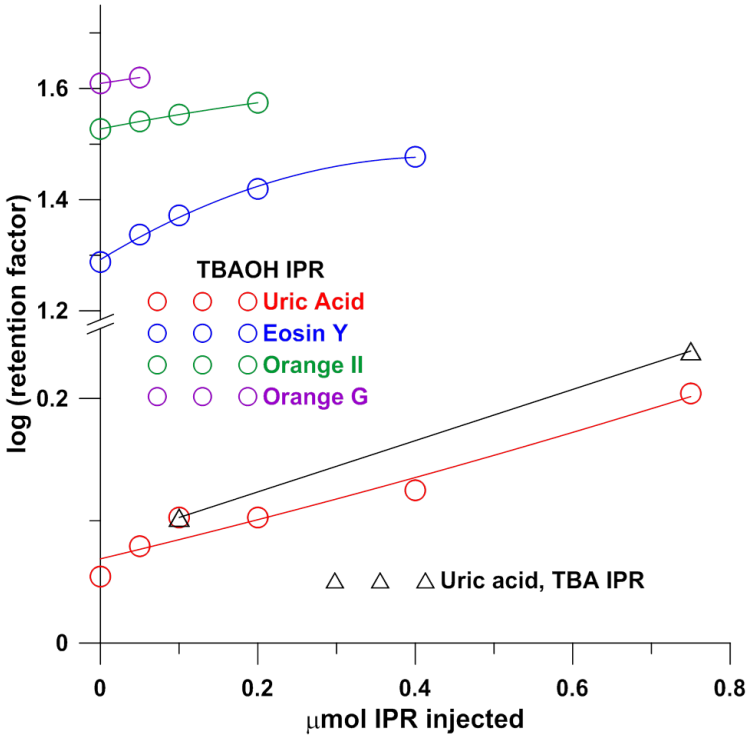

Figure G.4. Effect of IPR concentration on negatively charged analytes, negative ionization mode. Gradient elution conditions were used throughout. The best fit parameters appear in Table S5.

Column Compatibility and Gradient TIPs.

Stronger mobile phase strengths made both the analytes and the pairing reagent elute faster and thus decreased both t_b and t_R (see Table S6 in SI). A common reason for using IPC is to handle analytes that elute near the void volume; if a gradient is used, it needs to at least start with a mobile phase of relatively weak eluting power that maximizes analyte retention. Gradient elution clearly has benefits; compare the apparent efficiencies of NOR under gradient vs. isocratic elution in Table S3 (the very low numbers stem from relatively poor retention). To exploit the power of gradient elution in TIPS to the fullest, columns compatible with very weak mobile phases (down to purely aqueous phases) are preferred.

Effect of the Interinjection Interval.

It is difficult to predict *a priori* how the interval between the injections of the IPR and the introduction of the sample will affect the results. While it can be used under appropriate conditions to spread out / smear the reagent zone and increase the column length over which the analyte interacts with the reagent, it will also decrease t_b and reduce the available elution window. In addition, analyte retention is also proportional to the local concentration of the IPR in some manner, and increasing the length of the reagent zone but decreasing the extent of interaction may not result in any net gain. Indeed if retention is proportional not linearly to the [IPR] but to [IPR]^n where n>1, a smaller IPR zone of higher concentration will lead to greater overall retention. In the absence of any electrolytes in the eluent, application of the Stern-Guoy-Chapman double layer theory[257] will suggest that this is more likely to be the norm. For PFHA at %B ≤10% (and at even higher %B values for TBAOH), the retention factor is very high. If the mobile phase composition temporal profile is kept the same as has been described thus far, minor increases in the interinjection interval from the minimum 0.43 min was not expected to have a significant effect on t_R or signal intensity: virtually identical t_b values for various delay times for either PFHA or TBAOH as IPRs with gradient elution were observed with intervals between 0.43 and 2.43 min (see Table S7, zero interinjection interval with isocratic elution was achieved by drawing reagent and sample plugs sequentially and injecting them. This is essentially the same as mixing reagent and analyte beforehand and injecting the mixture.[258] However, this approach was not found to be especially attractive). Interestingly, NOR and TYR behaved in opposite ways with zero delay relative to 0.43 min delay: t_R decreased for NOR but increased for TYR in a minor fashion. For throughput considerations, the delay should not be long. Based on the overall pattern from the data in Table S7, it seems reasonable to assume that the delay will usually have limited effect on analyte retention in TIPS when the pairing reagent is strongly retained under the initial elution condition. However, as the process is complex, evaluating the effect of the delay has to remain a part of the TIPS method development for a new analyte or a new eluent composition.

The IPR zone broadens with increasing amounts of IPR due to overloading, and also with stronger initial mobile phase strength. When %B was kept at 20% until 1 min and

then lowered to 10% for isocratic elution, t_b for 0.2 μmol of PFHA was only 1.7 min, suggesting that the IPR zone now occupied the majority of the column. This extended IPR zone of diminished concentration led to somewhat reduced retention for TYR, NOR, and MGZ, in accordance with the double layer retention model.[13]

Comparison of TIPS with no IPR and Conventional IPC.

As previously stated, the use of an IPR in the mobile phase as in conventional IPC can contaminate the mass spectrometer ion source badly, requiring extensive cleaning. With certain IPRs, when used in the IPC mode, it is also very difficult to completely clean a column from the IPR, some experts assert that only dedicated columns should be used for IPC.[259] With affection for our best mass spectrometer and a new sub-2 μm column, we conducted the first half of the comparison experiment using a 3 μm particle size short length ODS column on an Agilent 1200 LC/MSD in ESI mode. Exact conditions for the gradient elution conditions are given in the Supporting Information. The red trace of Fig. G5 shows the best separation we could attain for NOR, TYR, MGZ, and Erythromycin (ERY), each monitored in the selected ion monitoring (SIM) mode. The blue trace is the best separation obtained with 10 mM PFHA in both components of the binary mobile phase. TYR has intrinsically poor sensitivity and this is not improved under any chromatographic condition. Without any IPR (red trace), MGZ tails badly and ERY exhibits an odd distorted peak shape. In the IPC mode (IPR in the mobile phase, blue trace), all of the peak shapes are dramatically better but response for MGZ and ERY are both dramatically worse (these chromatograms were obtained with the same detector sensitivity settings). This loss in sensitivity occurs even though PFHA is a volatile IPR and its effects are not as deleterious as some others we have had experience with. The upper traces utilize the column and described in the Experimental Section; the magnitudes of the upper and lower traces should not be compared as they are obtained with different mass spectrometers. On this column, NOR, TYR and MGZ essentially co-elute without any IPR (light gray trace), NOR eluting in the void volume. In the TIPS mode, all peaks are well separated and symmetric, NOR is moved off the void volume. The ERY peak actually elutes just after t_b, resulting in

appreciable loss of response but not as drastic as that observed with the IPR in the mobile phase.

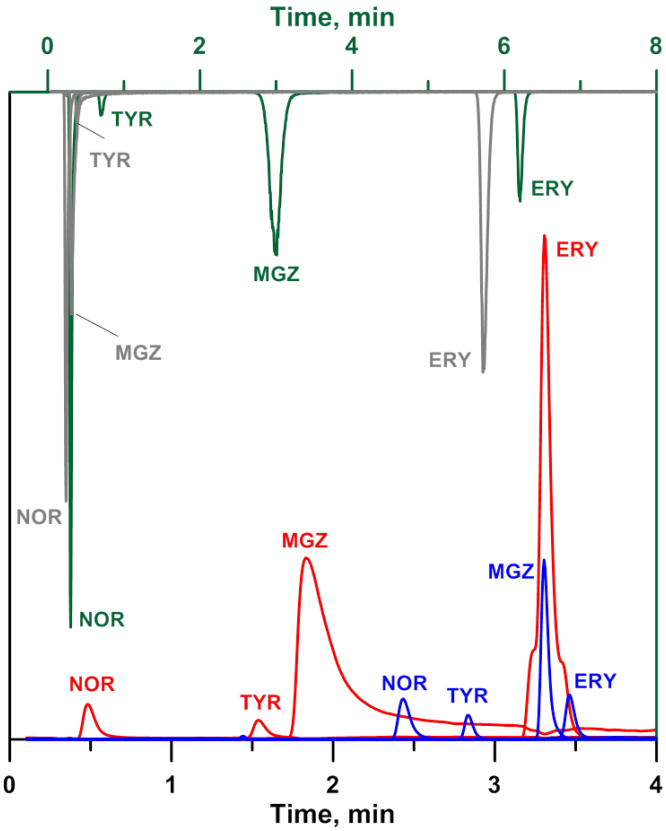

Figure G.5. Advantage of TIPS. Bottom Half: Separation on a 23 mm 3 μm C18 column. Red trace: without IPR, Blue trace: IPC mode with 10 mM PFHA. Top half: 50 mm 1.8 μm C18 column. Gray trace: without IPR, Green trace: TIPS 1 μmol PFHA. See SI for details.

Figure 6 shows the benefit of TIPS for some real samples containing hydrophilic charged moieties that have been problematic for us in the past. Figure 6a shows the TIPS chromatogram (m/z 142.069) for a small hydrophilic amine metabolite at very low levels in a microsomal incubation sample of a proprietary compound with 0.05 μmole PFHA as the IPR. This compound eluted in the void volume without an IPR. Figure 6b shows the TIPS chromatogram of 5 phosphates frequently encountered in biological samples on a reverse phase column with 0.75 μmole TBAOH as IPR; without the IPR, all eluted near the void volume.

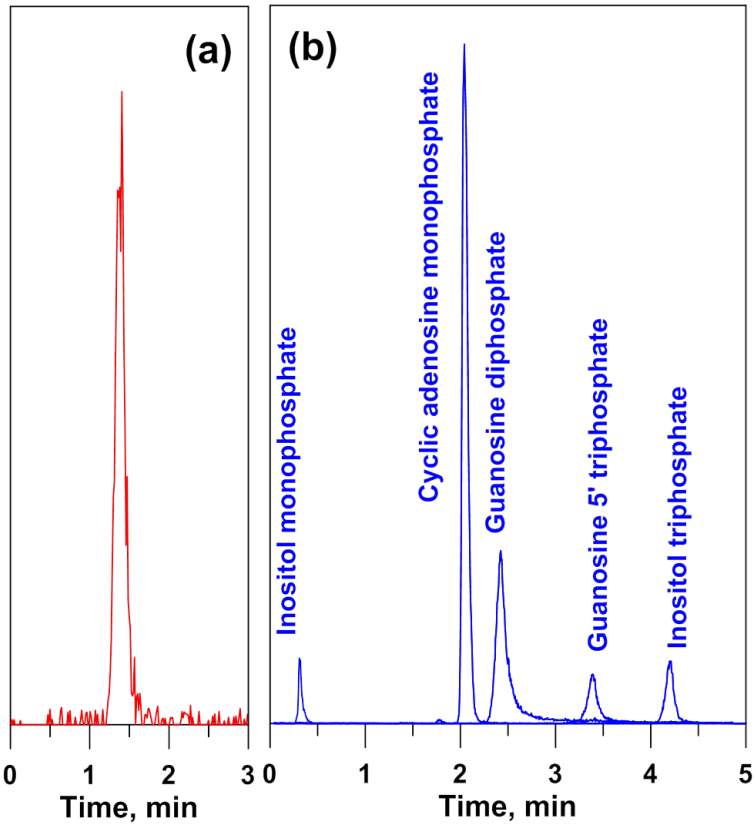

Figure G.6. (a) TIPS chromatograms for a highly hydrophilic metabolite form a microsomal incubation sample of a proprietary compound under 0.05 μmole PFHA as IPR, positive MS mode, 2%B isocratic elution; (b) mixture of phosphates (2.5 μM ea. with 0.75 μmole TBAOH as IPR, negative MS mode, gradient profile was the same as depicted in Fig. G2 but initiated with 0%B.

Tables S8 and S9 in Supporting Information respectively lists illustrative linear dynamic ranges, calibration parameters and t_R/peak area reproducibilities with and without TIPS. As TIPS causes increase retention, limits of detection generally decrease (but without TIPS separation is poor) and the linear dynamic range shifts up to a higher level. There were no discernible differences in reproducibilities with and without TIPS.

Illustrative Application to Ionic Separations. While we have focused this study towards the separation of charged or protolyzable organic species, a logical extension will be the separation of small organic and inorganic anions by using a cationic IPR, noting that

its IPC counterpart, often referred to as dynamic ion exchange or mobile phase ion chromatography, has been known for three decades.[3] Unlike what has been practiced, however, there will be a far larger choices of detection modes if detection is made before t_b. Figure 7 shows a separation of iodate and nitrate with an optical absorbance detector with optically transparent Na_2SO_4 as the eluent. The retention can be altered by either the nature or concentration of the eluent, or by the amount of IPR injected. This operational mode provides a very large working window before the IPR elutes.

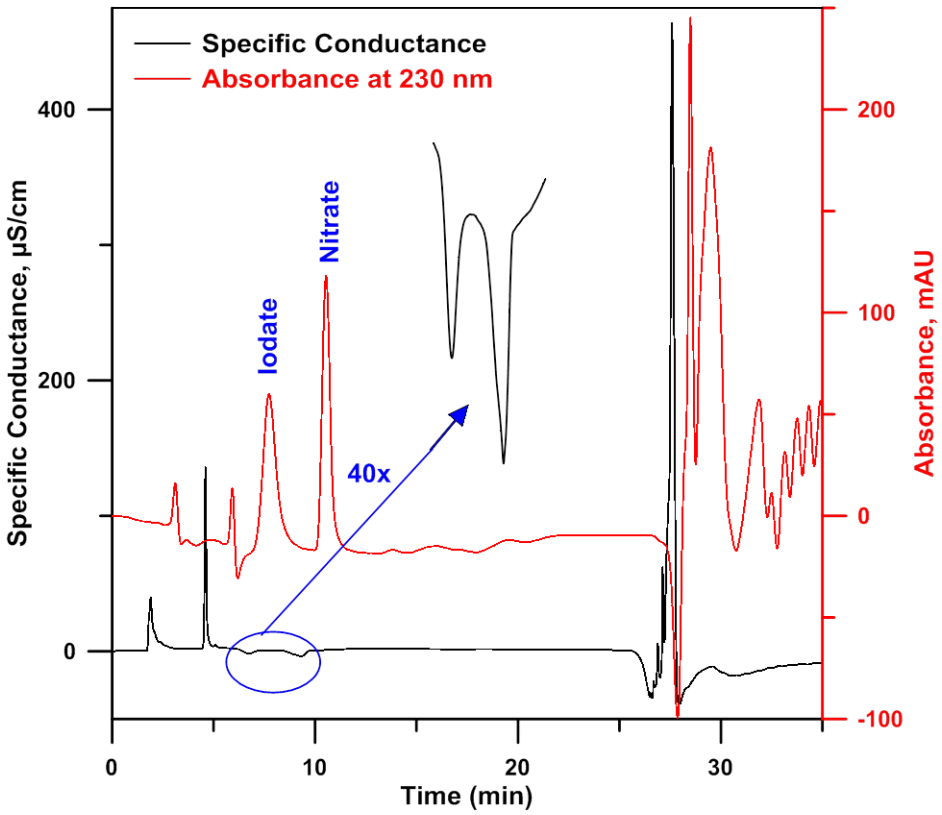

Figure G.7. Separation of two small inorganic ions on a reverse phase column using TIPS. The eluent was 0.2 mM Na_2SO_4 in 5;95 v/v acetonitrile water until 26.5 min when it was switched to 100% acetonitrile for 5 min and then returned to the original composition. Hexadecyltrimethylammonium chloride (100 nmol) was injected as the IPR followed 3 min later by 5 nmol ea. of KIO_3 and KNO_3. The column effluent went first through a conductivity detector and then an optical absorbance detector with a transit time of ~1.2 min. Note that while large positive peaks for the two optically absorbing analytes appear in the absorbance-based chromatogram – the same analytes are visible in the conductance trace as negative peaks as they replace the higher mobility sulfate ion. The IPR and the associated impurities do not actually elute until the eluent acetonitrile content is switched to 100% as a step function, leaving a large working window.

Simulations.

It is simple to simulate the basic separation process in TIPS. An IPR is injected and moves along according to its own chromatographic characteristics (retention factor). A pair (or more) of analytes is then injected and moves along rapidly without separation until it comes in contact with the IPR zone where their retention factor increases and is a function of the local IPR concentration and is different for the different analytes, resulting in the separation of the analytes as they move down the IPR zone. An illustrative video (TIPS.avi) generated by MS Excel simulation where the various retention factors can be input by the user and the progress of the different components down the column can be represented in a 4-bit color code are both given as a supplementary file and more details about it are given in the Supporting Information.

G.4 Conclusions

TIPS addresses two major drawbacks of IPC for ESI-MS, namely ion suppression and source contamination from the IPR. Like IPC it can significantly improve peak shape and retention for applicable analytes. Either volatile or nonvolatile IPRs can be used. Prior determination of t_b is important and can be carried out with suitable non-MS detectors to avoid source contamination. Unlike in IPC, the IPR does not enter pumping/degassing systems, facilitating optimization, cleanup, and switching between TIPS and non-TIPS methods and from one IPR to another.

TIPS is not a panacea, however. In addition to analytes that benefit from TIPS, there can be analytes of interest in a mixture that are retained strongly enough that they do not elute before t_b. If the choice of IPRs, their amounts, eluent gradients, etc. are all ineffective, alternate separation modes or running two chromatograms (with and without TIPS) will have to be considered.

The present paper is only an initial exploration of a concept: instead of seeking the perfect column for a given separation among myriad column choices, one picks from a small number of highly efficient stationary phases that can be modified with one or more reagents that are adsorbed on a transient basis. Importantly, in situations other than the analysis of charged species, the interaction does not need to be ionic or electrostatic and the adsorbed reagent and/or analytes may be uncharged. Chiral separations should be possible with a chiral reagent adsorbed in a transient fashion. With a zwitterionic agent that affects retention more than CHAPS, HILIC-like separation of uncharged hydrophilic compounds is another possibility. In most cases the curious experimenter has a far greater choice of reagents that can be adsorbed in a transient fashion than the choice of columns easily available to her. Appropriate observation of the retention behavior of the reagent itself, and that of the analyte(s) with the adsorbed reagent along with appropriate modeling can provide much quantitative information on the analyte-reagent interaction, including the study of host-guest systems, while utilizing relatively small amounts of material. We have only examined arguably the simplest possible configuration. The degree of complexity that such systems can be capable of, including the use of multiple injectors and multiple reagents simultaneously or sequentially introduced at variable intervals, the use of strong and weak eluent pulsing and the nature of the gradient profile, etc. are best left to imagination.

Appendix: H

Unfinished Projects

H.1 Electrodialytic Generations of Anions standards

This project involves Electrodialytic generation of anions (or cations) as Faradaically traceable standards for potential use in ion chromatography. Electrodialytic generation of ionic standards would eliminate the labor-extensive and error-prone standard preparation in Ion chromatography. The standard concentration ranges needed for typical ions analysis in ion Chromatography are often smaller than 1 mM. Thus the current range to be supplied to the bead should be in the nA level range (subject to the flow rate used). In order to provide such small current a power supply was built, commercial power supply providing nA current are very expensive (≥$2000).

The project was abandoned due to low efficiency and irreproducible results.

H.2 Cyanide detection paper device

This project used a cobinamide based reagent for the colorimetric determination of cyanide.

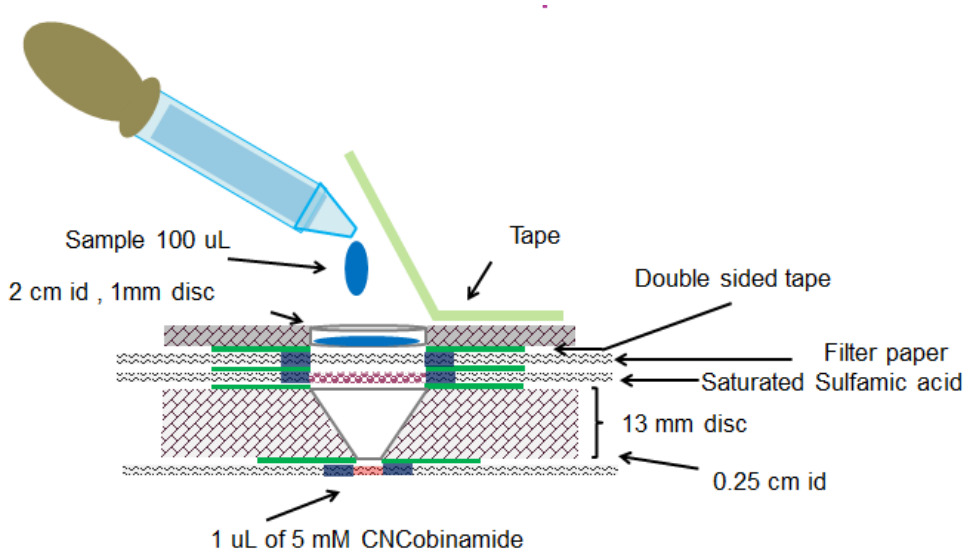

Figure H.1. Schematic of Cyanide detection paper device.

The project was abandoned due to insufficient available time.

Appendix I:

Ongoing Projects

I.1 Cations and Anions distributions in Dry Blood Spots

Cations and Anions distributions in an unaltered human blood spots are studied, along with spiked bovine blood spots, and Standards Cations and Anions without blood in an aqueous solvent. All of the punches extract undergo Anion and Cation chromatographic separations.

I.2 Optimum Detection Volume in HPLC Absorbance Detection

Absorbance Detection in Liquid Chromatography is studied: Sensitivity Improvement with Increasing Pathlength vs. Chromatographic Resolution Dilemma.

I.3 Simulating Dispersion under Laminar Flow

Microsoft Excel is used as a simulation tool. We show that through the repetition of molecular diffusion and laminar flow profile processes we can simulate dispersion.

I.4 Prediction of a dispersed signal

We demonstrate that by assuming a lognormal distribution or exponential distribution we can mathematically predict the dispersed signal knowing its original and the dispersion conditions.

LITERATURE CITED

(1) Kadjo, A; Dasgupta, P; Su, J; Liu, S; Kraiczek, K. *Analytical Chemistry*. **2017**, 89, 3884–3892.

(2) Kadjo, A; Liao, H; Dasgupta, P; Kraiczek, K. *Analytical Chemistry*. **2017**, 89, 3893–3900.

(3) Kadjo, A.; Stamos, B.; Berg, J.; Blount, B.; Dasgupta, P. *Analytical Chemistry*. **2016**, 88, 6531-6537.

(4) Hildenbrand, Z.L.; Carlton, D.D.; Fontenot, B.; Meik, J.M.; Walton, J.; Taylor, J.; Thacker, J.; Korlie, S.; Shelor, C. P.; Henderson, D.; Kadjo, A.F.; Roelke, C.; Hudak, P.F.; Burton, T.; Rifai, H.S.; Schug, K.A. *Environmental Science and Technology*. **2015**, 49, 8254-8262.

(5) Thacker, J. B.; Carlton, D.D.; Hildenbrand, Z.L.; Kadjo, A.F.; Schug, K.A. *Water*. **2015**, 7, 1568-1579.

(6) Hildenbrand, Z.L.; Carlton, D.D.; Fontenot, B.E.; Meik, J.M.; Walton, J.L.; Thacker, J.B.; Korlie, S.; Shelor, C. P.; Kadjo, A.F.; Clark, A.; Usenko, S.; Hamilton, J.S.; Mach, P.M.; Verbeck, G.F.; Hudak ,P.; Schug, K. A. *Science of The Total Environment.* **2016**, 1562, 906-913.

(7) Kadjo, A.F.; Dasgupta, P.K.; Boss, G.R. *Analytical Methods*. **2015**, 7, 5707-5711.

(8) Shelor, C.P.; Liao, H.; Kadjo, A.F.; Dasgupta, P.K. *Analytical Chemistry*. **2015**, 87, 4851-4855.

(9) Liao, H.; Kadjo, A.F.; Dasgupta, P.K. *Analytical Chemistry*. **2015**, 87, 8342-8346.

(10) Wahab, M. F.; Dasgupta, P.K.; Kadjo, A.F.; Armstrong D. W. *Analytica Chimica Acta*. **2016**, 907, 31-44.

(11) Liu, H.; Lam, L.; Chi, B.; Kadjo, A.F. Dasgupta, P.K. *Analytical Chemistry*. **2016**, 88, 2059–2064.

(12) Dyson, N. A. *Chromatographic integration methods*; Royal Society of Chemistry, Information Services: Cambridge, 1998.

(13) Bonsall, R. B. *Journal of Chromatographic Science.* **1964**, *2*, 277–284.

(14) Pietrzyk, D. in Kuwana, T. Ed. *Physical Methods in Modern Chemical Analysis, Vol. 2*, Academic Press, 1980.

(15) Hewlett Packard. *Laboratory Guide,* **1973,** 76. HP 3352 Lab Data System. http://pubs.acs.org /doi/pdf/10.1021/ac60332a722

(16) Hewlett Packard. *Anal. Chem.* **1975,** *47,* 432A

(17) Dionex Themo Fisher. Ultimate 3000. http://www.dionex.com/en-us/products/liquid-chromatography/lc-systems/rslc/lp-72455.html

(18) Stadermann,M.; McBrady, A. D.; Dick, B.; Reid, V. R.; Noy, A.; Synovec, R. E.; Bakajin, O. *Anal. Chem*. **2006**, *78*, 5639-5644.

(19) Fitz, B. D; Reaser, B. C.; Pinkerton, D. K.; Hoggard, J. C.; Skogerboe, K. J.; Synovec, R. E. *Anal. Chem*. **2014**, *86*, 3973-3979.

(20) Grant, D. W.; Clarke, A.; *Anal. Chem*. **1971**, *43,* 1951-1957

(21) Snyder, L. R.; *J chromatogr. Sci*. **1972**, *10,* 200-212.

(22) Meyer, V. R.; *Adv. Chromatogr*. **1995**, *35,* 383-416.

(23) McCoy, R. W.; Aiken, R. L.; Pauls, R. E.; Ziegel, E. R.; Wolf ,T.; Fritz, G. T.; Marmion, D. M.; *J. Chromatogr. Sci*. **1984**, *22,* 425-431.

(24) Cram, S. P.; Chesler, S. N.; Brown, A. C.; *J. Chromatogr.* **1976**, *126,* 279-300.

(25) Sharma, B.K. *Chromatography*; Goel Publishing House, Meerut: India, 1993

(26) Liu, H.; Lam, L.; Yan, L.; Chi, B. Dasgupta, P. K. *Anal. Chim. Acta* **2014,** *850*, 65-70.

(27) Ramsing, A. U.; Růžička, J.; Hansen, E. H. *Anal. Chim. Acta*. **1981**, *124*, 1-17.

(28) Stewart, K. K. *Anal. Chim. Acta*. **1986**, *179*, 59-68.

(29) Rhee, J.; Dasgupta, P. K.; *Mikrochim. Acta* **1985**, III, 49-64.

(30) Rhee, J.; Dasgupta, P. K.; *Mikrochim. Acta* **1985**, III, 107-122.

(31) Baeza-Baeza, J. J.; Ortiz-Bolsico, C.; García-Álvarez-Coque, M. C. *Anal. Chim. Acta* **2013,** *758,* 34-44.

(32) McGillicuddy, N.; Nesterenko, E. P.; Jones, P.; Caldarola, D.; Onida, B.; Townsend, A. D.; Mitev, D. P.; Nesterenko, P. N.; Paull, B. *Anal. Methods* **2013,** *5,* 2666-2673.

(33) Cassidy, R. M.; Elchuk, S.; Dasgupta, P. K. *Anal. Chem.* **1987,** *59*, 85-90.

(34) https://hmc.usp.org/sites/default/files/documents/HMC/GCs-Pdfs/GC_pdf_USP38/c621.pdf pp 7-8. Accessed January 17, 2017.

(35) Pápai, Zs.; Pap, T. L. *J. Chromatogr. A* **2002,** *953,* 31-38.

(36) Pauls, R. E.; Rogers, L. B.; *Anal. Chem*. **1977**, *49*, 625-628.

(37) Yau, W. W.; *Anal. Chem*. **1977**, *49*, 395–398.

(38) Foley, J. P.; Dorsey, J. G. *J. Chromatogr. Sci.* **1984,** *22,* 40-46.

(39) Torres-Lapasio, J. R.; Baeza-Baeza, J. J.; García-Alvarez-Coque, M. C. *Anal. Chem.* **1997,** *69,* 3822–3831.

(40) Kadjo, A; Liao, H; Dasgupta, P; Kraiczek, K. Width Based Quantitation of Chromatographic Peaks. Beyond Height and Area. Analytical Chemistry. 2017, 89, 3893–3900

(41) Petersen, K.; Lopez, J. L.; Dasgupta, P. K. *J. Chemometrics* **1989,** *3*, 601-608.

(42) Karnes, H. T.; Clark, M. *J. Pharm. Biomed. Anal.* **1991,** *9,* 911–918.

(43) Jurkiewicz, K.; Dasgupta, P. K. *Anal. Chem.* **1987,** *59***,** 1362-1364.

(44) Liao, H.; Dasgupta, P. K.; *Anal. Chem*. **2016**, *88,* 2198-2204

(45) Liao, H.; Shelor, C. P.; Dasgupta, P. K. *Anal. Chem.*, **2016,** *88*, 4965-4970

(46) Berglund, I.; Dasgupta, P. K.; Lopez, J. L.; Nara, O. *Anal*. *Chem.* **1993,** *65*, 1192-1198.

(47) Sjögren, A.; Dasgupta, P. K. *Anal. Chem.* **1995,** *67***,** 2110-2118.

(48) Sjögren, A.; Dasgupta, P. K. *Anal. Chim. Acta* **1999,** *384,* 135-141.

(49) Al-Horr, R.; Dasgupta, P. K.; Adams, R. L. *Anal. Chem.* **2001,** *73,* 4694-4703.

(50) Liao, H.; Dasgupta, P. K.; Srinivasan, K.; Liu, Y. *Anal. Chem.* **2015,** *87,* 793-800

(51) Liao, H.; Kadjo, A. F.; Dasgupta, P. K. *Anal. Chem.* **2015,** *87*, 8342-8346.

52 Agilent Technologies. HDR-DAD solution.

(53) Pendergrast, M. Mirror Mirror: A History of the Human Love Affair with Reflection. Basic Books, New York, 2009.

(54) Makin, A.; David, J.; Pecchinenda, A.; Bertamini, M.; *Emotion,* **2012,** *12,* 1021-1030.

(55) Baeza-Baeza, J. J.;Ortiz-Bolsico, C.; M. J.; García-Alvarez-Coque, M. C. *Chromatography* **2015,** *2,* 625-641.

(56) Yost, R.; Stoveken, J.; MacLean, W. *J. Chromatogr. A* **1977,** *134,* 73-82.

(57) Drouen, A. C. J. H.; Billiet, H. A. H.; De Galan, L. *Anal. Chem.* **1984,** *56*, 971-978.

(58) Seaton, G. G. R.; Fell, A. F. *Chromatographia* **1987**, *24*, 208-216.

(59) Maeder, M. *Anal. Chem.* **1987,** *59*, 527-530.

(60) Keller, H. R.; Massart, D. L. *Anal. Chim. Acta* **1991,** *246*, 379-390.

(61) Guthrie, R.; Susi, A. *Pediatrics*. **1963**, *32,* 338-343.

(62) Zytkovicz, T. H. Fitzgerald, E. F. Marsden, D. Larson, C. a; Shih, V. E. Johnson, D. M. Strauss, W. Comeau, M. Eaton, R. B.; Grady, G. F. *Clin. Chem*. **2001**, *47*, 1945-55.

(63) Therrell, B. L. Hannon, W. H. Pass, K. A.; Lorey, F. Brokopp, C. Eckman, J. Glass, M. Heidenreich, R. Kinney, S. Kling, S. Landenburger, G. Meaney, F. J. McCabe, E. R. Panny, S. Schwartz, M.; Shapira, E. *Biochem. Mol. Med*. **1996**, *57*, 116-24.

(64) Sherman, G. G.; Stevens, G.; Jones, S. A.; Horsfield, P. M. T; Stevens, Wendy, S. M. *J. AIDS* **2005**, *38*, 615-617.

(65) Allanson, A. L.; Cotton, M.M. Tettey, J. N. A.; Boytera, A.C. *J. Pharm. Biomed. Anal.* **2007,** *44*, 963-969.

(66) Otero-santos, S. M.; Delinsky, A. D.; Valentin-Blasini, L.; Schiffer, J.; Blount, B. C. *Anal. Chem.* **2009,** *81,* 1931-1936.

(67) Spooner, N. Lad, R.; Barfield, M. *Anal. Chem*. **2009**, *81*, 1557-63.

(68) Barfield, M.; Spooner, N.; Lad, R. Parry, S.; Fowles, S. *J. Chromatogr. B,* **2008**, *870*, 32-37.

(69) McCabe, E. R. *Genome Res*. **1991**, *1*, 99-106.

(70) Edelbroek, P. M.: van der Heijden, J.; Stolk, L. M. L. Dried Blood Spot Methods in Therapeutic Drug Monitoring: Methods, Assays, and Pitfalls. *Therap. Drug Monit*. **2009**, *31*, 327-336.

(71) Li, W.; Tse, F. L. S. *Biomed. Chromatogr*. **2010**, *24*, 49-65.

(72) Rashed, M. S.; Bucknall, M. P.; Little, D.; Awad, A.; Jacob, M.; Alamoudi, M.; Alwattar, M.; Ozand, P. T. *Clin. Chem*. **1997**, *43*, 1129-1141.

(73) Chace, D. H.; Kalas, T. A.; Naylor, E. W. *Clin. Chem*. **2003**, *49*, 1797-1817.

(74) Chace, D. H. Hillman, S. L. Millington, D. S. Kahler, S. G. Adam, B. W.; Levy, H. L. *Clin. Chem*. **1996**, *42*, 349-55.

(75) Chace, D. H. Lim, T. Hansen, C. R. Adam, B. W.; Hannon, W. H. *Clin. Chim. Acta* **2009**, *402*, 14-18.

(76) Dintenfass, L. *Angiology* **1962**, *13*, 333-344.

(77) Adam, B. W.; Alexander, J. R.; Smith, S. J.; Chace, D. H.; Loeber, J. G.; Elvers, L. H.; Hannon, W. H. *Clin. Chem.* **2000,** *46,* 126-128.

(78) Hilder, E. F. *Aust. J. Chem.* **2011**, *64*, 843.

(79) Hilder, E. F.; Hon, W. B. U. S. Pat. App. Publication US 20140127669 A1, May 8, 2014.

(80) Erhardt, J. G.; Craft, N. E.; Heinrich, F.; Biesalski, H. K. *J. Nutr.* **2002,** *132,* 318-321.

(81) Bremmer, R. H.; de Bruin, K. G.; van Gemert, M. J. C.; Leeuwen, T. G.; Aalders, M. C. G.; *Forensic Sci. Int.*, **2012**, *216*, 1-11.

(82) Strasser, S.; Zink, A.; Kada, G.; Hinterdorfer, P.; Peschel, O.; Heckl, W. M.; Nerlich, A.G.; Thalhammer, S.; *Forensic Sci. Int*, **2006**, *170*, 8-14.

(83) Atlas, S. A. *J. Manage. Care Pharm.* **2007**, *13*, S9-S20.

(84) Howanitz, J. H.; Howanitz, P. J. *Am. J. Clin. Path*. **2007**, *127*, 56-59.

(85) Rao, D. A.; Tao, L.; Bhusan, V. First Aid for US Mle. **2008.** McGraw Hill Medical, New York.

(86) Reference range list from Uppsala University Hospital. *Laborationslista*. Article No. 40284 Sj74a. April 22, 2008

(87) de Rosny, G.; Chanzy, A.; Parde´, M.; Gaudu, J.-C.; Frangi, J.-P.; Laurent, J.-P. *J. Soil Soc. Am.* **2001,** *65,* 13-18.

(88) Bolvin, H.; Chambarel, A.; Chanzy, A. *J. Soil Soc. Am.* **2004,** *68,* 440-446.

(89) Dasgupta, P. K.; Surowiec, K. *Analytical chemistry*. **1996**, *68*, 1164-1168.

(90) Dasgupta, P. K.; Surowiec, K. *Anal. Chem*. **1996**, *68*, 4291-4299.

(91) Park, S. R.; Swerdlow, H. *Electroanalysis*. **2007**, *19*, 2294-2300.

(92) Voloudakis, K.; Vrahliotis, P.; Kastrinakis, E. G.; Nychas, S. G. *Meas. Sci. Technol.* **1999,** *10,* 100-105.

(93) Haber, C.; Jones, W. R.; Soglia, J.; Surve, M. A.; McGlynn, M.; Caplan, A.; Reineck, J. R.; Krstanovic, C. *J. Cap. Electrophoresis* 1996, 3(1), 1-11.

(94) Kim, C. Y. *Prog. Electromagnetics Res. B*, **2008,** *8,* 179-194.

(95) Olthuis, W.; Streekstra, W.; Bergveld, P. *Sensors Actuators B,* **1995,** *24,* 252-256.

(96) la Marca, G.; Malvagia, S.; Pasquini, E.; Innocenti, M.; Fernandez, M. R.; Donati, M. A.; Zammarchi, E. *Rapid Comm. Mass Spectrom.* **2008**, *22*, 812–818.

(97) Fachiroh, J.; Prasetyanti, P. R.; Paramita, D. K.; Prasetyawati, A. T.; Anggrahini, D. W.; Haryana, S. M.; Middeldorp, S. M. *J. Clin. Microbiol.* **2008,** *46,* 1374-1380.

(98) Vidic, R.D; Brantley, S.L; Vandenbossche, J.M; Yoxtheimer, D; Abad JD. *Science,* **2013**, 340, 6134.

(99) Jackson, R.B; *et al. Annual Review of Environment and Resources,* **2014**, 39,1

(100) Healy, R.W; Bartos, T.T; Rice, C.A;, Mckinley, M.P; Smith, B.D. *Journal of Hydrology,* **2011**, 403, 37-48.

(101) Vengosh, A; Jackson, R.B; Warner, N; Darrah, T.H; Kondash, A .*Environ Sci Technol* , **2014** (in Eng).

(102) Mittal, A; Rusco, F. Report to the Ranking Member, Committee on Science, Space, and Technology, House of Representatives. Energy-Water Nexus Information on the Quantity, Quality, and Management of Water Produced during Oil and Gas Production, GAO-12-156. **2012**, (Government Accountability Office)

(103) Clark, C.E; Veil, J.A. Produced Water Volumes and Management Practices in the United States, ANL/EVS/R-09/1. **2009** (Argonne National Laboratory).

(104) Warner, N.R; Christie, C.A; Jackson, R.B; Vengosh, A. *Environ Sci Technol,* **2013**, 47, 11849-11857.

(105) Olmstead, S.M; Muehlenbachs, L.A; Shih, J.S; Chu, Z; Krupnick, A.J. *Proc Natl Acad Sci U S A,* **2013**, 110, 4962-4967.

(106) Darrah, T.H; Vengosh, A; Jackson, R.B; Warner, N; Poreda, R.J. *Proceedings of the National Academy of Sciences of the United States of America,* **2014**, 111, 14076-14081.

(107) Osborn, S.G; Vengosh, A; Warner, N.R; Jackson, R.B; Methane contamination of drinking water accompanying gas-well drilling and hydraulic fracturing. *Proc Natl Acad Sci U S A,* **2011**, 108, 8172-8176 (in eng).

(108) Jackson, R.B; *et al. Proc Natl Acad Sci U S A,* **2013**, 110, 11250-11255.

(109) Warner, N.R; *et al*. *Proceedings of the National Academy of Sciences,* **2012** 109, 11961-11966.

(110) Warner, N.R; Christie, C.A; Jackson, R.B; *Environ Sci Technol*, **2013**, 47, 11849-11857.

(111) Fontenot, B.E; *et al. Environ Sci Technol,* **2013**, 47, 10032-10040 (in eng).

(112) Jackson, R.E; *et al. Ground Water,* **2013**, 51, 488-510.

(113) Ingraffea, A.R. Fluid Migration Mechanism Due to Faulty Well Design and/or Construction: An Overview and Recent Experiences in the Pennsylvania Marcellus Play.

(114) Aquilina L. *et al.Science Of The Total Environment,* **2012**, 435, 436167-178.

(115) Flury, M; Papritz, A. *J. Environ. Qual.* **1993**, 22, 747-758.

(116) Chellemi DO. *et al*. *Crop Protection,* **2013**, 43, 94-103.

(117) C. Männel-Croisé and F. Zelder, *Anal. Methods,* **2012**, 4**,** 2632-2634.

(118) F. Zelder, *Inorg. Chem.*, **2008**, 47**,** 1264–1266.

(119) C. Männel-Croisé and F. Zelder, *Inorg. Chem.* **2009**, 48**,** 1272-1274.

(120) C. Männel-Croisé, B. Probst and F. Zelder, *Anal. Chem.,* **2009**, 81**,** 9493-9498.

(121) C. Männel-Croisé, C. Meister and F. Zelder, *Inorg. Chem.*, **2010**, 49**,** 10220-10222.

(122) C. Männel-Croisé and F. Zelder, *ACS Appl. Mater. Interfaces*, **2012**, 4**,** 725-729.

(123) J. Ma and P. K. Dasgupta, *Anal. Chim. Acta* **2010**, 673**,** 117-125.

(124) K. E. Broderick, P. Potluri, S. Zhuang, I. E. Scheffler, V. S. Sharma, R. B. Pilz and G. R. Boss, *Exp. Biol. Med.*, **2006**, 231**,** 641-649.

(125) K. E. Broderick, M. Balasubramanian, A, Chan, P. Potluri, J. Feala, D. D. Belke, A. McCulloch, V. S. Sharma, R. B. Pilz, T. D. Bigby and G. R. Boss, *Exp. Biol. Med.*, **2007**, 232**,** 789-798.

(126) K. A. Kreuter, J. Lee, S. B. Mahon, J. G. Kim, D. Mukai, O. Mohammmad, W. Blackledge, G. R. Boss, B. J. Tromberg, and M. Brenner, *Chest*, **2008**, 134 (4_MeetingAbstracts):p124001

(127) A. Chan, M. Balasubramanian, W. Blackledge, O. M. Mohammad, L. Alvarez, G. R. Boss and T. D. Bigby, *Clin. Toxicol.*, **2010**, 48, 709-717.

(128) J. Lee, O. Mohammad, M. Brenner, S. B. Mahon, V. S. Sharma, J. Kim, D. Mukai ; W. Blackledge, G. R. Boss, S. Goodman. K. A. Kreuter and R. Ahdout, *J. Biomed. Opt.,* **2010**,15(1), 017001

(129) M. Brenner, J. G. Kim, S. B. Mahon, J. Lee, K. A. Kreuter, W. Blackledge, D. Mukai, S. Patterson, O. Mohammad, V. S. Sharma and G. R. Boss, *Ann Emerg. Med.*, **2010**, 33**,** 352-363.

(130) A. Chan, D. L. Crankshaw, A. Monteil, S. E. Patterson, H. T. Nagasawa, J. E. Briggs, J. A. Kozocas, S. B. Mahon, M. Brenner, R. B. Pilz, T. D. Bigby and G. R. Boss, *Clin. Toxicol.,* **2011**, 49, 366-373.

(131) W. C. Blackledge, C. W. Blackledge, A. Griesel, S. B. Mahon, M. Brenner, R. B. Pilz and G. R. Boss, *Anal. Chem.*, **2010**, 82, 4216-4221.

(132) R. Swezey, W. Shinn, C. Green, D. R. Drover, G. B. Hammer, S. R. Schulman, A. Zajicek, D. A. Jett and G. R. Boss*, J. Anal. Toxicol.*, **2013**, 37, 382-385.

(133) H. Boehringer, W. Tong, R. Chung, G. Boss and B. O'Farrell, *Proc. SPI*E **2012**, 8317, 83710Z-1

(134) J. Ma, P. K. Dasgupta, W. Blackledge and G. R. Boss, *Anal. Chem*., **2010**, 82, 6244-6250.

(135) J. Ma, S.-I. Ohira, S. K. Mishra, M. Puanngam, P. K. Dasgupta, S. B. Mahon, M. Brenner and G. R. Boss, *Anal. Chem.,* **2011**, 83, 4319-4324.

(136) P. K. Dasgupta, S. B. Mahon, J. Ma, M. Brenner, J.-H. Wang, G. R. Boss, *Anal. Chim. Acta,* **2013**, 768, 129-135.

(137) J. Ma, P. K. Dasgupta, F. H. Zelder and G. R. Boss, *Anal. Chim. Acta*, **2012,** 736, 78-84.

(138) C. Lacroix, E. Saussereau, F. Boulanger and J. P. Goull, *J. Anal. Toxicol.,* **2011,** 35, 143–147.

(139) A. Sano, N. Kakimoto, and S. Takitani, *J. Chromatogr.*, **1992,** 582, 131–135.

(140) S. Chinaka, N. Takayama, Y. Michigami, and K. Ueda, *J. Chromatogr. B,* **1998**, 713, 353–359.

(141) P. Lundquist, H. Rosling and B.Sorbo, Clin. Chem. **1985**, 31, 591-595.

(142) C. J. Vessey, P. V. Cole and P. J. Simpson, *Br J Anaesth.* **1976**, 48, 651-660,

(143) S. R. Williams, http://toxicology.ucsd.edu/art%202%20methemoglobin.pdf

(144) http://www.drstandley.com/labvalues_hematology.shtml

(145) H. Uchida, L. J. Berliner and M. H. Klapper, *J. Biol. Chem.* **1970**, 245, 4606-4611.

(146) I. Uchida, C. Tashiro, Y. H. Koo, T. Mashimo and I. Yoshiya, *J. Clin. Anesth.* **1990**, 2, 86-90.

(147) M. H. Klapper and H. Uchida, *J. Biol. Chem.* **1971**, 246, 6849-6854.

(148) A. C. Anusiem, J. G. Beetlestone, and D. H. Irvine, *J. Chem. Soc. A*, **1968**, 960-969.

(149) D. C. Blumenthal and R. J. Kassner, , *J. Biol. Chem.* **1980**, 255, 5859-5863.

(150) Yang, B.; Takeuchi, T.; Dasgupta, P. K.; Umemura, T.; Ueki, Y.; Tsunoda, K-I. *Anal. Chem.* **2007**, *79,* 769-772

(151) Schlemmer, U.; Frolich, W.; Prieto, R. M.; Grases, F. *Mol. Nutr. Food Res.* **2009**, 53, S330−S375.

(152) Kell, D. B. *Arch. Toxicol*. **2010**, 84, 825−889.

(153) De Stefano, C.; Milea, D.; Sammartano, S. *J. Chem. Eng. Data.* **2003**, 48, 114-119

(154) Crea, F.; Crea, P.; De Stefano, C.; Milea, D.; Sammartano, S. *J. Mol. Liq*. **2008**, 138, 76-83.

(155) De Stefano, C.; Milea, D.; Pettignano, A.; Sammartano, S. *Anal. Bioanal. Chem.* **2003**, *376*. 1030-1040.

(156) Crea, F.; De Stefano, C.; Milea, D.; Sammartano, S. *Coord. Chem. Rev.* **2008**, *252*, 1108-1120.

(157) Liao, H.; Shelor, C. P.; Chen, Y.; Sabaa-Srur, A. U. O.; Smith, R. E.; Dasgupta, P. K. *J. Agric. Food Chem.* **2013,** *61,* 5928-5935

(158) Evans, W. J.; McCourtney, E. J.; Shrager, R. I. *J. Am. Oil Chem. Soc.* **1982**, *59*, 189-191.

(159) Talamond, P.; Gallon, G.; Treche, S. *J. Chromatogr. A***. 1998**, *805*, 143-147.

(160) Talamond, P.; Doulbeau, S.; Rochette, I.; Guyot, J. P.; Treche, S. *J. Chromatogr. A.* **2000**, *871*, 7-12.

(161) Chen, Q. C.; Li, B. W. *J. Chromatogr. A.* **2003**, *1018*. 41-52.

(162) Carlsson, N. G.; Bergman, E. L.; Skoglund, E.; Hasselblad, K.; Sandberg, A. S. *J. Agric. Food Chem.* **2001**, *49*, 1695-1701.

(163) Skoglund, E.; Carlsson, N. G.; Sandberg, A. S. *J. Agric. Food Chem.* **1998**, *46*, 1877-1882.

(164) Blaabjerg, K.; Hansen-Moller, J.; Poulsen, H. D. *J. Chromatogr. B.* **2010**, *878*, 347-354.

(165) Phillippy, B. Q.; Bland, J. M. *Anal. Biochem.* **1988**, *175*, 162-166.

(166) Binder, H.; Weber, P. C.; Siess, W. *Anal. Biochem.* **1985**, *148*, 220-227.

(167) Mathews, W. R.; Guido, D. M.; Huff, R. M. *Anal. Biochem.* **1988**, *168*, 63-70.

(168) Rounds, M. A.; Nielsen, S. S. *J. Chromatogr. A.* **1993**, *653*, 148-152.

(169) Shelor, C. P.; Liao, H.; Kadjo, A.; Dasgupta, P. K.; Ion Chromatographic Retention Behavior of a Sugar Polyphosphate. Pittsburgh Conference, **2013**. Abstract 1710-8

(170) Cosgrove, D. J. *Biochem. J.* **1963**, *89*, 172-175.

(171) Small, H. *Ion Chromatography*; Plenum Press: New York, 1989.

(172) Mo, Y. *Investigations in Capillary Liquid Chromatography*. MS Thesis, Texas Tech University. 1997.
(173) Walsh, S.; Diamond, D. *Talanta* **1995,** *42*, 561-572.
(174) Dasgupta, P. K. *J Chromatogr. A* **2008,** *1213,* 50-55.
(175) Caceci, M. S. *Anal. Chem.* **1989,** *61,* 2324-2327.
(176) Dasgupta, P. K. *Anal. Chem.* **1984,** *56,* 769-772.
(177) Lamb, J. D.; Smith, R. G. *J. Chromatogr. A* **1991,** *546,* 73-88
(178) Thermo Fisher Dionex. Ionpac Cryptand A1 Anion Exchange Column. October 2006. http://www.dionex.com/en-us/webdocs/4222-DS_IonPac_Cryptand%20A1_V30_released102706-R2.pdf Last accessed January 25, 2015.
(179) Karu, N.; Dicinoski, G.; Haddad, P. R. *TrAC, Trends Anal. Chem.* **2012,** *40,* 119–132.
(180) Al-Horr, R.; Dasgupta, P. K.; Adams, R. L. *Anal. Chem.* **2001,** *73,* 4694–4703.
(181) Liao, H.; Dasgupta, P. K.; Srinivasan, K.; Liu, Y. *Anal. Chem.* **2015,** *87,* 793–800.
(182) Li, L.; Rose, P.; Moore, P. K. *Annu. Rev. Pharmacol. Toxicol.* **2011,** *51*, 169–18**7.**
(183) Kuban, V.; Dasgupta, P. K. *Anal*. *Chem*. **1992,** *64*, 1106–1112.
(184) Lottermoser, B. *Mine Wastes. Characterization, Treatment and Environmental Impacts.* Springer, New York, 2010.
(185) Kuban, V.; Dasgupta, P. K.; Marx, J. N. *Anal*. *Chem*. **1992,** *64*, 36–43.
(186) Caliendo, G.; Cirino, G.; Santagada, V.; Wallace, J. L. *J. Med. Chem.* **2010,** *53*, 6275–6286.
(187) Ma, J.; Dasgupta, P. K. *Anal. Chim. Acta* **2010,** *673*, 117–125.
(188) Yang, X.; Du, J.; Li, Y. *Talanta* **2015,** *141,* 207-211.
(189) Ma, J.; Dasgupta, P. K.; Blackledge, W.; Boss, G. R. *Anal. Chem.* **2010,** *82,* 6244-6250.
(190) Giuriati, C.; Cavalli, S.; Gorni, A.; Badocco, D.; Pastore, P. *J. Chromatogr. A* **2004,** *1023,* 105–112.
(191) http://webbook.nist.gov/cgi/cbook.cgi?ID=C7783064&Mask=10#Solubility Last accessed February 19, 2015.
(192) Ma, J.; Dasgupta, P. K.; Blackledge, W.; Boss, G. R. *Environ. Sci. Technol.* **2010**, *44,* 3028-3034.

(193)Takeuchi, M.; Ishimine, K.; Miki, N.; Miyazaki, Y.; Tanaka, H. Abstract 401, 19th International Conference on Flow Injection Analysis and Related Techniques, November 30-December 5, 2014, Fukuoka, Japan.
(194) Kadjo, A. F.; Dasgupta, P. K. *Anal. Chim. Acta* **2013,** *773,* 1-8
(195) Ohira, S.I.; Kuhara, K.; Kudo, M.; Kodama, Y.; Dasgupta, P. K.; Toda, K. *Anal. Chem.* **2012,** *84,* 5421-5426.
(196) S. Fekete, I. Kohler, S. Rudaz, D. Guillarme. *J Pharmaceut Biomed*, 87, **2014**, 105-119.
(197) C.A. Lucy, M.F. Wahab. *Lc Gc Eur*, **2013**, 38-42.
(198)D.C. Patel, Z.S. Breitbach, M.F. Wahab, C.L. Barhate, D.W. Armstrong. *Analytical Chemistry*, **2015**, DOI: 10.1021/acs.analchem.5b00715.
(199) J.C. Giddings, R.A. Keller, Extracolumn contributions to chromatographic band broadening, Marcel Dekker, New York, 1966.
(200) H. Elgass, H. Engelhardt, I. Halász, Reproduzierbare Methode zum Packen von Trennsäulen für die Chromatographie mit Kieselgel (5–10 µm), Z. Anal. Chem., 294 (1979) 97-106.
(201) P. Hatsis, C.A. Lucy, Ultra-fast HPLC separation of common anions using a monolithic stationary phase, Analyst, 127 (2002) 451-454.
(202) J.J. Kirkland, Ultrafast Reversed-Phase High-Performance Liquid Chromatographic Separations: An Overview, Journal of Chromatographic Science, 38 (2000) 535-544.
(203) S. Fekete, K. Ganzler, J. Fekete, Efficiency of the new sub-2µm core–shell (Kinetex™) column in practice, applied for small and large molecule separation, J Pharmaceut Biomed, 54 (2011) 482-490.
(204) F. Gritti, S.J. Shiner, J.N. Fairchild, G. Guiochon, Evaluation of the kinetic performance of new prototype 2.1 mm narrow-bore columns packed with 1.6 µm superficially porous particles, Journal of Chromatography A, 1334 (2014) 30-43.
(205) T.H. Walter, R.W. Andrews, Recent innovations in UHPLC columns and instrumentation, TrAC Trends in Analytical Chemistry, 63 (2014) 14-20.
(206) S.N. Chesler, S.P. Cram, Effect of Peak Sensing and Random Noise on Precision and Accuracy of Statistical Moment Analyses from Digital Chromatographic Data, Analytical Chemistry, 43 (1971) 1922-&.

(207)P.C. Kelly, G. Horlick, Practical Considerations for Digitizing Analog Signals, Analytical Chemistry, 45 (1973) 518-527.
(208)N. Dyson, Peak distortion, data sampling errors and the integrator in the measurement of very narrow chromatographic peaks, Journal of Chromatography A, 842 (1999) 321-340.
(209)B.G. Vandeginste, D.L. Massart, L.M. Buydens, S.D. Jong, P. Lewi, J. Smeyers-Verbeke, Handbook of Chemometrics and Qualimetrics: Part B. Volume 20 B in Data Handling in Science and Technology Elsevier, Amsterdam, 1998.
(210)M. Goedert, G. Guiochon, Sources of error in chromatographic analysis. Effect of sampling parameters on the accuracy of numerical measurements, Chromatographia, 6 (1973) 76-83.
(211)H.J.G. Debets, A.W. Wijnsma, D.A. Doornbos, H.C. Smit, The Usefulness of the Deconvolution of Chromatograms into Orthogonal Polynomials for Characterizing the Quality of Separation, Anal Chim Acta, 171 (1985) 33-43.
(212)K.L. Rowlen, K.A. Duell, J.P. Avery, J.W. Birks, Whole column detection: application to high-performance liquid chromatography, Analytical Chemistry, 61 (1989) 2624-2630.
(213)J.M. Anderson, Data Acquisition and Processing for High-Speed Liquid-Chromatography, J Liq Chromatogr, 6 (1983) 2809-2828.
(214) P.K. Dasgupta, Y.J. Chen, C.A. Serrano, G. Guiochon, H.H. Liu, J.N. Fairchild, R.A. Shalliker, Black Box Linearization for Greater Linear Dynamic Range: The Effect of Power Transforms on the Representation of Data, Analytical Chemistry, 82 (2010) 10143-10150.
(215) R.A. Shalliker, P.G. Stevenson, D. Shock, M. Mnatsakanyan, P.K. Dasgupta, G. Guiochon, Application of power functions to chromatographic data for the enhancement of signal to noise ratios and separation resolution, Journal of Chromatography A, 1217 (2010) 5693-5699.
(216) D. Shock, G.R. Dennis, G. Guiochon, P.K. Dasgupta, R.A. Shalliker, Anomalies in evaporative light scattering detection, Anal Chim Acta, 703 (2011) 245-249.
(217) E.T. Whittaker, XVIII.—On the Functions which are represented by the Expansions of the Interpolation-Theory, Proceedings of the Royal Society of Edinburgh, 35 (1915) 181-194.

(218) H.D. Luke, The origins of the sampling theorem, Communications Magazine, IEEE, 37 (1999) 106-108.
(219) C.E. Shannon, Communication in the Presence of Noise, Proceedings of the IRE, 37 (1949) 10-21.
(220)R.M.C. Luciano da Fona Costa, Jr., Shape Classification and Analysis: Theory and Practice, 2nd ed., CRC Press, Taylor and Francis Group, Boca Raton, FL, 2009.
(221)R.G. Mortimer, Mathematics for Physical Chemistry, 4th ed., Academic Press, Amsterdam, 2013.
(222)R.G. Lyons, Understanding Digital Signal Processing, 3rd ed., Prentice Hall 2010.
(223)D. Schlichthärle, Digital Filters: Basics and Design, 2 ed., Springer Verlag, Berlin Heidelberg, 2011.
(224)K.J. Fountain, U.D. Neue, E.S. Grumbach, D.M. Diehl, Effects of extra-column band spreading, liquid chromatography system operating pressure, and column temperature on the performance of sub-2-μm porous particles, Journal of Chromatography A, 1216 (2009) 5979-5988.
(225)Kraiczek, K., Agilent Technologies, Germany. Personal communication July 2015
(226)Method E 1657: Standard Practice for Testing Variable-Wavelength Photometric Detectors Used in Liquid Chromatography
(227)C.G.E. Howard V. Malmstadt, Stanley R. Crouch, Microcomputers and Electronic Instrumentation-Making the Right Connections, American Chemical Society, Washington DC, 1994.
(228)P.K. Dasgupta, Chromatographic peak resolution using Microsoft Excel Solver: The merit of time shifting input arrays, Journal of Chromatography A, 1213 (2008) 50-55.
(229)A. Kadjo, P.K. Dasgupta, Tutorial: Simulating chromatography with Microsoft excel macros, Anal Chim Acta, 773 (2013) 1-8.
(230)F.X. Diebold, Elements of Forecasting, 4 ed., Thomson Higher Education, Mason, 2006.
(231)N.D. Laude, C.W. Atcherley, M.L. Heien, Rethinking Data Collection and Signal Processing. 1. Real-Time Oversampling Filter for Chemical Measurements, Analytical Chemistry, 84 (2012) 8422-8426.

(232)Texas Instruments; Direct RF-Sampling ADCs Sample Beyond 3.0 GHz, http://www.ti.com/lsds/ti/data-converters/high-speed-adc-greater-than-1gsps-rf-sampling.page
(233)A. Felinger, A. Kilar, B. Boros, The myth of data acquisition rate, Anal Chim Acta, 854 (2015) 178-182.
(234)J.C. Russ, The Image Processing Handbook, CRC Press, Taylor and Francis Group, Boca Raton, FL, 2011.
(235)L. M. Kegelmeyer, P.W. Fonga , S.M. Glenna, J. A. Liebmana, Local Area Signal-to-Noise Ratio (LASNR) algorithm for Image Segmentation, http://ai.stanford.edu/~fongpwf/LASNR11_spie_6696-85-o.pdf
(236)D. Bissieres, I. Campbell, Y. Lesperat, Analog to Digital Converter, http://ume.gatech.edu/mechatronics_course/ADC_F04.ppt (accessed August 2015)
(237)S. Butterworth, On the theory of filter amplifiers, Wireless Engineer, 7 (1930) 536-541.
(238)Maxim Integrated, Tutorial 733, Filter Primer, http://www.maximintegrated.com/en/app-notes/index.mvp/id/733 (accessed july 2015)
(239)S.W. Smith, The Scientist and Engineer's Guide to Digital Signal Processing; Chapter 15, Moving Average Filter, 1st edition ed., California Technical Pub San Diego, California, 1997.
(240)G.J. Butterworth, Effect of Detector Response Time on Distortion of Spectral Peaks of Gaussian Shape, J Phys E Sci Instrum, 1 (1968) 1165-&.
(241)J.V. Hinshaw, Handling fast peaks, LC-GC North America, 21 (2003) 268.
(242)R.A. Shalliker, S. Kayillo, G.R. Dennis, Optimizing Chromatographic Separation: An Experiment Using an HPLC Simulator, Journal of Chemical Education, 85 (2008) 1265.
(243)V.R. Meyer, Practical High-Performance Liquid Chromatography, Wiley, West Sussex, England, 1994.
(244)H.-J.K. Stavros Kromidas, Quantification in LC and GC: A Practical Guide to Good Chromatographic Data, Wiley VCH Verlah, Weinheim, 2009.
(245) Bidlingmeyer, B. A.; Deming, S. N.; Price, W. P., Jr.; Sachok, B.; Petrusek, M. *J. Chromatogr.* **1979,** *786,* 419-434.

(246) Bidlingmeyer, B. A. *J. Chromatogr. Sci.* **1980,** *18,* 525-539.

(247) Dasgupta, P. K. in "Ion Chromatography", Tarter, J. G., Ed.; Marcel-Dekker, 1987. P253-272.

(248) Snyder, L. R.; Glajch, J. L.; Kirkland, J. J. *Practical HPLC Method Development,* 2nd ed. Wiley, New York, 1997. P 317-341.

(249) Miller, C.; Fischer, S. "Impact of Ion-Pair Reagents on LC/MS Analysis." Agilent publication number 5968-8659E, January 2000. http://www.chem.agilent.com/Library/applications/5968-8659E.pdf Accessed November 12, 2009

(250) Holčapek, M.; Volna´ K.; Jandera, P.; Kolářová , Lemr, K.; Exner, M.; Ci'rkva, A. *J. Mass Spectrom.* **2004,** *39*, 43–50.

(251) Aruda, K. O. Aruda, W. O. *LC•GC North America, 28, 626-636,* August, 2009. http://www.chromatographyonline.com/node/222690?id=&sk=&date=&pageID=6 Accessed April 1, 2015.

(252) Lu W.; Bennett B. D.; Rabinowitz J. D. *J. Chromatogr.* B, **2008,** *871,* 236-242.

(253)Coulier, L.; Bas, R.; Jespersen, S.; Verheij, E.; van der Werf, M. J.; Hankemeier, T. *Anal Chem.* **2006**, *78*, 6573-6582.

(254) Coulier, L.; Bas, R.; Hekman, M.; van der Werff, B. J. C.; Burgering, M.; Thissen, U. *J. Food Sci.* **2011,** *76,* C1081–C1087.

(255) Ito, S.; Nakata, F.; Sawada, Y. Poster 291, Session LC/MS II, ASMS 2008, Denver, CO, USA. http://kinesis-australia.com.au/wp-content/uploads/downloads/2013/03/TP137.pdf Accessed April 1, 2015.

(256) Socher, G.; Nussbaum, R.; Rissler,K.; Lankmayr, E. *Chromatographia,* **2001,** *54,* 65-70.

(257) Liu, H.; Cantwell, F. F. *Anal. Chem.* **1991,** *63,* 2032-2037.

(258) Liu, H. Lam, L. "Transient ion-pair chromatography for ESI-MS", HPLC 2010, Boston, June, 2010.

(259) Dolan, J. W. *LCGC Europe* **2008,** *21(5)*, 258-263.